

2011

Dynamic Harmonic Domain Modeling of Flexible Alternating Current Transmission System Controllers

Bharat GNVS R Vyakaranam
Cleveland State University

Follow this and additional works at: <https://engagedscholarship.csuohio.edu/etdarchive>

 Part of the [Electrical and Computer Engineering Commons](#)

How does access to this work benefit you? Let us know!

Recommended Citation

Vyakaranam, Bharat GNVS R, "Dynamic Harmonic Domain Modeling of Flexible Alternating Current Transmission System Controllers" (2011). *ETD Archive*. 298.

<https://engagedscholarship.csuohio.edu/etdarchive/298>

This Dissertation is brought to you for free and open access by EngagedScholarship@CSU. It has been accepted for inclusion in ETD Archive by an authorized administrator of EngagedScholarship@CSU. For more information, please contact library.es@csuohio.edu.

**DYNAMIC HARMONIC DOMAIN MODELING OF FLEXIBLE
ALTERNATING CURRENT TRANSMISSION SYSTEM
CONTROLLERS**

BHARAT G N V S R VYAKARANAM

Bachelor of Technology in Electrical Engineering

Jawaharlal Nehru Technological University, Hyderabad, India

December, 2001

Master of Technology (Electrical Power Systems)

Jawaharlal Nehru Technological University, Anantapur, India

May, 2005

Submitted in partial fulfillment of requirements for the degree

DOCTOR OF ENGINEERING

at the

CLEVELAND STATE UNIVERSITY

October, 2011

This dissertation has been approved
for the Department of Electrical and Computer Engineering
and the College of Graduate Studies by

Advisor, Dr. F. Eugenio Villaseca

Department/Date

Dissertation Committee Chairperson, Dr. Ana Stankovic

Department/Date

Committee Member, Dr. Charles Alexander

Department/Date

Committee Member, Dr. Dan Simon

Department/Date

Committee Member, Dr. Lili Dong

Department/Date

Committee Member, Dr. James Lock

Department/Date

ACKNOWLEDGMENTS

The completion of this dissertation marks the end of an invaluable, positive learning experience. There are a number of people that I would like to acknowledge for their direct or indirect contribution to this dissertation. First and foremost, my sincere thanks to my advisor, Dr. Eugenio F. Villaseca, for his guidance, enthusiastic support, advice and encouragement.

Many thanks are also due to Drs. Charles Alexander, Dan Simon, Ana Stankovic, Lili Dong, and James Lock for their thoughtful discussions and suggestions.

My dearest friend Rick has patiently endured countless discussions and advice giving suggestions. Your advice, help and support in many occasions has rescued and inspired me. I am and will be immensely grateful for your friendship and precious time.

I thank my department secretaries Adrienne Fox and Jan Basch for their administrative assistance.

I would also like to express my gratefulness to my wife, Satya Subha Vyakaranam, for her support, love and encouragement throughout the course of study.

"The love of a family is life's greatest thing". These acknowledgments are incomplete without thanking my parents and other family members whose continual support, love and blessings have been and will always be my strengths.

DYNAMIC HARMONIC DOMAIN MODELING OF FLEXIBLE ALTERNATING CURRENT TRANSMISSION SYSTEM CONTROLLERS

BHARAT G N V S R VYAKARANAM

ABSTRACT

Flexible alternating current transmission system (FACTS) and multi-line FACTS controllers play an important role in electrical power transmission systems by improving power quality and increasing power transmission capacity. These controllers are nonlinear and highly complex when compared to mechanical switches. Consequently, during transient conditions, it is very difficult to use conventional time and frequency domain techniques alone to determine the precise dynamic behavior of the harmonics introduced into the system by these controllers. In particular, the time-varying nature of the harmonic components is not captured by these techniques. The contribution of this work to the state of power systems analysis is the development of new models for seven important and widely-used FACTS controllers (static synchronous series compensator (SSSC), unified power flow controller (UPFC), fixed capacitor-thyristor controlled reactor (FC-TCR), thyristor controlled switched capacitor (TCSC), generalized unified power flow controller (GUPFC), interline power flow controller (IPFC), and generalized interline power flow controller (GIPFC)) using a technique called the *dynamic harmonic domain* method. These models are more accurate than existing models and aid the power

systems engineer in designing improved control systems. The models were simulated in the presence of disturbances to show the evolution in time of the harmonic coefficients and power quality indices. The results of these simulations show the dynamic harmonic response of these FACTS controllers under transient conditions in much more detail than can be obtained from time-domain simulations, and they can also be used to analyze system performance under steady-state conditions. Some of the FACTS controllers' models discussed in this work have a common DC link, but for proper operation, the DC side voltage must be held constant. The dynamic harmonic domain method was applied to the FACTS devices to design feedback controllers, which help in maintaining constant DC side voltage. It allows us to see the effect of the control circuit on power quality indices, thus giving more insight into how the controllers react to the control circuit. This detailed information about dynamic harmonic response is useful for power quality assessment and can be used as a tool for analyzing the system under the steady state and transient conditions and designing better control circuits.

TABLE OF CONTENTS

| | Page |
|--|-------------|
| NOMENCLATURE | xii |
| LIST OF TABLES | xiv |
| LIST OF FIGURES | xv |
| CHAPTER I..... | 1 |
| INTRODUCTION | 1 |
| 1.1 Motivation for the research..... | 1 |
| 1.2 Background..... | 4 |
| 1.2.1 The transmission system problem..... | 6 |
| 1.2.2 The transmission system solution | 9 |
| 1.2.3 No free lunch – nonlinearities, distortion, and chaos..... | 10 |
| 1.2.4 Description and classification of FACTS controllers | 11 |
| 1.2.5 Multi-line FACTS controllers..... | 19 |
| 1.3 Dissertation objectives | 26 |
| 1.4 Outline..... | 27 |
| CHAPTER II..... | 29 |
| A REVIEW OF GENERAL HARMONIC TECHNIQUES | 29 |
| 2.1 Introduction..... | 29 |

| | | |
|--|--|-----|
| 2.2 | Time domain modeling | 30 |
| 2.3 | Harmonic domain modeling | 31 |
| 2.3.1 | Linearization of a simple nonlinear relation | 33 |
| 2.3.2 | Dynamic relations | 43 |
| 2.2.3 | Norton equivalent circuit | 45 |
| 2.3 | Conclusion | 47 |
| CHAPTER III | | 48 |
| FACTS CONTROLLERS MODELING IN DYNAMIC HARMONIC DOMAIN..... | | 48 |
| 3.1 | Introduction..... | 48 |
| 3.2 | Dynamic harmonic domain method..... | 50 |
| 3.3 | Selective harmonic elimination..... | 54 |
| 3.4 | Static synchronous series compensator..... | 61 |
| 3.4.1 | Development of the DHD model of the SSSC..... | 62 |
| 3.4.2 | Simulation of the proposed SSSC model..... | 65 |
| 3.5 | Sequence components..... | 75 |
| 3.6 | Unified power flow controller | 80 |
| 3.6.1 | Development of the DHD model of the UPFC | 82 |
| 3.6.2 | Simulation of the proposed UPFC model | 87 |
| 3.6.3 | Validation of the proposed DHD model of the UPFC | 101 |

| | | |
|---|--|-----|
| 3.7 | Fixed capacitor-thyristor controlled reactor..... | 104 |
| 3.7.1 | Development of the DHD model of the FC-TCR..... | 105 |
| 3.7.2 | Simulation of the proposed FC-TCR model..... | 108 |
| 3.8 | Thyristor-controlled series controller | 111 |
| 3.8.1 | Simulation of the proposed TCSC model..... | 113 |
| 3.9 | Conclusion | 119 |
| CHAPTER IV | | 120 |
| DYNAMIC HARMONIC DOMAIN MODELING OF MULTI-LINE POWER FLOW CONTROLLERS..... | | 120 |
| 4.1 | Introduction..... | 120 |
| 4.2 | Generalized Unified Power Flow Controller | 122 |
| 4.2.1 | Harmonic domain model of the GUPFC | 123 |
| 4.3.2 | Dynamic harmonic domain model of the GUPFC..... | 126 |
| 4.3.3 | Simulation of the proposed DHD model of GUPFC | 131 |
| 4.3.4 | Validation of the proposed DHD method of the GUPFC | 147 |
| 4.4 | Interline power flow controller | 150 |
| 4.4.1 | Development of the dynamic harmonic domain model of the IPFC | 152 |
| 4.4.2 | Simulation of proposed DHD model of IPFC..... | 154 |
| 4.4.3 | Validation of the proposed DHD model of the IPFC | 165 |
| 4.5 | Generalized interline power flow controller | 167 |

| | | |
|--|--|-----|
| 4.5.1 | Development of the harmonic domain model of the GIPFC | 168 |
| 4.5.2 | Development of the dynamic harmonic domain model of the GIPFC ... | 170 |
| 4.5.3 | Simulation of the proposed DHD model of GIPFC..... | 174 |
| 4.5.4 | Validation of the proposed DHD model of the GIPFC..... | 189 |
| 4.6 | Conclusion | 192 |
| CHAPTER V | | 193 |
| ANALYSIS OF POWER QUALITY INDICES OF THE MULTI-LINE FACTS CONTROLLERS WITH VARIOUS SWITCHING FUNCTIONS..... | | 193 |
| 5.1 | Introduction..... | 193 |
| 5.2 | Pulse width modulation..... | 194 |
| 5.3 | Multi-module switching function | 197 |
| 5.4 | Simulation of the DHD model of the GUPFC with multi-module switching..... | 201 |
| 5.5 | Simulation of the DHD model of the GIPFC with multi-module switching | 208 |
| 5.6 | Comparison of average distortions with various switching functions | 220 |
| 5.7 | Conclusion | 228 |
| CHAPTER VI..... | | 229 |
| CONCLUSIONS AND RECOMMENDATIONS FOR FUTURE WORK..... | | 229 |
| 6.1 | Conclusions..... | 229 |
| 6.2 | Future research work..... | 231 |
| REFERENCES | | 234 |

| | |
|--|-----|
| APPENDICES | 244 |
| APPENDIX A | 245 |
| A.1 Three-phase voltage source converter | 245 |
| A.2 Harmonic domain model of three-phase voltage source converter | 246 |
| APPENDIX B | 248 |
| B.1 Analysis of power quality indices of the GIPFC with various switching functions | 248 |
| APPENDIX C | 261 |
| C.1 Matlab [®] code..... | 261 |

NOMENCLATURE

| | |
|----------|---|
| AC | alternating current |
| DC | direct current |
| CBEMA | computer business equipment manufacturers association |
| CP | custom power devices |
| DHD | dynamic harmonic domain |
| DVR | dynamic voltage restorer |
| DSTATCOM | distribution static synchronous compensator |
| FACTS | flexible AC transmission systems |
| FC-TCR | fixed capacitor, thyristor-controlled reactor |
| FFT | fast Fourier transform |
| GTO | gate turn off thyristor |
| GUPFC | generalized unified power flow controller |
| GIPFC | generalized interline power flow controller |
| HD | harmonic domain |
| HVDC | high voltage direct current transmission |
| IGBT | insulated gate bipolar transistor |
| IPFC | interline power flow controller |
| LTI | linear time invariant |
| LTP | linear time periodic |
| MPWM | multi-pulse pulse width modulation |
| PCC | point of common coupling |
| PF | power factor |
| PI | proportional plus integral |
| PWM | pulse width modulation |
| RMS | root mean square |
| STATCOM | static synchronous compensator |
| SSSC | static synchronous series compensator |
| SVC | static var compensator |
| TCR | thyristor-controlled reactor |

| | |
|--|---|
| TCSC | thyristor-controlled series compensator |
| THD | total harmonic distortion |
| UPFC | unified power flow controller |
| UPQC | unified power quality conditioner |
| VSC | voltage source converter |
| WFFT | windowed fast Fourier transform |
| p.u. | per unit |
| s | Seconds |
| ms | Milliseconds |
| H | Henries |
| mH | Millihenries |
| F | Farads |
| μF | Microfarads |
| V | Volts |
| A | Amperes |
| h | harmonic order |
| \otimes | convolution operator |
| t | Time |
| k | iteration counter |
| j | $\sqrt{-1}$ |
| e | Exponential |
| R | series resistance in Ω |
| L | series inductance in H |
| C | shunt capacitance in F |
| ω_0 | angular frequency in rad/s |
| f_0 | fundamental frequency |
| $\mathbf{D}(j\hbar\omega_0)$ | matrix of differentiation |
| \mathbf{U} | identity matrix |
| $v(t)$ | time domain voltage waveform |
| $i(t)$ | time domain current waveform |

Bold face type represents matrix quantities in this dissertation.

LIST OF TABLES

| TABLE | Title | Page |
|--------------|---|-------------|
| I | Significant waveform distortions associated with poor power quality | 8 |
| II | Four quarter switching angles | 58 |
| III | Absolute values of harmonic coefficients | 60 |
| IV | Power quality parameters | 70 |
| V | Harmonics in the sequence components | 78 |
| VI | Configuration of different switching functions | 201 |
| VII | THD in current of VSCs of the GUPFC through steady state | 204 |
| VIII | THD in voltage of VSCs of the GUPFC through steady state | 206 |
| IX | Distortion power outputs of VSCs of the GUPFC through steady state | 208 |
| X | Selected switching functions | 213 |
| B-I | Distortion power output | 250 |
| B-II | Apparent power output | 252 |
| B-III | Active power output | 254 |
| B-IV | Reactive power output | 256 |
| B-V | RMS value of output current | 258 |
| B-VI | THD in output current | 260 |

LIST OF FIGURES

| Figure | Title | Page |
|---------------|--|-------------|
| 1 | General power system | 4 |
| 2 | A 500 kV static var compensator, Allegheny power, Black Oak substation, Maryland USA [31] | 5 |
| 3 | Single line diagram of two-bus system | 12 |
| 4 | (a) Static synchronous series compensator (b) equivalent circuit | 15 |
| 5 | (a) Thyristor controlled series controller (b) equivalent circuit | 16 |
| 6 | (a) Fixed capacitor thyristor-controlled reactor (b) equivalent circuit | 17 |
| 7 | (a) Unified power flow controller (b) equivalent circuit | 19 |
| 8 | (a) Generalized unified power flow controller (b) equivalent circuit | 21 |
| 9 | (a) Interline power flow controller (b) equivalent circuit | 23 |
| 10 | (a) Generalized interline power flow controller (b) equivalent circuit | 25 |
| 11 | Norton equivalent circuit | 46 |
| 12 | Harmonic input-output relationship | 47 |
| 13 | Generalized output waveform of a full-bridge inverter with normalized magnitude | 55 |
| 14 | Switching function waveform | 59 |
| 15 | Harmonic content of the switching waveform | 61 |
| 16 | Static synchronous series compensator | 62 |
| 17 | The phase <i>a</i> current of VSC (a) Harmonic content of disturbance interval (b) Time domain representation (c) Harmonic content of phase <i>a</i> voltage (d) Time domain representation of voltage | 67 |
| 18 | DC side voltage (a) Time domain representation (b) Harmonic content of disturbance interval | 68 |
| 19 | Power cube | 71 |
| 20.1 | Power quality indices (a) RMS values of the output currents (b) RMS values of the output voltages (c) Per-phase output apparent powers (d) Per-phase output active powers | 73 |
| 20.2 | Power quality indices (a) Per-phase output reactive powers (b) Per-phase output distortion powers of VSC 2 | 74 |
| 21 | Total harmonic distortion (a) in current (IABC) (b) in voltage (VABC1) | 74 |

| | | |
|------|--|-----|
| 22.1 | Sequence currents of SSSC: Harmonic content of disturbance interval (a) Positive sequence (b) Zero sequence | 79 |
| 22.2 | Sequence currents of SSSC: Harmonic content of disturbance interval (c) Negative sequence | 80 |
| 23 | Unified power-flow controller | 81 |
| 24 | Control system | 88 |
| 25 | DC side voltage in UPFC (a) Without control system (b) With control system | 89 |
| 26.1 | The THD in (a) The per-phase output voltages of VSC 2 (without control) (b) The per-phase output voltages of VSC 2 (with control) (c) The per-phase output voltages of VSC 1 (without control) (d) The per-phase output voltages of VSC 1 (with control) | 91 |
| 26.2 | The THD in (a) The per-phase output currents of VSC 2 (without control) (b) The per-phase output currents of VSC 2 (with control) | 92 |
| 27.1 | Power quality indices (a) RMS values of the output currents of VSC 1 (b) Per-phase output apparent powers of VSC 1 (c) Per-phase output reactive powers of VSC 2 (d) Per-phase output apparent powers of VSC 2 | 93 |
| 27.2 | Power quality indices (a) RMS values of the output voltages of VSC 2 (b) Per-phase output distortion powers of VSC 2 | 94 |
| 28 | Harmonic content of VSC 1 of (a) The output voltage of phase <i>c</i> (b) The output current of phase <i>a</i> | 95 |
| 29 | Time domain waveforms of VSC 1 of (a) The output current of phase <i>a</i> , (b) The output voltage of phase <i>c</i> | 96 |
| 30 | Harmonic content of VSC 2 of phase <i>a</i> (a) Output voltage (b) Output current | 97 |
| 31 | Time domain waveforms of VSC 2 of phase <i>a</i> (a) output voltage (b) output current | 98 |
| 32 | Positive sequence currents of (a) VSC 1 (b) VSC 2 | 99 |
| 33 | Zero sequence currents of (a) VSC 1 (b) VSC 2 | 100 |
| 34 | Negative sequence currents of (a) VSC 1 (b) VSC 2 | 101 |
| 35 | DHD and time domain results comparison of (a) VSC 1 (b) VSC 2 | 103 |
| 36 | Static VAR compensator | 104 |
| 37 | Voltages and currents (a) The TCR output currents of phase <i>a</i> (b) The TCR output voltages of phase <i>a</i> (c) The RMS values of the per-phase output currents of the FC-TCR (d) the RMS values of the per-phase output voltages of the FC-TCR | 110 |

| | | |
|------|--|-----|
| 38 | Electrical power quantities of FC-TCR (a) Per-phase output apparent powers (b) Per-phase output reactive powers | 111 |
| 39 | Thyristor-controlled series controller | 112 |
| 40 | TCSC equivalent circuit | 112 |
| 41.1 | Voltages and currents of the TCSC (a) The harmonic content of the output currents of phase <i>a</i> (b)) The harmonic content of the output voltage of phase <i>a</i> (c) The harmonic content of the RMS value of the output currents (d) The harmonic content of the RMS value of the output voltages | 115 |
| 41.2 | Voltages and currents of the TCSC (a) The output current waveform of phase <i>a</i> (b) The output voltage waveform of phase <i>a</i> | 116 |
| 42 | Power quality indices at the terminals of TCSC (a) Per-phase output apparent powers (b) Per-phase output reactive powers | 117 |
| 43.1 | Dynamic sequence currents of the TCSC (a) Zero sequence (b) Positive sequence | 118 |
| 43.2 | Dynamic sequence currents of the TCSC (a) Negative sequence | 119 |
| 44 | Generalized unified power controller | 122 |
| 45 | DC-side voltage of GUPFC: (a) Without control system (b) With control system | 133 |
| 46 | The RMS value of the output currents of VSC 1 (a) With control system (b) Without control system | 134 |
| 47 | The THD in output currents of VSC 2 (a) With control system (b) Without control system | 135 |
| 48 | The output reactive powers of each phase of VSC 1 (a) With control system (b) Without control system | 135 |
| 49.1 | Power quality indices (a) THD in output currents of VSC 1 (b) Per-phase output reactive powers of VSC 3 (c) Per-phase output active powers of VSC 1 (d) RMS values of the output currents of VSC 2 | 137 |
| 49.2 | Power quality indices (a) RMS values of the output currents of VSC 3 (b) Per-phase output apparent powers of VSC 3 | 138 |
| 50 | The output voltage of phase <i>a</i> of VSC 2 (a) Voltage waveform (b) Voltage harmonic content | 139 |
| 51 | The output voltage of phase <i>a</i> of VSC 3 (a) Voltage waveform (b) Voltage harmonic content | 140 |
| 52 | The harmonic content of output current of phase <i>a</i> of (a) VSC 2 (b) VSC 3 | 141 |
| 53 | Time domain waveforms of output currents of phase <i>a</i> of (a) VSC 2 (b) VSC 3 | 142 |
| 54 | The zero sequence currents of (a) VSC 1 (b) VSC 2 (c) VSC 3 | 143 |

| | | |
|------|--|-----|
| 55.1 | Positive sequence currents of (a) VSC 1 (b) VSC 2 | 144 |
| 55.2 | Positive sequence currents of (a) VSC 3 | 145 |
| 56 | The negative sequence currents of (a) VSC 1 (b) VSC 2 (c) VSC 3 | 146 |
| 57 | Time domain waveform of the positive sequence currents of (a) VSC 1 (b) VSC 2 | 147 |
| 58.1 | Time domain waveforms of currents of each phase of (a) VSC 1 | 148 |
| 58.2 | Time domain waveforms of currents of each phase of (a) VSC 2 (b) VSC 3 | 149 |
| 59 | Interline power flow controller | 150 |
| 60 | DC-side voltage of IPFC (a) Without control system (b) With control system | 156 |
| 61 | The THD in the output currents of VSC 1 (a) Without control system (b) With control system | 157 |
| 62 | The output current of phase <i>a</i> of VSC 1 (a) Current waveform (b) Current harmonic content | 158 |
| 63 | The output voltage of phase <i>a</i> of VSC 1 (a) Voltage waveform (b) Voltage harmonic content | 158 |
| 64 | The output voltage of phase <i>a</i> of VSC 2 (a) Voltage waveform (b) Voltage harmonic content | 159 |
| 65 | The output current of phase <i>a</i> of VSC 2 (a) Current waveform (b) Current harmonic content | 160 |
| 66 | Power quality indices (a) RMS values of the output currents of VSC 1 (b) RMS values of the output voltages of VSC 1 (c) Per-phase output apparent powers of VSC 1 (d) RMS values of the output currents of VSC 2 | 161 |
| 67 | The zero sequence currents of (a) VSC 1 (b) VSC 2 | 162 |
| 68 | The positive sequence currents of (a) VSC 1 (b) VSC 2 | 163 |
| 69 | The negative sequence currents of (a) VSC 1 (b) VSC 2 | 164 |
| 70 | Time domain waveforms of currents of each phase of (a) VSC 1 and (b) VSC 2 | 166 |
| 71 | Generalized interline power flow controller | 167 |
| 72 | DC-side voltage of GIPFC, (a) Without control system (b) With control system | 176 |
| 73 | THD in output currents of VSC 1 (a) With control system (b) Without control system | 177 |
| 74 | The harmonic content of output voltage of phase <i>a</i> of VSC 1 (a) With control system (b) Without control system | 178 |

| | | |
|------|---|-----|
| 75 | The harmonic content of output current of phase <i>a</i> of VSC 2 (a) With control system (b) Without control system | 178 |
| 76.1 | Power quality indices (a) The per-phase output reactive powers of VSC 2 (b) The per-phase output active powers of VSC 2 (c) The per-phase output reactive powers of VSC 4 (d) The per-phase output active powers of VSC 4 | 180 |
| 76.2 | Power quality indices (a) The per-phase output reactive powers of VSC 3 (b) The per-phase output active powers of VSC 1 | 181 |
| 77 | Power quality indices (a) THD in output currents of VSC 2 (b) THD in output currents of VSC 3 (c) RMS values of output currents of VSC 2 (d) RMS values of output currents of VSC 4 | 182 |
| 78 | The output voltages of Phase <i>b</i> of VSC 1 (a) Voltage waveform (b) Voltage harmonic content | 183 |
| 79 | The output voltages of phase <i>a</i> of VSC 4 (a) Voltage waveform (b) Voltage harmonic content | 183 |
| 80 | The harmonic content of output current of phase <i>a</i> of (a) At VSC 3 (b) At VSC 4 | 184 |
| 81 | Time domain waveforms of output currents of phase <i>a</i> of (a) VSC 1 (b) VSC 4 | 185 |
| 82 | The negative sequence currents of (a) VSC 1 (b) VSC 2 | 186 |
| 83 | The positive sequence currents of (a) VSC 1 (b) VSC 2 | 187 |
| 84 | The zero sequence currents of (a) VSC 1 (b) VSC 2 | 188 |
| 85 | Time domain waveforms of the positive sequence currents of (a) VSC 1 (b) VSC 2 (c) VSC 3 (d) VSC 4 | 189 |
| 86.1 | Time domain waveforms of currents of each phase of (a) VSC 1 (b) VSC 2 | 190 |
| 86.2 | Time domain waveforms of currents of each phase of (a) VSC 3 (b) VSC 4 | 191 |
| 87 | Unipolar voltage switching function (a) with one PWM converter (b) Harmonic content of the switching waveform | 196 |
| 88 | Unipolar voltage switching function (a) with two PWM converters (b) Harmonic content of the switching waveform | 198 |
| 89 | Unipolar voltage switching function (a) with three PWM converters (b) Harmonic content of the switching waveform | 200 |
| 90 | ITHD in VSC 1 output current (a) Type 1 (b) Type 2 (c) Type 3 (d) ITHD in steady state of VSC 1 | 203 |
| 91 | THD in VSC 1 output voltage (a) Type 1 (b) Type 2 (c) Type 3 (d) THD in steady state voltage of VSC 1 | 205 |

| | | |
|-------|---|-----|
| 92 | Distortion power output of VSC 3 (a) Type 1 (b) Type 2 (c) Type 3 (d) Distortion power in steady state of VSC 3 | 207 |
| 93 | Switching function - Case C (a) with three PWM converters (b) Harmonic content of the switching waveform | 210 |
| 94 | Switching function - Case D (a) with three PWM converters (b) Harmonic content of the switching waveform | 212 |
| 95 | DC voltage (a) Case A (b) Case B (c) Case C (d) Case D | 215 |
| 96 | Magnitude of DC component of DC voltage during steady state | 216 |
| 97 | Distortion power output of all four VSCs | 217 |
| 98 | Apparent power output of all four VSCs | 218 |
| 99 | THD in output voltage of VSC 1 | 219 |
| 100 | THD in output current of VSC 1 | 219 |
| 101 | The average change in per-phase RMS values of VSC 4 of (a) The output current (b) The output voltage | 222 |
| 102.1 | The average change in per-phase output (a) Apparent power (b) Active power | 224 |
| 102.2 | The average change in per-phase output (a) Reactive power (b) Distortion power of VSC 4 | 225 |
| 103 | The average change in per-phase THD in output (a) Voltage of VSC 4 (b) Current of VSC 4 | 227 |
| A-1 | Three-phase voltage source converter | 245 |
| B-1 | RMS value of output current of all VSCs | 249 |
| B-2 | Distortion power output of all VSCs | 251 |
| B-3 | Apparent power output of all VSCs | 253 |
| B-4 | Active power output of all VSCs | 255 |
| B-5 | Reactive power output of all VSCs | 257 |
| B-6 | THD in current of all VSCs | 259 |

CHAPTER I

INTRODUCTION

1.1 Motivation for the research

Over the last few decades, the use of semiconductor devices in large-scale power systems has spread around the world due to the increased ratings of these devices, and resulting in an area of academic study we now call high-power electronics [1], [2]. These devices are used to improve the electrical and economic performance of power transmission systems, which the electric utilities companies use to deliver electricity to their customers [3]. But since they are nonlinear devices, they produce undesirable distortions in the voltage and current waveforms in the circuits to which they are connected. These distortions also result in the presence of undesirable harmonics [4].

The study of the harmonic content of distorted, but periodic, waveforms via the simulation of time-domain (TD) models require long simulation run times. This is a consequence of the need to let the transients die out and to allow sufficient time, under steady-state conditions, for the accurate calculation of the harmonics via the fast Fourier

transform (FFT) [5]–[10]. During time-varying conditions (transients), the FFT computations lose accuracy due to leakage, aliasing, picket-fence effects, and edge effects [11].

An alternative methodology has been proposed, which models the systems in the harmonic-domain (HD) rather than in the time domain, thus producing models for the steady-state simulation [8]. This has been demonstrated by its application to high-voltage DC (HVDC) transmission systems [12]–[15], and in flexible AC transmission systems (FACTS) such as fixed capacitor-thyristor controlled reactor (FC-TCR) [16], [17], thyristor-controlled reactor (TCR) [18], thyristor-controlled switched capacitors (TCSC) [16], static compensators (STATCOM) [19], [20], static synchronous series compensators (SSSC) [21], and unified power flow controllers (UPFC) [15], [22], [23]. A brief description of each of these FACTS devices is presented in the next section of this chapter. Therefore, the ability to determine the dynamic behavior of harmonics during transient conditions can lead to improved control system designs, which is not possible with either the TD or HD methods [24], [25]. Although the windowed fast Fourier transform (WFFT) method has been proposed for such studies, the accuracy of the harmonic calculations is proportional to window size, especially when disturbance intervals are very short [11].

Recently, a new methodology, the dynamic harmonic domain (DHD) technique, for the modeling and simulation of such systems, has been proposed [24]. The DHD technique, which is an extension of the HD method, allows for the determination of the harmonic content of distorted waveforms, not only in the steady state, but also during transients [15].

The proposed DHD methodology has been demonstrated by its application to the study of the dynamic behavior of harmonics in HVDC [15], TCR [26], and STATCOM [24] systems, and has shown that it has several advantages over the use of the WFFT [24], [26].

However, there are several FACTS devices for which the application of DHD methodology has not been investigated. These include the TCSC, SSSC, UPFC, and more complex devices such as the class of multi-line controllers. Among these are the shunt-series controllers such as the generalized unified power flow controllers (GUPFC), the generalized interline power flow controllers (GIPFC), and the interline power flow controller (IPFC) which is a series-series controller. A brief description of these FACTS devices is also included in the next section of this chapter.

The exciting challenge of the research required to approach these sophisticated systems is the main motivation of this dissertation. This clearly involves learning the HD and the DHD methodologies, the latter of which has not yet appeared in book form, and developing a very clear understanding of the purpose and the means by which these FACTS devices control the flow of power under normal conditions.

1.2 Background

Power systems are generally divided into two regions: the *transmission* region and the *distribution* region (Figure 1).

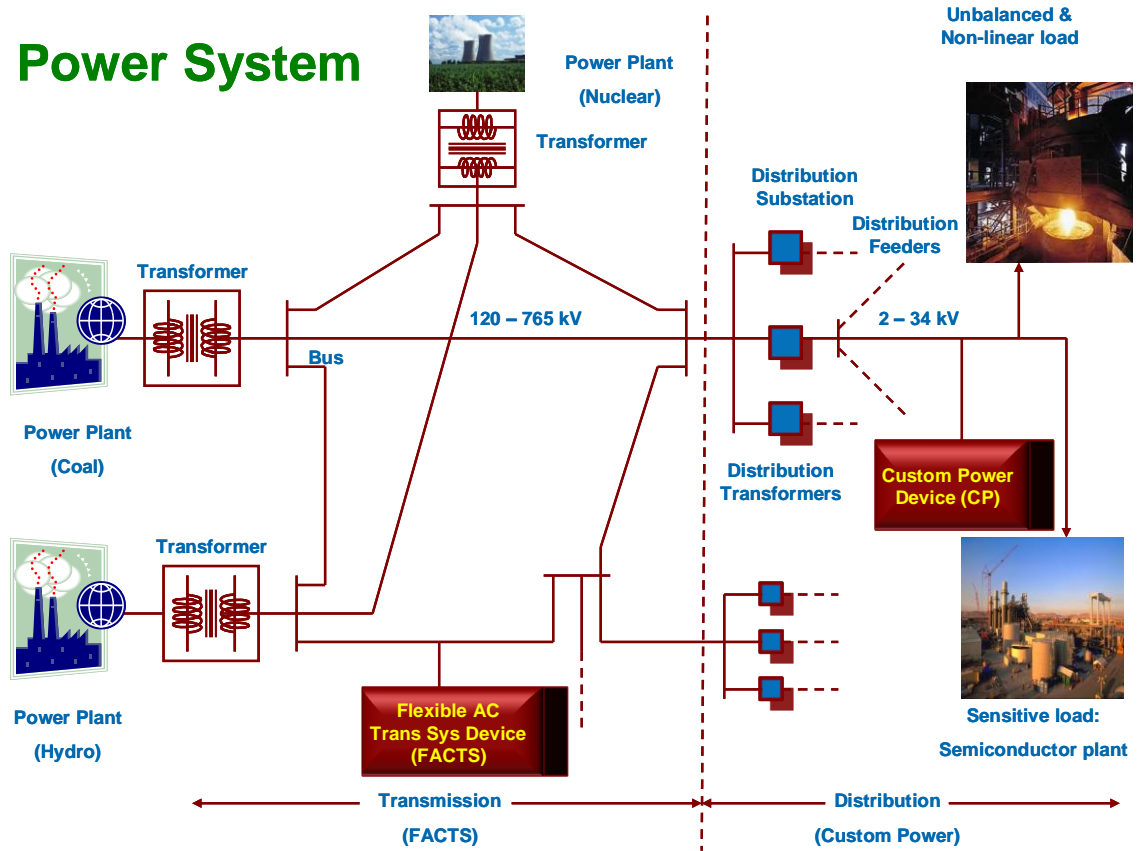


Figure 1: General power system

Power electronic devices fall into one of the two major categories depending on the region in which they are located and their function in the system. Devices which are located in the transmission region are called *flexible AC transmission system* (FACTS) controllers [3] such as the static var compensator (SVC) shown in Figure 2. They operate at very high voltage levels between 120 and 765 kilovolts, and they play an important

role in improving power quality indices, increasing power transmission capacity, and increasing efficiency.



Figure 2: A 500 kV static var compensator, Allegheny power, Black Oak substation, Maryland USA [31]

Devices which are located in the distribution region are called *custom power* (CP) devices [32], [33]. These CP devices are similar to FACTS devices in function, and operate at much lower voltage levels, typically in the range of 2 to 34 kilovolts. They are used near or at sites that have strict requirements on power quality and very low tolerance

for even momentary power quality problems such as voltage sags or interruptions, harmonics in the line voltage, phase unbalance, and flicker in supply voltage [34]. This dissertation will focus on FACTS devices, and CP devices will not be discussed further in the remainder of the work.

1.2.1 The transmission system problem

Except in a very few special situations, electrical energy is generated, transmitted, distributed, and utilized as alternating current (AC). However, alternating current has several distinct disadvantages. One of these is that reactive power must be supplied along with active power to the load. Transmission systems which are carrying heavy loads incur high reactive power losses. This is the major cause of reactive power deficiencies of sufficient magnitude that cause voltage collapse and instability in the system. In order to mitigate voltage instability, it is necessary to inject reactive power into the system dynamically. Restrictions related to voltage stability and reactive power has become an increasing concern for electric utilities. A very important problem in the design and operation of a power system is the maintenance of the voltage and other power quality factors within specified limits at various locations in the system. Therefore, standards have been developed to maintain the performance quality of power transmission systems. The North American Electric Reliability Council (NERC) planning standard states [35]:

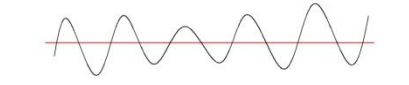
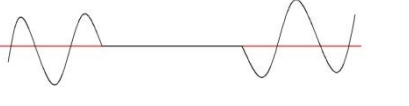
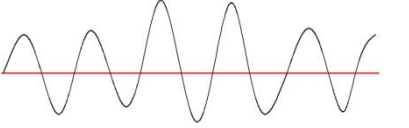
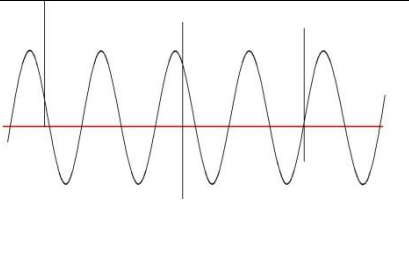
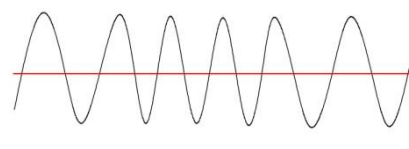
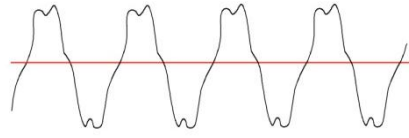
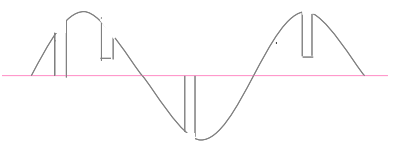
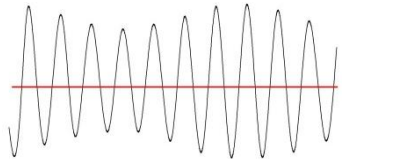
"Proper control of reactive power supply and provision of adequate reactive power supply reserve on the transmission system are required to maintain stability limits and reliable system performance. Entities should plan for

coordinated use of voltage control equipment to maintain transmission voltages and reactive power margin at sufficient levels to ensure system stability within the operating range of electrical equipment.”

Another important (and the most frequent) source of problems in power transmission systems is natural phenomena such as ice storms and lightning. The most significant and critical problems are voltage sags or complete interruptions of the power supply.

The significant waveform distortions associated with poor power quality are depicted in Table I. The IEEE Standards Coordinating Committee (Power Quality) and other international committees [36] recommend that the following technical terms be used to describe main power quality disturbances, as shown in Table I.

Table I: Significant waveform distortions associated with poor power quality [37]—[38]

| | | |
|---|--|--|
| <p>Sag</p> | <p>A decrease in RMS voltage or current for durations of 0.5 cycles or 1 minute</p> |  |
| <p>Interruption</p> | <p>A complete loss of voltage (below 0.1 per-unit) on one or more phase conductors for a certain period of time</p> |  |
| <p>Swell</p> | <p>An increase in RMS voltage or current at power frequency for durations of 0.5 cycles to 1 minute</p> |  |
| <p>Transient</p> | <p>The figure on the right shows typical impulsive transients. These transients have a fast rise time, rising to hundreds or thousands of volts, and a fairly rapid decay. Their typical duration is in the range of nanoseconds to microseconds.</p> |  |
| <p>Frequency Deviation</p> | <p>Deviation of the power system fundamental frequency from its specified nominal value</p> |  |
| <p>Harmonic</p> | <p>A sinusoidal voltage or current having a frequency that is a multiple of the fundamental frequency</p> |  |
| <p>Notch</p> | <p>Periodic voltage disturbance of the normal power voltage waveform, lasting less than a half-cycle. This disturbance is typically in the opposite polarity of the normal waveform. A complete loss of voltage for up to half-cycle is also considered as notching.</p> |  |
| <p>Voltage Fluctuation (Flicker)</p> | <p>Systematic variations in a series of random voltage changes with a magnitude which does not normally exceed the voltage ranges of 0.9 to 1.1 per-unit</p> |  |

1.2.2 The transmission system solution

Flexible AC transmission systems is a term that is used for various types of power electronic devices that control the power flow in high-voltage AC transmission systems. Over the last 30 years, advances in the design of power electronic devices have driven a significant increase in the application of FACTS devices to power systems. In summary, FACTS devices are used to achieve the following major goals [34]:

- Control power flow along desired transmission corridors.
- Increase transmission capacity without requiring new transmission infrastructure.
- Improve dynamic stability, transient stability and voltage stability of the system.
- Provide damping for inter-area oscillations.

Various types of FACTS devices are employed to control different parameters of the transmission system, such as line impedance, voltage magnitude, and voltage phase angle. These in turn are used to control power flow and increase stability margins. The application of FACTS technology equipped with smart control systems maintains and improves steady state and dynamic system performance [7]. It also helps to prevent voltage instability and blackouts caused by unscheduled generation or transmission anomalies during high load conditions.

1.2.3 No free lunch – nonlinearities, distortion, and chaos

As mentioned previously, a major drawback of using FACTS devices to correct problems that occur in power transmission systems is that they are nonlinear and cause harmonic distortion in the system, particularly in the current waveforms. In addition, the nonlinearities can be the source of chaotic (aperiodic, unpredictable) responses and limit cycle oscillations. Over the years, many adverse technical and economic problems have been traced to the existence of this distortion, and many countries now regulate the permissible levels of that distortion [61]–[64]. Even with these regulations in place, the growth of world-wide demands on the power infrastructure has exacerbated the distortion problem because the distortion becomes more pronounced as load increases.

The power electronic components used in modern power systems are among the primary sources of harmonic distortion. All power electronic circuits share the following properties [4]:

- The circuit topology is time-varying; switches are used to toggle the circuit between two or more different sets of differential equations at different times. This usually results in a discontinuous, nonlinear system.
- The storage elements (inductors and capacitors) absorb and release energy to the system.
- The switching times are nonlinear functions of the variables to be controlled (typically the output voltage).

There are additional sources of nonlinearities:

- The nonlinear $v-i$ characteristic of switches.
- The nonlinear characteristics of resistors, inductors, and capacitors.

- The nonlinear characteristics of magnetic couplings in transformers and between components in the circuit.

Nevertheless, the primary sources of nonlinearities are the switching elements which make power electronic circuits very nonlinear even if all other circuit elements are assumed to be ideal.

The effect of the harmonics is to cause increased dielectric stress on the capacitor banks and an increase in the temperatures of system components caused by higher RMS currents and I^2R losses. The increased temperature of the components reduces their expected life span and lowers their efficiency through increased heat loss to the environment. It may also lead to insulation breakdown and faults in the system. Furthermore, depending on the magnitude of the harmonics in the system, malfunctioning or total failure of the protection and control systems may result [3]. Hence, research efforts in the area of power system harmonics are growing at a rapid pace throughout the world. These efforts are focused on the steady-state and dynamic analysis of power systems, including the interaction between sources of harmonic distortion. The goal of this research is to develop accurate and reliable models for predicting and reducing harmonic distortion in power systems in order to design systems with adequate power quality.

1.2.4 Description and classification of FACTS controllers

As mentioned before, FACTS controllers are used to control power flow and improve stability of the system by controlling one or more transmission system parameters, such as the voltage source magnitudes, phase angles, and effective line

impedance. Figure 3 shows the single line diagram of a two-bus system. It is assumed that the transmission line has an inductive reactance $X \Omega$, and the resistance and capacitance are ignored.

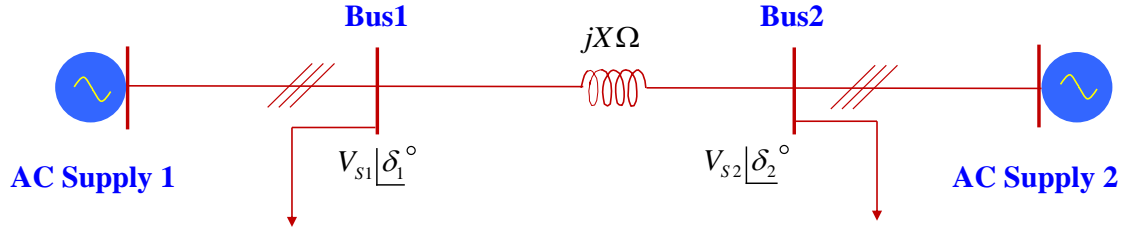


Figure 3: Single line diagram of two-bus system

The real power flow at bus 1 is given as

$$P_{s1} = \frac{V_{s1} V_{s2} \sin(\delta)}{X} \quad (1.1)$$

where V_{s1} and V_{s2} are the voltage magnitudes of the bus voltages, δ is the phase angle between them, and X is the transmission line reactance between the two buses. The real power flow at bus 2 is given as

$$P_{s2} = \frac{V_{s2} V_{s1} \sin(\delta)}{X} \quad (1.2)$$

From equations (1.1) and (1.2), it is obvious that P_{s1} and P_{s2} are the same

$$P_{s1} = P_{s2} = P_s = \frac{V_{s1} V_{s2} \sin(\delta)}{X} \quad (1.3)$$

The reactive power flow at bus 1 is given as

$$Q_{s1} = \frac{V_{s1}(V_{s1} - V_{s2} \cos(\delta))}{X} \quad (1.4)$$

The reactive power flow at bus 2 is given as

$$Q_{s2} = \frac{V_{s2}(V_{s2} - V_{s1} \cos(\delta))}{X} \quad (1.5)$$

Different FACTS controllers control one or more of these transmission system parameters in order to enhance power flow and system stability.

The FACTS controllers play an important role in AC transmission systems to enhance controllability and power transfer capability. The application of FACTS technology, equipped with smart control systems, maintains and improves steady-state and dynamic system performance of the transmission system. It also helps to prevent voltage instability and blackouts caused by unscheduled generation or transmission contingencies during high load conditions.

FACTS controllers can be divided into the following categories:

1. Series controllers

Static Synchronous Series Compensator (SSSC)

- Thyristor-Controlled Series Compensator (TCSC)

2. Shunt controllers

- Fixed Capacitor, Thyristor-Controlled Reactor (FC-TCR)
- Static Synchronous Compensator (STATCOM)

3. Shunt-series controllers

- Unified Power Flow Controller (UPFC)

Static synchronous series compensator (SSSC)

Figure 4(a) shows the schematic diagram of the Static Synchronous Series Compensator which was proposed by Gyugyi [39], [40]. The SSSC controls the real and reactive power flow in the transmission line by adding a voltage source $V_c \angle \theta_c$ in series with the line as shown in Figure 4(b). The power added to the line is controlled by varying the phase angle of the SSSC voltage with respect to the phase angle of the line current. Here, V_1 and V_2 are the voltages at buses 1 and 2, respectively.

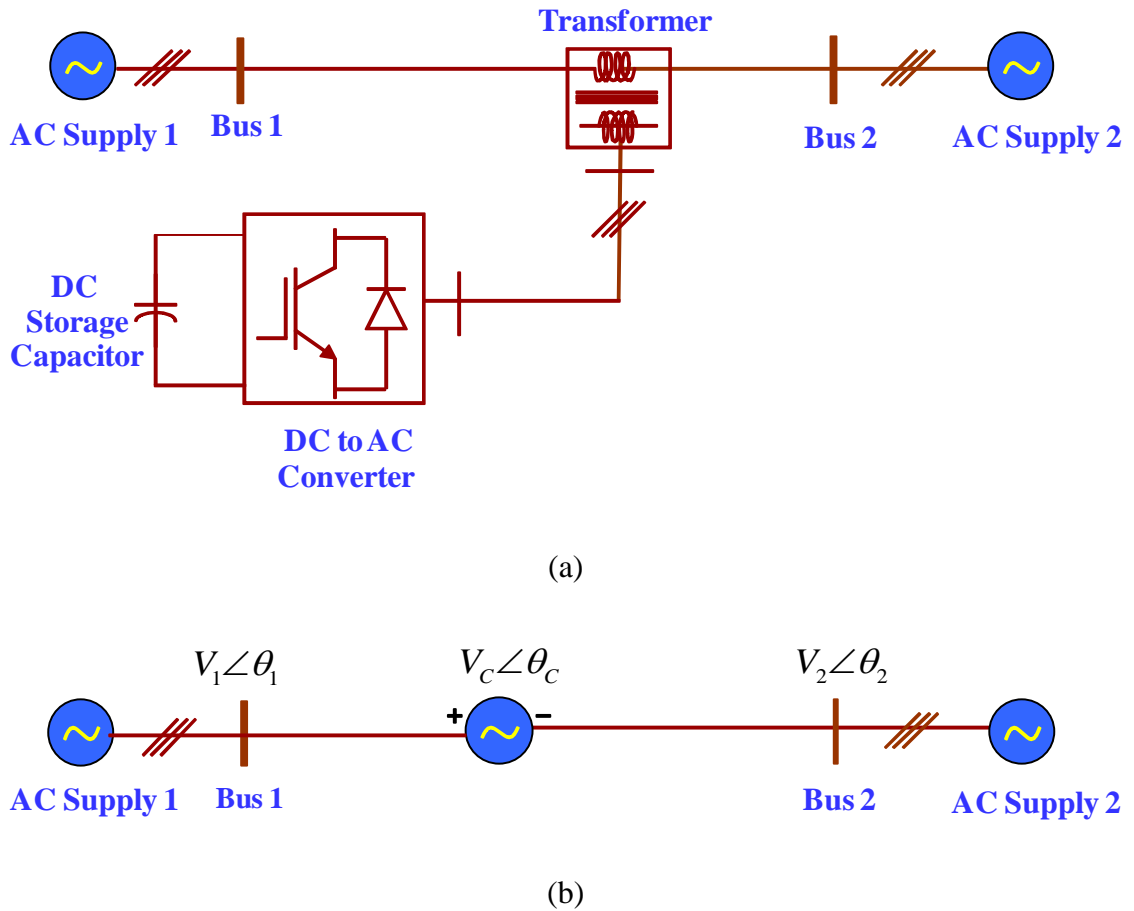


Figure 4: (a) Static synchronous series compensator (b) equivalent circuit

Thyristor-controlled series controller (TCSC)

Figure 5(a) shows the schematic diagram of a Thyristor-Controlled Series Controller, and its equivalent circuit is shown in Figure 5(b), which was proposed by Vithayathil [3]. The TCSC controls the real and reactive power flow in the line by adding a variable reactance X_{TCSC} in series with the line. This changes the transmission line impedance and hence the power flow in the line.

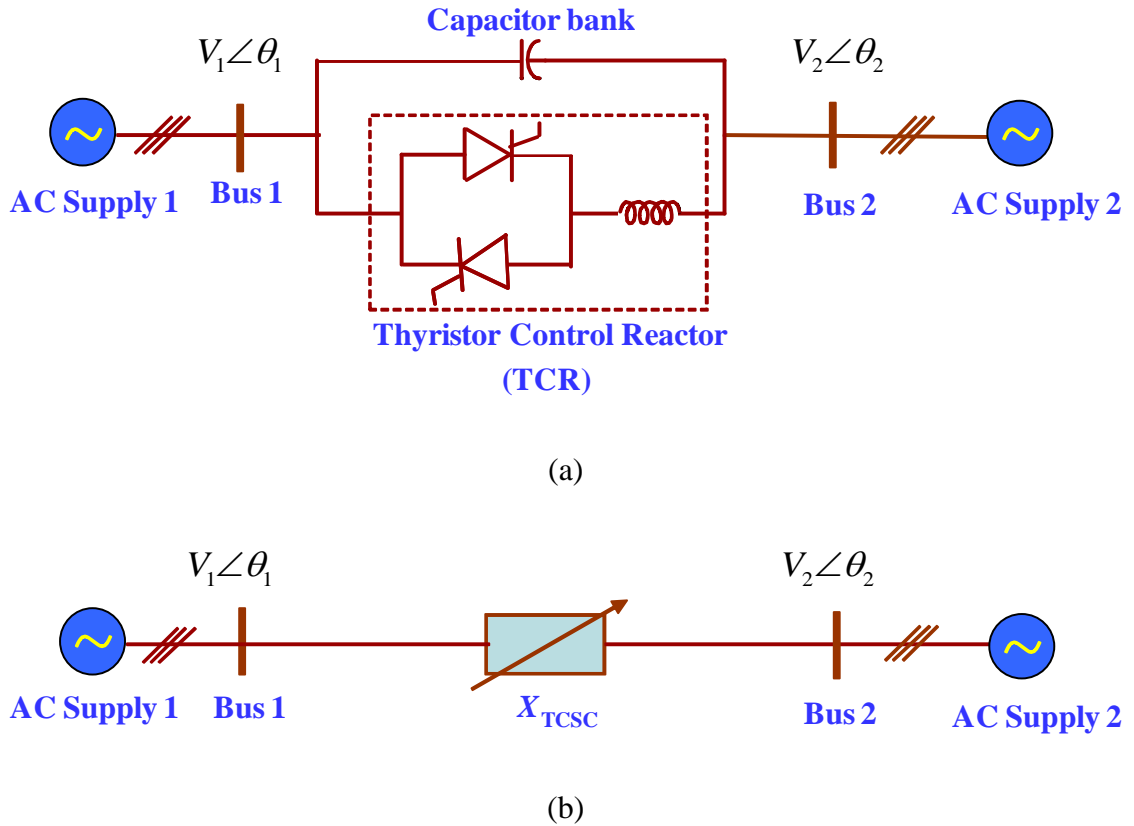
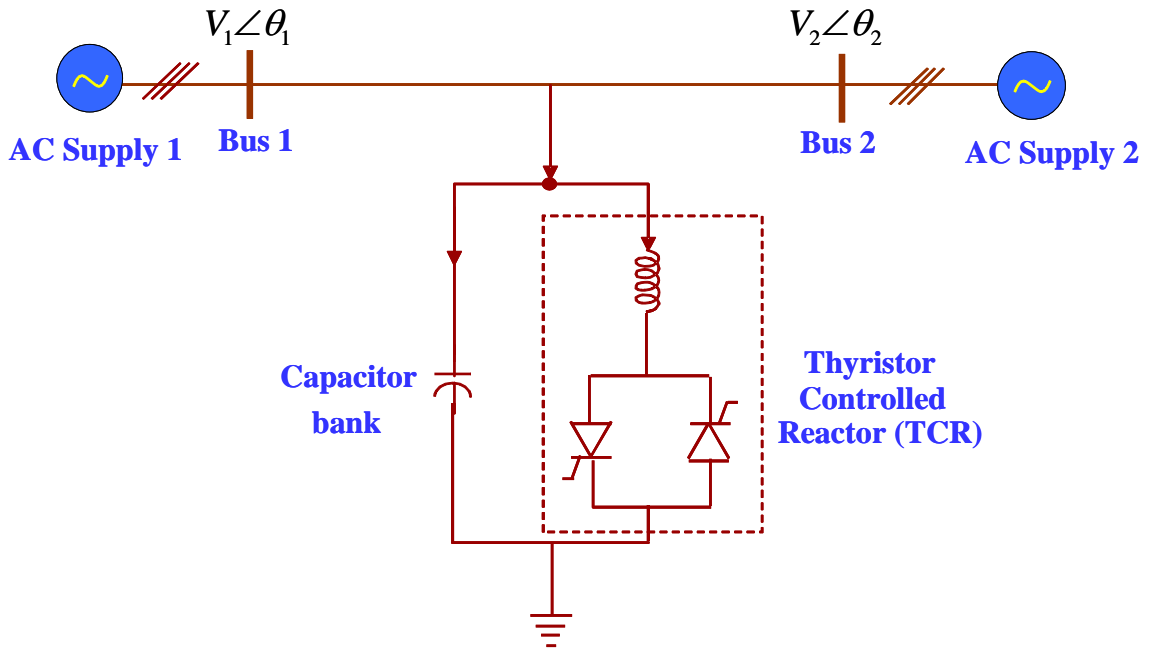


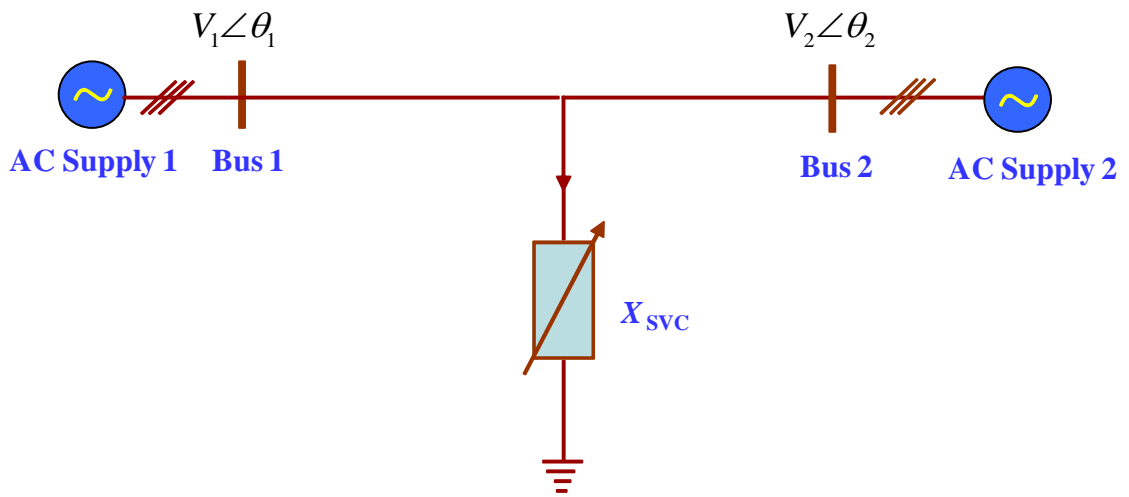
Figure 5: (a) Thyristor controlled series controller (b) equivalent circuit

Fixed capacitor, thyristor-controlled reactor (FC-TCR)

Figure 6(a) shows the schematic diagram of a Fixed Capacitor, Thyristor-Controlled Reactor and its equivalent circuit. The FC-TCR controls the real and reactive power flow in the line by adding a variable reactance X_{SVC} in series with the line. This changes the transmission line impedance and hence the power flow in the line [3].



(a)

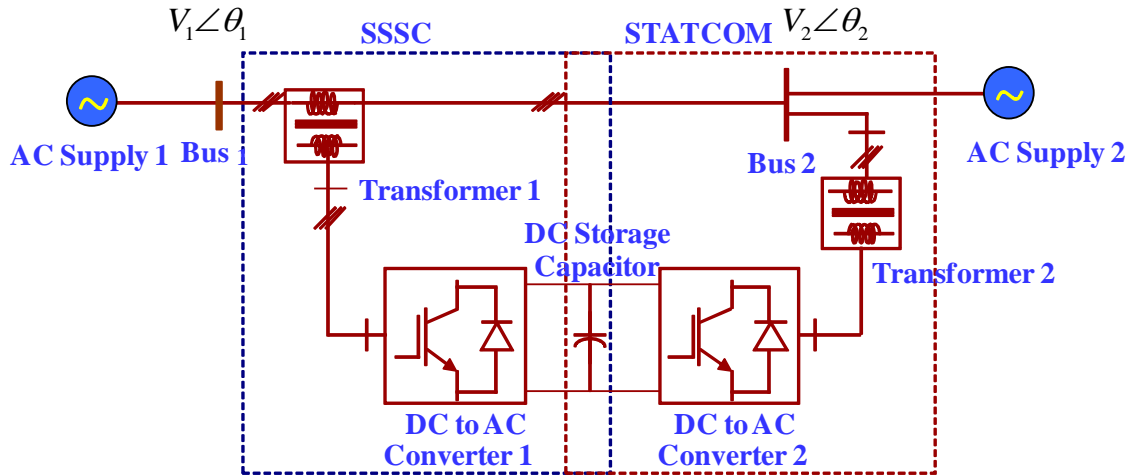


(b)

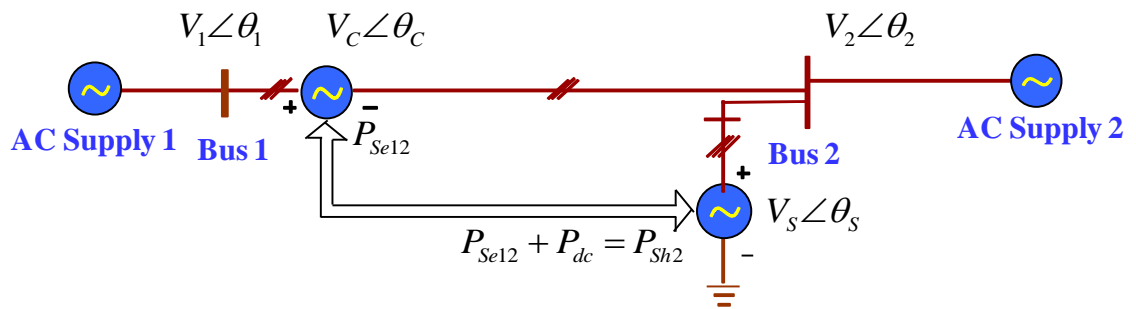
Figure 6: (a) Fixed capacitor, thyristor-controlled reactor (b) equivalent circuit

Unified power flow controller (UPFC)

Figure 7(a) shows the schematic diagram of the Unified Power Flow Controller, which is the combination of a STATCOM and an SSSC, and which was proposed by Gyugyi [41]–[43]. The shunt controller (STATCOM) in the UPFC adds voltage $V_s \angle \theta_s$ in shunt and the series controller (SSSC) adds voltage $V_c \angle \theta_c$ in series with the transmission line as shown in Figure 7(b). The power added to the line is controlled by varying the phase angle of the SSSC and STATCOM voltages with respect to the phase angle of the line current. P_{sh2} and P_{sc12} are the power exchange of the shunt converter and series converter respectively, via the common DC link. P_{dc} is the power loss of the DC circuit of the UPFC.



(a)



(b)

Figure 7: (a) Unified power flow controller (b) equivalent circuit

1.2.5 Multi-line FACTS controllers

The most common FACTS controllers, such as the UPFC, SSSC, and STATCOM controllers, are used to control a single three phase transmission line. Several innovative concepts have been introduced that combine two or more converter blocks to control the bus voltages and power flows of more than one line. Those FACTS controllers are called

multi-line FACTS controllers. There are three important multi-line FACTS controllers that are discussed in this chapter. They are called the Generalized Unified Power Flow Controller (GUPFC) or multi-line UPFC, the Interline Power Flow Controller (IPFC), and the Generalized Interline Power Flow Controller (GIPFC) or the multi-line IPFC, which can control the bus voltage and power flows of more than one line or even a sub-network.

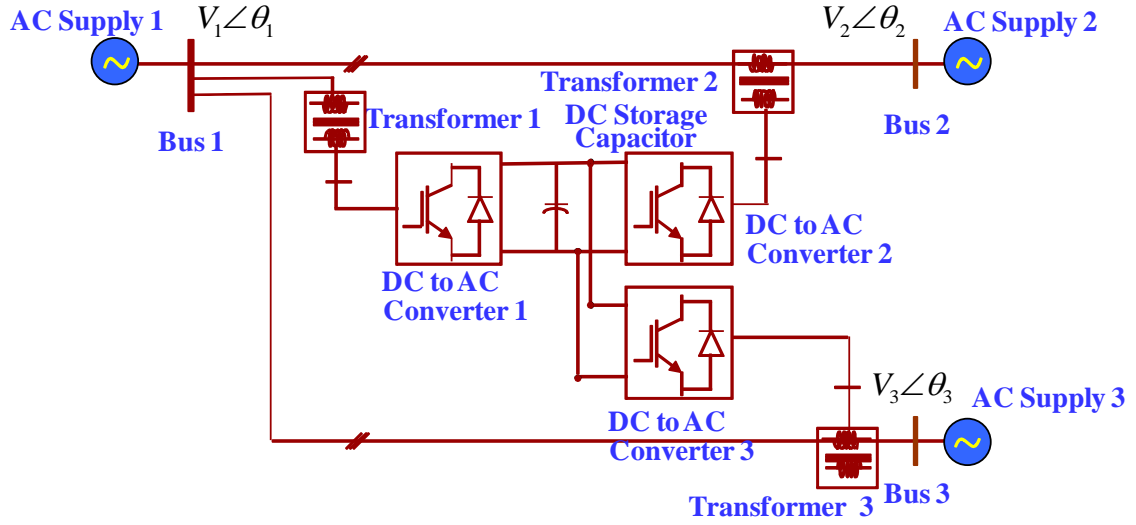
Multi-line FACTS controllers can be divided into the following categories:

1. Shunt-series controllers
 - Generalized Unified Power Flow Controller (GUPFC)
 - Generalized Interline Power Flow Controller (GIPFC)
2. Series-series controllers
 - Interline Power Flow Controller (IPFC)

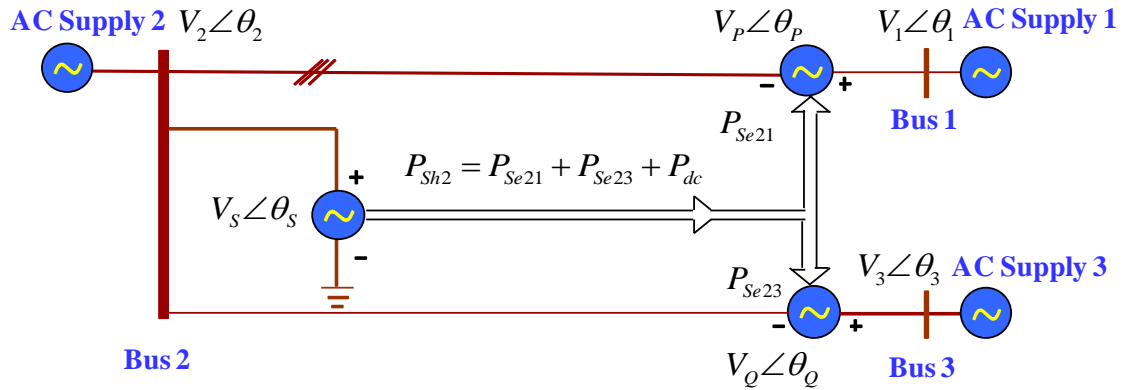
Generalized unified power flow controller (GUPFC)

Figure 8(a) shows the schematic diagram of the Generalized Unified Power Flow Controller, which is the combination of a UPFC and an SSSC [44]. The shunt controller (STATCOM) in the UPFC adds voltage $V_s \angle \theta_s$ in shunt and the series controllers (SSSC) add voltages $V_p \angle \theta_p$ and $V_q \angle \theta_q$ in series with the transmission lines as shown in Figure 8(b). The power added to the line is controlled by varying the phase angles of the SSSCs and STATCOM voltages with respect to the phase angle of the line current. P_{Sh2} is the power exchange of the shunt converter and P_{Se21} and P_{Se23} are the power exchange

of the series converters, via the common DC link. P_{dc} is the power loss of the DC circuit of the GUPFC.



(a)



(b)

Figure 8: (a) Generalized unified power flow controller (b) equivalent circuit

Interline power flow controller (IPFC)

Figure 9(a) shows the schematic diagram of the Interline Power Flow Controller which is the combination of multiple SSSCs, and which was proposed by Gyugyi in 1999 [45]. The series controllers (SSSC) add voltages $V_p \angle \theta_p$ and $V_q \angle \theta_q$ in series with the transmission lines as shown in Figure 9(b). The power added to the line is controlled by varying the phase angle of the SSSC voltages with respect to the phase angle of the line current. P_{Se12} and P_{Se34} are the power exchange of the series converters, via the common DC link. P_{dc} is the power loss of the DC circuit of the IPFC.

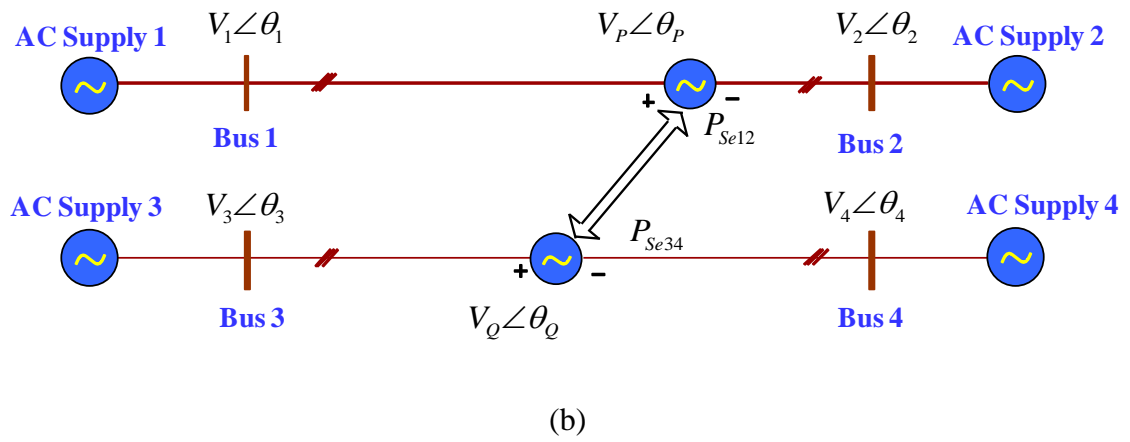
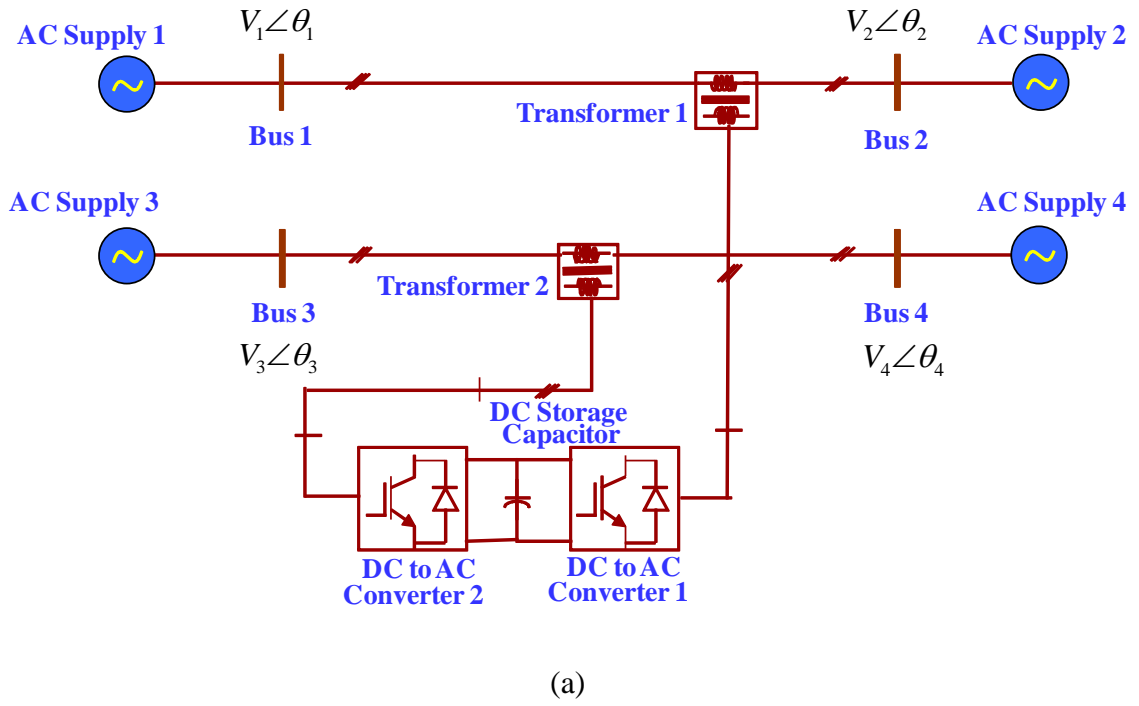
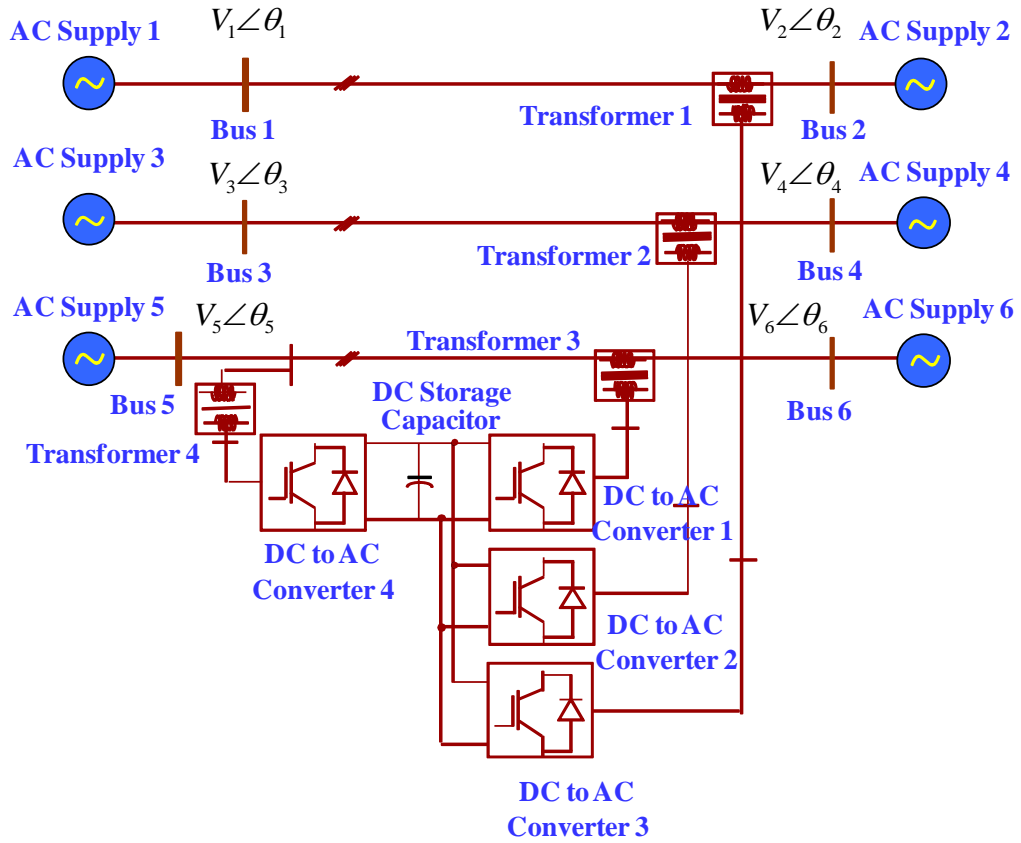


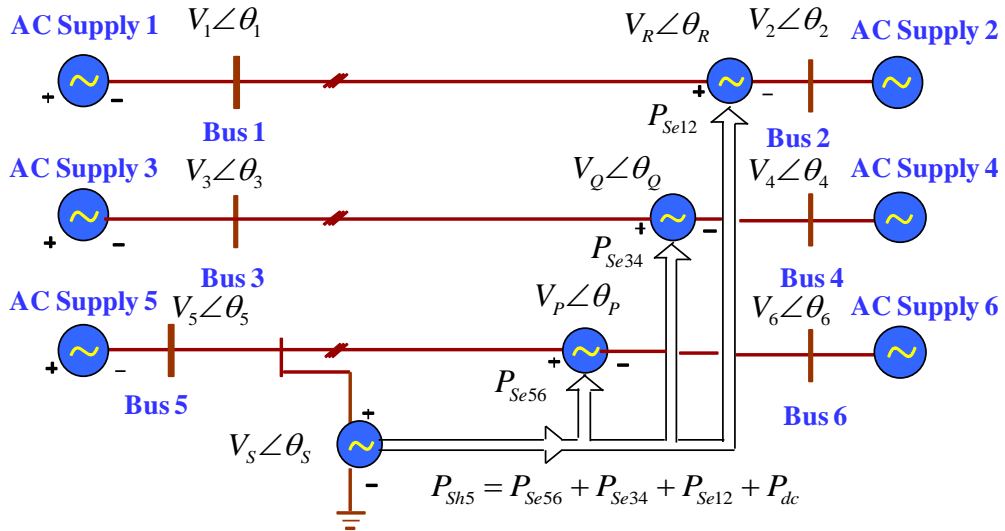
Figure 9: (a) Interline power flow controller (b) equivalent circuit

Generalized interline power flow controller (GIPFC)

Figure 10(a) shows the schematic diagram of the Generalized Interline Power Flow Controller (GIPFC), which is the combination of a STATCOM and SSSCs [46]–[48]. The shunt controller (STATCOM) in the GIPFC adds voltage $|V_s|\angle\theta_s$ in shunt, and three series controllers (SSSCs) add voltages $|V_p|\angle\theta_p$, $|V_q|\angle\theta_q$, and $|V_r|\angle\theta_r$ in series with the transmission lines as shown in Figure 10(b). The power added to the line is controlled by varying the phase angle of the SSSCs and STATCOM voltages with respect to the phase angle of the line current. P_{Sh5} is the power exchange of the shunt converter and P_{Se12} , P_{Se34} and P_{Se56} are the power exchange of the series converters, via the common DC link. P_{dc} is the power loss of the DC circuit of the GIPFC.



(a)



(b)

Figure 10: (a) Generalized interline power flow controller (b) equivalent circuit

1.3 Dissertation objectives

FACTS controllers are used to enhance the power transfer capability of transmission systems. The static and dynamic behavior of these controllers should be well defined in order to analyze their steady state and dynamic performance. DHD models are suitable for studying such behavior of the controllers. These models, unlike time domain models, are independent of window size such that they provide dynamic harmonic information accurately even at a lower magnitude and shorter duration disturbances. No literature has been found on DHD models for the FACTS controllers: SSSC, UPFC, FC-TCR, TCSC, GUPFC, IPFC, and GIPFC. The work presented in this dissertation is focused on developing DHD models for these FACTS controllers. In order to evaluate the power quality indices, the DHD models for FACTS controllers were simulated using PWM switching functions. These models were able to estimate the harmonic behavior of FACTS controllers under both steady state and transient conditions. DHD models for the: UPFC, GUPFC, IPFC, and GIPFC controllers were validated by comparing the results obtained from time domain simulations.

HD models for the GUPFC and the GIPFC were also developed for the first time. These HD models should facilitate the resonance prediction analysis and harmonic propagation studies under steady state conditions.

Practically, the UPFC, GUPFC, IPFC, and GIPFC controllers are required to maintain a constant DC voltage in order to limit the total harmonic distortion. This research work compares the power quality indices for the following conditions: 1) constant DC voltage and 2) varying DC voltage.

Also, the DHD models of GUPFC and GIPFC were simulated using multi-pulse switching functions to understand the reaction of these controllers to various switching functions and their influence on power quality indices under steady and disturbance conditions.

1.4 Outline

The dissertation is organized into six chapters. Chapter II reviews the literature available on the fundamental concepts of harmonic domain analysis, linearization of a simple non-linear relation, dynamic relations and Norton equivalent in harmonic domain.

Chapter III begins with the summary of the dynamic harmonic domain (DHD) [24] method that is successfully used to analyze the dynamic and steady state response of electrical networks that contain non-linearities and embedded power electronics. Dynamic and steady state harmonic models for the following FACTS devices are developed in this chapter using DHD method: static synchronous series compensators (SSSC), unified power flow controllers (UPFC), static reactive power compensators (SVC), and thyristor controlled series compensator (TCSC). These derived models are simulated using PWM switching functions in the presence of voltage disturbances using MATLAB[®], and graphical depictions are used to illustrate the evolution in time of the harmonic coefficients and power quality indices such as RMS voltage and current, apparent power, active power, reactive power, distortion power, and total harmonic distortion in voltage and current. Finally, the UPFC model is validated with its time domain counterpart.

In Chapter IV, the same DHD method is used to develop dynamic harmonic models for the three important multi-line FACTS controllers: Interline Power flow Controller (IPFC), the Generalized Unified Power Flow Controller (GUPFC) or multi-line UPFC, and the Generalized Interline Power Flow Controller (GIPFC) or the multi-line IPFC. The above mentioned models can control the bus voltage and power flows of more than one line or even a sub-network. The usefulness of these DHD models, in establishing the harmonic response of these controllers to a disturbance, is also explained and demonstrated. For proper operation of GUPFC, IPFC, and GIPFC controllers, the DC side voltage should be held constant. Thus, feedback controllers are designed to maintain constant DC voltage. The effect of the control circuit on power quality indices and the reaction of the controllers to the control circuit are presented in this chapter. Also, the harmonic domain models that give the harmonic interaction of a controller with transmission lines under steady state conditions for the two most common multi-line controllers, namely, the GUPFC and GIPFC, are developed. The usefulness of these models is also discussed in this chapter. Finally, the dynamic harmonics models of these multi-line FACTS controllers are validated with their time domain counterparts.

In Chapter V, the DHD models of GUPFC and GIPFC are simulated using multi-pulse switching functions in order to investigate the performances of these controllers to various switching functions under steady and disturbance periods. The chapter ends with a comparison of the performance of these converters for various switching functions.

Chapter VI presents the concluding remarks for the dissertation and elaborates on some possible areas for further study.

CHAPTER II

A REVIEW OF GENERAL HARMONIC TECHNIQUES

2.1 Introduction

Various methods have been proposed to model nonlinear power electronic devices which are used in power systems [5]–[10]. This chapter briefly examines the basic concepts of modeling for time-domain simulations and harmonic domain techniques which have been published in the literature. In recent years accurate models of high voltage DC transmission systems (HVDC) and FACTS devices have been obtained using harmonic domain modeling. A discussion of current literature related to this technique will be presented.

2.2 Time domain modeling

In general, the steady-state analysis of power electronic devices is based on time-domain characteristics by considering idealized terminal conditions such as pure DC currents or undistorted sinusoidal voltages. This type of analysis only provides information about the characteristic harmonics of a device. In practice, however, the device is working under non-ideal conditions, such as an unbalanced AC supply, unbalanced switching, and unbalanced impedances. Under these conditions, a wide range of uncharacteristic harmonics will be generated. The characteristic and/or uncharacteristic harmonics generated by a converter depends on the pulse number. The following equation facilitates in differentiating these harmonics [49], [50]:

$$h=(IP)\pm 1 \quad (2.1)$$

where

I = an integer: 1,2,3....

P = pulse number of the converter

h = characteristic harmonics

For example, under balanced conditions, a 6-pulse converter generates the characteristic harmonics 5, 7, 11, 13, 17, 19, 23, 25, etc. All the other orders are uncharacteristic harmonics. These harmonic distortions may also vary as the operating conditions change.

Power systems are highly nonlinear in nature. Using numerical integration, the time-domain solution of a nonlinear system can be analyzed to determine the steady-state

harmonic content in the circuit variables. In order to obtain the steady-state response, the integration must be carried out beyond the transient response period. This process becomes unwieldy for systems that are governed by large transient time constants because the number of integration steps to be performed becomes excessively large before the transients become small enough to be ignored [5]–[10]. The computational cost of time domain algorithms discourage the use of numerical integration for finding the steady state response of nonlinear circuits.

Another problem with time domain analysis is the difficulty of modeling components with distributed or frequency dependent parameters. In recent years accurate models of high voltage DC transmission systems and flexible AC transmission systems (FACTS) devices have been obtained using harmonic domain analysis. A discussion of current literature related to this technique follows.

2.3 Harmonic domain modeling

With the drawbacks and difficulties of modeling nonlinear power electronic devices with time-domain algorithms described above, some researchers were motivated to develop efficient harmonic analysis techniques to determine periodic solution of nonlinear circuits. These steady-state analysis techniques have been separated into two groups: harmonic balance methods and shooting methods, the former being a frequency domain technique and the latter a time domain technique. The harmonic balance methods make use of Newton type iterative techniques to solve nonlinear problems [51]. These

methods are popular because of their convergence characteristics. Shooting methods adopt integration of a dynamic equations approach for one or two full periods, after which they make use of iterative techniques by solving a two-point boundary problem. Harmonic balance methods are based on the linearization of the nonlinear system about a nominal operating point, where the linearization of the process takes place in the harmonic domain [10].

An alternative frame of reference to the time-domain technique, for the analysis of power system, containing linear and nonlinear components in the steady state is Harmonic Domain [52]. The periodic steady-state phenomena are investigated directly in the harmonic domain, using convolutions corresponding to the multiplications in the time-domain. This permits the correct representation of nonlinear characteristics in the harmonic domain, provided they are mathematically represented by polynomials. In harmonic domain analysis, nonlinear components are converted into harmonic Norton equivalents, and then are combined with the rest of the system and solved iteratively by the Newton-Raphson technique.

Harmonic domain modeling has been successfully investigated in high-power electronics systems such as HVDC systems and FACTS devices. A brief overview of harmonic domain modeling will be given next. The harmonic domain is the general frame of reference for power system analysis in the steady state which models the coupling of the various harmonics caused by the nonlinear characteristics of the system [52]. The harmonics are represented in the phasor domain. The procedure is based on a polynomial approximation of nonlinear characteristics.

2.3.1 Linearization of a simple nonlinear relation

In the steady-state operation of most power circuits, the voltage and current each consist of a fundamental frequency component. The harmonics caused by the nonlinearity of the system are superimposed on the fundamental component. In most cases the magnitude of these harmonic components is small when compared to the magnitude of the fundamental, and therefore these harmonic components are generally called ripple voltages and currents. This is a key physical characteristic that justifies the use of linearization of the nonlinear equations around the base operating point [6], [10].

By way of example, consider the following magnetization characteristic

$$\begin{aligned}i &= f(\phi) \\v &= \dot{\phi}\end{aligned}\tag{2.2}$$

where i represents current, v represents voltage, and ϕ represents magnetic flux. Assuming that f is a continuous function defined on a closed, bounded interval, the Weierstrass Approximation Theorem states that f can be approximated with arbitrarily small error by an algebraic polynomial of sufficiently high degree n . In this example, a cubic polynomial is chosen, so assume that

$$f(\phi) = b_0\phi^0 + b_1\phi^1 + b_2\phi^2 + b_3\phi^3\tag{2.3}$$

Since the power system is operating in steady-state, the base operating point is a periodic function. For this example, the base operating point for linearization is assumed to be following a sinusoidal flux:

$$\phi_b(t) = \sin \omega_0 t = \frac{e^{j\omega_0 t} - e^{-j\omega_0 t}}{2j} \quad (2.4)$$

this assumption is based on [53].

With this choice of operating point, the base operating current is given by

$$i_b = f(\phi_b) = b_0 \phi_b^0 + b_1 \phi_b^1 + b_2 \phi_b^2 + b_3 \phi_b^3 \quad (2.5)$$

As a first step in the evaluation of the polynomial in (2.5) the ϕ_b^2 term will be calculated in the complex Fourier harmonic domain [8]–[10]. First write $\phi_b(t)$ as

$$\phi_b(t) = \frac{j}{2} e^{-j\omega_0 t} + 0 \cdot e^{j0\omega_0 t} + \frac{j}{2} e^{j\omega_0 t} \quad (2.6)$$

The coefficients of the complex exponentials in (2.6) can be viewed as phasors, and these coefficients can be represented in a vector of phasors in \mathbb{C}^3 . This vector of phasors will also be referred to as a *phasor* for convenience.

$$\Phi_b = \begin{bmatrix} \frac{j}{2} \\ 0 \\ -\frac{j}{2} \end{bmatrix} \quad (2.7)$$

In order to evaluate the polynomial in (2.7), a multiplication operation must be defined between two vectors of phasors. The multiplication is called convolution. To illustrate how the convolution of two phasors can be defined, consider the product

$$\begin{aligned}
\phi_b^2(t) &= \phi_b(t) \phi_b(t) = \left(\frac{e^{j\omega_0 t} - e^{-j\omega_0 t}}{2j} \right) \left(\frac{e^{j\omega_0 t} - e^{-j\omega_0 t}}{2j} \right) \\
&= -\frac{1}{4} e^{-2j\omega_0 t} + \frac{1}{2} - \frac{1}{4} e^{2j\omega_0 t} \\
&= -\frac{1}{4} e^{-2j\omega_0 t} + 0 \cdot e^{-j\omega_0 t} + \frac{1}{2} \cdot e^{j0\omega_0 t} + 0 \cdot e^{j\omega_0 t} - \frac{1}{4} e^{2j\omega_0 t}
\end{aligned} \tag{2.8}$$

The coefficients of the complex exponentials in (2.8) are phasors which, as already stated, are represented as a vector in \mathbb{C}^5 :

$$\Phi_b \otimes \Phi_b = \begin{bmatrix} \frac{1}{4} \\ -\frac{1}{4} \\ 0 \\ \frac{1}{2} \\ 0 \\ \frac{1}{4} \\ -\frac{1}{4} \end{bmatrix} \tag{2.9}$$

The equation (2.9) defines the operation \otimes . In order that the convolution operator \otimes be well-defined, the operation should carry vectors in $\mathbb{C}^5 \times \mathbb{C}^5$ to vectors in \mathbb{C}^5 , that is,

$$\otimes: \mathbb{C}^5 \times \mathbb{C}^5 \rightarrow \mathbb{C}^5 \tag{2.10}$$

So, it is necessary to insert zero as first and last elements of pad the vector Φ_b in (2.10):

$$\Phi_b = \begin{bmatrix} 0 \\ \frac{j}{2} \\ 0 \\ -\frac{j}{2} \\ 0 \end{bmatrix} \tag{2.11}$$

Note that the same symbol is being used for $\Phi_b \in \mathbb{C}^3$ and for $\Phi_b \in \mathbb{C}^5$. Now the convolution of Φ_b with itself can be written as

$$\Phi_b^2 \triangleq \Phi_b \otimes \Phi_b = \begin{bmatrix} 0 \\ \frac{j}{2} \\ 0 \\ -\frac{j}{2} \\ 0 \end{bmatrix} \otimes \begin{bmatrix} 0 \\ \frac{j}{2} \\ 0 \\ -\frac{j}{2} \\ 0 \end{bmatrix} = \begin{bmatrix} -\frac{1}{4} \\ 0 \\ \frac{1}{2} \\ 0 \\ -\frac{1}{4} \end{bmatrix} \quad (2.12)$$

In order to generalize the convolution operation, the same operation will be performed symbolically. Beginning with (2.6),

$$\begin{aligned} \phi_b(t) &= \frac{j}{2} e^{-j\omega_0 t} + 0 \cdot e^{j0\omega_0 t} + \frac{-j}{2} e^{j\omega_0 t} \\ &= \phi_{-1} e^{-j\omega_0 t} + \phi_0 e^{j0\omega_0 t} + \phi_1 e^{j\omega_0 t} \end{aligned} \quad (2.13)$$

where ϕ_{-1} , ϕ_0 , and ϕ_1 are phasors defined in an obvious manner from the above equation (here, $\phi_{-1} = \phi_1^*$).

Hence, in vector notation

$$\Phi_b = \begin{bmatrix} 0 \\ \phi_{-1} \\ 0 \\ \phi_1 \\ 0 \end{bmatrix} \quad (2.14)$$

Also,

$$\begin{aligned}
\phi_b^2(t) &= (\phi_{-1}e^{-j\omega_0 t} + \phi_0e^{j0\omega_0 t} + \phi_1e^{j\omega_0 t})^2 \\
&= (\phi_{-1}\phi_{-1})e^{-j2\omega_0 t} + (\phi_{-1}\phi_0 + \phi_0\phi_{-1})e^{-j\omega_0 t} + (\phi_1\phi_{-1} + \phi_0\phi_0 + \phi_{-1}\phi_1) \\
&\quad + (\phi_1\phi_0 + \phi_0\phi_1)e^{j\omega_0 t} + (\phi_1\phi_1)e^{j2\omega_0 t}
\end{aligned} \tag{2.15}$$

or, in vector notation

$$\Phi_b^2 = \Phi_b \otimes \Phi_b = \begin{bmatrix} 0 \\ \phi_{-1} \\ \phi_0 \\ \phi_1 \\ 0 \end{bmatrix} \otimes \begin{bmatrix} 0 \\ \phi_{-1} \\ \phi_0 \\ \phi_1 \\ 0 \end{bmatrix} = \begin{bmatrix} \phi_{-1}\phi_{-1} \\ \phi_{-1}\phi_0 + \phi_0\phi_{-1} \\ \phi_1\phi_{-1} + \phi_0\phi_0 + \phi_{-1}\phi_1 \\ \phi_1\phi_0 + \phi_0\phi_1 \\ \phi_1\phi_1 \end{bmatrix} \tag{2.16}$$

Note that Φ_b^2 can be written as

$$\Phi_b^2 = \begin{bmatrix} \phi_0 & \phi_{-1} & & & \\ \phi_1 & \phi_0 & \phi_{-1} & & \\ & \phi_1 & \phi_0 & \phi_{-1} & \\ & & \phi_1 & \phi_0 & \phi_{-1} \\ & & & \phi_1 & \phi_0 \end{bmatrix} \begin{bmatrix} 0 \\ \phi_{-1} \\ \phi_0 \\ \phi_1 \\ 0 \end{bmatrix} \tag{2.17}$$

Note also that the rows of the matrix on the left are formed by placing ϕ_0 on the diagonal, ϕ_{-1} on the super-diagonal, and ϕ_1 on the sub-diagonal. The matrix is Hermitian and has a Toeplitz structure; that is, all of the elements in each diagonal are equal.

Although Φ_b^3 is not needed in the current example, the calculation will be performed to better illustrate the convolution operation. Using (2.17), one obtains

Writing the current $i_b(t)$ in the phasor domain as

$$\mathbf{I}_b = \begin{bmatrix} i_{-1} \\ i_0 \\ i_1 \end{bmatrix} \quad (2.22)$$

the current increment can be written as:

$$\Delta \mathbf{I} = \begin{bmatrix} \Delta I_{-1} \\ \Delta I_0 \\ \Delta I_1 \end{bmatrix} \triangleq \mathbf{I} - \mathbf{I}_b = \begin{bmatrix} I_{-1} - i_{-1} \\ I_0 - i_0 \\ I_1 - i_1 \end{bmatrix} \quad (2.23)$$

With this notation, the incremental flux and current can be written as

$$\begin{aligned} \Delta \phi(t) &= \Delta \Phi_{-1} e^{-j\omega_0 t} + \Delta \Phi_0 e^{j0\omega_0 t} + \Delta \Phi_1 e^{j\omega_0 t} \\ \Delta i(t) &= \Delta I_{-1} e^{-j\omega_0 t} + \Delta I_0 e^{j0\omega_0 t} + \Delta I_1 e^{j\omega_0 t} \end{aligned} \quad (2.24)$$

Since the nonlinear function in (2.3) is a polynomial, it is differentiable. Therefore, for small increments of ϕ and i near ϕ_b and i_b , a first-order Taylor approximation of f (from equation 2.3) yields

$$\Delta i(t) = \frac{df(\phi_b)}{d\phi} \Delta \phi(t) \quad (2.25)$$

Returning to the derivative,

$$\frac{df(\phi_b)}{d\phi} = b_1 + 2b_2\phi_b + 3b_3\phi_b^2 \quad (2.26)$$

Recalling that

$$\phi_b(t) = \frac{j}{2} e^{-j\omega_0 t} + 0 \cdot e^{j0\omega_0 t} - \frac{j}{2} e^{j\omega_0 t} \quad (2.27)$$

the derivative becomes

$$\begin{aligned} \frac{df(\phi_b)}{d\phi} &= -\frac{3b_3}{4} e^{-2j\omega_0 t} + jb_2 e^{-j\omega_0 t} + \frac{3b_3}{2} e^{j0\omega_0 t} - jb_2 e^{j\omega_0 t} - \frac{3b_3}{4} e^{2j\omega_0 t} \\ &= \xi_{-2} e^{-2j\omega_0 t} + \xi_{-1} e^{-j\omega_0 t} + \xi_0 e^{j0\omega_0 t} + \xi_1 e^{j\omega_0 t} + \xi_2 e^{2j\omega_0 t} \end{aligned} \quad (2.28)$$

Transforming this derivative to the phasor domain yields

$$\mathbf{F}' = \begin{bmatrix} \xi_{-2} \\ \xi_{-1} \\ \xi_0 \\ \xi_1 \\ \xi_2 \end{bmatrix} \quad (2.29)$$

Now (2.25) can be written in phasor notation as

$$\Delta \mathbf{I} = \mathbf{F}' \otimes \Delta \Phi \quad (2.30)$$

Using the previously discussed definition of convolution of phasors, this becomes

$$\begin{bmatrix} \Delta I_{-2} \\ \Delta I_{-1} \\ \Delta I_0 \\ \Delta I_1 \\ \Delta I_2 \end{bmatrix} = \begin{bmatrix} \xi_0 & \xi_{-1} & \xi_{-2} & & \\ \xi_1 & \xi_0 & \xi_{-1} & \xi_{-2} & \\ \xi_2 & \xi_1 & \xi_0 & \xi_{-1} & \xi_{-2} \\ & \xi_2 & \xi_1 & \xi_0 & \xi_{-1} \\ & & \xi_2 & \xi_1 & \xi_0 \end{bmatrix} \begin{bmatrix} \Delta \Phi_{-2} \\ \Delta \Phi_{-1} \\ \Delta \Phi_0 \\ \Delta \Phi_1 \\ \Delta \Phi_2 \end{bmatrix} \quad (2.31)$$

Let

$$\bar{\mathbf{F}} = \begin{bmatrix} \xi_0 & \xi_{-1} & \xi_{-2} & & \\ \xi_1 & \xi_0 & \xi_{-1} & \xi_{-2} & \\ \xi_2 & \xi_1 & \xi_0 & \xi_{-1} & \xi_{-2} \\ & \xi_2 & \xi_1 & \xi_0 & \xi_{-1} \\ & & \xi_2 & \xi_1 & \xi_0 \end{bmatrix} \quad (2.32)$$

Then, (2.31) can be written as

$$\Delta \mathbf{I} = \bar{\mathbf{F}} \Delta \Phi \quad (2.33)$$

The matrix $\bar{\mathbf{F}}$ represents the linearization of the nonlinear system about the fundamental harmonic components of the voltage and current. It is this encompassing of the harmonic components in the linearized system (2.33) from which harmonic domain analysis derives its name.

In the previous discussion, the voltage and current in (2.20) were sinusoids. These voltages and currents can be generalized into two arbitrary periodic functions using an infinite complex Fourier series expansion, and this will be done in the following summary.

$$\phi(t) = \sum_{m=-\infty}^{\infty} \Phi_m e^{jm\omega_0 t} \quad (2.34)$$

$$i(t) = \sum_{k=-\infty}^{\infty} I_m e^{jk\omega_0 t} \quad (2.35)$$

Again,

$$\Delta i(t) = \frac{df(\phi_b)}{d\phi} \Delta \phi(t) \quad (2.36)$$

where

$$\Delta\phi(t) = \sum_{m=-\infty}^{\infty} \Delta\Phi_m e^{jm\omega_0 t} \quad (2.37)$$

$$\Delta i(t) = \sum_{k=-\infty}^{\infty} \Delta I_k e^{jk\omega_0 t} \quad (2.38)$$

$$\frac{df(\phi_b)}{d\phi} = \sum_{i=-\infty}^{\infty} \xi_i e^{ji\omega_0 t} \quad (2.39)$$

Using the properties of convolutions presented previously, the following relation between harmonics coefficients can be obtained from the infinite dimensional case:

$$\begin{bmatrix} \vdots \\ \Delta I_{-2} \\ \Delta I_{-1} \\ \Delta I_0 \\ \Delta I_1 \\ \Delta I_2 \\ \vdots \end{bmatrix} = \begin{bmatrix} \ddots & & & & & & \\ & \xi_0 & \xi_{-1} & \xi_{-2} & \xi_{-3} & & \\ & \xi_1 & \xi_0 & \xi_{-1} & \xi_{-2} & \xi_{-3} & \\ & \xi_2 & \xi_1 & \xi_0 & \xi_{-1} & \xi_{-2} & \\ & \xi_3 & \xi_2 & \xi_1 & \xi_0 & \xi_{-1} & \\ & & \xi_3 & \xi_2 & \xi_1 & \xi_0 & \\ & & & & & & \ddots \end{bmatrix} \begin{bmatrix} \vdots \\ \Delta\Phi_{-2} \\ \Delta\Phi_{-1} \\ \Delta\Phi_0 \\ \Delta\Phi_1 \\ \Delta\Phi_2 \\ \vdots \end{bmatrix} \quad (2.40)$$

As in (2.33) a similar equation exists, namely,

$$\Delta\mathbf{I} = \bar{\mathbf{F}}\Delta\Phi \quad (2.41)$$

where

$$\begin{aligned}
\bar{\mathbf{F}} &= \begin{bmatrix} \ddots & & & & & \\ & \xi_0 & \xi_{-1} & \xi_{-2} & \xi_{-3} & \\ & \xi_1 & \xi_0 & \xi_{-1} & \xi_{-2} & \xi_{-3} \\ & \xi_2 & \xi_1 & \xi_0 & \xi_{-1} & \xi_{-2} \\ & \xi_3 & \xi_2 & \xi_1 & \xi_0 & \xi_{-1} \\ & & \xi_3 & \xi_2 & \xi_1 & \xi_0 \\ & & & & & \ddots \end{bmatrix} \\
\Delta\Phi &= \begin{bmatrix} \vdots \\ \Delta\Phi_{-1} \\ \Delta\Phi_0 \\ \Delta\Phi_1 \\ \vdots \end{bmatrix} \triangleq \Phi - \Phi_b = \begin{bmatrix} \vdots \\ \psi_{-1} - \phi_{-1} \\ \psi_0 - \phi_0 \\ \psi_1 - \phi_1 \\ \vdots \end{bmatrix}; \Delta\mathbf{I} = \begin{bmatrix} \vdots \\ \Delta I_{-1} \\ \Delta I_0 \\ \Delta I_1 \\ \vdots \end{bmatrix} \triangleq \mathbf{I} - \mathbf{I}_b = \begin{bmatrix} \vdots \\ I_{-1} - i_{-1} \\ I_0 - i_0 \\ I_1 - i_1 \\ \vdots \end{bmatrix} \quad (2.42)
\end{aligned}$$

2.3.2 Dynamic relations

Consider the basic dynamic relation in (2.2)

$$v = \dot{\phi} \quad (2.43)$$

where both variables are periodic, that is

$$\phi(t) = \sum_{m=-\infty}^{\infty} \Phi_m e^{jm\omega_0 t} \quad (2.44)$$

$$v(t) = \sum_{n=-\infty}^{\infty} V_n e^{jn\omega_0 t} \quad (2.45)$$

With these relations, (2.43) can be written as:

$$\sum_{n=-\infty}^{\infty} V_n e^{jn\omega_0 t} = \frac{d}{dt} \sum_{m=-\infty}^{\infty} \Phi_m e^{jm\omega_0 t} = \sum_{m=-\infty}^{\infty} jm\omega_0 \Phi_m e^{jm\omega_0 t} \quad (2.46)$$

For small increments of ϕ and v around ϕ_b and v_b , and in terms harmonic coefficients,

$$\begin{bmatrix} \vdots \\ \Delta V_{-2} \\ \Delta V_{-1} \\ \Delta V_0 \\ \Delta V_1 \\ \Delta V_2 \\ \vdots \end{bmatrix} = \begin{bmatrix} \ddots & & & & & & \\ & -j2\omega_0 & & & & & \\ & & -j\omega_0 & & & & \\ & & & 0 & & & \\ & & & & j\omega_0 & & \\ & & & & & j2\omega_0 & \\ & & & & & & \ddots \end{bmatrix} \begin{bmatrix} \vdots \\ \Delta\Phi_{-2} \\ \Delta\Phi_{-1} \\ \Delta\Phi_0 \\ \Delta\Phi_1 \\ \Delta\Phi_2 \\ \vdots \end{bmatrix} \quad (2.47)$$

In compact form,

$$\Delta\mathbf{V} = \mathbf{D}(j\omega_0)\Delta\Phi \quad (2.48)$$

where the matrix $\mathbf{D}(j\omega_0)$ is called the matrix of differentiation defined by

$$\mathbf{D}(j\omega_0) = \begin{bmatrix} \ddots & & & & & & \\ & -j2\omega_0 & & & & & \\ & & -j\omega_0 & & & & \\ & & & 0 & & & \\ & & & & j\omega_0 & & \\ & & & & & j2\omega_0 & \\ & & & & & & \ddots \end{bmatrix} \quad (2.49)$$

Using the relations in (2.41) and (2.48),

$$\Delta\mathbf{I} = \bar{\mathbf{F}}\Delta\Phi \quad (2.50)$$

$$\Delta\mathbf{V} = \mathbf{D}(j\omega_0)\Delta\Phi \quad (2.51)$$

$$\Delta\Phi = \mathbf{D}^{-1}(j\omega_0)\Delta\mathbf{V} \quad (2.52)$$

$$\Delta\mathbf{I} = \bar{\mathbf{F}}\mathbf{D}^{-1}(j\omega_0)\Delta\mathbf{V} \quad (2.53)$$

This yields

$$\Delta \mathbf{I} = \mathbf{Y} \Delta \mathbf{V} \quad (2.54)$$

where

$$\mathbf{Y} = \bar{\mathbf{F}} \mathbf{D}^{-1}(j\omega_0) \quad (2.55)$$

2.2.3 Norton equivalent circuit

The linearization of equation (2.1) in the harmonic domain is at a base operating point i_b and ϕ_b . However, it is more practical to use the voltage instead of the flux as a system variable. Hence, only the voltage and current variables will be used in the following incremental equations:

$$\Delta \mathbf{I} = \mathbf{I} - \mathbf{I}_b \quad (2.56)$$

$$\Delta \mathbf{V} = \mathbf{V} - \mathbf{V}_b \quad (2.57)$$

From (2.54)

$$\Delta \mathbf{I} = \mathbf{Y} \Delta \mathbf{V} \quad (2.58)$$

$$\mathbf{I} - \mathbf{I}_b = \mathbf{Y} (\mathbf{V} - \mathbf{V}_b) \quad (2.59)$$

$$\mathbf{I} = \mathbf{Y} \mathbf{V} + \mathbf{I}_b - \mathbf{Y} \mathbf{V}_b \quad (2.60)$$

This yields

$$\mathbf{I} = \mathbf{Y}\mathbf{V} + \mathbf{I}_N \quad (2.61)$$

where

$$\mathbf{I}_N = \mathbf{I}_b - \mathbf{Y}\mathbf{V}_b \quad (2.62)$$

Note that (2.61) can be represented by the harmonic Norton equivalent circuit (in the complex conjugate harmonic space) in Figure 11.

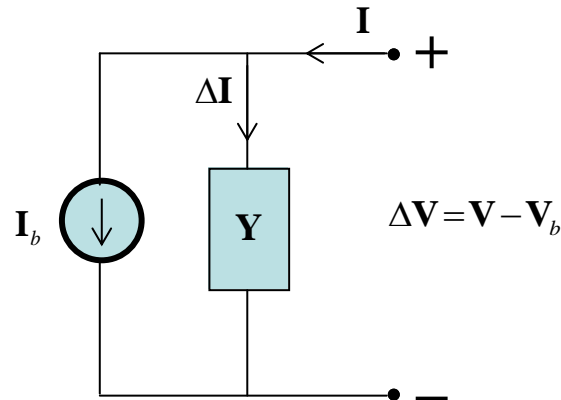


Figure 11: Norton equivalent circuit

The relationship in (2.59) and (2.55) can be represented by the harmonic input-output relationships shown in Figure 12.

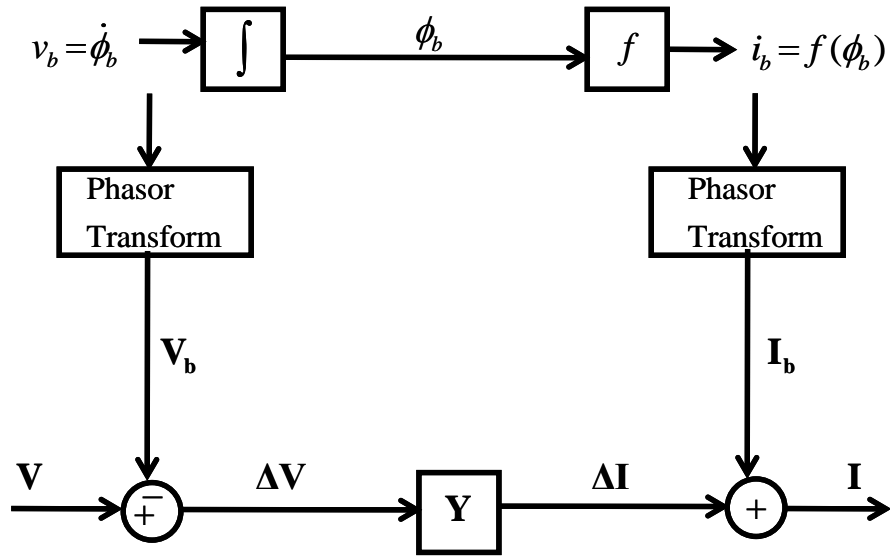


Figure 12: Harmonic input-output relationship

2.3 Conclusion

The drawbacks and difficulties of modeling nonlinear power electronic devices with time-domain algorithms along with a new frame of reference for the harmonic analysis of power systems, the harmonic domain, have been discussed. The harmonic representation of linear and nonlinear components in this frame of reference has been explained. The linearization procedure of a simple nonlinear relationship has been discussed by considering the magnetization characteristic. This frame of reference is the basis for the presented research work and is used to develop steady state models of multi-line FACTS controllers in Chapter 4. The extension of the HD method is DHD, which is used to develop dynamic models for SSSC, FC-TCR, TCSC, and UPFC in Chapter 3.

CHAPTER III

FACTS CONTROLLERS MODELING IN DYNAMIC HARMONIC DOMAIN

3.1 Introduction

A new method, called Dynamic Harmonic Domain (DHD) analysis, has been used successfully to analyze the transient and steady state responses of electrical networks that contain nonlinearities and embedded power electronics [15], [24] [26]. The method makes use of an orthogonal basis (the complex Fourier series), complex differential operators, and approximations of these operators. The DHD method is an extension of the HD method, and it expands the scope of the usage of power quality indices from measuring the performance of steady state applications to the transient range [24]. An important feature of the DHD method is that it reduces a linear time-periodic (LTP) system to a linear time-invariant (LTI) system, which improves the available tools and techniques that are used to solve LTP systems.

In order to obtain this harmonic information using time domain, Windowed Fast Fourier Transform (WFFT) method has been used. However, this method has some

drawbacks such as leakage picket-fence, aliasing, and edge effect [11]. Additionally, this method is dependent on the size of the window to achieve accuracy in results. However, adjusting the size of this window is not a small procedure. Hence, keeping in mind these drawbacks, it is difficult to accurately assess power quality. On the other hand, the DHD method has none of these disadvantages and therefore it is a possible method to be used for the accurate assessment of power quality [24].

The DHD method has been successfully applied to FACTS devices such as the static compensator (STATCOM) [24] and the thyristor controlled reactor (TCR) and the advantages have been reported [26]. In this chapter the DHD modeling methodology is applied to develop models for the static synchronous series compensators (SSSC), the unified power flow controllers (UPFC), the fixed capacitor, thyristor-controlled reactor (FC-TCR) [28], and thyristor controlled series compensators (TCSC). The DHD model of SSSC is presented in [29], which is derived based on a 24-pulse VSC multi-pulse configuration. The dynamic model of SSSC presented in this dissertation is similar to [27], but is not based on VSC multi-pulse configuration. The dynamic model of FC-TCR presented in this dissertation is simulated in the presence of disturbance and graphical depictions are used to illustrate the evolution in time of the harmonic coefficients and power quality indices. In [28], [30], dynamic companion harmonic model, which combines DHD and discrete companion circuit models, of three-node power system with embedded FC-TCR is presented for complete dynamic harmonic analysis. However, the dynamic model of FC-TCR presented in this dissertation is not a dynamic companion harmonic model.

3.2 Dynamic harmonic domain method

The following development of the dynamic harmonic domain method is adapted from [24], [54], [55]. A continuous, periodic function $x(t)$ with $t \in (-\infty, \infty)$ and period T may be represented to any degree of accuracy by the time-dependent complex Fourier series given by [53]

$$x(t) = \sum_{n=-\infty}^{\infty} X_n(t) e^{jn\omega_0 t} \quad (3.1)$$

where $\omega_0 = 2\pi/T$. Note that the complex Fourier coefficients $X_n(t)$ depend on time in the following manner. At any time t , consider a time window of length T just prior to t , namely the interval $[t-T, t]$. Then the Fourier coefficients that are assigned to t are taken to be

$$X_n(t) = \frac{1}{T} \int_{t-T}^t x(\tau) e^{-jn\omega_0 \tau} d\tau \quad (3.2)$$

The complex coefficients in (3.2) are referred to as *dynamic phasors* [54]. This representation of the signal $x(t)$ is the fundamental concept which underlies the DHD method. Equation (3.2) gives the time-evolution of the complex Fourier coefficients as a window of length T is translated along the waveform $x(t)$.

For numerical calculations the infinite sum in (3.1) can be limited to a finite number of harmonics, say $n \in [-h, h]$. Then $x(t)$ may be approximated by

$$x(t) \approx \sum_{n=-h}^h X_n(t) e^{jn\omega_0 t} \quad (3.3)$$

In this case, (3.3) may be represented in matrix notation by

$$x(t) = \mathbf{G}^T(t) \mathbf{X}(t) \quad (3.4)$$

where

$$\mathbf{G}(t) = \begin{bmatrix} e^{-jh\omega_0 t} \\ \vdots \\ e^{-j\omega_0 t} \\ 1 \\ e^{j\omega_0 t} \\ \vdots \\ e^{jh\omega_0 t} \end{bmatrix} \quad \text{and} \quad \mathbf{X}(t) = \begin{bmatrix} X_{-h}(t) \\ \vdots \\ X_{-1}(t) \\ X_0(t) \\ X_1(t) \\ \vdots \\ X_h(t) \end{bmatrix} \quad (3.5)$$

The vector $\mathbf{G}(t)$ is made up of the first $2h+1$ orthogonal basis elements in the complex Fourier series representation of $x(t)$, and $\mathbf{X}(t)$ is the vector whose components are the harmonic coefficients of $x(t)$.

State-space models can be expressed in the DHD as follows. Consider the linear time-periodic (LTP) system

$$\begin{aligned} \dot{x}(t) &= a(t)x(t) + b(t)u(t) \\ y(t) &= c(t)x(t) + e(t)u(t) \end{aligned} \quad (3.6)$$

where all functions are assumed to have period T .

In order to transform (3.6) into the harmonic domain, some preliminary results are needed. Differentiating (3.4) gives

$$\dot{x}(t) = \mathbf{G}^T(t) \dot{\mathbf{X}}(t) + \dot{\mathbf{G}}^T(t) \mathbf{X}(t) \quad (3.7)$$

The derivative of the basis vector $\mathbf{G}(t)$ can be expressed as

$$\dot{\mathbf{G}}(t) = \mathbf{D}(j h \omega_0) \mathbf{G}(t) \quad (3.8)$$

where $\mathbf{D}(j\omega_0)$ is the matrix of differentiation defined by

$$\mathbf{D}(j\omega_0) = \begin{bmatrix} -j\omega_0 & 0 & 0 & 0 & 0 & 0 & 0 \\ 0 & \ddots & 0 & 0 & 0 & 0 & 0 \\ 0 & 0 & -j\omega_0 & 0 & 0 & 0 & 0 \\ 0 & 0 & 0 & 0 & 0 & 0 & 0 \\ 0 & 0 & 0 & 0 & j\omega_0 & 0 & 0 \\ 0 & 0 & 0 & 0 & 0 & \ddots & 0 \\ 0 & 0 & 0 & 0 & 0 & 0 & j\omega_0 \end{bmatrix} \quad (3.9)$$

Transposing (3.8) gives

$$\dot{\mathbf{G}}^T(t) = \mathbf{G}^T(t)\mathbf{D}(j\omega_0) \quad (3.10)$$

and substituting this result into (3.7) gives

$$\dot{x}(t) = \mathbf{G}^T(t)\dot{\mathbf{X}}(t) + \mathbf{G}^T(t)\mathbf{D}(j\omega_0)\mathbf{X}(t) \quad (3.11)$$

Next, the product of two periodic functions such as $a(t)x(t)$ is transformed as follows. Expand $x(t)$ as into its finite Fourier series approximation as

$$\begin{aligned} x(t) &= X_{-h}e^{-jh\omega_0 t} + \dots + X_{-1}e^{-j\omega_0 t} + X_0 + X_1e^{j\omega_0 t} + \dots + X_h e^{jh\omega_0 t} \\ &= \mathbf{G}^T(t)\mathbf{X} \end{aligned} \quad (3.12)$$

where

$$\mathbf{X} = \begin{bmatrix} X_{-h}(t) \\ \vdots \\ X_{-1}(t) \\ X_0(t) \\ X_1(t) \\ \vdots \\ X_h(t) \end{bmatrix} \quad (3.13)$$

Finally, rearranging and cancelling the common vectors of basis elements \mathbf{G}^T gives the compact representation of the system in the DHD:

$$\begin{aligned}\dot{\mathbf{X}} &= (\mathbf{A} - \mathbf{D}(jh\omega_0))\mathbf{X} + \mathbf{BU} \\ \mathbf{Y} &= \mathbf{CX} + \mathbf{EU}\end{aligned}\tag{3.19}$$

The full harmonic dynamic behavior of variables $x(t)$ and $y(t)$ can be obtained by solving the equations in (3.19). These equations are the key to the DHD methodology.

3.3 Selective harmonic elimination

Since the operation of power electronics devices generates harmonics, it is important to be able to cancel as many of them as possible and, ideally, without having to resort to robust filtering. One available technique used to perform harmonic cancellation is the selective harmonic elimination (SHE) method [56]. Since this technique will be applied to the FACTS devices the subject of this research, its theory will be briefly outlined here. Cancellation of harmonics is achieved by an appropriate semiconductor device's turn-on and turn-off regime. This regime is established, by design, by means of a switching function. This function, or waveform, is a series of pulses representing the 'on' and 'off' intervals of the semiconductor devices.

The general procedure to achieve the desired switching waveform is as follows. Consider a single-phase, full-bridge inverter, whose output voltage waveform is a square wave. Assume further, that it has been chopped by the semiconductor switch being turned

on and turned off regime, yielding the generalized output waveform with normalized magnitude shown in Figure 13 [56].

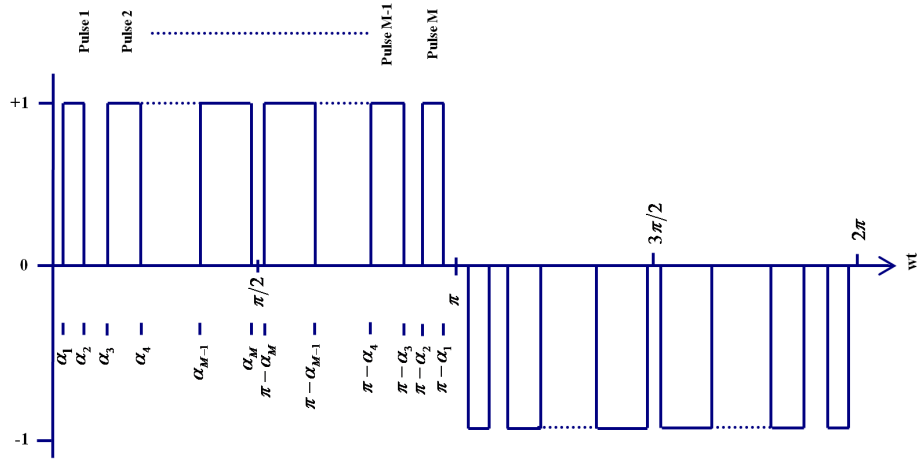


Figure 13: Generalized output waveform of a full-bridge inverter with normalized magnitude

In the above figure, M is the number of harmonics to be eliminated and $\alpha_1, \alpha_2, \dots, \alpha_M$ are the angles at which the devices are switched in order to eliminate the specific set of M harmonics.

Positive and negative signal in the switching waveform imply that the semiconductor switch is ON and a zero signal implies that it is OFF. The width of the pulse is the duration of the time for which the switch is ON. Here, for a chosen set of M harmonics, α_1 is the angle needed to eliminate the desired first harmonic, α_2 for the second, and so on. The width of 'Pulse 1' is equal to $\alpha_2 - \alpha_1$. The number of pulses for one half-cycle is equal to the number of harmonics to be eliminated.

Since the waveform has odd and quarter-wave symmetries, the Fourier series coefficients a_n for odd n , and odd and even M

$$a_n = \frac{4}{n\pi} \sum_{k=1}^M (-1)^{k+1} \cos n\alpha_k \quad (3.20)$$

$$a_n = 0 \quad \text{for } n \text{ even} \quad (3.21)$$

and

$$b_n = 0 \quad \text{for all } n \quad (3.22)$$

where $0 < \alpha_1 < \alpha_2 \cdots < \alpha_M < \frac{\pi}{2}$

In order to eliminate the M harmonics, (3.20) is set to zero

$$f_i(\alpha) = \frac{4}{n_i\pi} \sum_{k=1}^M (-1)^{k+1} \cos n_i\alpha_k = 0 \quad (3.23)$$

where $i = 1, 2, 3, \dots, M$, where n_1, n_2, \dots, n_M are the harmonics to be eliminated.

Consider the number of harmonics to be eliminated as 5 and $n_i, i=1, 2, \dots, 5$.

Also, the initial angles are $\alpha_1, \alpha_2, \alpha_3, \alpha_4, \alpha_5$. Now, the angles needed in order to eliminate

the 5 harmonics are calculated by solving (3.23) as given below.

$$\begin{aligned}
f_1(\alpha_1, \alpha_2, \dots, \alpha_5) &= \frac{4}{5\pi} \left(\frac{(-1)^{1+1} \cos 5\alpha_1 + (-1)^{2+1} \cos 5\alpha_2 + (-1)^{3+1} \cos 5\alpha_3 +}{(-1)^{4+1} \cos 5\alpha_4 + (-1)^{5+1} \cos 5\alpha_5} \right) = 0 \\
f_2(\alpha_1, \alpha_2, \dots, \alpha_5) &= \frac{4}{7\pi} \left(\frac{(-1)^{1+1} \cos 7\alpha_1 + (-1)^{2+1} \cos 7\alpha_2 + (-1)^{3+1} \cos 7\alpha_3 +}{(-1)^{4+1} \cos 7\alpha_4 + (-1)^{5+1} \cos 7\alpha_5} \right) = 0 \\
f_3(\alpha_1, \alpha_2, \dots, \alpha_5) &= \frac{4}{11\pi} \left(\frac{(-1)^{1+1} \cos 11\alpha_1 + (-1)^{2+1} \cos 11\alpha_2 + (-1)^{3+1} \cos 11\alpha_3 +}{(-1)^{4+1} \cos 11\alpha_4 + (-1)^{5+1} \cos 11\alpha_5} \right) = 0 \\
f_4(\alpha_1, \alpha_2, \dots, \alpha_5) &= \frac{4}{13\pi} \left(\frac{(-1)^{1+1} \cos 13\alpha_1 + (-1)^{2+1} \cos 13\alpha_2 + (-1)^{3+1} \cos 13\alpha_3 +}{(-1)^{4+1} \cos 13\alpha_4 + (-1)^{5+1} \cos 13\alpha_5} \right) = 0 \\
f_5(\alpha_1, \alpha_2, \dots, \alpha_5) &= \frac{4}{17\pi} \left(\frac{(-1)^{1+1} \cos 17\alpha_1 + (-1)^{2+1} \cos 17\alpha_2 + (-1)^{3+1} \cos 17\alpha_3 +}{(-1)^{4+1} \cos 17\alpha_4 + (-1)^{5+1} \cos 17\alpha_5} \right) = 0
\end{aligned}$$

The angles obtained by solving the above equations are needed to eliminate harmonics 5, 7, 11, 13, and 17.

The method just described was used in [19] to obtain the switching function in the harmonic domain, and is given by

$$s(\omega t) = \sum_{n=-h}^h S_n e^{jn\omega t} \quad (3.24)$$

where

$$S_n = -\frac{2j}{n\pi} \sum_{k=1}^M (-1)^{k+1} \cos n\alpha_k \quad (3.25)$$

for any odd n and $S_{-n} = S_n^*$. The harmonic elimination method is used to obtain angles $\alpha_1, \alpha_2, \dots, \alpha_M$ in order to eliminate M harmonics by solving the M simultaneous, nonlinear equations obtained by fixing the magnitudes to zero, that is $S_{n1} = 0, S_{n2} = 0, \dots, S_{nM} = 0$,

$$S_{ni}(\alpha) = -\frac{2j}{n_i\pi} \sum_{k=1}^M (-1)^{k+1} \cos n_i\alpha_k = 0 \quad (3.26)$$

Consider the number of harmonics to be eliminated as 5 and $i=1,2,\dots,5$. The set of simultaneous equations obtained from (3.26) were solved using Newton Raphson method to calculate $\alpha_1, \alpha_2, \alpha_3, \alpha_4$, and α_5 , giving

$$\alpha_1=11.35^\circ, \alpha_2=17.26^\circ, \alpha_3=23.80^\circ, \alpha_4=34.67^\circ, \text{ and } \alpha_5=37.26^\circ.$$

Using symmetry arguments, the remaining angles in each of the three quarters of the period are shown in Table II. The resulting switching waveform is shown in Figure 14.

Table II: Four quarter switching angles

| Quarters | α_5 | α_7 | α_{11} | α_{13} | α_{17} |
|-----------------|----------------|----------------|----------------|----------------|----------------|
| First | 11.35° | 17.26° | 23.80° | 34.67° | 37.26° |
| Second | 168.65° | 162.74° | 156.2° | 145.33° | 142.74° |
| Third | 191.35° | 197.26° | 203.80° | 214.67° | 217.26° |
| Fourth | 348.65° | 342.74° | 336.2° | 325.33° | 322.74° |

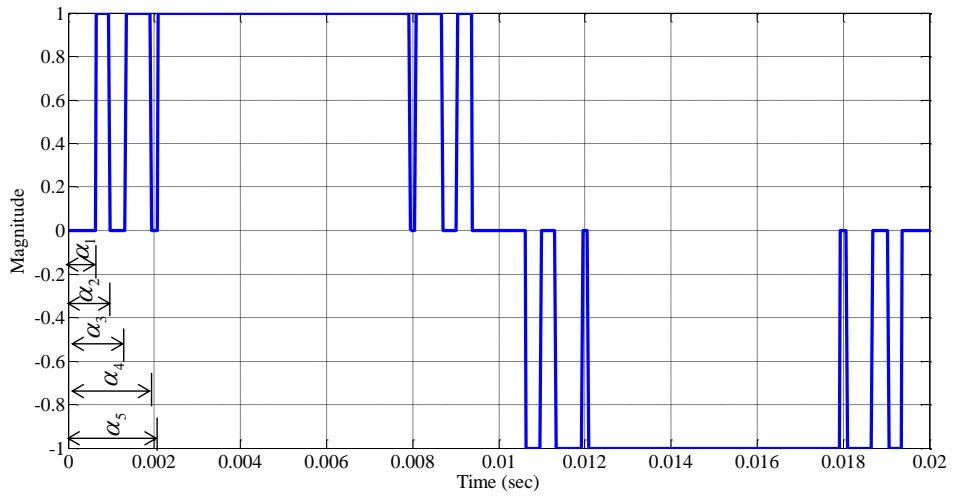


Figure 14: Switching function waveform

The absolute values of harmonic coefficients (HC) of the switching waveform are listed in Table III and plotted in Figure 15. Both Table III and Figure 15 clearly show that the even harmonics are not present and the selected harmonics for cancellation (5, 7, 11, 13, and 17) are effectively eliminated.

Table III: Absolute values of harmonic coefficients

| Harmonic order | Absolute value of harmonic coefficient | Harmonic order | Absolute value of harmonic coefficient |
|-----------------------|---|-----------------------|---|
| 1 | 1.1661 | 27 | 0.1002 |
| 3 | 0.174 | 29 | 0.1377 |
| 5 | 0 | 31 | 0.0899 |
| 7 | 0 | 33 | 0.0408 |
| 9 | 0.0124 | 35 | 0.0325 |
| 11 | 0 | 37 | 0.0256 |
| 13 | 0 | 39 | 0.0212 |
| 15 | 0.0183 | 41 | 0.0756 |
| 17 | 0 | 43 | 0.0722 |
| 19 | 0.0848 | 45 | 0.0093 |
| 21 | 0.1701 | 47 | 0.0384 |
| 23 | 0.1555 | 49 | 0.0155 |
| 25 | 0.0311 | | |

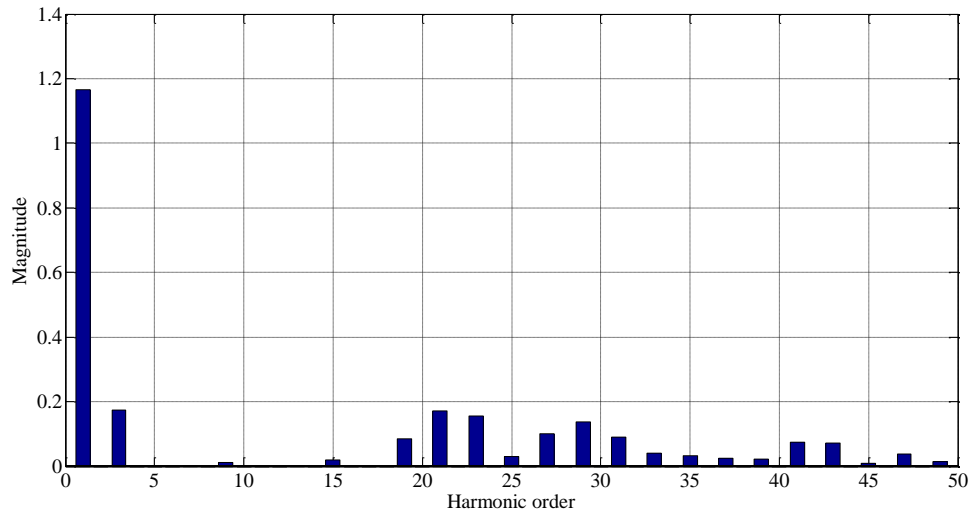


Figure 15: Harmonic content of the switching waveform

3.4 Static synchronous series compensator

The SSSC is a series connected FACTS controller [39], [40] which is shown in Figure 16. It consists of a VSC, a storage capacitor, and a coupling transformer. The capacitor is connected to one side of the terminals of VSC that converts DC to three-phase AC voltage with the fundamental frequency of the AC system. The output voltage of VSC is injected in series with the transmission line through a coupling transformer as shown in Figure 16. As long as this injected voltage is in quadrature (90°) with the transmission line current, only a reactive power exchange takes place. Any other phase relationships lead to active power exchange. The three-phase voltage source converter is shown in Figure A-1, Appendix A.

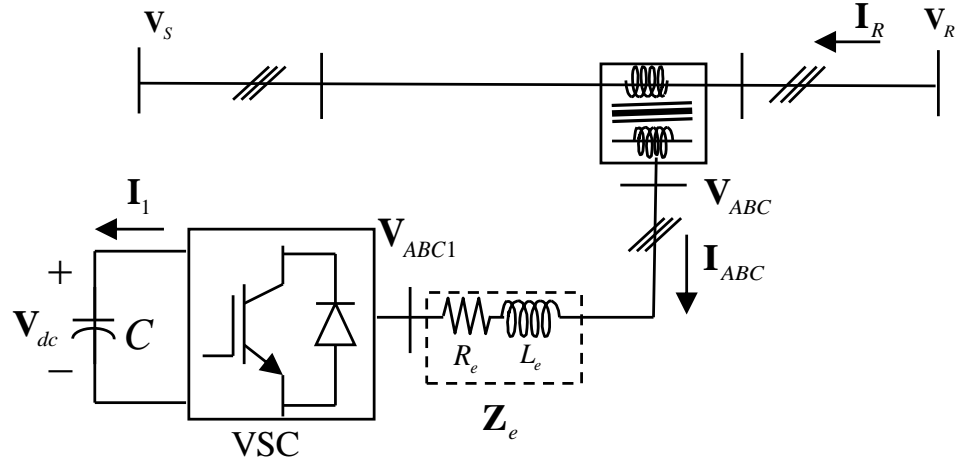


Figure 16: Static synchronous series compensator

3.4.1 Development of the DHD model of the SSSC

The derivation presented below is one of the contributions of this research to the state of power systems analysis by extending the application of DHD modeling methodology to the SSSC. The three-phase voltages and currents on the AC side of the SSSC are $\mathbf{v}_{ABC1}(t)$ and $\mathbf{i}_{ABC}(t)$, respectively, and can be expressed in terms of DC side voltage $\mathbf{v}_{dc}(t)$, DC side current $i_1(t)$ and the switching functions as

$$\mathbf{v}_{ABC1}(t) = \mathbf{p}_s(t) \mathbf{v}_{dc}(t) \quad (3.27)$$

$$i_1(t) = \mathbf{q}_s(t) \mathbf{i}_{ABC}(t) \quad (3.28)$$

where $\mathbf{v}_{ABC1}(t)$, $\mathbf{p}_s(t)$, $\mathbf{q}_s(t)$, and $\mathbf{i}_{ABC}(t)$ are vectors given by:

$$\mathbf{v}_{ABC1}(t) = \begin{bmatrix} v_{A1}(t) \\ v_{B1}(t) \\ v_{C1}(t) \end{bmatrix}$$

$$\mathbf{i}_{ABC}(t) = \begin{bmatrix} i_A(t) \\ i_B(t) \\ i_C(t) \end{bmatrix}$$

$$\mathbf{p}_s(t) = \begin{bmatrix} s_{ab}(t) \\ s_{bc}(t) \\ s_{ca}(t) \end{bmatrix} \quad \text{and} \quad \mathbf{q}_s = [s_{ab}(t) \quad s_{bc}(t) \quad s_{ca}(t)] \quad (3.29)$$

$s_{ab}(t)$, $s_{bc}(t)$, and $s_{ca}(t)$ are switching functions [10]. The voltage source converter consists of six switches as shown in Figure A-1, Appendix A.

The following state-space equations describe the dynamics of the SSSC:

$$\frac{d v_{dc}(t)}{dt} = \frac{1}{C} i_1(t) = \frac{1}{C} \mathbf{q}_s(t) \mathbf{i}_{ABC}(t) \quad (3.30)$$

$$R_e \mathbf{i}_{ABC}(t) + L_e \frac{d \mathbf{i}_{ABC}(t)}{dt} = \mathbf{v}_{ABC}(t) - \mathbf{v}_{ABC1}(t) \quad (3.31)$$

$$\frac{d \mathbf{i}_{ABC}(t)}{dt} = -\frac{R_e}{L_e} \mathbf{i}_{ABC}(t) + \frac{1}{L_e} \mathbf{v}_{ABC}(t) - \frac{1}{L_e} \mathbf{p}_{s1}(t) \mathbf{v}_{dc}(t)$$

where L_e and R_e are the per phase equivalent inductance and resistance, respectively of the transformer referred to the secondary, C is the capacitance of the capacitor, and $i_1(t)$ is the DC side current. The boundary conditions of the SSSC are

$$\mathbf{v}_{ABC}(t) = \mathbf{v}_R(t) - \mathbf{v}_S(t) \quad (3.32)$$

$$\mathbf{i}_{ABC}(t) = \mathbf{i}_R(t)$$

The state-space equations in (3.30) and (3.31) that describe the dynamics of the SSSC may be expressed by

$$\begin{bmatrix} \frac{d \mathbf{i}_{ABC}(t)}{dt} \\ \frac{d v_{dc}(t)}{dt} \end{bmatrix} = \begin{bmatrix} -\frac{R_e}{L_e} & -\frac{1}{L_e} \mathbf{P}_s(t) \\ \frac{1}{C} \mathbf{Q}_s(t) & 0 \end{bmatrix} \begin{bmatrix} \mathbf{i}_{ABC}(t) \\ v_{dc}(t) \end{bmatrix} + \frac{1}{L_e} \begin{bmatrix} \mathbf{V}_{ABC}(t) \\ 0 \end{bmatrix} \quad (3.33)$$

The state-space model in (3.33) can be transformed into a DHD representation by making use of the procedure described in Section 3.2. The resulting DHD model is given by

$$\begin{bmatrix} \dot{\mathbf{I}}_{ABC}(t) \\ \dot{\mathbf{V}}_{dc}(t) \end{bmatrix} = \begin{bmatrix} -\frac{R_e}{L_e} \mathbf{U}_1 - \mathbf{D}(jh\omega_0) & -\frac{1}{L_e} \mathbf{P}_s(t) \\ \frac{1}{C} \mathbf{Q}_s(t) & -\mathbf{D}(jh\omega_0) \end{bmatrix} \begin{bmatrix} \mathbf{I}_{ABC}(t) \\ \mathbf{V}_{dc}(t) \end{bmatrix} + \frac{1}{L_e} \begin{bmatrix} \mathbf{V}_{ABC} \\ 0 \end{bmatrix} \quad (3.34)$$

where $\mathbf{V}_{ABC} = \mathbf{V}_R(t) - \mathbf{V}_S(t)$ (assuming that magnitude of $\mathbf{V}_R(t)$ is greater than $\mathbf{V}_S(t)$) and \mathbf{U}_1 is the identity matrix (\mathbf{U} is used instead of \mathbf{I} to avoid confusion with the current vector).

The solution of the DHD state equations (3.34) gives a complete description of the harmonics in the SSSC under steady and dynamic state conditions. The steady state solution of (3.34) can be obtained by setting the derivatives $\dot{\mathbf{I}}_{ABC}(t)$ and $\dot{\mathbf{V}}_{dc}(t)$ to zero, resulting in

$$\begin{bmatrix} \mathbf{I}_{ABC}(t) \\ \mathbf{V}_{dc}(t) \end{bmatrix} = \frac{1}{L_e} \begin{bmatrix} -\frac{R_e}{L_e} \mathbf{U} - \mathbf{D}(jh\omega_0) & -\frac{1}{L_e} \mathbf{P}_s(t) \\ \frac{1}{C} \mathbf{Q}_s(t) & -\mathbf{D}(jh\omega_0) \end{bmatrix}^{-1} \begin{bmatrix} \mathbf{V}_{ABC}(t) \\ 0 \end{bmatrix} \quad (3.35)$$

$$\begin{bmatrix} \mathbf{I}_{ABC}(t) \\ \mathbf{V}_{dc}(t) \end{bmatrix} = -\frac{1}{L_e} [\mathbf{A}_{SSSC}]^{-1} \begin{bmatrix} \mathbf{V}_{ABC}(t) \\ 0 \end{bmatrix}$$

where

$$\mathbf{A}_{SSSC} = \begin{bmatrix} -\frac{R_e}{L_e} \mathbf{U}_1 - \mathbf{D}(jh\omega_0) & -\frac{1}{L_e} \mathbf{P}_s(t) \\ \frac{1}{C} \mathbf{Q}_s(t) & -\mathbf{D}(jh\omega_0) \end{bmatrix}$$

The equation (3.35) is used as the initial steady state condition (only if inverse of the matrix \mathbf{A}_{SSSC} exists) for solving (3.34) where the voltage $\mathbf{V}_{dc}(t)$ is a complex vector with harmonic coefficients given by

$$\mathbf{V}_{dc}(t) = [V_{dc_{-h}}(t) \cdots V_{dc_0}(t) \cdots V_{dc_h}(t)]^T$$

3.4.2 Simulation of the proposed SSSC model

The DHD model of the SSSC in (3.34) will now be used to investigate its dynamic harmonic response to a given disturbance. A PWM converter was used, and the switching function was calculated to eliminate the 5th, 7th, 11th, 13th, and 17th harmonics. (Since output waveform distortion is mainly due to higher order harmonics, 5th, 7th, 11th, 13th, and 17th are chosen for elimination). The magnitude of the inverter voltage can be adjusted by controlling the voltage across the capacitor. This can be achieved by changing the phase angle of the operation of the inverter switches with respect to the AC system [57]. In this case a phase angle of 15^o was considered. The per-phase inductive reactance and resistance of the feed to the transformer and the capacitance of the

capacitor are $L_e = 0.2$ mH, $R_e = 0.04 \Omega$, and $C = 5000 \mu\text{F}$, respectively. The balanced per-phase source voltages V_R and V_S in per unit (p.u), at a frequency of 60 Hz, and under steady state condition are

$$\begin{aligned} v_{Sa}(t) &= \sin \omega_0 t & v_{Ra}(t) &= 2 \sin \omega_0 t \\ v_{Sb}(t) &= \sin (\omega_0 t - 120^\circ) & v_{Rb}(t) &= 2 \sin (\omega_0 t - 120^\circ) \\ v_{Sc}(t) &= \sin (\omega_0 t + 120^\circ) & v_{Rc}(t) &= 2 \sin (\omega_0 t + 120^\circ) \end{aligned}$$

A disturbance is assumed in the voltage starting at 0.04 seconds and lasting for 0.005 seconds, in which $v_{Sa}(t)$ is reduced to 50% of its original value. The simulation starts at $t_0 = 0$ seconds with final time $t_f = 0.1$ seconds, and a time step of $\Delta t = 0.01$ ms. For accuracy purposes, 50 harmonics are considered. The simulations are performed using MATLAB[®] software. The integration method used for these simulations is ode45(), which is a fourth-order-Runge-Kutta algorithm that is built-in MATLAB[®] software.

The dynamic harmonic responses of the fundamental 3rd, 5th, and 7th harmonic currents of VSC are shown in Figure 17(a). The VSC is connected between buses R and S , whose relationship is established by equation (3.32). Since the disturbance affects the output voltage of phase a at bus S to drop by 50% of its steady state value, it causes an increase at the terminals, as expected, leading to a rise in the fundamental components of the output current of phase a . The time domain waveform of the output current of phase a of VSC is shown in Figure 17(b). Here, it is evident that the output voltage of the VSC of phase a is reduced by a considerable magnitude. This is because the increase in the output current of phase a of the VSC causes a larger drop at its terminals, thus leading to a decrease in the voltage of the same during the disturbance interval. The time domain

waveform of the output voltage of phase a of VSC is shown in Figure 17(d). In steady state, 5th and 7th harmonics generated by the VSC have been successfully eliminated and no attempt is made to eliminate the triplen harmonics.

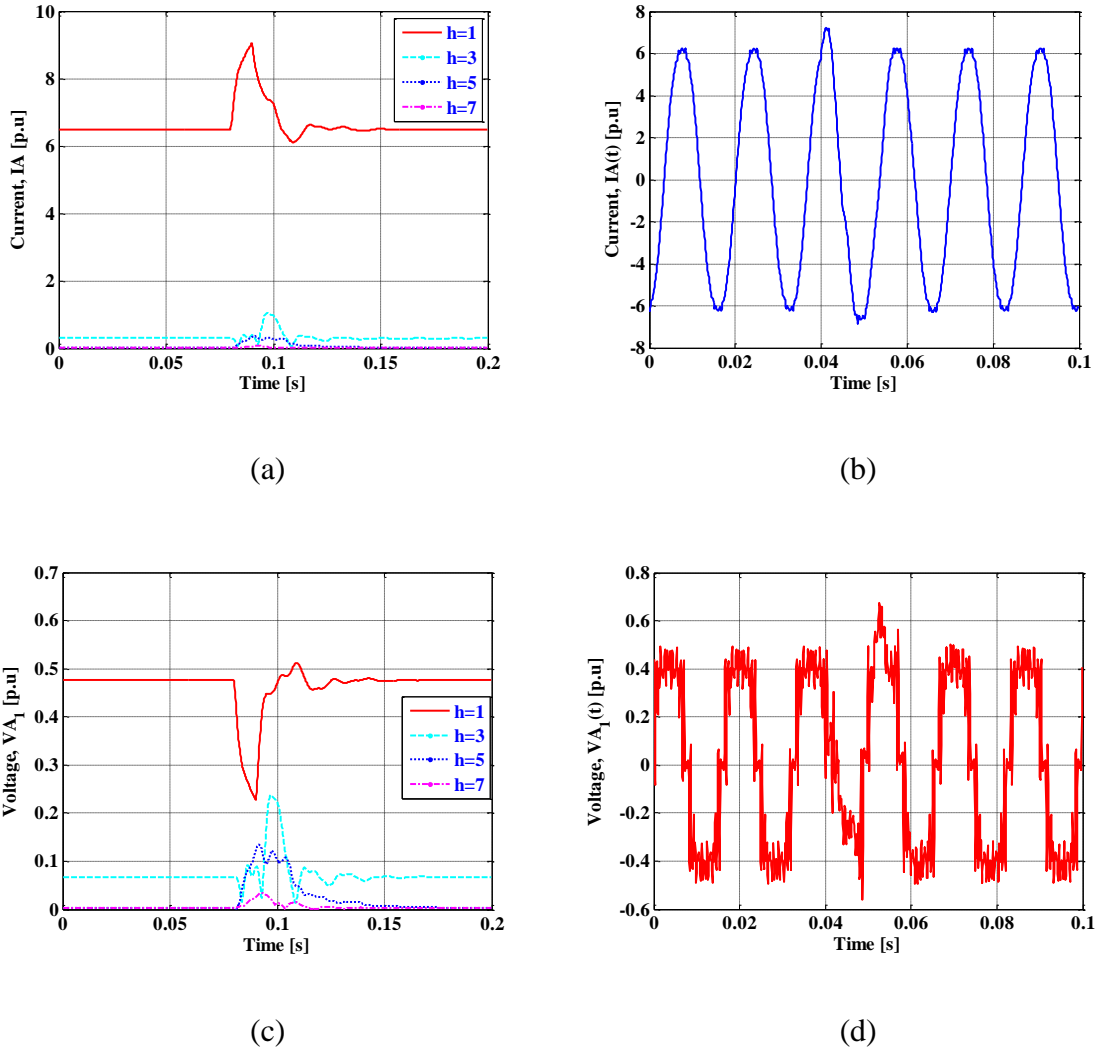


Figure 17: The phase a current of VSC (a) Harmonic content of disturbance interval (b) Time domain representation (c) Harmonic content of phase a voltage (d) Time domain representation of voltage

The results show no change in these quantities for periodic steady state operation before and after the disturbance. However, the dynamic behavior of the harmonics

exhibits changes during the transient conditions. The above results are definitive in determining the instant of the disturbance commencement and closure. Thus, it can be concluded that harmonics change acutely under a system disturbance.

The dynamic harmonic response of the DC side voltage of the converter is shown in Figure 18(b). The non-characteristic harmonics (2nd, 4th, 6th) are present in the DC side voltage because of the unbalanced nature of the disturbance. Figure 18(a) and (b) show the time domain representation and the harmonic content of the disturbance interval of the DC side voltage of the SSSC.

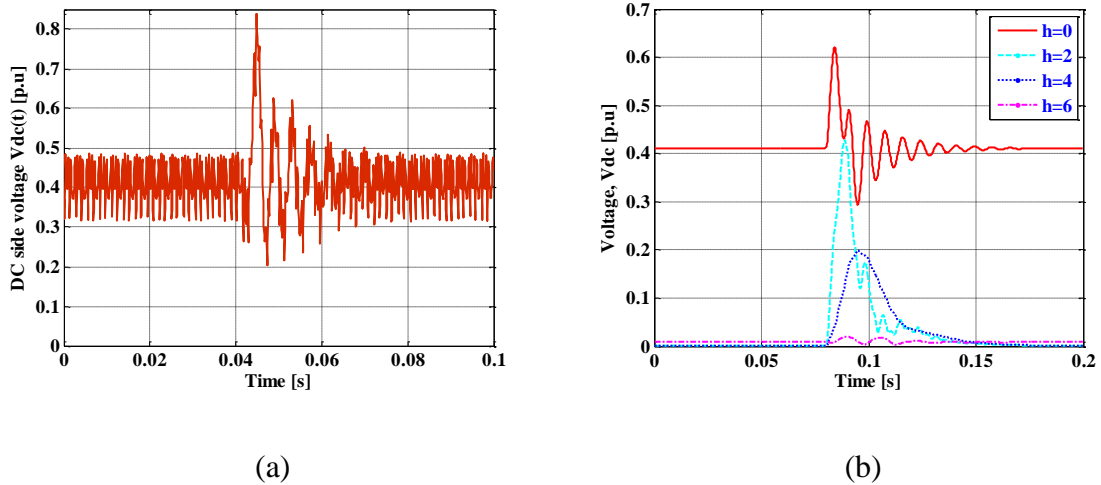


Figure 18: DC side voltage (a) Time domain representation (b) Harmonic content of disturbance interval

The time-domain methods with WFFT achieve harmonic behavior of the system under stationary conditions. However, these methods lose their accuracy during time-varying conditions [11], [58]. Therefore, it is not possible to capture the accurate harmonic response of the system using these methods with WFFT during fast disturbances. The DHD method does not have the same problems associated with FFT-

based methods, and thus permits an analysis of the transient and steady state response of electrical networks that contain nonlinearities and embedded power electronics. The accurate harmonic information obtained from the SSSC DHD model is very useful for power quality (PQ) assessment. Some of the PQ indices, such as RMS voltages and currents, apparent power, reactive power, active power, and distortion power in all three phases are of interest for PQ assessments and control. Their definitions are listed in Table IV [24].

Table IV: Power quality parameters

| Parameter | Definition |
|--------------------------------------|--|
| RMS voltage | $V_{rms} = \sqrt{\sum_{n=-h}^h V_n ^2}$ |
| RMS current | $I_{rms} = \sqrt{\sum_{n=-h}^h I_n ^2}$ |
| Apparent power | $S = V_{rms} I_{rms}$ |
| Active power | $P = \sum_{n=-h}^h V_n I_{-n}$ |
| Reactive power | $Q_H = \sqrt{\sum_{n=-h}^h (V_n ^2 I_n ^2 - V_n I_{-n} V_n I_{-n})}$ |
| Distortion power | $D_H = \sqrt{S^2 - P^2 - Q_H^2}$ |
| Power factor | $PF = \frac{P}{S}$ |
| Total harmonic distortion in voltage | $THD(V) = \sqrt{\frac{\sum_{n=h+3}^{2h+1} V_n ^2}{ V_{h+2} ^2}} \times 100$ |
| Total harmonic distortion in current | $THD(I) = \sqrt{\frac{\sum_{n=h+3}^{2h+1} I_n ^2}{ I_{h+2} ^2}} \times 100$ |

As shown in Table IV, active power is given by the inner product of complex vector V and complex conjugate of vector I . In the active power equation, I has negative index, denoting the current complex conjugate. The multiplication of voltages and currents of the same frequency result in reactive power, whereas for different

frequencies the result is distortion power. Active, reactive, and distortion powers are orthogonal components as shown in Figure 19 [10].

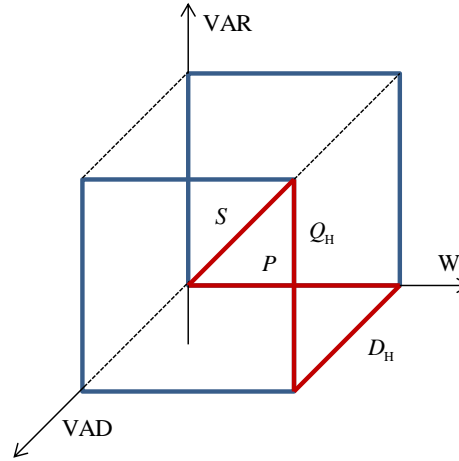


Figure 19: Power cube

In other words,

$$S^2 = P^2 + Q_H^2 + D_H^2 \quad (3.36)$$

Equation (3.36) should be satisfied at every instant.

Here, reactive power Q is decomposed into two orthogonal components Q_H and D_H . The first component is given by the multiplication of harmonic voltages and currents of the same frequency (Q_H), and the second component is given by the multiplication of harmonic voltages and currents of different frequency, called the distortion power (D_H).

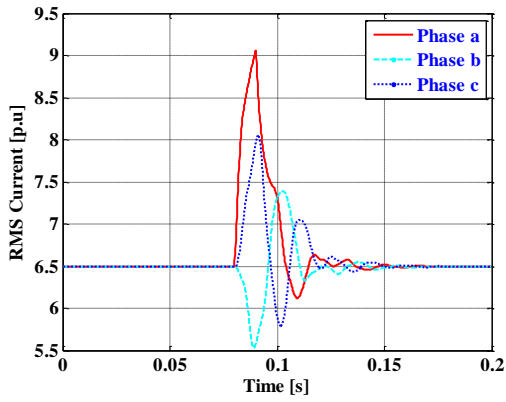
The sub-index notation serves two purposes:

1. The regular notation of reactive power (Q) is without sub-index (H), but when harmonics are considered, we cannot represent Q_H with Q because Q is not just Q_H , it has the other component, the distortion power (D_H).

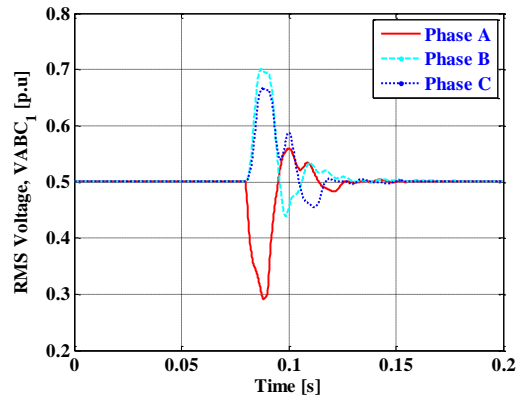
2. Since Q_H and D_H are the orthogonal components of the reactive power Q , they both use same index for emphasis.

Some of the PQ indices at the terminals of the SSSC before, during, and after the disturbance are shown in Figure 20.1 and Figure 20.2. It can be observed, from Figure 20.1(a) that the RMS output current of phase a increased due to a rise in the output voltage of phase a at the terminals as shown in Figure 20.1(b) of the VSC during the disturbance interval. The variations in phases b and c are due to a change in the DC side voltage and switching functions of each phase. The increase in the output current of phase a of the VSC causes a larger drop at its terminals, thus leading to a decrease in the voltage of the same during the disturbance interval. The variations in the voltages of phases b and c are due to the changes in the corresponding output currents of both the phases.

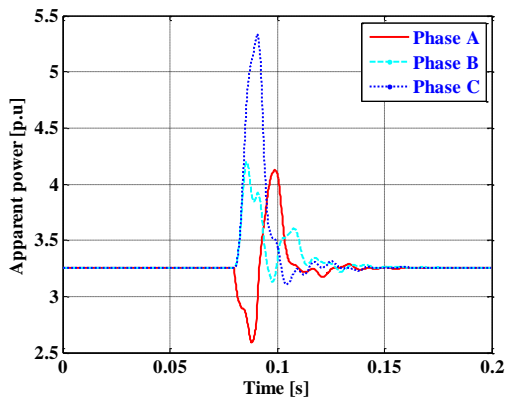
The variation of the per-phase output of apparent, active, reactive and distortion powers, shown in Figure 20.1(c), (d) and Figure 20.2(a) and (b), are due to the mutual effects of the per-phase output voltages and currents of VSC. Though voltages and currents of the VSC were positive, the phase angle between them is 90° , causing zero active power at all three phases during the steady state period. The distortions in the active power output, in each phase, during the disturbance interval, are due to the variations in the VSC output currents and voltages.



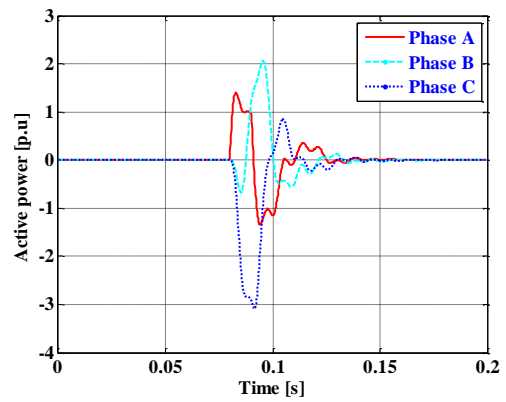
(a)



(b)

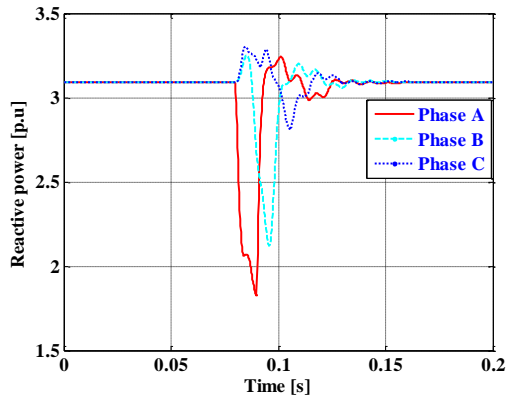


(c)

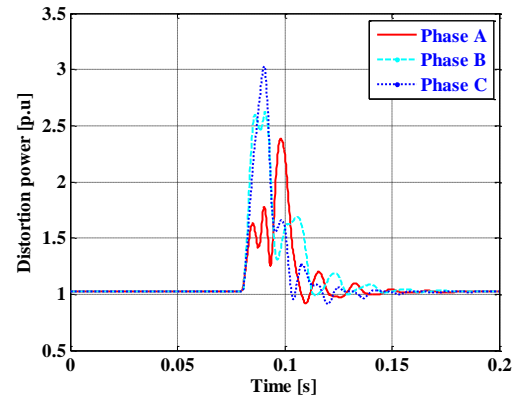


(d)

Figure 20.1: Power quality indices (a) RMS values of the output currents (b) RMS values of the output voltages (c) Per-phase output apparent powers (d) Per-phase output active powers



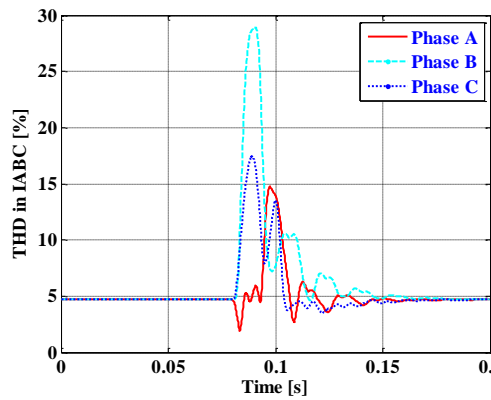
(a)



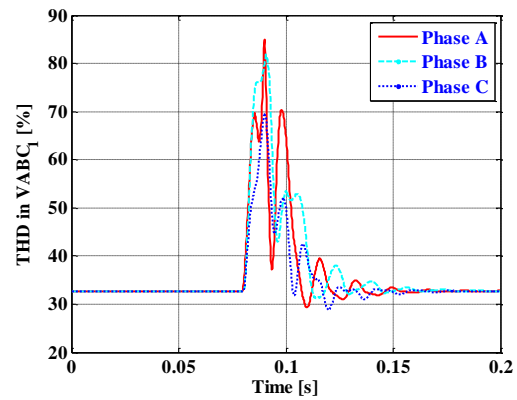
(b)

Figure 20.2: Power quality indices (a) Per-phase output reactive powers (b) Per-phase output distortion powers of VSC 2

The total harmonic distortions (THD) in voltage and current at the terminals of the VSC before, during, and after the disturbance are shown in Figure 21.



(a)



(b)

Figure 21: Total harmonic distortion (a) in current (IABC) (b) in voltage (VABC₁)

The symmetrical component method [59] is a modeling technique that permits systematic analysis and design of three-phase systems. The method of symmetrical components is a general one, applicable to any polyphase system. The usefulness of this method in power system analysis, and the harmonic currents and voltages that are present in individual sequence components under steady and dynamic conditions, are discussed in the following section.

3.5 Sequence components

The sequence currents and voltages under dynamic and steady state conditions of FACTS devices can be obtained by the application of C.L. Fortescue's theorem [59], decomposing the unbalanced three-phase currents into three, three-phase and symmetrical current components. The theorem states that [59]

"Any three vectors $I_a, I_b,$ and I_c can be resolved into a system of three equal vectors $I_{a0}, I_{b0} = I_{a0}, I_{c0} = I_{a0}$ (the zero phase sequence) and two symmetrical three-phase systems, $I_{a1}, I_{b1} = a^2 I_{a1}$ (the positive phase sequence), and $I_{c1} = a I_{a1}$ and $I_{a2}, I_{b2} = a I_{a2}, I_{c2} = a^2 I_{a2}$, (the negative phase sequence)".

According to this theorem, the three unbalanced current phasors $I_a, I_b,$ and I_c are expressed in terms of their symmetrical components as

$$\begin{bmatrix} I_a \\ I_b \\ I_c \end{bmatrix} = \begin{bmatrix} 1 & 1 & 1 \\ 1 & a^2 & a \\ 1 & a & a^2 \end{bmatrix} \begin{bmatrix} I_{a0} \\ I_{a1} \\ I_{a2} \end{bmatrix} \quad (3.37)$$

where the coefficients a and a^2 are complex numbers given by $a=1\angle 120^\circ$, and $a^2=1\angle -120^\circ$.

Inversion of equation (3.37) results in

$$\begin{bmatrix} I_{a0} \\ I_{a1} \\ I_{a2} \end{bmatrix} = \frac{1}{3} \begin{bmatrix} 1 & 1 & 1 \\ 1 & a & a^2 \\ 1 & a^2 & a \end{bmatrix} \begin{bmatrix} I_a \\ I_b \\ I_c \end{bmatrix} \quad (3.38)$$

Under balanced conditions, equation (3.38) becomes

$$\begin{bmatrix} I_{a0} \\ I_{a1} \\ I_{a2} \end{bmatrix} = \frac{1}{3} \begin{bmatrix} 1 & 1 & 1 \\ 1 & a & a^2 \\ 1 & a^2 & a \end{bmatrix} \begin{bmatrix} I\angle 0^\circ \\ I\angle -120^\circ \\ I\angle 120^\circ \end{bmatrix} = \begin{bmatrix} 0 \\ I \\ 0 \end{bmatrix} \quad (3.39)$$

Voltage distortions result in harmonics in the system, which cause the production of harmonic currents, and vice versa. For a given harmonic h , (3.39) yields [10]

$$\begin{bmatrix} I_{a0} \\ I_{a1} \\ I_{a2} \end{bmatrix} = \frac{1}{3} \begin{bmatrix} 1 & 1 & 1 \\ 1 & a & a^2 \\ 1 & a^2 & a \end{bmatrix} \begin{bmatrix} I_h\angle\phi_h \\ I_h\angle(-h120^\circ + \phi_h) \\ I_h\angle(h120^\circ + \phi_h) \end{bmatrix} \quad (3.40)$$

The zero-sequence component of the current is given by

$$I_0 = \frac{1}{3} \left(I_h \angle \phi_h + I_h \angle (-h120^\circ + \phi_h) + I_h \angle (h120^\circ + \phi_h) \right) \text{ or}$$

$$I_0 = \frac{I_h \angle \phi_h}{3} \left(1 + 2 \cos(h120^\circ) \right) \quad (3.41)$$

$$\text{That is, } I_0 = \begin{cases} 0, h \neq 3m \\ I_h \angle \phi_h, h = 3m \end{cases} \quad (3.42)$$

where m is a positive integer.

The positive sequence of the harmonic current is given by

$$I_1 = \frac{1}{3} \left(I_h \angle \phi_h + \left(1 \angle 120^\circ \right) I_h \angle (-h120^\circ + \phi_h) + \left(1 \angle -120^\circ \right) I_h \angle (h120^\circ + \phi_h) \right) \text{ or}$$

$$I_1 = \frac{I_h \angle \phi_h}{3} \left(1 + 2 \cos((h-1)120^\circ) \right) \quad (3.43)$$

That is,

$$I_1 = \begin{cases} 0, h \neq 3m+1 \\ I_h \angle \phi_h, h = 3m+1 \end{cases} \quad (3.44)$$

where m is a positive integer.

The negative sequence of the harmonic current is given by

$$I_2 = \frac{1}{3} \left(I_h \angle \phi_h + \left(1 \angle -120^\circ \right) I_h \angle (-h120^\circ + \phi_h) + \left(1 \angle 120^\circ \right) I_h \angle (h120^\circ + \phi_h) \right) \text{ or}$$

$$I_2 = \frac{I_h \angle \phi_h}{3} \left(1 + 2 \cos((h+1)120^\circ) \right) \quad (3.45)$$

That is,

$$I_2 = \begin{cases} 0, h \neq 3m-1 \\ I_h \angle \phi_h, h = 3m-1 \end{cases} \quad (3.46)$$

where m is a positive integer. From equations (3.42), (3.44), and (3.46) the harmonics present in the sequence components, under steady state, are shown in Table V.

Table V: Harmonics in the sequence components

| Sequence component | Harmonics present during steady state |
|--------------------|---------------------------------------|
| Zero | 3, 6, 9, 12 |
| Positive | 4, 7, 10, 13..... |
| Negative | 2, 5, 8, 11 |

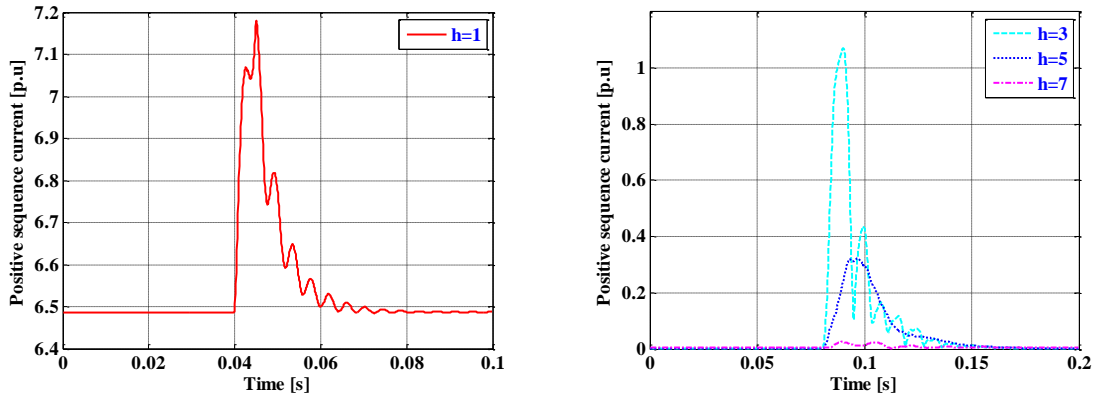
In a balanced power system, only the positive sequence components are present. Whereas, in an unbalanced and faulted system, negative- and zero- sequence quantities are also present. These quantities are a measure of the amount of unbalance that exists in the system. Verifying harmonics present in the sequence currents derived from the proposed SSSC model in Table V, is one way to confirm this model.

Even harmonics are not present at the output of the VSC, since the voltage and current waveforms have half-wave symmetry. The harmonic contents of positive sequence currents of the VSC are shown in Figure 22.1 (a). From these plots it is evident that the fundamental and the 7th harmonic currents are present during the steady state and all the odd harmonics are present during the disturbance interval.

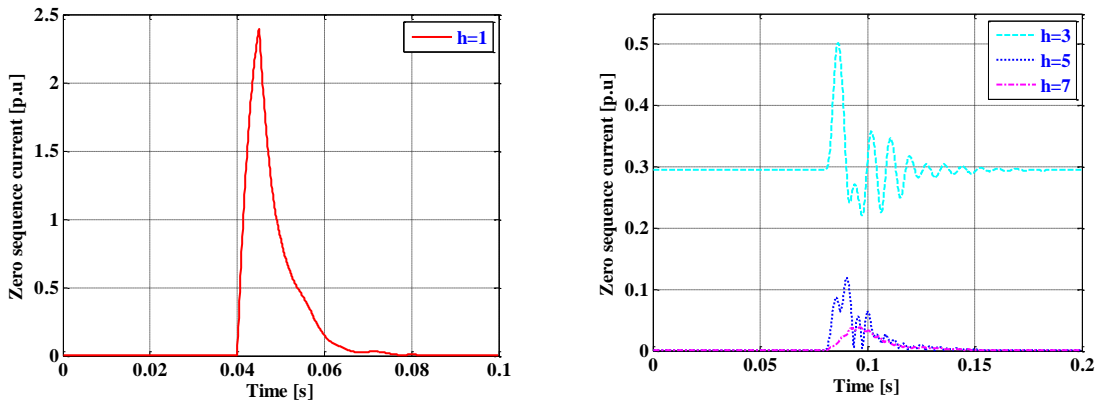
The harmonic components of zero sequence currents of the VSC in the SSSC are shown in Figure 22.1 (b). These plots show that the 3rd harmonic component of the zero

sequence current exists only when the system is under the steady state and all the other odd harmonics are present during the disturbance interval.

The harmonic contents of negative sequence currents of the VSC in the SSSC are shown in Figure 22.2 (c). Out of all four harmonics considered, only the 5th component of the negative sequence currents appears during the steady state, while all the odd harmonic components including the 5th component are present during the disturbance.



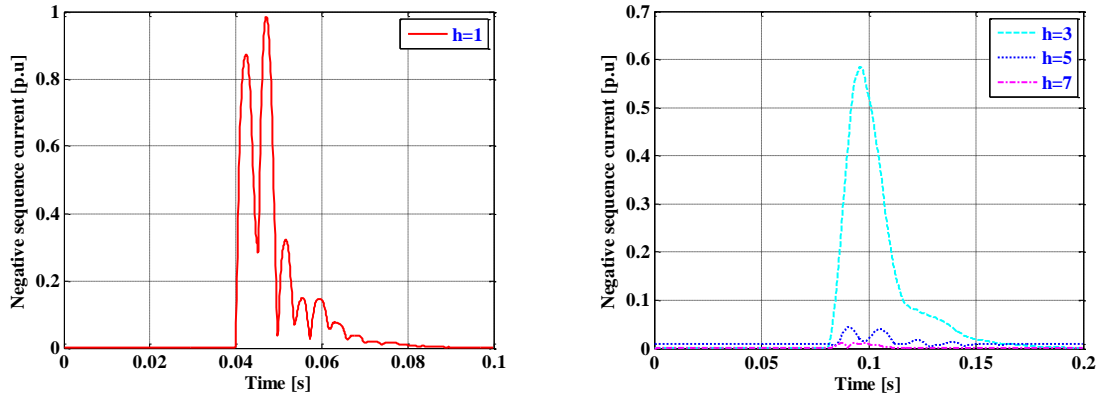
(a)



(b)

Figure 22.1: Sequence currents of SSSC: Harmonic content of disturbance interval (a)

Positive sequence (b) Zero sequence



(c)

Figure 22.2: Sequence currents of SSSC: Harmonic content of disturbance interval (c)

Negative sequence

3.6 Unified power flow controller

The UPFC is the combination of a STATCOM and an SSSC as shown in Figure 23, which was proposed by Gyugyi in 1992 [41], [42]. Theory, modeling and application of the UPFC are discussed in [43]. It is equipped with two VSCs, labeled VSC 1 and VSC 2. These are connected back-to-back across a storage capacitor, which allows real power transfer.

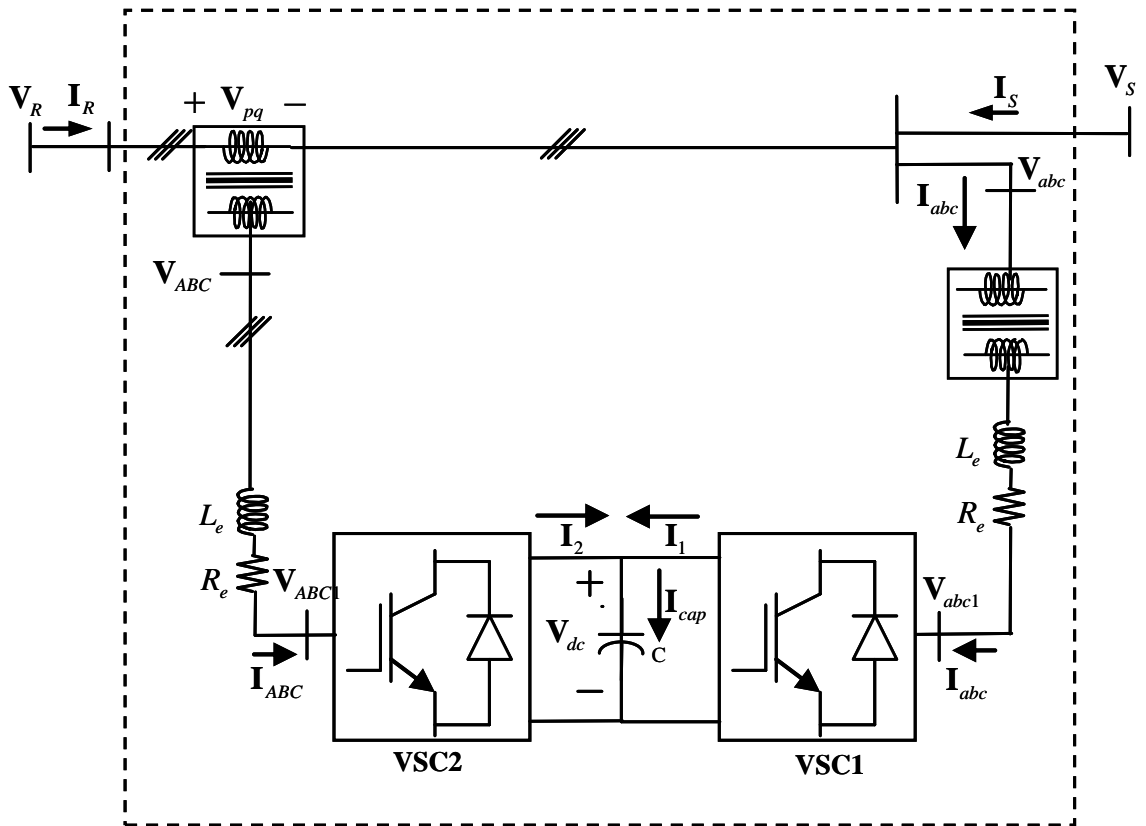


Figure 23: Unified power-flow controller

The shunt controller in the UPFC (VSC 1) injects three-phase currents and the series controller (VSC 2) injects three-phase voltages, into the AC system. The benefit of this design is that these two converters can independently generate or absorb reactive power. This capability of separately controlling both the real and reactive power makes UPFC one of the most important controllers of voltage and power flow control in AC transmission systems.

In the following section, another contribution to the state of power system analysis, the proposed dynamic harmonic domain model of the UPFC, is developed.

3.6.1 Development of the DHD model of the UPFC

The three-phase voltages and currents on the AC sides of the UPFC are $\mathbf{v}_{ABC1}(t)$, $\mathbf{v}_{abc1}(t)$, $\mathbf{i}_{ABC}(t)$ and $\mathbf{i}_{abc}(t)$, respectively, and can be expressed in terms of the DC side voltage $v_{dc}(t)$, the DC side currents $i_1(t)$ and $i_2(t)$, and the switching functions as

$$\begin{aligned}\mathbf{v}_{abc1}(t) &= \mathbf{p}_{s1}(t)v_{dc}(t) \\ \mathbf{v}_{ABC1}(t) &= \mathbf{p}_{s2}(t)v_{dc}(t)\end{aligned}\quad (3.47)$$

$$\begin{aligned}i_1(t) &= \mathbf{q}_{s1}(t)\mathbf{i}_{abc}(t) \\ i_2(t) &= \mathbf{q}_{s2}(t)\mathbf{i}_{ABC}(t)\end{aligned}\quad (3.48)$$

where $\mathbf{p}_{s1}(t)$, $\mathbf{p}_{s2}(t)$, $\mathbf{q}_{s1}(t)$ and $\mathbf{q}_{s2}(t)$ are transformation vectors, given by

$$\begin{aligned}\mathbf{p}_{s1}(t) &= \begin{bmatrix} s_{ab1}(t) \\ s_{bc1}(t) \\ s_{ca1}(t) \end{bmatrix} \quad \text{and} \quad \mathbf{p}_{s2}(t) = \begin{bmatrix} s_{ab2}(t) \\ s_{bc2}(t) \\ s_{ca2}(t) \end{bmatrix} \\ \mathbf{q}_{s1}(t) &= [s_{ab1}(t) \quad s_{bc1}(t) \quad s_{ca1}(t)] \\ \mathbf{q}_{s2}(t) &= [s_{ab2}(t) \quad s_{bc2}(t) \quad s_{ca2}(t)]\end{aligned}\quad (3.49)$$

and $s_{ab1}(t)$, $s_{bc1}(t)$, and $s_{ca1}(t)$ are the switching functions of VSC 1 and $s_{ab2}(t)$, $s_{bc2}(t)$, and $s_{ca2}(t)$ are the switching functions of VSC 2, which were introduced in Section 3.5.

The voltage source converter switches and their order are shown in Figure A-1, Appendix A. The equivalent impedance, Z_e , represents the per-phase inductive reactance (X_e) and resistance (R_e) of the feed to the transformer. The following state-space equation can be written to describe the dynamics of the UPFC:

$$\frac{dv_{dc}(t)}{dt} = \frac{1}{C}(i_1(t) + i_2(t)) \quad (3.50)$$

Substitution of equation (3.48) into equation (3.50) yields

$$\frac{dv_{dc}(t)}{dt} = \frac{1}{C}(\mathbf{q}_{s1}(t)\mathbf{i}_{abc}(t) + \mathbf{q}_{s2}(t)\mathbf{i}_{ABC}(t)) \quad (3.51)$$

The voltage drop across the equivalent impedances of the two transformers is

$$R_e\mathbf{i}_{abc}(t) + L_e \frac{d\mathbf{i}_{abc}(t)}{dt} = \mathbf{v}_{abc}(t) - \mathbf{v}_{abc1}(t)$$

$$\frac{d\mathbf{i}_{abc}(t)}{dt} = -\frac{R_e}{L_e}\mathbf{i}_{abc}(t) + \mathbf{v}_{abc}(t) - \mathbf{v}_{abc1}(t) \quad (3.52)$$

$$R_e\mathbf{i}_{ABC}(t) + L_e \frac{d\mathbf{i}_{ABC}(t)}{dt} = \mathbf{v}_{ABC}(t) - \mathbf{v}_{ABC1}(t)$$

$$\frac{d\mathbf{i}_{ABC}(t)}{dt} = -\frac{R_e}{L_e}\mathbf{i}_{ABC}(t) + \mathbf{v}_{ABC}(t) - \mathbf{v}_{ABC1}(t) \quad (3.53)$$

Substitution of equations (3.47) into equations (3.53) and (3.52) yields

$$\frac{d\mathbf{i}_{abc}(t)}{dt} = -\frac{R_e}{L_e}\mathbf{i}_{abc}(t) + \frac{1}{L_e}(\mathbf{v}_{abc}(t) - \mathbf{p}_{s1}(t)v_{dc}(t)) \quad (3.54)$$

$$\frac{d\mathbf{i}_{ABC}(t)}{dt} = -\frac{R_e}{L_e}\mathbf{i}_{ABC}(t) + \frac{1}{L_e}(\mathbf{v}_{ABC}(t) - \mathbf{p}_{s2}(t)v_{dc}(t)) \quad (3.55)$$

The boundary conditions for this controller are

$$\begin{aligned}
\mathbf{i}_{abc}(t) &= \mathbf{i}_S(t) + \mathbf{i}_R(t) \\
\mathbf{i}_{ABC}(t) &= \mathbf{i}_R(t) \\
\mathbf{v}_{abc}(t) &= \mathbf{v}_S(t) \\
\mathbf{v}_{ABC}(t) &= \mathbf{v}_R(t) - \mathbf{v}_S(t)
\end{aligned} \tag{3.56}$$

Substitution of these conditions into the state-space equations (3.51), (3.54) and (3.55) yield

$$\begin{aligned}
\begin{bmatrix} \frac{d\mathbf{i}_S(t)}{dt} \\ \frac{d\mathbf{i}_R(t)}{dt} \\ \frac{dv_{dc}(t)}{dt} \end{bmatrix} &= \begin{bmatrix} -\frac{R_e}{L_e} & 0 & -\frac{1}{L_e}(\mathbf{p}_{S1} - \mathbf{p}_{S2}) \\ 0 & -\frac{R_e}{L_e} & -\frac{1}{L_e}\mathbf{p}_{S2}(t) \\ \frac{1}{C}\mathbf{q}_{S1}(t) & \frac{1}{C}(\mathbf{q}_{S1}(t) + \mathbf{q}_{S2}(t)) & 0 \end{bmatrix} \begin{bmatrix} \mathbf{i}_S(t) \\ \mathbf{i}_R(t) \\ v_{dc}(t) \end{bmatrix} + \\
&\frac{1}{L_e} \begin{bmatrix} 2 & -1 & 0 \\ -1 & 1 & 0 \\ 0 & 0 & 0 \end{bmatrix} \begin{bmatrix} \mathbf{v}_S(t) \\ \mathbf{v}_R(t) \\ 0 \end{bmatrix}
\end{aligned} \tag{3.57}$$

State equation (3.57) can be transformed into an LTI system state equation by the procedure introduced in Section 3.2, resulting in the proposed UPFC DHD model

$$\begin{aligned}
\begin{bmatrix} \dot{\mathbf{I}}_S(t) \\ \dot{\mathbf{I}}_R(t) \\ \dot{\mathbf{V}}_{dc}(t) \end{bmatrix} &= \begin{bmatrix} -\frac{R_e}{L_e}\mathbf{U}_1 - \mathbf{D}(jm\omega_0) & \mathbf{O}_4 & -\frac{1}{L_e}(\mathbf{P}_{S1} - \mathbf{P}_{S2}) \\ \mathbf{O}_4 & -\frac{R_e}{L_e}\mathbf{U}_1 - \mathbf{D}(jm\omega_0) & -\frac{1}{L_e}\mathbf{P}_{S2}(t) \\ \frac{1}{C}\mathbf{Q}_{S1}(t) & \frac{1}{C}(\mathbf{Q}_{S1}(t) + \mathbf{Q}_{S2}(t)) & -\mathbf{D}(jm\omega_0) \end{bmatrix} \\
&\begin{bmatrix} \mathbf{I}_S(t) \\ \mathbf{I}_R(t) \\ \mathbf{V}_{dc}(t) \end{bmatrix} + \frac{1}{L_e} \begin{bmatrix} 2\mathbf{U}_1 & -\mathbf{U}_1 & \mathbf{O}_2 \\ -\mathbf{U}_1 & \mathbf{U}_1 & \mathbf{O}_2 \\ \mathbf{O}_1 & \mathbf{O}_1 & \mathbf{O}_3 \end{bmatrix} \begin{bmatrix} \mathbf{V}_S \\ \mathbf{V}_R \\ \mathbf{O} \end{bmatrix}
\end{aligned} \tag{3.58}$$

where \mathbf{U}_1 is the unit matrix (303×303). \mathbf{O} , \mathbf{O}_1 , \mathbf{O}_2 , \mathbf{O}_3 and \mathbf{O}_4 are the zero matrices with dimensions (101×1) , (101×303) , (303×101) , (101×101) and, (303×303) respectively.

$\mathbf{I}_S(t)$ and $\mathbf{I}_R(t)$ are three-phase source currents. The representation of $\mathbf{I}_S(t)$ in the three phase frame of reference, takes the form,

$$\mathbf{I}_S(t) \Rightarrow \begin{matrix} \mathbf{I}_S^A(t) \\ \mathbf{I}_S^B(t) \\ \mathbf{I}_S^C(t) \end{matrix} \begin{matrix} \mathbf{I}_S^A(t) \\ \mathbf{I}_S^B(t) \\ \mathbf{I}_S^C(t) \end{matrix} ; \mathbf{I}_S^A(t) = \begin{matrix} I_{s_{-h}}^A(t) \\ \vdots \\ I_{s_{-1}}^A(t) \\ I_{s_0}^A(t) \\ I_{s_1}^A(t) \\ \vdots \\ I_{s_h}^A(t) \end{matrix} ; \mathbf{I}_S^B(t) = \begin{matrix} I_{s_{-h}}^B(t) \\ \vdots \\ I_{s_{-1}}^B(t) \\ I_{s_0}^B(t) \\ I_{s_1}^B(t) \\ \vdots \\ I_{s_h}^B(t) \end{matrix} ; \mathbf{I}_S^C(t) = \begin{matrix} I_{s_{-h}}^C(t) \\ \vdots \\ I_{s_{-1}}^C(t) \\ I_{s_0}^C(t) \\ I_{s_1}^C(t) \\ \vdots \\ I_{s_h}^C(t) \end{matrix}$$

$\underbrace{\hspace{10em}}_{101 \times 1} \quad \underbrace{\hspace{10em}}_{101 \times 1} \quad \underbrace{\hspace{10em}}_{101 \times 1}$

$\mathbf{I}_R(t)$, $\mathbf{V}_S(t)$, and $\mathbf{V}_R(t)$ also take the same form as $\mathbf{I}_S(t)$. The size of each phase current and voltage is equal to $2h + 1$. Total harmonics considered for the UPFC case study is 50. Therefore, dimension of each phase current or voltage is 101×1 . The DC side voltage, $\mathbf{V}_{dc}(t)$ in harmonic coefficients vector form,

$$\mathbf{V}_{dc}(t) = \underbrace{\left[V_{dc_{-h}}(t) \quad \cdots \quad V_{dc_{-1}}(t) \quad V_{dc_0}(t) \quad V_{dc_1}(t) \quad \cdots \quad V_{dc_2}(t) \right]^T}_{101 \times 1}$$

The dimensions of all the vectors in the equation (3.58) are:

$$\begin{bmatrix} 303 \times 1 \\ 303 \times 1 \\ 101 \times 1 \end{bmatrix} = \begin{bmatrix} 303 \times 303 & 303 \times 303 & 303 \times 101 \\ 303 \times 303 & 303 \times 303 & 303 \times 101 \\ 101 \times 303 & 101 \times 303 & 101 \times 101 \end{bmatrix} \begin{bmatrix} 303 \times 1 \\ 303 \times 1 \\ 101 \times 1 \end{bmatrix} + \begin{bmatrix} 303 \times 303 & 303 \times 303 & 303 \times 101 \\ 303 \times 303 & 303 \times 303 & 303 \times 101 \\ 101 \times 303 & 101 \times 303 & 101 \times 101 \end{bmatrix} \begin{bmatrix} 303 \times 1 \\ 303 \times 1 \\ 101 \times 1 \end{bmatrix}$$

The solution of equation (3.58) gives the complete description of the harmonics in the UPFC equipment under steady state and dynamic conditions. Again, the steady state solution of (3.58) is obtained by setting $\dot{\mathbf{I}}_S(t)$, $\dot{\mathbf{I}}_R(t)$ and $\dot{\mathbf{V}}_{dc}(t)$ to zero, yielding

$$\begin{bmatrix} \mathbf{I}_S(t) \\ \mathbf{I}_R(t) \\ \mathbf{V}_{dc}(t) \end{bmatrix} = -\mathbf{A}(t)^{-1} \frac{1}{L_e} \begin{bmatrix} 2\mathbf{U}_1 & -\mathbf{U}_1 & \mathbf{O}_2 \\ -\mathbf{U}_1 & \mathbf{U}_1 & \mathbf{O}_2 \\ \mathbf{O}_1 & \mathbf{O}_1 & \mathbf{O}_3 \end{bmatrix} \begin{bmatrix} \mathbf{V}_S \\ \mathbf{V}_R \\ \mathbf{O} \end{bmatrix} \quad (3.59)$$

where

$$\mathbf{A}(t) = \begin{bmatrix} -\frac{R_e}{L_e} \mathbf{U}_1 - \mathbf{D}(jm\omega_0) & \mathbf{O}_4 & -\frac{1}{L_e} (\mathbf{P}_{S1} - \mathbf{P}_{S2}) \\ \mathbf{O}_4 & -\frac{R_e}{L_e} \mathbf{U}_1 - \mathbf{D}(jm\omega_0) & -\frac{1}{L_e} \mathbf{P}_{S2}(t) \\ \frac{1}{C} \mathbf{Q}_{S1}(t) & \frac{1}{C} (\mathbf{Q}_{S1}(t) + \mathbf{Q}_{S2}(t)) & -\mathbf{D}(jm\omega_0) \end{bmatrix}$$

and (3.59) is used, as introduced earlier, as the initial steady state conditions for solving (3.58). Here, the steady state conditions are shown as a function of time so that, if the condition of the system changes at any time t , during the simulation interval, these steady state values, calculated at the previous instant, will be used as initial values for estimating the new values for the next time step (only if inverse of $\mathbf{A}(t)$ exists).

3.6.2 Simulation of the proposed UPFC model

The DHD model of the UPFC in (3.58) is used to investigate the dynamic response of harmonics to a given disturbance. PWM switching was used, and the switching function was calculated using the harmonic elimination method, to eliminate harmonics $i = 5, 7, 11, 13,$ and 17 .

The magnitude of the fundamental of the AC voltage inverter can be adjusted by controlling the voltage across the capacitor. This can be achieved by changing the phase angle of the operation of the inverter switches with respect to the AC system. In this case a phase angle of 15° was considered. The per-phase equivalent leakage inductance, winding resistance of the transformer, and capacitance of the DC capacitor are $L_e = 0.2 \text{ mH}$, $R_e = 0.04 \Omega$, and $C = 5000 \mu\text{F}$, respectively. Under steady state conditions, the bus per-phase voltages V_S , and V_R per unit at a frequency of 60 Hz, are assumed to be identical, a condition known in the industry as a "flat voltage profile," that is

$$\begin{aligned} v_{Sa}(t) &= \sin \omega_0 t & v_{Ra}(t) &= \sin \omega_0 t \\ v_{Sb}(t) &= \sin(\omega_0 t - 120^\circ) & v_{Rb}(t) &= \sin(\omega_0 t - 120^\circ) \\ v_{Sc}(t) &= \sin(\omega_0 t + 120^\circ) & v_{Rc}(t) &= \sin(\omega_0 t + 120^\circ) \end{aligned}$$

A disturbance is assumed in the voltages starting at 0.04 seconds and lasting for 0.015 seconds, and during the disturbance the phase a voltage of $v_s(t)$ is 150% of its original value. The simulation was started at $t_0 = 0$ seconds with final time $t_f = 0.1$ seconds and used an integration step $\Delta t = 0.08 \text{ ms}$.

For the proper operation of the UPFC, it is necessary to keep the DC voltage as constant as possible during the steady state and the disturbance period. The voltage across

the capacitor can be controlled by varying the phase, $\beta_1^{(0)}$, the phase angle of the inverter switches, with respect to the corresponding phase angle of the AC system voltage, to achieve the added advantage of being able to control the inverter output voltage [57]. The control system [17] shown in Figure 24 is used to maintain the DC voltage across the capacitor, as constant as possible, in the simulation of the dynamic model of the UPFC.

Solving the UPFC steady state equation (3.59) yields the reference DC voltage of V_{dc_ref} . A new phase angle, β_1 , for the converter is calculated by adding the phase angle from control system $\Delta\beta_1$ to the steady state angle $\beta_1^{(0)}$. Now the new switching angle for the VSC 1 is calculated from β_1 .

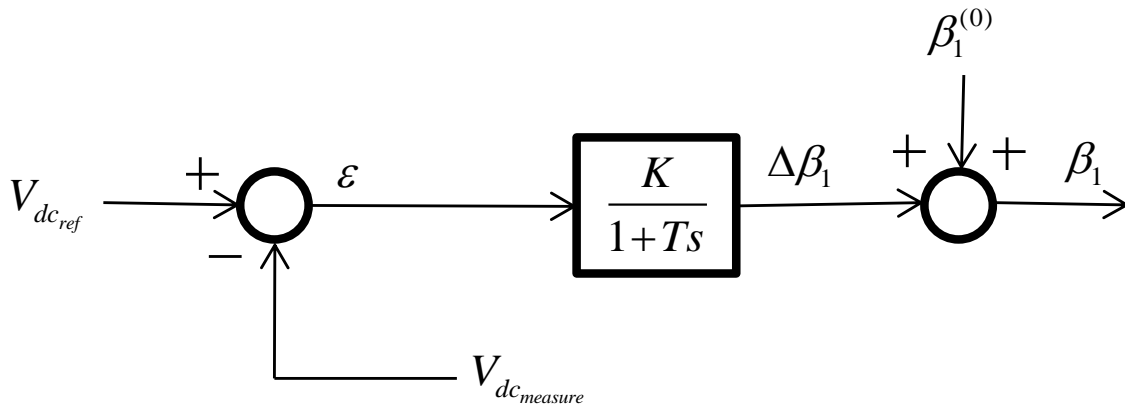


Figure 24: Control system

The following is the state-space equation for the control:

$$\frac{d\Delta\beta_1}{dt} = -\frac{1}{T}\Delta\beta_1 + \frac{K}{T}\varepsilon$$

$$\varepsilon = V_{dc_ref} - V_{dc_measure}$$

$$\beta_1 = \Delta\beta_1 + \beta_1^{(0)}$$

where $V_{dc_{measure}}$ is the DC-term of the actual V_{dc} .

The simulation results presented in Figure 25 shows the harmonic content of the DC voltage with and without control system during the disturbance. Due to the unbalanced nature of the disturbance, non-characteristic harmonics (the 2nd, the 4th, and the 6th) are present in the system. The fundamental component of the DC side voltage drops by 33% of its steady state value, as shown in Figure 18(a). Figure 18(b) demonstrates that the DC component of the voltage is very close to its steady state value, thus indicating that the control system does mitigate the distortion through the disturbance. While the harmonic voltages have not changed with the control, there is a change in the 6th harmonic voltage; however, this could also be eliminated by proper gain and time constant values.

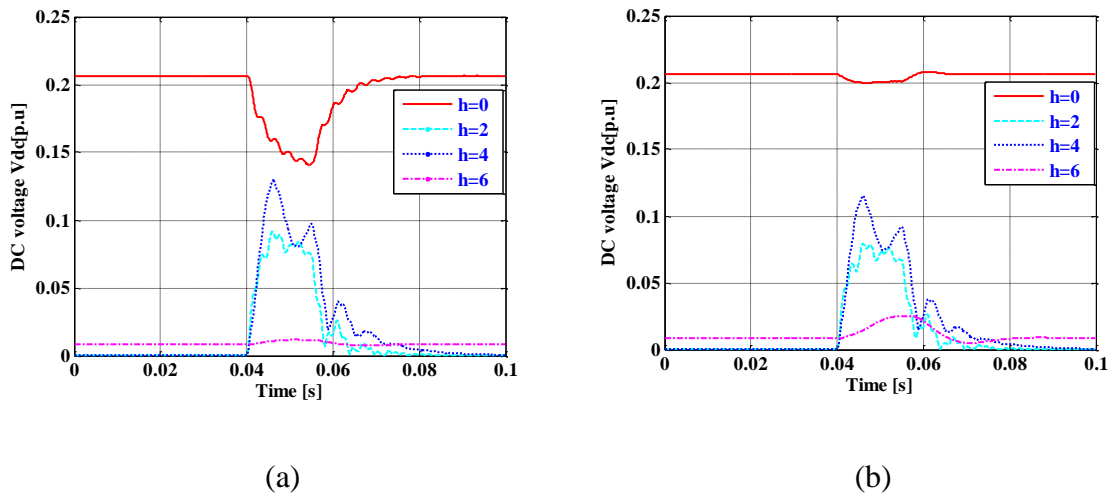
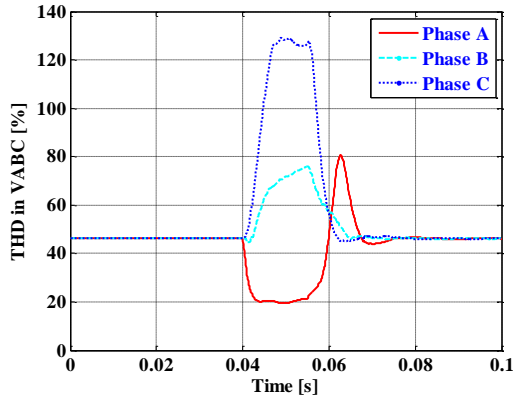


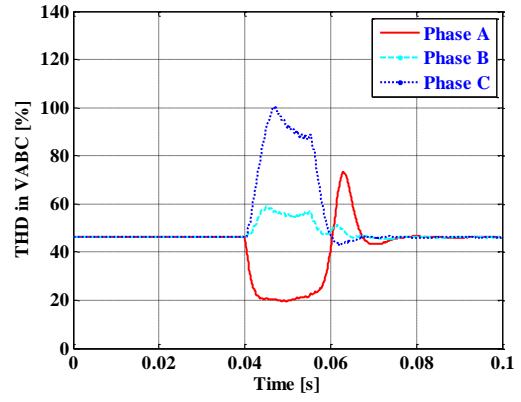
Figure 25: DC side voltage in UPFC (a) Without control system (b) With control system

Keeping the DC voltage constant during the disturbance interval further helped to minimize some of the PQ indices at the terminals of the UPFC during a disturbance such as THD in per-phase output voltages and currents of VSC 2 and THD in per-phase output

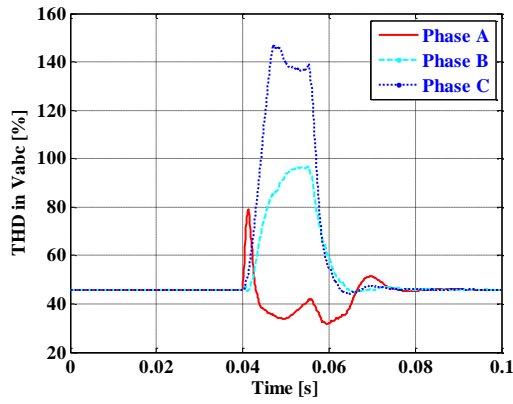
voltage of VSC 1, presented in Figure 26.1 and Figure 26.2. The decrease in the THD in per-phase output currents of VSC 2, and per-phase output voltages of VSC 1 and VSC 2, are due to the fact that keeping the DC side voltage close to its steady state value during the disturbance interval causes an increase in the fundamental component of the per-phase output currents of VSC 1, and per-phase output voltages of VSC 1 and VSC 2. This further leads to the reduction in the THD of those currents and voltages. These results demonstrate that the control system reduces the above mentioned PQ indices.



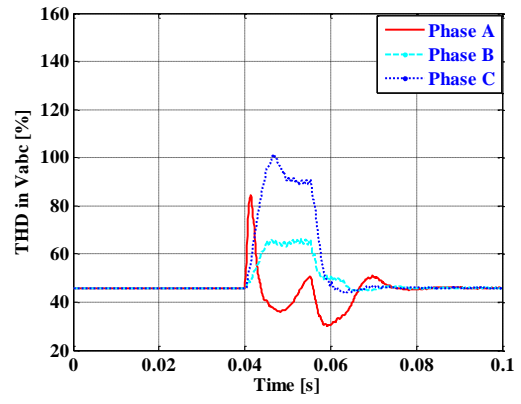
(a)



(b)



(c)



(d)

Figure 26.1: The THD in (a) The per-phase output voltages of VSC 2 (without control) (b) The per-phase output voltages of VSC 2 (with control) (c) The per-phase output voltages of VSC 1 (without control) (d) The per-phase output voltages of VSC 1 (with control)

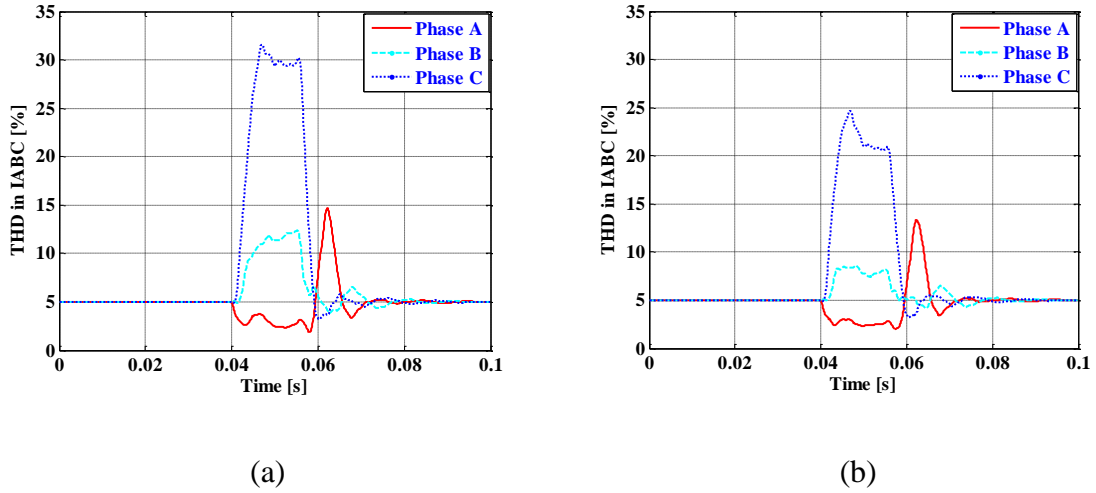
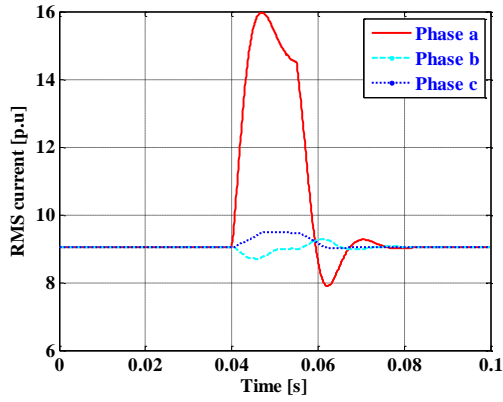
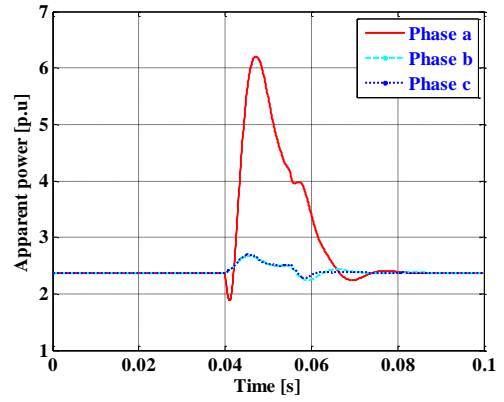


Figure 26.2: The THD in (a) The per-phase output currents of VSC 2 (without control)
 (b) The per-phase output currents of VSC 2 (with control)

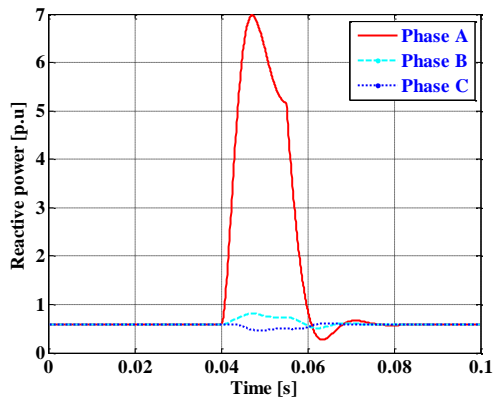
IEEE and CIGRE standards, specifically IEEE Standard 519 [60], limit the harmonics that are allowed in power systems. To facilitate an effective design of the control system, it is necessary to determine the power quality indices that show the performance of the device under most operating conditions. These indices include RMS voltages and currents, active, reactive, apparent and distortion powers, and THD in voltages and currents. Some of the power quality indices, such as RMS current and apparent power of VSC 1, as well as reactive, apparent, distortion powers and RMS voltages of VSC 2, are presented in Figure 27.1 and Figure 27.2. It is observed that at VSC 1 and VSC 2 outputs, the harmonic content during the disturbance of phase *a* is more significant than that at the other phases. This is because the voltage disturbance occurred at phase *a* of $v_s(t)$, during which this voltage increased by 50% of its original value.



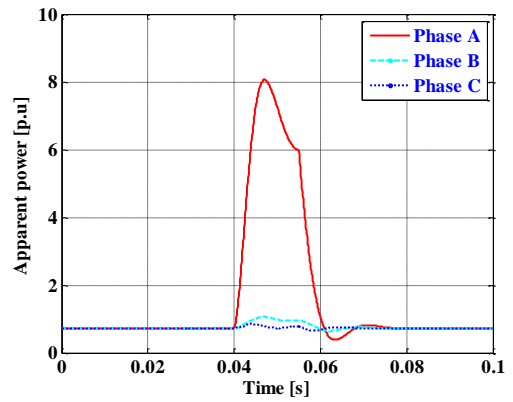
(a)



(b)



(c)



(d)

Figure 27.1: Power quality indices (a) RMS values of the output currents of VSC 1 (b) Per-phase output apparent powers of VSC 1 (c) Per-phase output reactive powers of VSC 2 (d) Per-phase output apparent powers of VSC 2

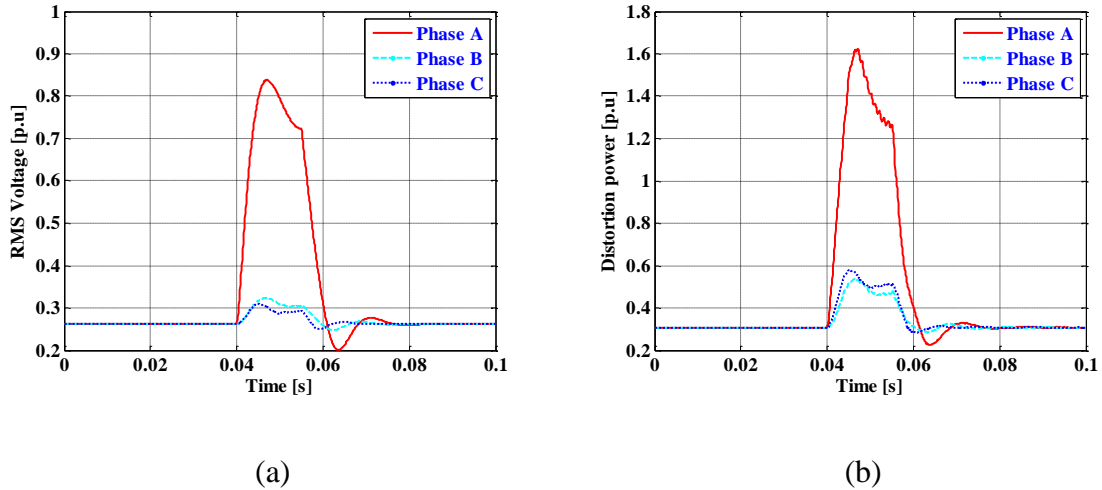
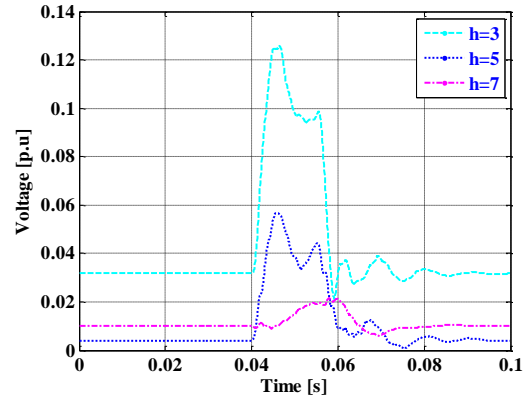
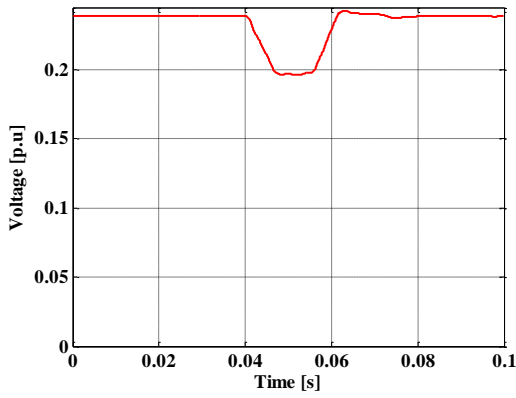


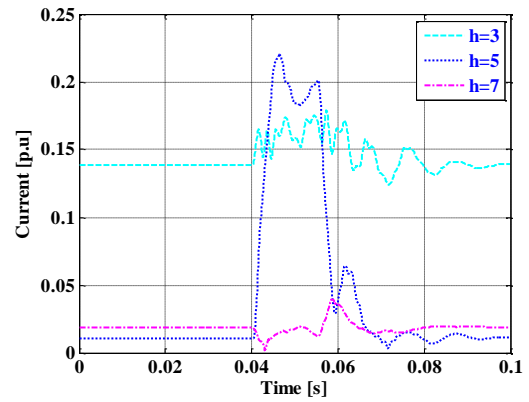
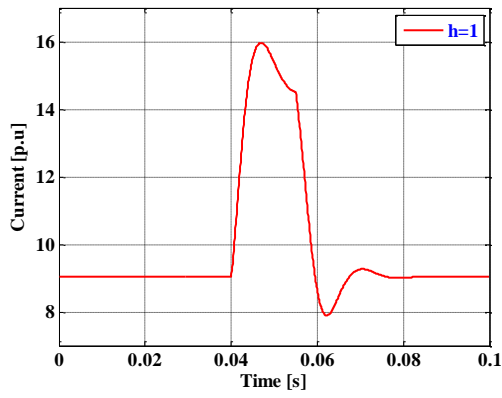
Figure 27.2: Power quality indices (a) RMS values of the output voltages of VSC 2 (b)

Per-phase output distortion powers of VSC 2

The effect of the disturbance on the harmonic content of voltage and current outputs of VSC 1 of phases *c* and *a* of the UPFC, respectively, are shown in Figure 28. Apart from the fundamental voltage and current, other harmonics such as the 3rd, 5th, and 7th are also shown. The time domain waveform of the same is shown in Figure 29. The drop in the fundamental component of the phase *c* of VSC 1 is due to the decrease in the DC side voltage during the disturbance interval. The VSC 1 is connected to the bus *S*. The voltage of the phase *a* at the bus *S* increased by 50% of its steady state value, causing more voltage to appear at the terminals of VSC 1 during that period. The time domain plots are derived from the corresponding harmonic contents of the output voltages and currents of VSC 1. They exhibit more distortions during the disturbance interval than when in steady period.

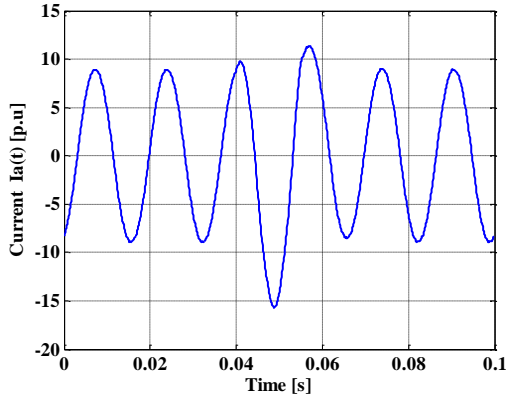


(a)

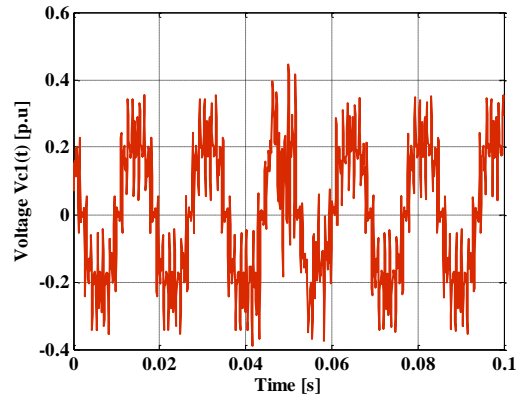


(b)

Figure 28: Harmonic content of VSC 1 of (a) The output voltage of phase c (b) The output current of phase a



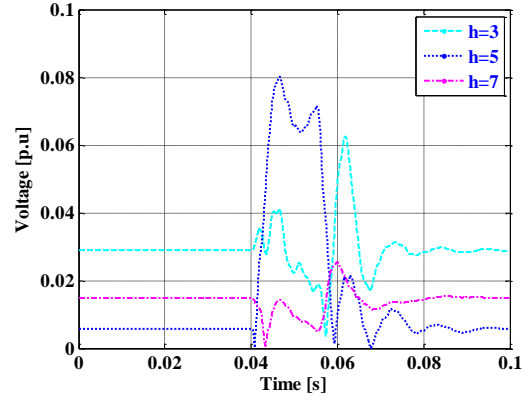
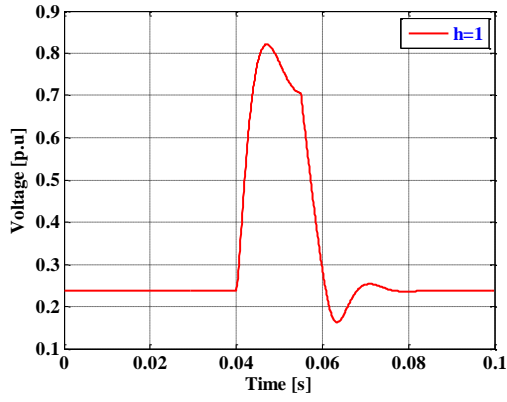
(a)



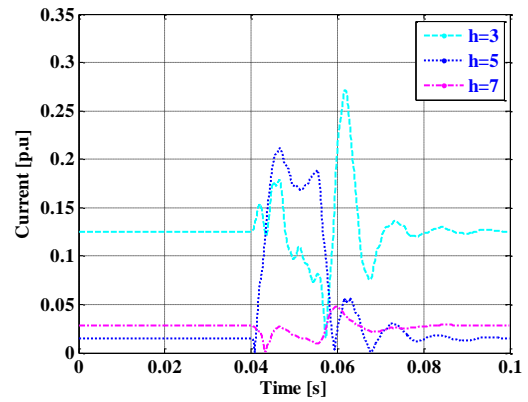
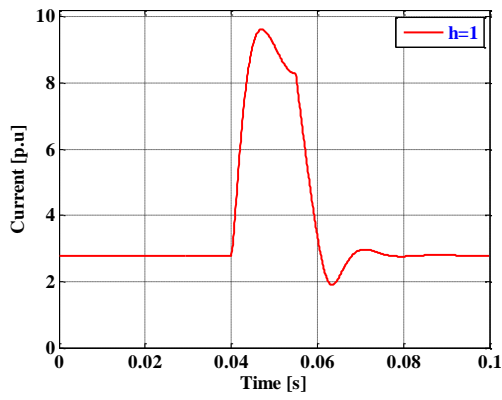
(b)

Figure 29: Time domain waveforms of VSC 1 of (a) The output current of phase a , (b) The output voltage of phase c

The harmonic content of the output voltage and current of VSC 2 of phase a in the UPFC are shown in Figure 30. The time domain waveforms of the same are shown in Figure 31. The VSC 2 is connected between the buses R and S , whose relationship is shown in (3.56). The voltage at the bus S increased by 50% of its steady state value, causing more voltage and currents to appear at the terminals of VSC 2 during that period.



(a)



(b)

Figure 30: Harmonic content of VSC 2 of phase *a* (a) Output voltage (b) Output current

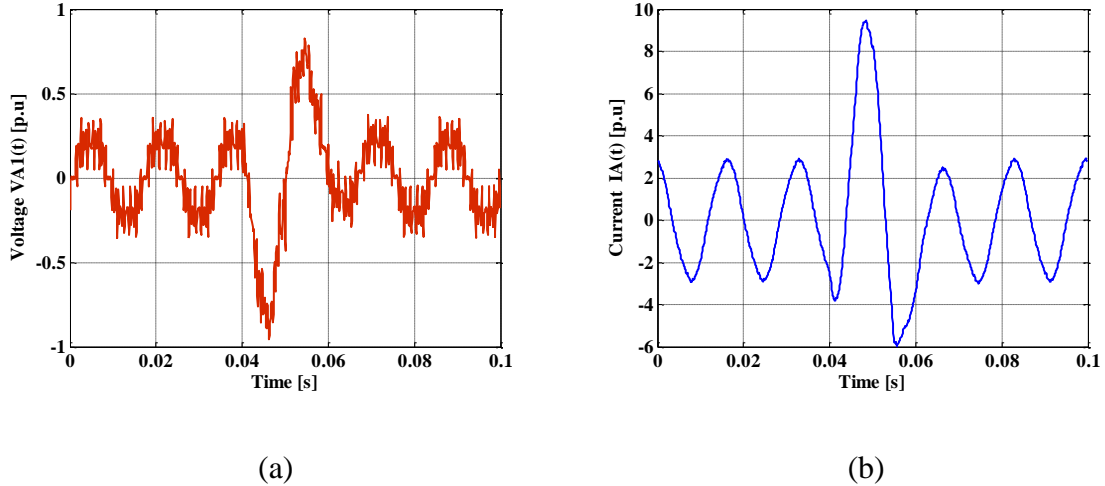
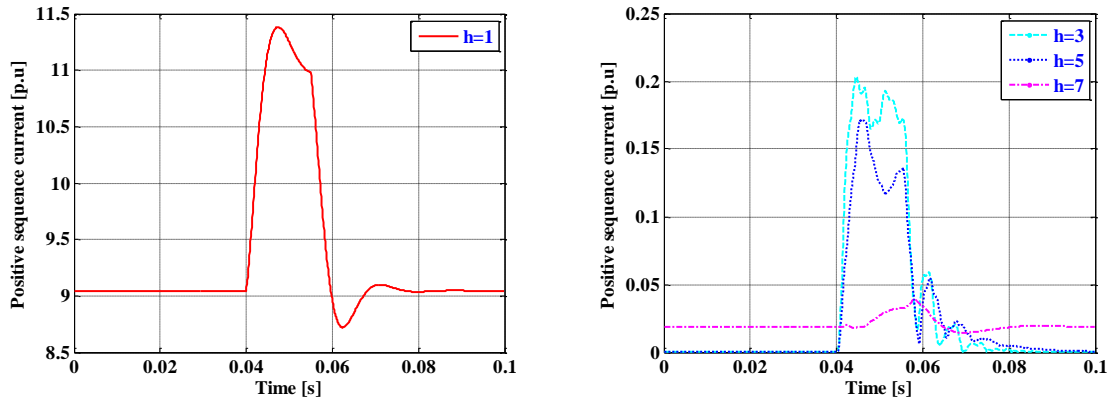


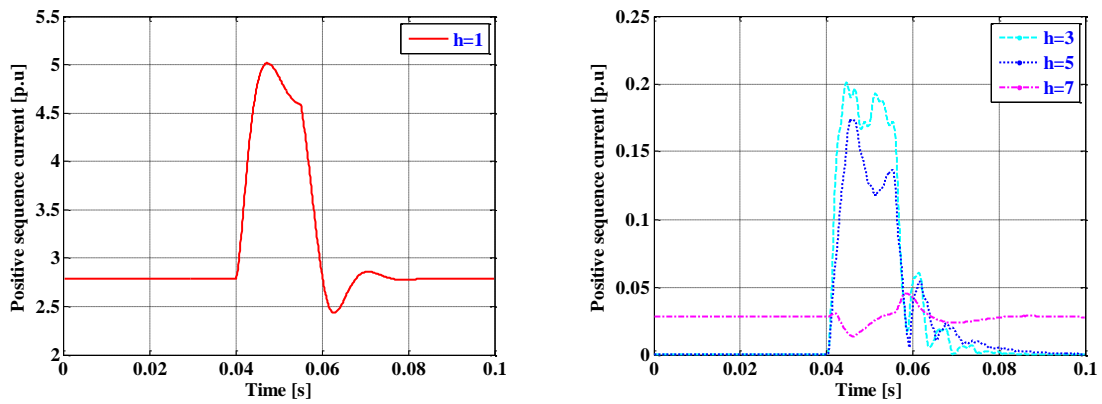
Figure 31: Time domain waveforms of VSC 2 of phase a (a) output voltage (b) output current

The results demonstrate no change in these quantities during steady state operation; that is, no changes occur before and after the disturbance, but significant changes are registered in the harmonic response during the disturbance period.

Dynamic sequence components are important for analyzing the balanced and unbalanced disturbances. This gives additional information that provides more insight in the behavior of the controller under different operating conditions. The harmonic content of the positive sequence currents of VSC 1 and VSC 2 are shown in Figure 32 (for visual clarity the fundamental plot is shown separately from the others in (a) and (b)). According to the mathematical discussion in Section 3.5, only the fundamental and the 7th harmonic currents are present in the steady state as predicted, while all odd harmonic currents are present during the disturbance interval.



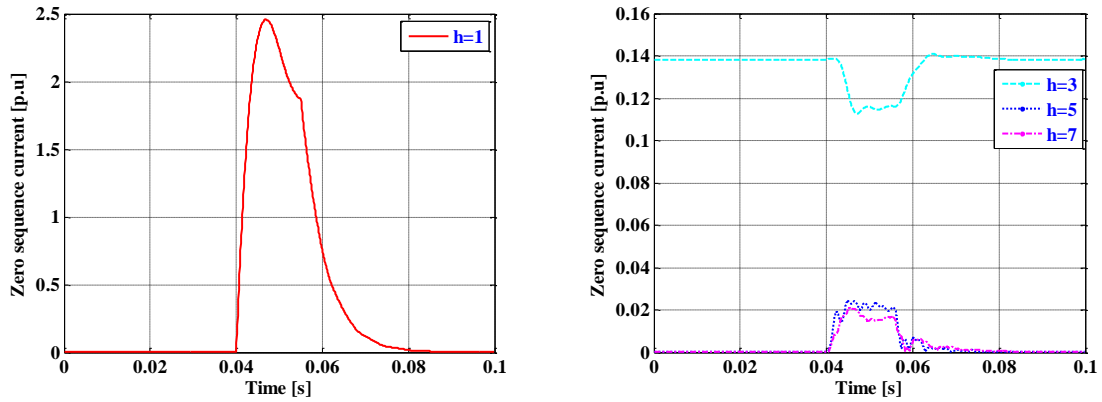
(a)



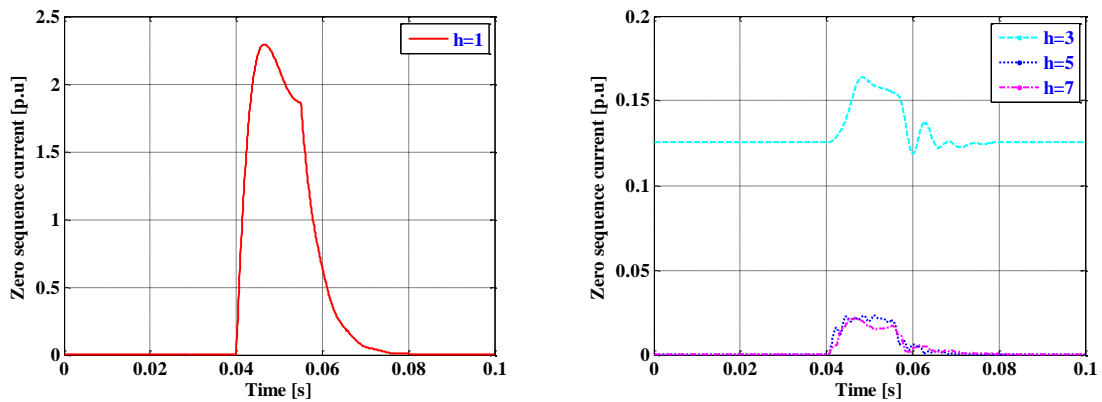
(b)

Figure 32: Positive sequence currents of (a) VSC 1 (b) VSC 2

The harmonic content of zero sequence currents of VSC 1 and VSC 2 are shown in Figure 33 (a) and (b), respectively. Again, according to the mathematical discussion in Section 3.5, the 3rd harmonic current alone is present in the steady state while all the odd harmonic currents are present during the disturbance interval.



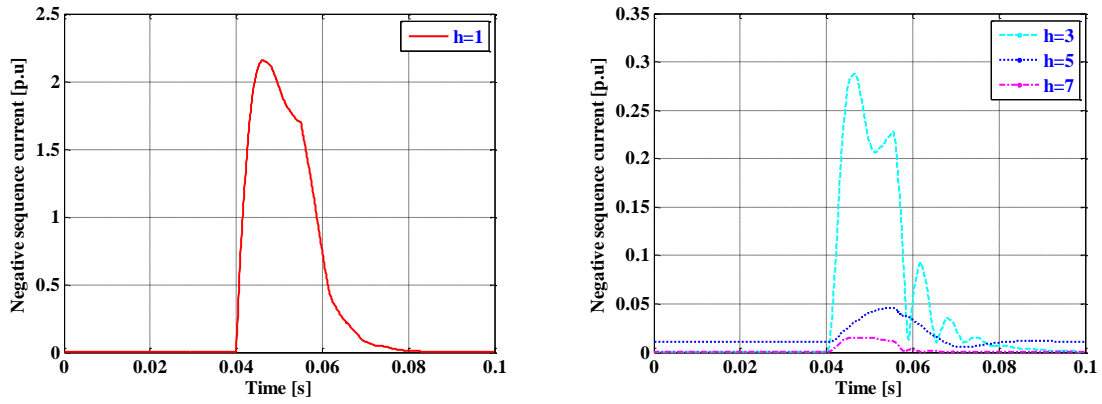
(a)



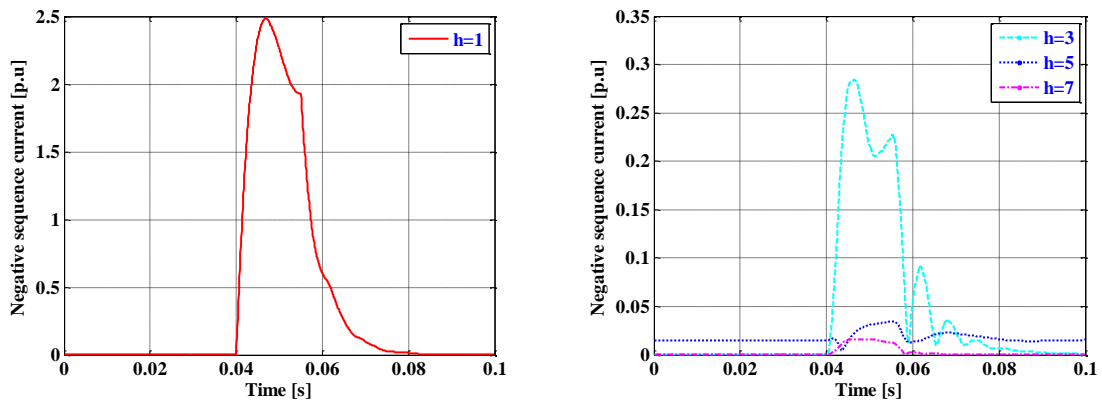
(b)

Figure 33: Zero sequence currents of (a) VSC 1 (b) VSC 2

The harmonic content of negative sequence currents for VSC 1 and VSC 2 are shown in Figure 34. The 5th harmonic component of the negative sequence current appears during the steady state and all the other odd harmonics are present through the disturbance interval. The sequence component plots justify the mathematical explanation discussed in the Section 3.5.



(a)



(b)

Figure 34: Negative sequence currents of (a) VSC 1 (b) VSC 2

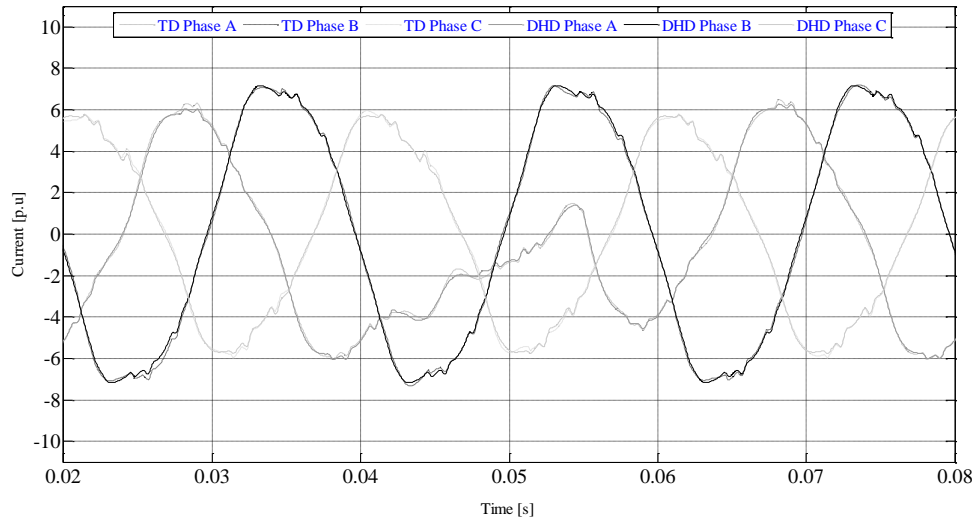
3.6.3 Validation of the proposed DHD model of the UPFC

The time domain solution of the UPFC can be obtained by the following two methods:

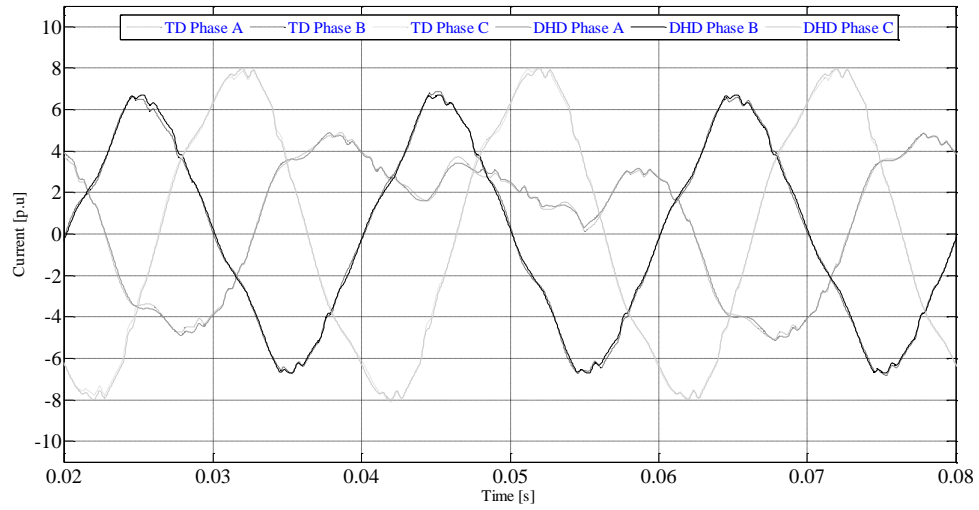
Method 1: solving state space equations that describe the dynamics of the UPFC, by a standard numeric integration method.

Method 2: converting the harmonic information obtained from the DHD model into time domain.

The time domain solutions obtained from Methods 1 and 2 are compared. If the results from Method 2 match with that of Method 1, it implies that the DHD model is correct. This is because the harmonic information obtained from the DHD model is used to obtain the time domain solution in Method 2. If the harmonic information is incorrect, the TD solution obtained from Method 2 does not match with that of Method 1. The VSC 1 and VSC 2 output currents obtained from the above two methods were compared and Figure 35 shows that all three phase currents obtained from Method 1 with that of Method 2.



(a)



(b)

Figure 35: DHD and time domain results comparison of (a) VSC 1 (b) VSC 2

3.7 Fixed capacitor-thyristor controlled reactor

The fixed capacitor-thyristor controlled reactor (FC-TCR) is a shunt controller. The function of this controller is based on the principle of injecting current into the system at the point of common coupling [3]. The Figure 36 shows one phase of the FC-TCR composed of a fixed capacitor and a thyristor-controlled reactor (TCR) in a parallel combination. This TCR consists of a fixed (usually air-core) reactor of inductance L_{re} in series with thyristors in antiparallel connection. L_e and R_e are the equivalent inductance and resistance of the transformer, respectively. The FC-TCR supplies or consumes variable reactive power if the injecting current is in phase quadrature with the line voltage. When it is not in quadrature the real power is exchanged as well.

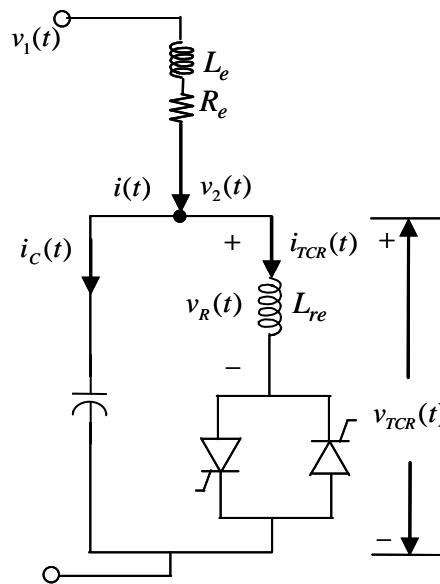


Figure 36: Static VAR compensator

By controlling the firing or delay angle, the current in the reactor can be controlled. Along with the desired fundamental current, the TCR also generates

harmonics in the system. The firing angle is a key factor in determining the amplitude of the harmonics where they are a function of these angles. Three single phase TCRs, which are usually in a delta connection, are used in a three-phase system. With this configuration, the triplen harmonic currents circulate in the TCRs, but do not enter the power system. By varying the firing angle, the inherent reactive control power capability of the TCR makes FC-TCR supply or absorb reactive power. The most important and fundamental objective behind applying a static compensator in a power transmission network is to enhance the power transfer capability from generators to the load. The following Section is a contribution to the state of power systems analysis by extending the application of DHD modeling to the FC-TCR.

3.7.1 Development of the DHD model of the FC-TCR

The following state-space equations can be written to describe the dynamics of an FC-TCR shown in Figure 36.

By Ohm's Law for capacitors,

$$\frac{d \mathbf{v}_{TCR}(t)}{dt} = \frac{1}{C} (\mathbf{i}(t) - \mathbf{i}_{TCR}(t)) \quad (3.60)$$

Here, $\mathbf{v}_{TCR}(t)$ is the voltage across the TCR, $\mathbf{i}_{TCR}(t)$ is the current through the TCR, $\mathbf{i}(t)$ is the current entering into the FC-TCR, and C is the capacitance of the capacitor.

By Ohm's law for inductors,

$$\frac{d\mathbf{i}_{TCR}(t)}{dt} = \frac{s(t)\mathbf{v}_{TCR}(t)}{L_{re}} \quad (3.61)$$

where $s(t)$ is the switching function that represents the conduction intervals of the thyristors [10], [26]. The switching function depends on the TCR voltage $\mathbf{v}_{TCR}(t)$, and the firing angle.

$$\frac{d\mathbf{i}(t)}{dt} = \frac{1}{L_e}(\mathbf{v}_1(t) - \mathbf{v}_{TCR}(t)) - \frac{R_e}{L_e}\mathbf{i}(t) \quad (3.62)$$

where $\mathbf{v}_1(t)$ is the supply voltage to the FC-TCR. The above state-space equations (3.60)

- (3.62) that describe the dynamics of FC-TCR in matrix form is

$$\begin{bmatrix} \frac{d\mathbf{i}(t)}{dt} \\ \frac{d\mathbf{v}_{TCR}(t)}{dt} \\ \frac{d\mathbf{i}_{TCR}(t)}{dt} \end{bmatrix} = \begin{bmatrix} -\frac{R_e}{L_e} & -\frac{1}{L_e} & 0 \\ \frac{1}{C} & 0 & -\frac{1}{C} \\ 0 & \frac{s(t)}{L_{re}} & 0 \end{bmatrix} \begin{bmatrix} \mathbf{i}(t) \\ \mathbf{v}_{TCR}(t) \\ \mathbf{i}_{TCR}(t) \end{bmatrix} + \frac{1}{L_e} \begin{bmatrix} \mathbf{v}_1(t) \\ 0 \\ 0 \end{bmatrix} \quad (3.63)$$

Equation (3.63) can be expressed as LTI system using the DHD that is,

$$\begin{bmatrix} \dot{\mathbf{I}}(t) \\ \dot{\mathbf{V}}_{TCR}(t) \\ \dot{\mathbf{I}}_{TCR}(t) \end{bmatrix} = \begin{bmatrix} -\frac{R_e}{L_e}\mathbf{U}_1 - \mathbf{D}(j\hbar\omega_0) & -\frac{\mathbf{U}_1}{L_e} & \mathbf{O}_4 \\ \frac{\mathbf{U}_1}{C} & -\mathbf{D}(j\hbar\omega_0) & -\frac{\mathbf{U}_1}{C} \\ \mathbf{O}_4 & \frac{\mathbf{S}(t)}{L_{re}} & -\mathbf{D}(j\hbar\omega_0) \end{bmatrix} \begin{bmatrix} \mathbf{I}(t) \\ \mathbf{V}_{TCR}(t) \\ \mathbf{I}_{TCR}(t) \end{bmatrix} + \frac{1}{L_e} \begin{bmatrix} \mathbf{V}_1(t) \\ \mathbf{O}_2 \\ \mathbf{O}_2 \end{bmatrix} \quad (3.64)$$

where \mathbf{U}_1 is the unit matrix (303×303). \mathbf{O}_2 and \mathbf{O}_4 are the zero matrices with dimensions (303×101) and (303×303) respectively.

The solution of the DHD equation (3.64) details harmonics in the FC-TCR under steady and dynamic state conditions. As already stated, the steady state solution of (3.64) can be obtained by setting the derivatives $\dot{\mathbf{I}}(t)$, $\dot{\mathbf{V}}_{TCR}(t)$, and $\dot{\mathbf{I}}_{TCR}(t)$ to zero. The following equation represents the steady state of the FC-TCR.

$$\begin{bmatrix} \mathbf{I}(t) \\ \mathbf{V}_{TCR}(t) \\ \mathbf{I}_{TCR}(t) \end{bmatrix} = -\mathbf{G}_{SVC}(t)^{-1} \frac{1}{L_e} \begin{bmatrix} \mathbf{V}_1(t) \\ \mathbf{O}_2 \\ \mathbf{O}_2 \end{bmatrix} \quad (3.65)$$

where

$$\mathbf{G}_{SVC}(t) = \begin{bmatrix} -\frac{\mathbf{R}_e}{L_e} \mathbf{U}_1 - \mathbf{D}(jh\omega_0) & -\frac{\mathbf{U}_1}{L_e} & \mathbf{O}_4 \\ \frac{\mathbf{U}_1}{C} & -\mathbf{D}(jh\omega_0) & -\frac{\mathbf{U}_1}{C} \\ \mathbf{O}_4 & \frac{\mathbf{S}(t)}{L_{re}} & -\mathbf{D}(jh\omega_0) \end{bmatrix}$$

The solution of the steady-state equation (3.65) is used as the initial condition for solving (3.64) provided, inverse of $\mathbf{G}_{SVC}(t)$ exists.

3.7.2 Simulation of the proposed FC-TCR model

Consider a three-phase delta connected FC-TCR to a source, shown in only one phase in Figure 36, with system frequency of 60 Hz. The balanced three-phase source voltage $v_1(t)$ per unit are given by

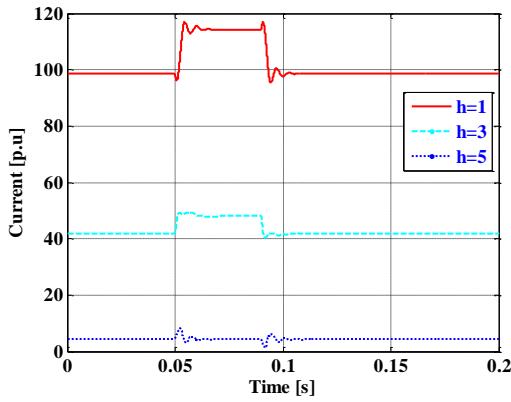
$$\begin{aligned}v_a(t) &= \sin \omega_0 t \\v_b(t) &= \sin (\omega_0 t - 120^\circ) \\v_c(t) &= \sin (\omega_0 t + 120^\circ)\end{aligned}$$

The per phase line resistance and inductive reactance are 0.01Ω and $1 \text{ m}\Omega$, respectively. The TCRs have firing angles $\alpha_a = \alpha_b = \alpha_c = 120^\circ$ which indicates how the FC-TCR absorbs reactive power from the system. The per phase inductive reactance of the reactor and capacitive reactance of the capacitor bank are $3 \text{ m}\Omega$ and $15 \text{ m}\Omega$, respectively, at a frequency of 60 Hz. Assuming a disturbance in voltage magnitudes and phase angles starting at 0.05 seconds, lasting for 0.5 seconds, as

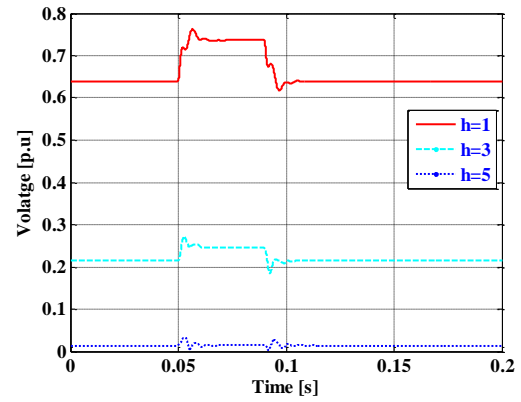
$$\begin{aligned}v_a(t) &= 1.2 \sin \omega_0 t \\v_b(t) &= 0.9 \sin (\omega_0 t - 122^\circ) \\v_c(t) &= 1.1 \sin (\omega_0 t + 118^\circ)\end{aligned}$$

As already discussed, the accuracy of the DHD method is directly proportional to the number of harmonic coefficients. Hence, for simplicity a total of 15 harmonics were considered for this study. The simulations were started at $t_0 = 0$ seconds with final time $t_f = 0.2$ seconds and used an integration time step of $\Delta t = 0.2$ ms.

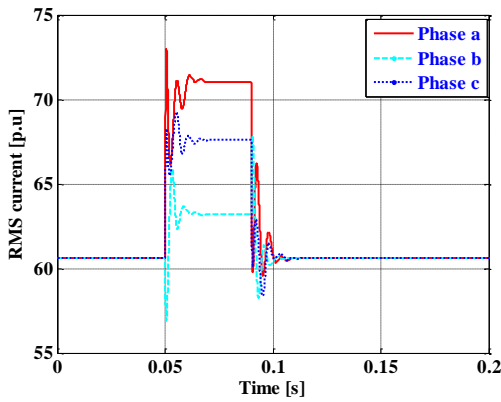
The dynamic harmonic response of FC-TCR voltages and currents for the disturbance are shown in Figure 37. The increase in the fundamental component of the output currents and voltages of the TCR of phase a is due to the fact that, during the disturbance interval, this phase voltage of v_1 is greater than before by 20% of its steady state value. Similarly, the RMS values of the output voltages of phases a and c (v_2) are larger due to a 20% and 10% increase, respectively, in the steady state values of their phase voltages of v_1 . The RMS values of the output voltage of phase b (v_2) is decreased due to a 10% drop in the steady state values of its phase voltage of v_1 during the disturbance interval.



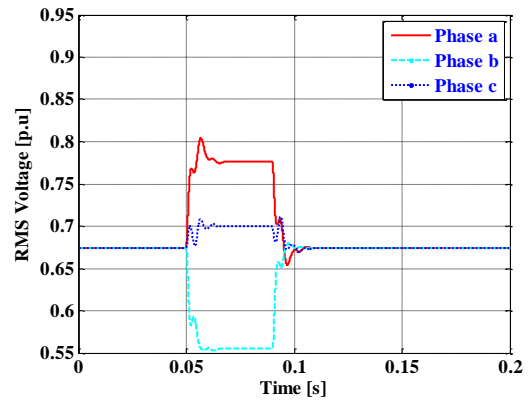
(a)



(b)



(c)



(d)

Figure 37: Voltages and currents (a) The TCR output currents of phase *a* (b) The TCR output voltages of phase *a* (c) The RMS values of the per-phase output currents of the FC-TCR (d) the RMS values of the per-phase output voltages of the FC-TCR

Figure 38 shows the per-phase output apparent and reactive powers at the terminals of FC-TCR. It is evident from the plots that active power exchange between FC-TCR and an AC system is almost negligible. This is because magnitude of per-phase output reactive power is very close to that of the apparent power. The mutual effects of

voltages at the terminals of the FC-TCR cause changes in the apparent and active power outputs.

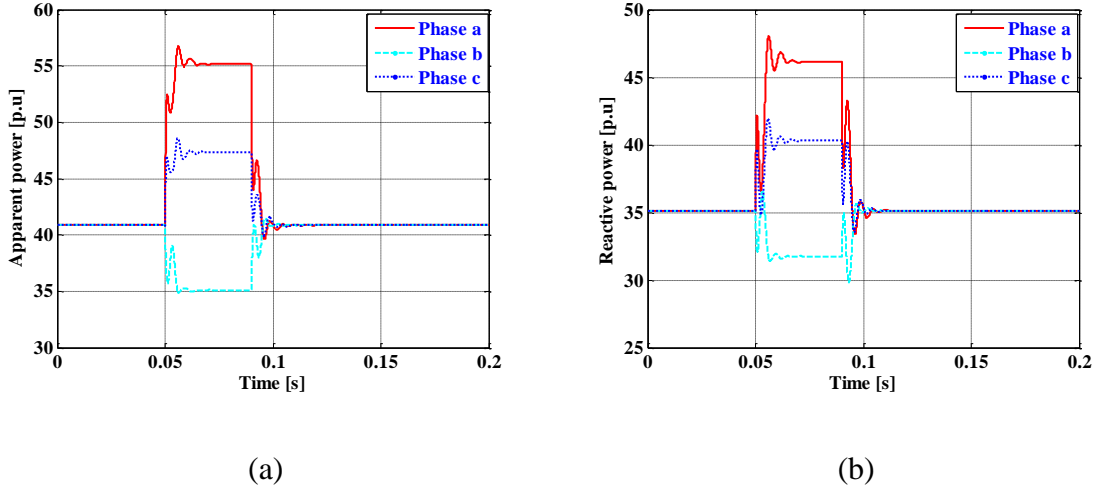


Figure 38: Electrical power quantities of FC-TCR: (a) Per-phase output apparent powers
(b) Per-phase output reactive powers

3.8 Thyristor-controlled series controller

The TCSC is a series compensator which injects voltage in series with the line according to the principle of operation. Basically, the structure of the TCSC is the same as that of FC-TCR as shown in Figure 39 but the difference lies in the manner that it is connected with the transmission line. The reactance (neglecting the resistance of the line) of the line can be varied by connecting it in series with the transmission line. The equivalent circuit of the TCSC is shown in Figure 40.

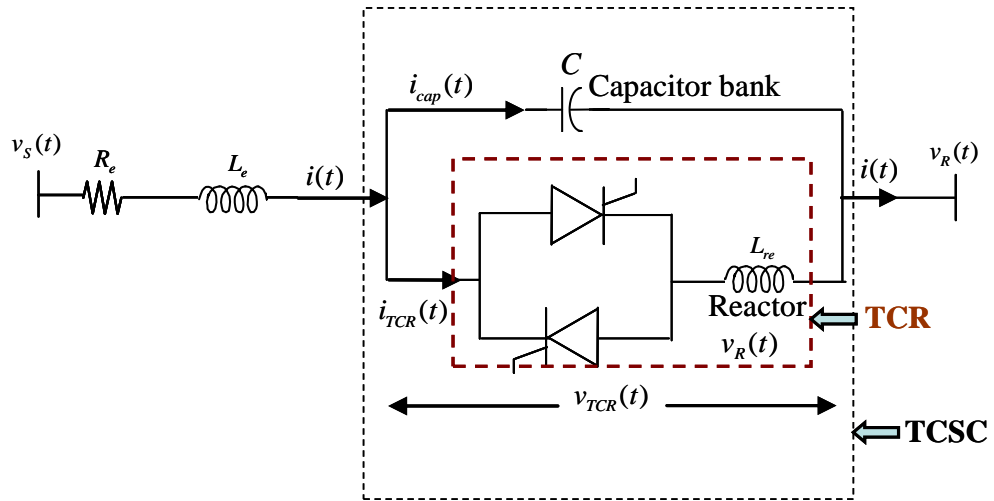


Figure 39: Thyristor-controlled series controller

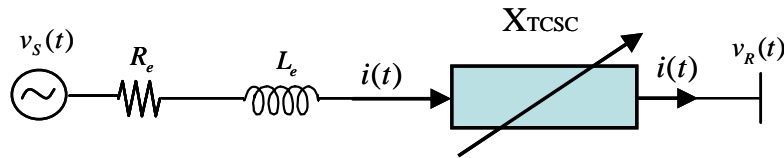


Figure 40: TCSC equivalent circuit

The equivalent reactance is given by

$$X_{TCSC} = \frac{(-jX_C)(jX_{TCR})}{j(X_{TCR} - X_C)} = \frac{(-jX_C)}{\left(1 - \frac{X_C}{X_{TCR}}\right)} \quad (3.66)$$

where

X_C = Capacitive reactance of the capacitor bank

X_{TCR} = Reactance of the TCR

The reactance of the TCSC is altered by varying the firing angles of the thyristors. Current can be controlled by controlling the reactance of the line. This variable reactance is multiplied by the current flowing through the line, resulting in an injected voltage in series with the line. If this injected voltage is in phase quadrature with the line current, the TCSC can supply variable reactive power. Any other phase relationships lead to real power exchange. Because of the thyristor switching, TCR injects harmonics into the system.

The behavior of TCSC depends on the magnitudes of the capacitive and inductive reactances of the circuit. For instance, if $X_C > X_{TCR}$, the TCSC behaves like a capacitor. If $X_C < X_{TCR}$, the TCSC behaves like an inductor. The dynamic TCSC model is identical to the dynamic model of the FC-TCR shown in (3.64).

3.8.1 Simulation of the proposed TCSC model

Consider a three-phase delta connected TCSC to a source with system frequency of 60 Hz, as shown in Figure 39. The balanced source voltages in p.u are given as follows:

$$\begin{aligned}v_a(t) &= \sin \omega_0 t \\v_b(t) &= \sin (\omega_0 t - 120^\circ) \\v_c(t) &= \sin (\omega_0 t + 120^\circ)\end{aligned}$$

The per phase line resistance and inductive reactance are 0.01Ω and $1 \text{ m}\Omega$, respectively. The TCRs have firing angles $\alpha_a = \alpha_b = \alpha_c = 95^\circ$ which indicates that the

TCSC is absorbing reactive power from the system. The per phase inductive reactance of the reactor and capacitive reactance of the capacitor bank are $3 \text{ m}\Omega$ and $15 \text{ m}\Omega$, respectively at a frequency of 60 Hz . A disturbance was assumed in the voltage magnitudes and angles at 0.05 seconds, lasting for 1 ms . Then,

$$\begin{aligned}v_a(t) &= 1.2 \sin \omega_0 t \\v_b(t) &= 0.9 \sin (\omega_0 t - 122^\circ) \\v_c(t) &= 1.1 \sin (\omega_0 t + 118^\circ)\end{aligned}$$

The accuracy of the DHD method is directly proportional to the number of harmonic coefficients. Therefore, a total of 15 harmonics are considered for this study. The simulation starts at $t_0 = 0$ seconds with final time of $t_f = 0.1$ seconds and uses an integration time step of $\Delta t = 0.1 \text{ ms}$.

Figure 41.1(a) - (d) show the harmonic content of the voltages and currents of the TCSC at its terminals. The dynamic response of the TCSC is more evident soon after the disturbance occurs while these voltages and currents remain constant after it attains the steady value. The increase in the phase a and phase c voltages at the terminals of TCSC during the disturbance interval causes, a rise in fundamental component of their phase a output current and voltage. This leads to increase in output RMS voltages and currents of TCSC. The drop in phase b voltage at the terminals of TCSC during the disturbance causes, a drop in phase b output RMS voltage and currents. The current and voltage waveforms of phase a are shown in Figure 41.2(a) and (b), respectively. These plots, as expected, show sinusoidal behavior during steady state and slightly (almost invisible) non-sinusoidal behavior through the disturbance interval. Please note that it is nearly impossible to determine from these plots when and where the disturbance in the system

occurs, especially if it is very small and/or it is present for a short duration, such as the one under study. This detection of small disturbances is another advantage that is highlighted by the availability and utilization of the proposed model.

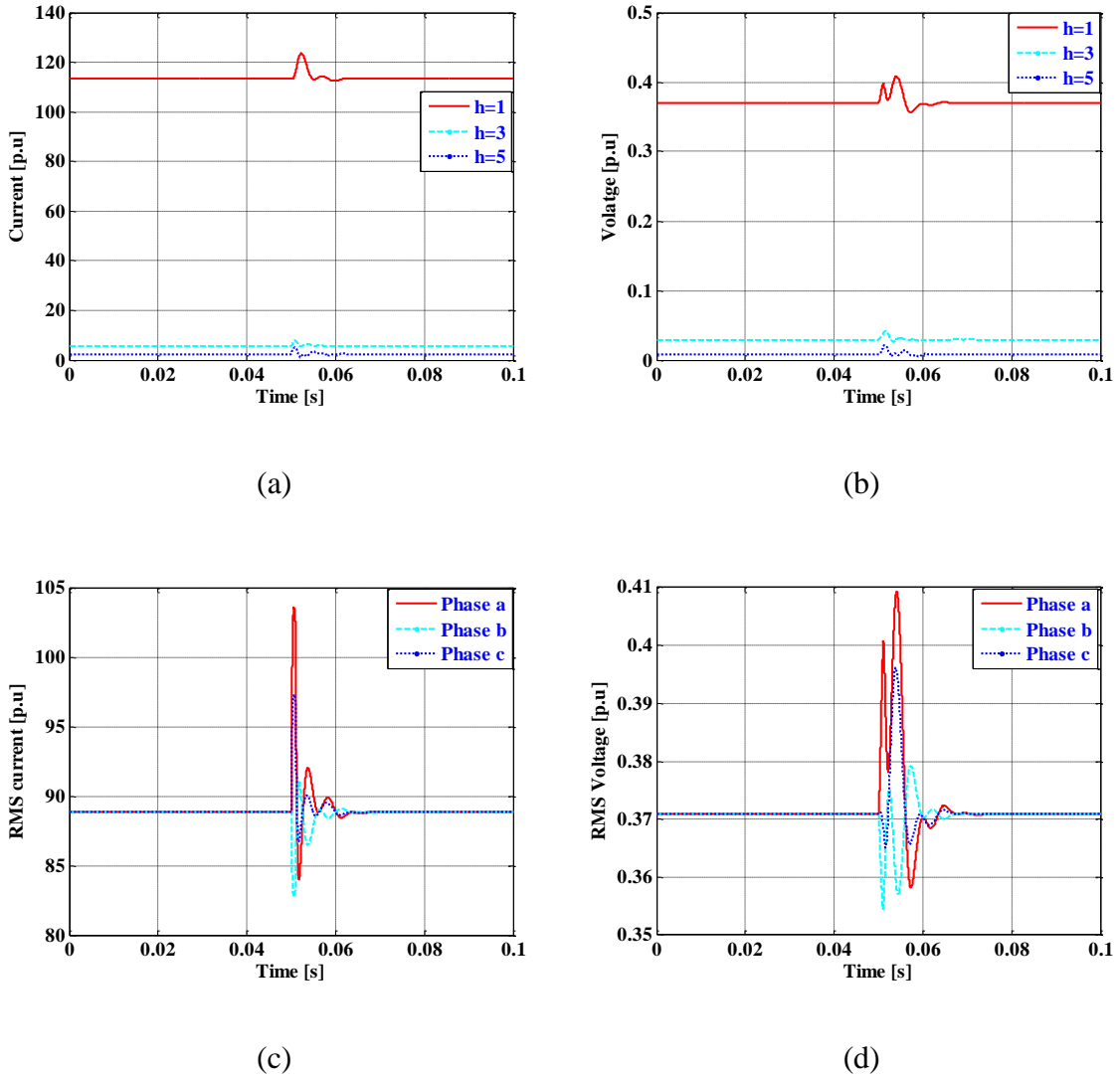
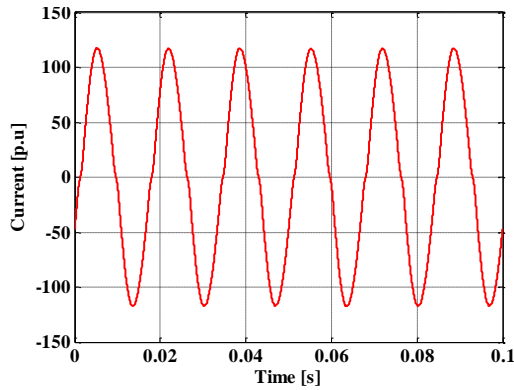
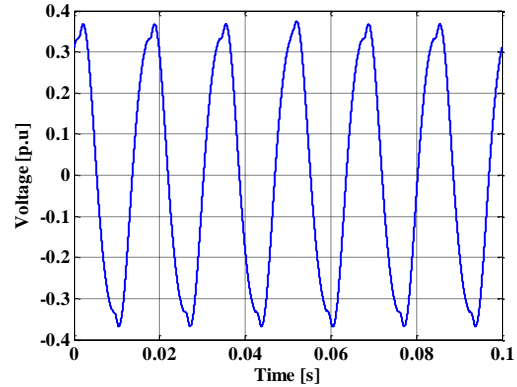


Figure 41.1: Voltages and currents of the TCSC (a) The harmonic content of the output currents of phase *a* (b)) The harmonic content of the output voltage of phase *a* (c) The harmonic content of the RMS value of the output currents (d) The harmonic content of the RMS value of the output voltages



(a)



(b)

Figure 41.2: Voltages and currents of the TCSC (a) The output current waveform of phase *a* (b) The output voltage waveform of phase *a*

Figure 42 shows some electrical power quality indices at the terminals of TCSC such as the per-phase output of apparent powers and reactive powers. The increase in the phase *a* and phase *c* at the terminals of TCSC during the disturbance interval causes, a rise in apparent and reactive power outputs. The drop in phase *b* voltage at the terminals of TCSC during the disturbance causes, a drop in the apparent and reactive power outputs.

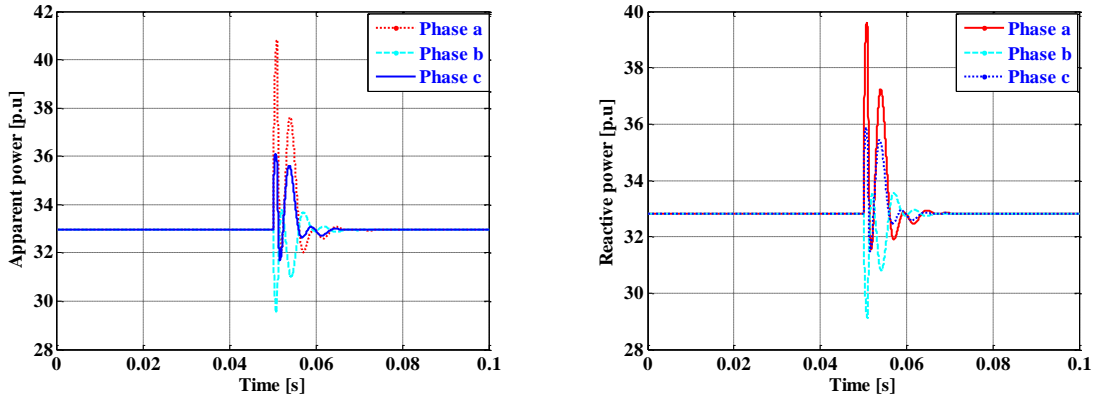
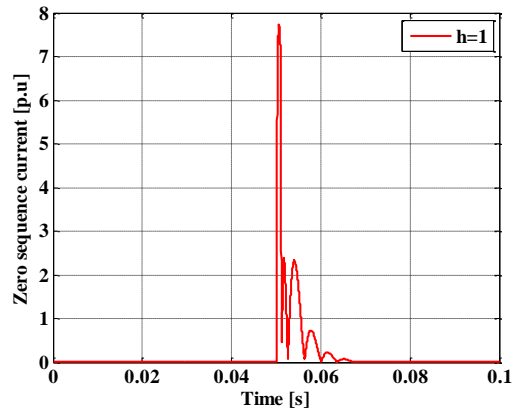
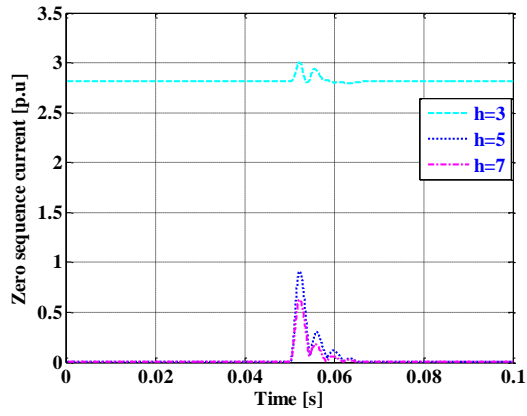
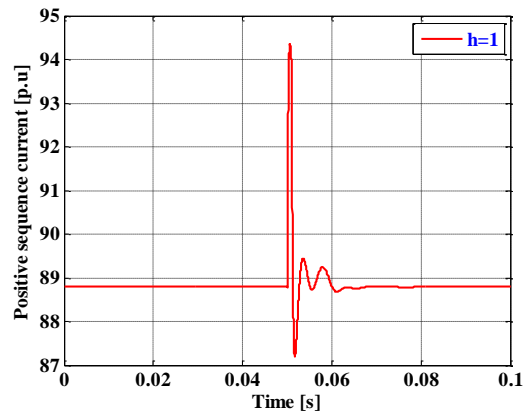
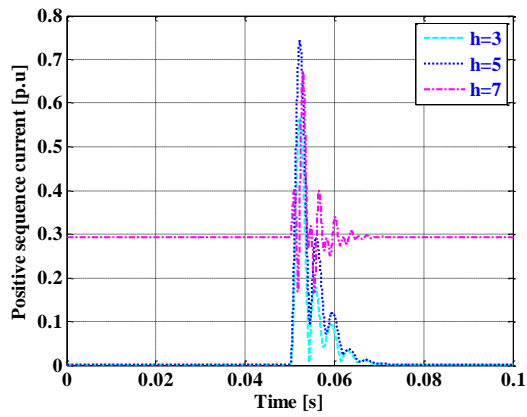


Figure 42: Power quality indices at the terminals of TCSC (a) Per-phase output apparent powers (b) Per-phase output reactive powers

The harmonic content of the zero, positive and negative sequence currents for the TCSC are shown in Figure 43.1 and Figure 43.2. Out of all four harmonics that were considered, only the 3rd component of the zero sequence current, 7th component of positive sequence current, and 5th component of negative sequence current appear during the steady state (for visual clarity the fundamental plot is shown separately from others in (a), (b), and (c)). All the odd harmonic components are present during the disturbance interval. The sequence component plots justify the mathematical explanation discussed in Section 3.5.

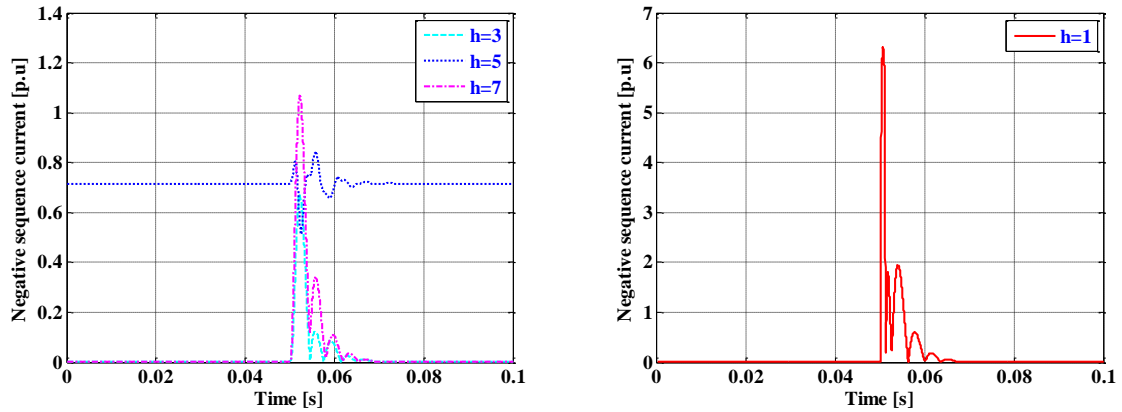


(a)



(b)

Figure 43.1: Dynamic sequence currents of the TCSC (a) Zero sequence (b) Positive sequence



(a)

Figure 43.2: Dynamic sequence currents of the TCSC (a) Negative sequence

3.9 Conclusion

This chapter has presented the dynamic harmonic domain models of SSSC, UPFC, SVC, and TCSC and the efficacy of these models in highlighting the sensitivity of these controllers' harmonic response to disturbances. The harmonic content of the sequence currents of these controllers was also presented. The harmonic information obtained from these DHD models is very beneficial for obtaining accurate power quality indices that will be useful in the study and analysis of the performance of these controllers under various operating conditions.

CHAPTER IV

**DYNAMIC HARMONIC DOMAIN MODELING OF MULTI-LINE POWER
FLOW CONTROLLERS**

4.1 Introduction

The most common FACTS controllers, such as the UPFC, SSSC, STATCOM controllers, are used to control a single three phase transmission line. Several innovative concepts have been introduced that combine two or more converter blocks to control the bus voltages and power flow of more than one line. These controllers are called multi-line FACTS controllers of which three are important and the subject of the work presented in this chapter: the Interline Power Flow Controller (IPFC), the Generalized Unified Power Flow Controller (GUPFC) or multi-line UPFC, and the Generalized Interline Power Flow Controller (GIPFC) or the multi-line IPFC. These three controllers have stronger control capabilities than the UPFC and SSSC, since they provide bus voltage control as well as power flow control in more than one line, or even a sub-network.

The conventional models of these controllers are not accurate enough to capture the harmonic interaction between them and the transmission lines. This interaction occurs because these controllers generate harmonics that cause voltage distortions on the system. In order to simulate and analyze the performance of a power system when these controllers are used, it is necessary to obtain precise information about the harmonics of the system.

In this chapter, the proposed HD models for two multi-line controllers, namely, the GUPFC and the GIPFC are developed. It is not only important to develop these models because they are useful in obtaining a harmonic propagation analysis and performing resonance prediction analyses in the steady-state.

Furthermore this chapter also includes DHD models proposed for the most sophisticated FACTS controllers, the GUPFC, IPFC, and GIPFC, and their corresponding developments. The validation of the proper functionality of these DHD models is presented and demonstrated.

All of the above mentioned FACTS controllers utilize several voltage source controllers (VSC) as shown in Figure A-1, Appendix A. Since the model for the VSC has been presented in the literature [15] and will be utilized throughout this work, it is briefly discussed in Section A.2, Appendix A.

4.2 Generalized Unified Power Flow Controller

The development of the Generalized Unified Power Flow Controller model will now be presented. The GUPFC consists of three voltage source converters, VSC 1, VSC 2, and VSC 3 [44] as shown in Figure 44.

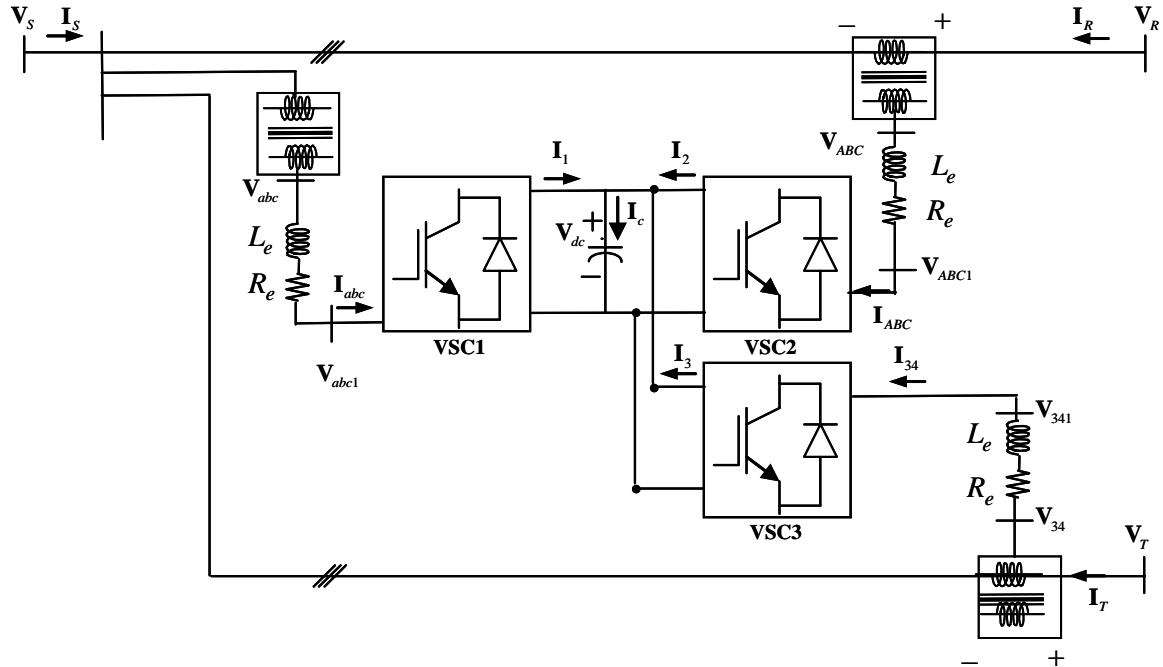


Figure 44: Generalized unified power controller

Here, one converter is connected in shunt and the other two in series with two transmission lines. The shunt controller injects three-phase current and the series controllers inject three-phase voltages into the AC system. These converters are connected back-to-back across a common DC link, a storage capacitor, thus facilitating real power transfer. The benefit of this design is that these three converters can independently generate or absorb reactive power.

4.2.1 Harmonic domain model of the GUPFC

The voltage equations of the three converters from Equation (4.1) and Figure 44 are as follows:

For VSC 1

$$\mathbf{V}_{abc} = (\mathbf{Z}_e + \mathbf{P}_{s1} \mathbf{Z}_{\text{cap}} \mathbf{Q}_{s1}) \mathbf{I}_{abc} + \mathbf{P}_{s1} \mathbf{Z}_{\text{cap}} \mathbf{I}_{dc} + \mathbf{P}_{s1} \mathbf{V}_0 \quad (4.1)$$

$$\mathbf{V}_{dc1} = \mathbf{Z}_{\text{cap}} \mathbf{Q}_{s1} \mathbf{I}_{abc} + \mathbf{Z}_{\text{cap}} \mathbf{I}_{dc} + \mathbf{V}_0 \quad (4.2)$$

For VSC 2

$$\mathbf{V}_{ABC} = (\mathbf{Z}_e + \mathbf{P}_{s2} \mathbf{Z}_{\text{cap}} \mathbf{Q}_{s2}) \mathbf{I}_{ABC} - \mathbf{P}_{s2} \mathbf{Z}_{\text{cap}} \mathbf{I}_{dc} + \mathbf{P}_{s2} \mathbf{V}_0 \quad (4.3)$$

$$\mathbf{V}_{dc2} = \mathbf{Z}_{\text{cap}} \mathbf{Q}_{s2} \mathbf{I}_{ABC} - \mathbf{Z}_{\text{cap}} \mathbf{I}_{dc} + \mathbf{V}_0 \quad (4.4)$$

For VSC 3

$$\mathbf{V}_{34} = (\mathbf{Z}_e + \mathbf{P}_{s3} \mathbf{Z}_{\text{cap}} \mathbf{Q}_{s3}) \mathbf{I}_{34} - \mathbf{P}_{s3} \mathbf{Z}_{\text{cap}} \mathbf{I}_{dc} + \mathbf{P}_{s3} \mathbf{V}_0 \quad (4.5)$$

$$\mathbf{V}_{dc3} = \mathbf{Z}_{\text{cap}} \mathbf{Q}_{s3} \mathbf{I}_{34} - \mathbf{Z}_{\text{cap}} \mathbf{I}_{dc} + \mathbf{V}_0 \quad (4.6)$$

Since all three converters in the GUPFC are connected across a common DC storage capacitor, then

$$\mathbf{V}_{dc1} = \mathbf{V}_{dc2} = \mathbf{V}_{dc3} = \mathbf{V}_{dc} \quad (4.7)$$

Solving equations (4.2) and (4.4) yields

$$\mathbf{I}_{dc} = \frac{\mathbf{Q}_{s2} \mathbf{I}_{ABC} - \mathbf{Q}_{s1} \mathbf{I}_{abc}}{2} \quad (4.8)$$

Solving equations (4.2) and (4.6) gives

$$\mathbf{I}_{dc} = \frac{\mathbf{Q}_{s3} \mathbf{I}_{34} - \mathbf{Q}_{s1} \mathbf{I}_{abc}}{2} \quad (4.9)$$

Substituting equations (4.8) into (4.1), (4.3) and (4.9) into (4.6) give

$$\mathbf{V}_{abc} = \left(\mathbf{Z}_e + \frac{\mathbf{P}_{s1} \mathbf{Z}_{cap} \mathbf{Q}_{s1}}{2} \right) \mathbf{I}_{abc} + \frac{\mathbf{P}_{s1} \mathbf{Z}_{cap} \mathbf{Q}_{s2}}{2} \mathbf{I}_{ABC} + \mathbf{P}_{s1} \mathbf{V}_0 \quad (4.10)$$

$$\mathbf{V}_{ABC} = \left(\mathbf{Z}_e + \frac{\mathbf{P}_{s2} \mathbf{Z}_{cap} \mathbf{Q}_{s2}}{2} \right) \mathbf{I}_{ABC} + \frac{\mathbf{P}_{s2} \mathbf{Z}_{cap} \mathbf{Q}_{s1}}{2} \mathbf{I}_{abc} + \mathbf{P}_{s2} \mathbf{V}_0 \quad (4.11)$$

$$\mathbf{V}_{34} = \left(\mathbf{Z}_e + \frac{\mathbf{P}_{s3} \mathbf{Z}_{cap} \mathbf{Q}_{s3}}{2} \right) \mathbf{I}_{34} + \frac{\mathbf{P}_{s3} \mathbf{Z}_{cap} \mathbf{Q}_{s1}}{2} \mathbf{I}_{abc} + \mathbf{P}_{s3} \mathbf{V}_0 \quad (4.12)$$

The boundary conditions of the GUPFC are defined based on how the VSCs are connected to the transmission system. They are

$$\begin{aligned} \mathbf{I}_{ABC} &= \mathbf{I}_R & \mathbf{I}_{abc} &= \mathbf{I}_S + \mathbf{I}_R & \mathbf{I}_{34} &= \mathbf{I}_T \\ \mathbf{V}_{ABC} &= \mathbf{V}_R - \mathbf{V}_S & \mathbf{V}_{34} &= \mathbf{V}_T - \mathbf{V}_S & \mathbf{V}_{abc} &= \mathbf{V}_S \end{aligned} \quad (4.13)$$

where the values on the right hand sides are defined in Figure 44. Substitution of these conditions into equations, (4.10), (4.11), and (4.12) yields

$$\begin{bmatrix} \mathbf{V}_R \\ \mathbf{V}_S \\ \mathbf{V}_T \end{bmatrix} = \begin{bmatrix} \mathbf{A}_1 & \mathbf{A}_2 & \mathbf{A}_3 \\ \mathbf{B}_1 & \mathbf{B}_2 & \mathbf{B}_3 \\ \mathbf{C}_1 & \mathbf{C}_2 & \mathbf{C}_3 \end{bmatrix} \begin{bmatrix} \mathbf{I}_R \\ \mathbf{I}_S \\ \mathbf{I}_T \end{bmatrix} + \begin{bmatrix} \mathbf{P}_{S1} + \mathbf{P}_{S2} \\ \mathbf{P}_{S1} \\ \mathbf{P}_{S1} + \mathbf{P}_{S3} \end{bmatrix} \mathbf{V}_0 \quad (4.14)$$

The set of algebraic equations (4.14) constitutes the HD model of the GUPFC,

where

$$\begin{aligned}
 \mathbf{A}_1 &= 2\mathbf{Z}_e + \frac{(\mathbf{P}_{s1} + \mathbf{P}_{s2})\mathbf{Z}_{\text{cap}}(\mathbf{Q}_{s1} + \mathbf{Q}_{s2})}{2} \\
 \mathbf{A}_2 &= \mathbf{Z}_e + \mathbf{Z}_{\text{cap}}\mathbf{Q}_{s1} \frac{(\mathbf{P}_{s1} + \mathbf{P}_{s2})}{2}; \mathbf{A}_3 = \mathbf{B}_3 = 0 \\
 \mathbf{B}_1 &= \mathbf{Z}_e + \frac{\mathbf{P}_{s1}\mathbf{Z}_{\text{cap}}}{2}(\mathbf{Q}_{s1} + \mathbf{Q}_{s2}); \mathbf{B}_2 = \mathbf{Z}_e + \frac{\mathbf{P}_{s1}\mathbf{Z}_{\text{cap}}\mathbf{Q}_{s1}}{2} \\
 \mathbf{C}_1 &= \mathbf{Z}_e + \mathbf{Z}_{\text{cap}}\mathbf{Q}_{s1} \frac{(\mathbf{P}_{s3} + \mathbf{P}_{s1})}{2} + \frac{\mathbf{P}_{s1}\mathbf{Z}_{\text{cap}}\mathbf{Q}_{s2}}{2} \\
 \mathbf{C}_2 &= \mathbf{Z}_e + \mathbf{Z}_{\text{cap}}\mathbf{Q}_{s1} \frac{(\mathbf{P}_{s1} + \mathbf{P}_{s3})}{2}; \mathbf{C}_3 = \mathbf{Z}_e + \frac{\mathbf{P}_{s3}\mathbf{Z}_{\text{cap}}\mathbf{Q}_{s3}}{2}
 \end{aligned} \tag{4.15}$$

At a particular frequency of harmonics, the capacitive reactance of the GUPFC and the inductive reactance of the system become equal. This causes harmonic resonance. In a power system, resonance may be classified into series or parallel, depending upon the configuration of the resonance circuit. Series resonance causes voltage amplification and parallel resonance produces current multiplication within a network. Both these types are present in a rich harmonic environment. There is a probability that these resonant conditions cause high-low voltage disturbances that may lead to damage in the capacitor banks, transformer windings and other electrical equipment of the system. GUPFC HD model will be useful to predict the capacitance at which this resonance may occur, and also to estimate the total harmonic distortion in the voltages and currents at its terminals under the resonance conditions.

4.3.2 Dynamic harmonic domain model of the GUPFC

The derivation of the proposed GUPFC DHD model, also not currently available in the literature, is now presented.

The three-phase voltages and currents on the AC sides of the GUPFC Figure 44 are $\mathbf{v}_{abc1}(t)$, $\mathbf{v}_{ABC1}(t)$, $\mathbf{v}_{341}(t)$, $\mathbf{i}_{abc}(t)$, $\mathbf{i}_{ABC}(t)$ and $\mathbf{i}_{34}(t)$, respectively, and can be expressed in terms of DC-side voltage $\mathbf{v}_{dc}(t)$, DC-side current $i_1(t)$, $i_2(t)$, and $i_3(t)$, and the switching functions as

$$\begin{aligned}\mathbf{v}_{abc1}(t) &= \mathbf{p}_{s1}(t) \mathbf{v}_{dc}(t) \\ \mathbf{v}_{ABC1}(t) &= \mathbf{p}_{s2}(t) \mathbf{v}_{dc}(t) \\ \mathbf{v}_{341}(t) &= \mathbf{p}_{s3}(t) \mathbf{v}_{dc}(t)\end{aligned}\quad (4.16)$$

$$\begin{aligned}i_1(t) &= \mathbf{q}_{s1}(t) \mathbf{i}_{abc}(t) \\ i_2(t) &= \mathbf{q}_{s2}(t) \mathbf{i}_{ABC}(t) \\ i_3(t) &= \mathbf{q}_{s3}(t) \mathbf{i}_{34}(t)\end{aligned}\quad (4.17)$$

where $\mathbf{p}_{s1}(t)$, $\mathbf{p}_{s2}(t)$, $\mathbf{p}_{s3}(t)$, $\mathbf{q}_{s1}(t)$, $\mathbf{q}_{s2}(t)$ and $\mathbf{q}_{s3}(t)$ are transformation vectors, given by

$$\begin{aligned}\mathbf{p}_{s1}(t) &= \begin{bmatrix} s_{ab1}(t) \\ s_{bc1}(t) \\ s_{ca1}(t) \end{bmatrix}; & \mathbf{p}_{s2}(t) &= \begin{bmatrix} s_{ab2}(t) \\ s_{bc2}(t) \\ s_{ca2}(t) \end{bmatrix}; & \mathbf{p}_{s3}(t) &= \begin{bmatrix} s_{ab3}(t) \\ s_{bc3}(t) \\ s_{ca3}(t) \end{bmatrix} \\ \mathbf{q}_{s1}(t) &= [s_{ab1}(t) \quad s_{bc1}(t) \quad s_{ca1}(t)] \\ \mathbf{q}_{s2}(t) &= [s_{ab2}(t) \quad s_{bc2}(t) \quad s_{ca2}(t)] \\ \mathbf{q}_{s3}(t) &= [s_{ab3}(t) \quad s_{bc3}(t) \quad s_{ca3}(t)]\end{aligned}\quad (4.18)$$

$s_{ab1}(t)$, $s_{bc1}(t)$, and $s_{ca1}(t)$ are the switching functions of VSC 1, $s_{ab2}(t)$, $s_{bc2}(t)$, and $s_{ca2}(t)$ are for VSC 2 and $s_{ab3}(t)$, $s_{bc3}(t)$, and $s_{ca3}(t)$ are for VSC 3. Each VSC consists of six switches as shown in Figure A-1, Appendix A. These functions are defined in Section A.2, Appendix A.

The following state equation describes the circuit dynamics on the DC-side of the GUPFC:

$$\frac{dv_{dc}(t)}{dt} = \frac{1}{C}(i_1(t) + i_2(t) + i_3(t)) \quad (4.19)$$

Substitution of equations (4.17) into equation (4.19) yields

$$\frac{dv_{dc}(t)}{dt} = \frac{1}{C}(\mathbf{q}_{s1}(t)\mathbf{i}_{abc}(t) + \mathbf{q}_{s2}(t)\mathbf{i}_{ABC}(t) + \mathbf{q}_{s3}(t)\mathbf{i}_{34}(t)) \quad (4.20)$$

The voltage drop across the equivalent three-phase impedance of the transformer connected to the VSC 1 is

$$\begin{aligned} R_e \mathbf{i}_{abc}(t) + L_e \frac{d\mathbf{i}_{abc}(t)}{dt} &= \mathbf{v}_{abc}(t) - \mathbf{v}_{abc1}(t) \\ \frac{d\mathbf{i}_{abc}(t)}{dt} &= -\frac{R_e}{L_e} \mathbf{i}_{abc}(t) + \frac{\mathbf{v}_{abc}(t) - \mathbf{v}_{abc1}(t)}{L_e} \end{aligned} \quad (4.21)$$

Similarly for VSC 2 is

$$\begin{aligned} R_e \mathbf{i}_{ABC}(t) + L_e \frac{d\mathbf{i}_{ABC}(t)}{dt} &= \mathbf{v}_{ABC}(t) - \mathbf{v}_{ABC1}(t) \\ \frac{d\mathbf{i}_{ABC}(t)}{dt} &= -\frac{R_e}{L_e} \mathbf{i}_{ABC}(t) + \frac{\mathbf{v}_{ABC}(t) - \mathbf{v}_{ABC1}(t)}{L_e} \end{aligned} \quad (4.22)$$

For VSC 3 is

$$R_e \mathbf{i}_{34}(t) + L_e \frac{d\mathbf{i}_{34}(t)}{dt} = \mathbf{v}_{34}(t) - \mathbf{v}_{341}(t)$$

$$\frac{d\mathbf{i}_{34}(t)}{dt} = -\frac{R_e}{L_e} \mathbf{i}_{34}(t) + \frac{\mathbf{v}_{34}(t) - \mathbf{v}_{341}(t)}{L_e} \quad (4.23)$$

Substitution of equations (4.16) into equations (4.21), (4.22), and (4.23) yields

$$\frac{d\mathbf{i}_{abc}(t)}{dt} = -\frac{R_e}{L_e} \mathbf{i}_{abc}(t) + \frac{1}{L_e} (\mathbf{v}_{abc}(t) - \mathbf{p}_{s1}(t)v_{dc}(t)) \quad (4.24)$$

$$\frac{d\mathbf{i}_{ABC}(t)}{dt} = -\frac{R_e}{L_e} \mathbf{i}_{ABC}(t) + \frac{1}{L_e} (\mathbf{v}_{ABC}(t) - \mathbf{p}_{s2}(t)v_{dc}(t)) \quad (4.25)$$

$$\frac{d\mathbf{i}_{34}(t)}{dt} = -\frac{R_e}{L_e} \mathbf{i}_{34}(t) + \frac{1}{L_e} (\mathbf{v}_{34}(t) - \mathbf{p}_{s3}(t)v_{dc}(t)) \quad (4.26)$$

The boundary conditions of the GUPFC are

$$\begin{aligned} \mathbf{i}_{abc}(t) &= \mathbf{i}_R(t) + \mathbf{i}_S(t) & \mathbf{v}_{abc}(t) &= \mathbf{v}_S(t) \\ \mathbf{i}_{ABC}(t) &= \mathbf{i}_R(t) & \mathbf{v}_{ABC}(t) &= \mathbf{v}_R(t) - \mathbf{v}_S(t) \\ \mathbf{i}_{34}(t) &= \mathbf{i}_T(t) & \mathbf{v}_{34}(t) &= \mathbf{v}_T(t) - \mathbf{v}_S(t) \end{aligned} \quad (4.27)$$

Substitution of (4.27) into (4.20), (4.24), (4.25), and (4.26) yields

$$\frac{dv_{dc}(t)}{dt} = \frac{1}{C} (\mathbf{q}_{s1}(t)\mathbf{i}_S(t) + (\mathbf{q}_{s1}(t) + \mathbf{q}_{s2}(t))\mathbf{i}_R(t) + \mathbf{q}_{s3}(t)\mathbf{i}_T(t)) \quad (4.28)$$

$$\frac{d(\mathbf{i}_R(t) + \mathbf{i}_S(t))}{dt} = -\frac{R_e}{L_e} (\mathbf{i}_R(t) + \mathbf{i}_S(t)) + \frac{1}{L_e} (\mathbf{v}_S(t) - \mathbf{p}_{s1}(t)v_{dc}(t)) \quad (4.29)$$

$$\frac{d\mathbf{i}_R(t)}{dt} = -\frac{R_e}{L_e} \mathbf{i}_R(t) + \frac{1}{L_e} (\mathbf{v}_R(t) - \mathbf{v}_S(t) - \mathbf{p}_{s2}(t)v_{dc}(t)) \quad (4.30)$$

$$\frac{d\mathbf{i}_T(t)}{dt} = -\frac{R_e}{L_e}\mathbf{i}_T(t) + \frac{1}{L_e}(\mathbf{v}_T(t) - \mathbf{v}_S(t) - \mathbf{p}_{s3}(t)v_{dc}(t)) \quad (4.31)$$

Substituting (4.30) into (4.29) gives

$$\frac{d\mathbf{i}_S(t)}{dt} = -\frac{R_e}{L_e}\mathbf{i}_S(t) + \frac{2\mathbf{v}_S(t)}{L_e} - \frac{\mathbf{v}_R(t)}{L_e} + \frac{v_{dc}(t)}{L_e}(\mathbf{p}_{s2}(t) - \mathbf{p}_{s1}(t)) \quad (4.32)$$

The state equations (4.28), (4.30) (4.31) and (4.32) of the GUPFC are

$$\begin{bmatrix} \frac{d\mathbf{i}_R(t)}{dt} \\ \frac{d\mathbf{i}_S(t)}{dt} \\ \frac{d\mathbf{i}_T(t)}{dt} \\ \frac{dv_{dc}(t)}{dt} \end{bmatrix} = \begin{bmatrix} -\frac{R_e}{L_e} & 0 & 0 & -\frac{\mathbf{p}_{s2}(t)}{L_e} \\ 0 & -\frac{R_e}{L_e} & 0 & -\left(\frac{\mathbf{p}_{s1}(t) - \mathbf{p}_{s2}(t)}{L_e}\right) \\ 0 & 0 & -\frac{R_e}{L_e} & -\frac{\mathbf{p}_{s3}(t)}{L_e} \\ \frac{\mathbf{q}_{s1}(t) + \mathbf{q}_{s2}(t)}{C} & \frac{\mathbf{q}_{s1}(t)}{C} & \frac{\mathbf{q}_{s3}(t)}{C} & 0 \end{bmatrix} \begin{bmatrix} \mathbf{i}_R(t) \\ \mathbf{i}_S(t) \\ \mathbf{i}_T(t) \\ v_{dc}(t) \end{bmatrix} + \frac{1}{L_e} \begin{bmatrix} 1 & -1 & 0 & 0 \\ -1 & 2 & 0 & 0 \\ 0 & -1 & 1 & 0 \\ 0 & 0 & 0 & 0 \end{bmatrix} \begin{bmatrix} \mathbf{v}_R(t) \\ \mathbf{v}_S(t) \\ \mathbf{v}_T(t) \\ 0 \end{bmatrix} \quad (4.33)$$

The state-space GUPFC model in (4.33) can be transformed into a DHD representation by making use of the procedure presented in Section 3.2. The resulting DHD model is given by

$$\begin{bmatrix} \dot{\mathbf{i}}_R(t) \\ \dot{\mathbf{i}}_S(t) \\ \dot{\mathbf{i}}_T(t) \\ \dot{\mathbf{V}}_{dc}(t) \end{bmatrix} = \mathbf{G}_U(t) \begin{bmatrix} \mathbf{I}_R(t) \\ \mathbf{I}_S(t) \\ \mathbf{I}_T(t) \\ \mathbf{V}_{dc}(t) \end{bmatrix} + \frac{1}{L_e} \begin{bmatrix} \mathbf{U}_1 & -\mathbf{U}_1 & \mathbf{O}_4 & \mathbf{O}_2 \\ -\mathbf{U}_1 & 2\mathbf{U}_1 & \mathbf{O}_4 & \mathbf{O}_2 \\ \mathbf{O}_4 & -\mathbf{U}_1 & \mathbf{U}_1 & \mathbf{O}_2 \\ \mathbf{O}_1 & \mathbf{O}_1 & \mathbf{O}_1 & \mathbf{O}_3 \end{bmatrix} \begin{bmatrix} \mathbf{V}_R(t) \\ \mathbf{V}_S(t) \\ \mathbf{V}_T(t) \\ \mathbf{0} \end{bmatrix} \quad (4.34)$$

where

$$\mathbf{G}_U(t) = \begin{bmatrix} -\frac{R_e}{L_e}\mathbf{U}_1 - \mathbf{D}(jh\omega_0) & \mathbf{O}_4 & \mathbf{O}_4 & -\frac{1}{L_e}\mathbf{P}_{S2} \\ \mathbf{O}_4 & -\frac{R_e}{L_e}\mathbf{U}_1 - \mathbf{D}(jh\omega_0) & \mathbf{O}_4 & -\left(\frac{\mathbf{P}_{S1} - \mathbf{P}_{S2}}{L_e}\right) \\ \mathbf{O}_4 & \mathbf{O}_4 & -\frac{R_e}{L_e}\mathbf{U}_1 - \mathbf{D}(jh\omega_0) & -\frac{1}{L_e}\mathbf{P}_{S3} \\ \frac{\mathbf{Q}_{S1} + \mathbf{Q}_{S2}}{C} & \frac{1}{C}\mathbf{Q}_{S1} & \frac{1}{C}\mathbf{Q}_{S3} & \mathbf{O}_3 \end{bmatrix}$$

and \mathbf{U}_1 is the unit matrix (303×303). \mathbf{O} , \mathbf{O}_1 , \mathbf{O}_2 , \mathbf{O}_3 and \mathbf{O}_4 are the zero matrices with dimensions (101×1) , (101×303) , (303×101) , (101×101) and (303×303) respectively.

The solution of equation (4.34) gives complete information about the harmonics in the GUPFC, under steady and dynamic state conditions. The steady state solution of (4.34) can be obtained by setting $\dot{\mathbf{I}}_R(t)$, $\dot{\mathbf{I}}_S(t)$, $\dot{\mathbf{I}}_T(t)$ and $\dot{\mathbf{V}}_{dc}(t)$ to zero. Thus, the following algebraic equations represent the steady state

$$\begin{bmatrix} \mathbf{I}_R(t) \\ \mathbf{I}_S(t) \\ \mathbf{I}_T(t) \\ \mathbf{V}_{dc}(t) \end{bmatrix} = -\frac{\mathbf{G}_U^{-1}(t)}{L_e} \begin{bmatrix} \mathbf{U}_1 & -\mathbf{U}_1 & \mathbf{O}_4 & \mathbf{O}_2 \\ -\mathbf{U}_1 & 2\mathbf{U}_1 & \mathbf{O}_4 & \mathbf{O}_2 \\ \mathbf{O}_4 & -\mathbf{U}_1 & \mathbf{U}_1 & \mathbf{O}_2 \\ \mathbf{O}_1 & \mathbf{O}_1 & \mathbf{O}_1 & \mathbf{O}_3 \end{bmatrix} \begin{bmatrix} \mathbf{V}_R(t) \\ \mathbf{V}_S(t) \\ \mathbf{V}_T(t) \\ \mathbf{O} \end{bmatrix} \quad (4.35)$$

The solutions of the steady state equations (4.35) are used as the initial conditions for solving (4.34) provided, inverse of $\mathbf{G}_U(t)$ exists.

4.3.3 Simulation of the proposed DHD model of GUPFC

The DHD model of the GUPFC in (4.34) is used to investigate the dynamic response of harmonics to a given disturbance. PWM switching technique is used, whose function is calculated using the harmonic elimination method, to eliminate harmonics $i = 5, 7, 11, 13,$ and 17 .

The magnitude of the fundamental of the inverter AC voltage can be adjusted by controlling the voltage across the capacitor. This can be achieved by changing the phase angle of the operation of the inverter switches with respect to the AC system. In this case a phase angle of 15° is considered. The per-phase equivalent leakage inductance and winding resistance of the transformer and the capacitance of the DC capacitor are $L_e = 0.2$ mH, $R_e = 0.04$ Ω , and $C = 5000$ μF , respectively. Under steady state conditions, the bus per-phase voltages V_S , V_R , and V_T per unit at a frequency of 60 Hz, are

$$\begin{aligned}
 v_{Sa}(t) &= 1.5 \sin \omega_0 t & v_{Sb}(t) &= 1.5 \sin(\omega_0 t - 120^\circ) & v_{Sc}(t) &= 1.5 \sin(\omega_0 t + 120^\circ) \\
 v_{Ra}(t) &= 1.6 \sin \omega_0 t & v_{Rb}(t) &= 1.6 \sin(\omega_0 t - 120^\circ) & v_{Rc}(t) &= 1.6 \sin(\omega_0 t + 120^\circ) \\
 v_{Ta}(t) &= 1.95 \sin \omega_0 t & v_{Tb}(t) &= 1.95 \sin(\omega_0 t - 120^\circ) & v_{Tc}(t) &= 1.95 \sin(\omega_0 t + 120^\circ)
 \end{aligned} \tag{4.36}$$

A disturbance in the system is assumed, starting at 0.08 seconds and lasting for 0.05 seconds, resulting in the reduction of the voltage on phase a by 50% of its given operating value. The simulation starts at $t_0 = 0$ and ends at the final time of $t_f = 0.2$ seconds with an integration time step of $\Delta t = 0.2$ ms. For accuracy, a total of 50 harmonics are considered. The simulations are performed using MATLAB[®] software. The integration method used for these simulations is ode45(), which is a fourth-order-Runge-

Kutta algorithm that is built-in MATLAB[®] software. The same integration is used to simulate all dynamic models developed on the multi-line FACTS controllers in this research work.

The control system shown in Figure 24 is again used to maintain constant DC voltage across the capacitor in the GUPFC dynamic model.

Figure 45 shows the harmonic content of the DC voltage with and without control system during the disturbance. The letter "h" in the plots represents the harmonic number. These results were obtained with a controller using a time constant (T) of 0.0001 seconds and a gain (K) of 20. Due to the unbalanced nature of the disturbance, non-characteristic harmonics (the 2nd, the 4th, and the 6th) are present in the system.

These results show that, during the disturbance period and without control, the DC component of the voltage on the DC side drops by 38% of its steady state value, as shown in Figure 45(a). Figure 45(b) demonstrates that the DC component of the voltage is very close to its steady state value, thus indicating that the control system does decrease the distortion during the disturbance. Although the harmonic voltages have not changed with the control, there is a change in the 6th harmonic voltage; however this could also be eliminated by proper gain and time constant values.

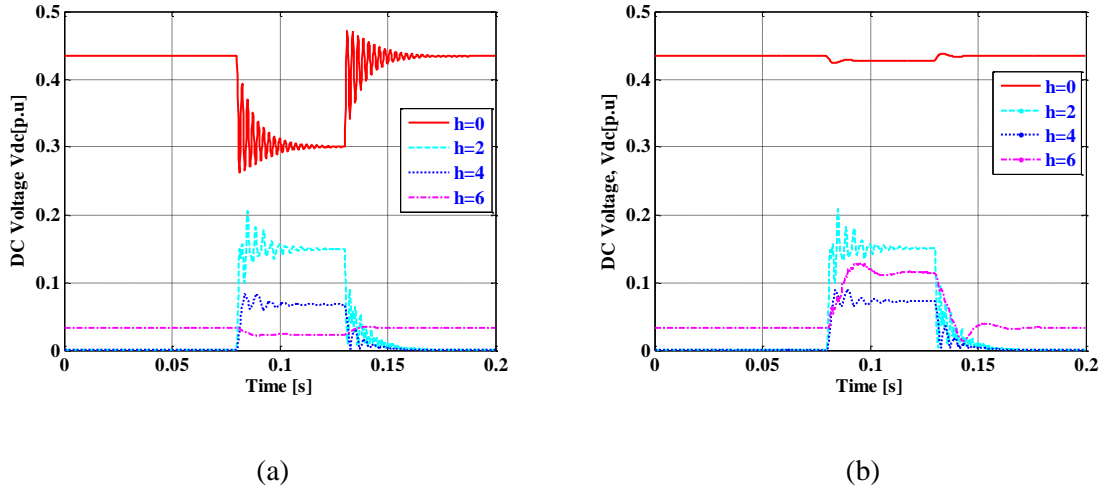


Figure 45: DC-side voltage of GUPFC: (a) Without control system (b) With control system

Keeping the DC voltage constant during the disturbance further helped to minimize some of the power quality indices at the GUPFC terminals, such as the RMS value of the output currents of VSC 1, the THD in output currents $i_{ABC}(t)$ of VSC 2, and the output reactive powers per phase of each phase of VSC 1, as evident from Figure 46, Figure 47, and Figure 48, respectively. These results demonstrate the importance of keeping the capacitor voltage as constant as possible to its steady-state value. The absolute change in the per-phase voltages at the VSC 1 output depends on the DC voltage and per-phase voltages at the terminals of the same. In this case study, the terminal voltage at this voltage source converter is higher than that of the voltage at the terminals of VSC 2. This is the reason for higher absolute per-phase currents of VSC 1 even for a slight drop in the DC component value. Also, their variation is not uniform because of the switching functions in each phase.

The THD in the output currents of VSC 2 are shown in Figure 47. The distortion in the per-phase output currents of the same depends on the DC side voltage and switching function of each phase, as is predicted by equation (4.30). The THD is not uniform because of the switching functions in each phase. The per-phase reactive output powers of VSC 1 are shown in Figure 48. The increase in per-phase RMS output current of VSC 1 causes voltage drop at the terminals of the corresponding phases. The mutual effects of currents and voltage outputs of VSC 1 result in a drop in the reactive power from their steady state values during the disturbance period.

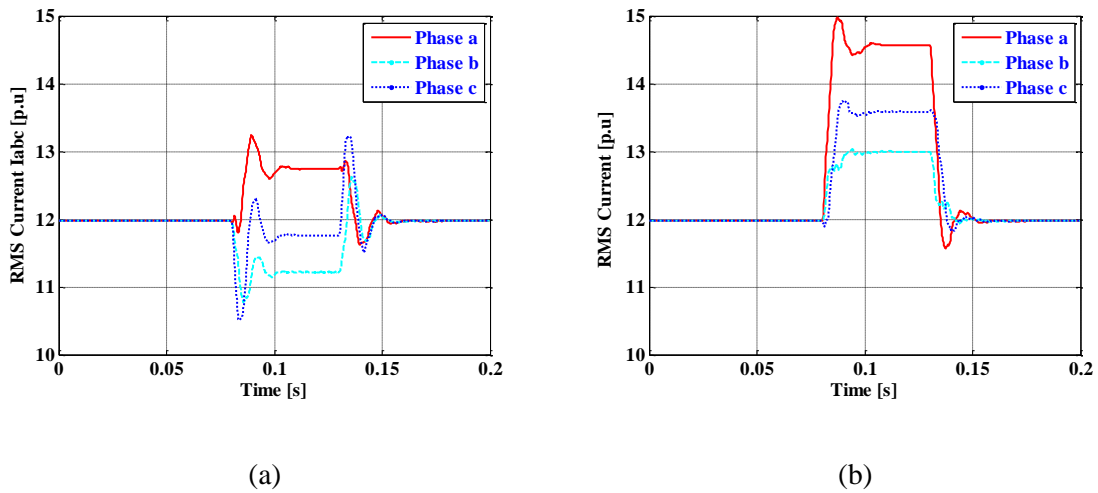
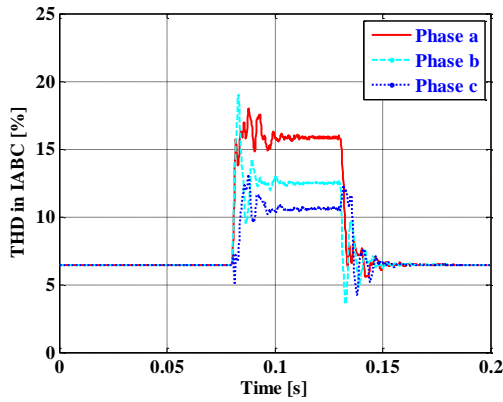
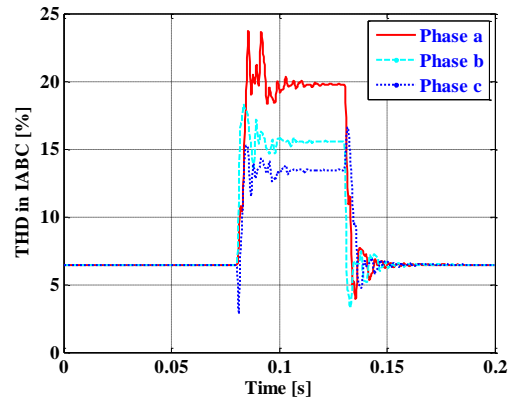


Figure 46: The RMS value of the output currents of VSC 1 (a) With control system (b)

Without control system

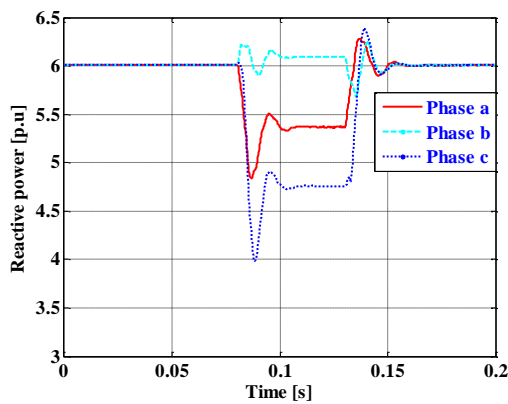


(a)

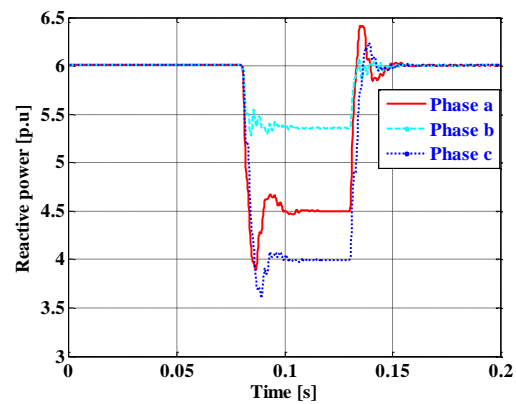


(b)

Figure 47: The THD in output currents of VSC 2 (a) With control system (b) Without control system



(a)



(b)

Figure 48: The output reactive powers of each phase of VSC 1 (a) With control system (b) Without control system

Figure 49.1 and Figure 49.2 below, show some additional power quality indices such as the THD in currents $i_{abc}(t)$ of VSC 1, the per-phase output reactive powers of each phase of VSC 3, the RMS values of the currents $i_{ABC}(t)$ of VSC 2, the per-phase

output active powers of each phase of VSC 1, the RMS values of the output currents of VSC 3, and the per phase output apparent powers of each phase of VSC 3.

From Figure 44 and equation (4.37) the per-phase current of bus R, at any instant depends on three variables as

$$\begin{aligned} \dot{\mathbf{I}}_R(t) = & \left(-\frac{R_e}{L_e} \mathbf{U}_1 - \mathbf{D}(j h \omega_0) \right) \mathbf{I}_R(t) - \left(\frac{1}{L_e} \right) \mathbf{P}_{S2} \mathbf{V}_{dc}(t) \\ & + \frac{1}{L_e} \underbrace{(\mathbf{V}_R(t) - \mathbf{V}_S(t))}_{(3)} \end{aligned} \quad (4.37)$$

These variables are: (1) the switching function of each phase, (2) the DC side voltage, and (3) the corresponding bus per-phase voltages.

The DC side voltage varies only when the bus per-phase voltage changes. Figure 49.1(d) shows the RMS output currents in each phase of VSC 2. During the disturbance period, the per-phase voltages at the terminals of the VSC 2 are constant and the changes in its RMS output currents are due to the variations in the DC voltage. Although the DC component of this voltage is close to its steady state value, with the application of the control system as shown in Figure 24, there are variations in the RMS output currents of the VSC 2 due to the slight drop in this DC component value. The per-phase RMS output currents of VSC 2 during the disturbance period do not change uniformly because of the switching functions in each phase. Due to the variations in output currents of each phase of a VSC, there are changes in voltages and in all other power quality indices.

From these plots we learn how the power quality indices vary during the steady and disturbance periods. These results will somewhat change with the choice of controller parameters. However, their analysis is not the focus of this chapter.

Though VSC 1 and VSC 2 are not directly connected to the T-bus, there is a significant harmonic distortion in active power at VSC 1, and RMS current at VSC 2, as shown in Figure 49.1(c) and (d), respectively. This can be attributed to the fact that the proposed GUPFC DHD model is capable of representing mutual effects between phases

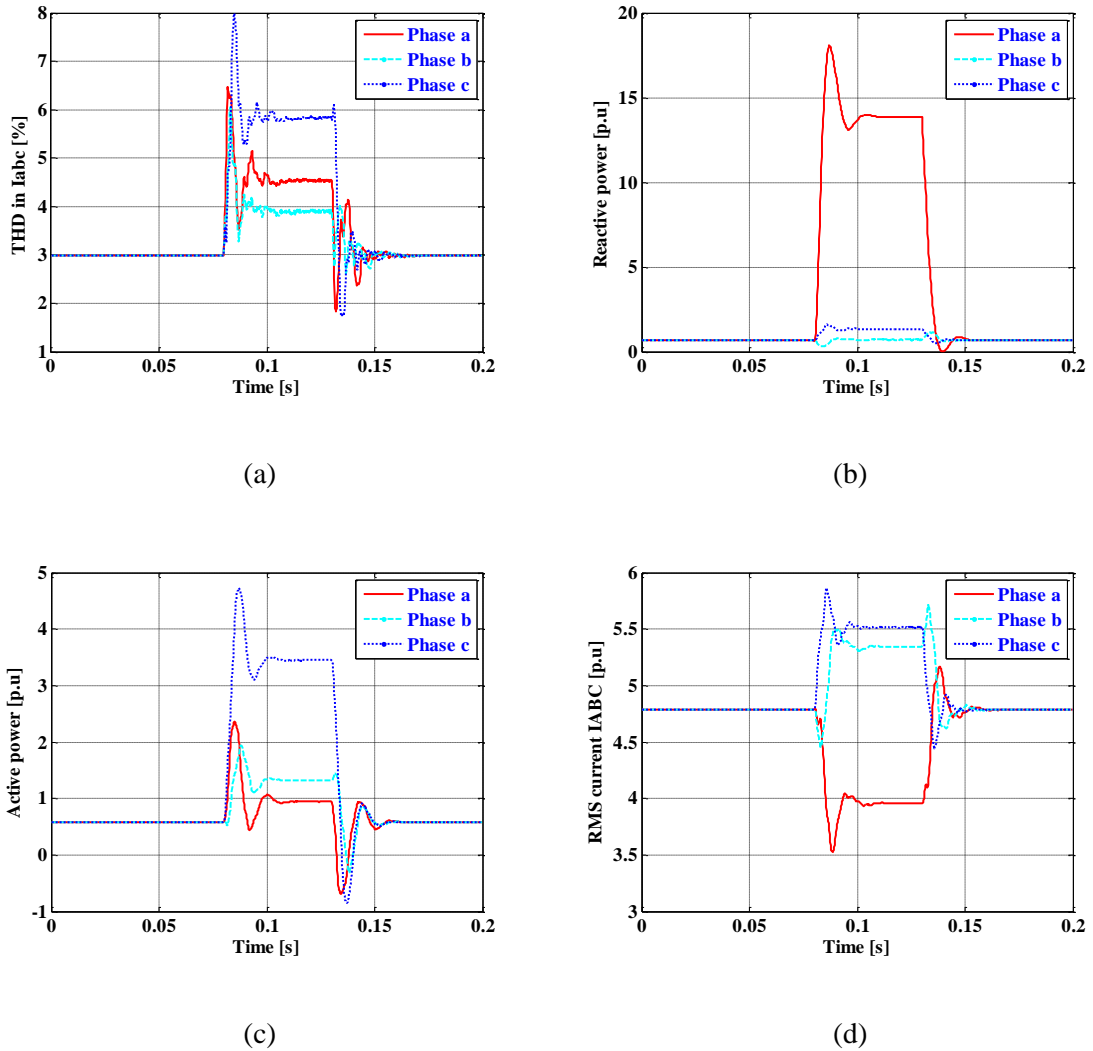


Figure 49.1: Power quality indices (a) THD in output currents of VSC 1 (b) Per-phase output reactive powers of VSC 3 (c) Per-phase output active powers of VSC 1 (d) RMS values of the output currents of VSC 2

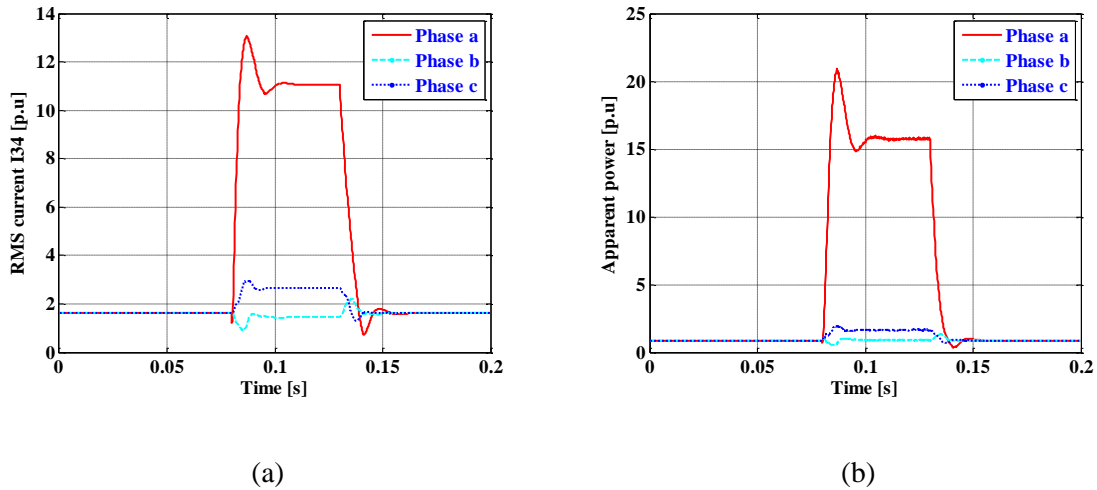


Figure 49.2: Power quality indices (a) RMS values of the output currents of VSC 3 (b)

Per-phase output apparent powers of VSC 3

The time plots of output voltages of VSC 2 and VSC 3 of phase *a*, over the steady state and disturbance intervals, that depict the actual voltage waveforms, are shown in Figure 50(a) and Figure 51(a), respectively. These plots are derived from the harmonic domain information of the corresponding voltages. They exhibit more distortions during the disturbance than when in normal period. Although the VSC 2 terminals are not connected to the bus, where the voltage has changed during the disturbance period, the drop in the DC side voltage during that period causes a drop in the fundamental component of the phase *a* voltage of VSC 2. The individual magnitudes of the most dominant harmonics of these voltages are shown in Figure 50(b), and Figure 51(b), respectively.

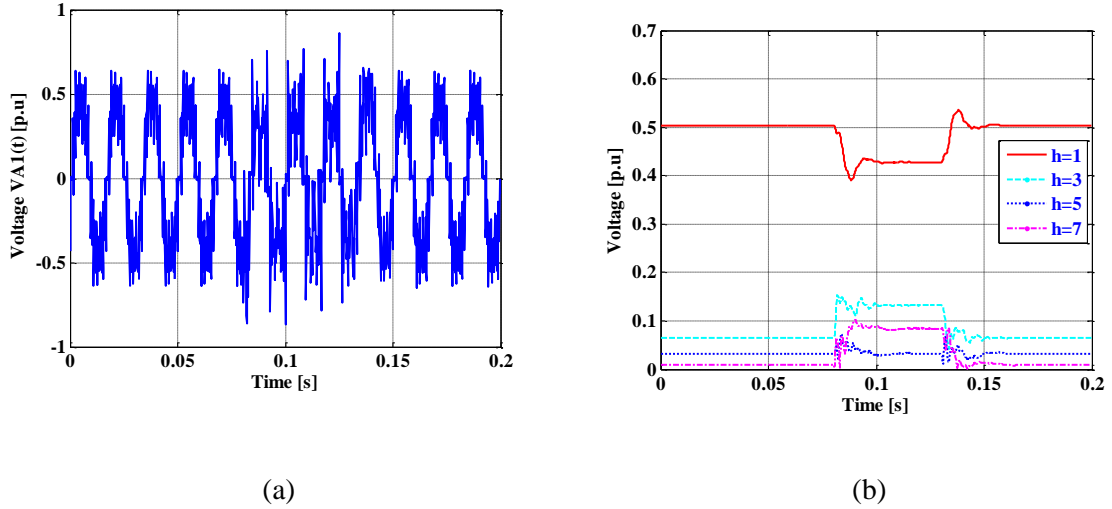


Figure 50: The output voltage of phase a of VSC 2 (a) Voltage waveform (b) Voltage harmonic content

From Figure 51(b) it can be observed that the fundamental component of phase a voltage is three times that of its steady state value. This is due to the fact that VSC 3 is connected between buses T and S , with their relationship established by equation (4.27). Since the disturbance causes the voltage at bus T to drop by 50% of its steady state value, the equation (4.30) predicts a larger voltage will appear at the terminals of VSC 3 during this interval. This effect is also evident in the time domain plot shown in Figure 51(a)

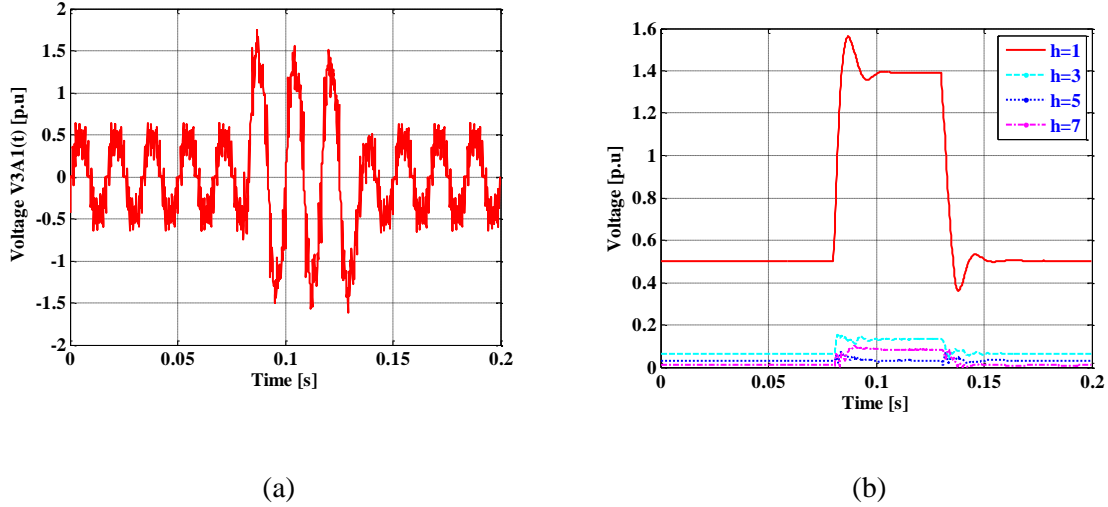
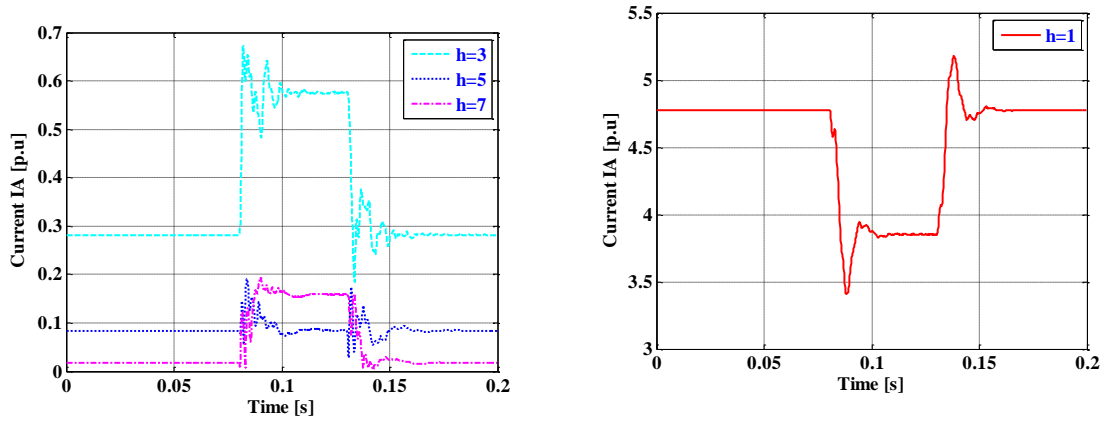
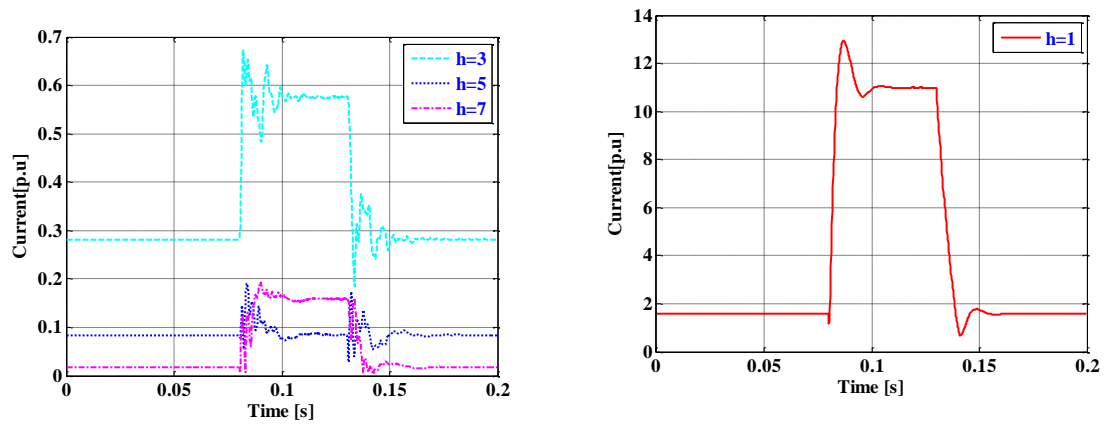


Figure 51: The output voltage of phase a of VSC 3 (a) Voltage waveform (b) Voltage harmonic content

The impact of the disturbance on the harmonic content of the output currents of VSC 2 and VSC 3 are shown in Figure 52(a) and (b), respectively. Apart from the fundamental currents, the voltages of other harmonics (3^{rd} , 5^{th} , and 7^{th}) are also shown. The drop in the fundamental component of the output current in phase a of VSC 2 is due to the change in the DC side voltage, as is predicted by equation (4.30). The increase in the phase a voltage at the terminals of VSC 3 during the disturbance interval causes, as expected, a rise in the fundamental component of its phase a output current. The time domain waveforms of the output currents of the phase a of VSC 2 and VSC 3 are shown in Figure 53.



(a)



(b)

Figure 52: The harmonic content of output current of phase *a* of (a) VSC 2 (b) VSC 3

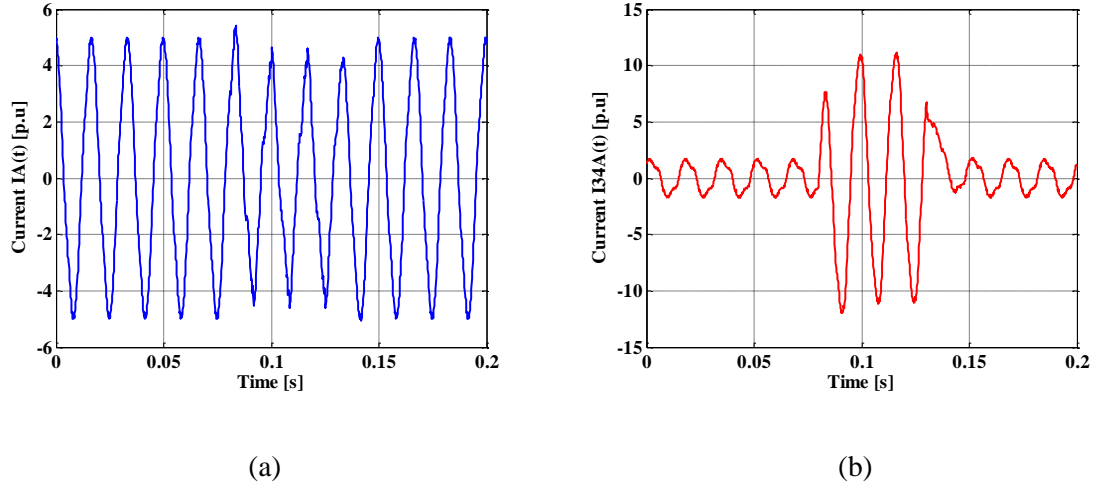
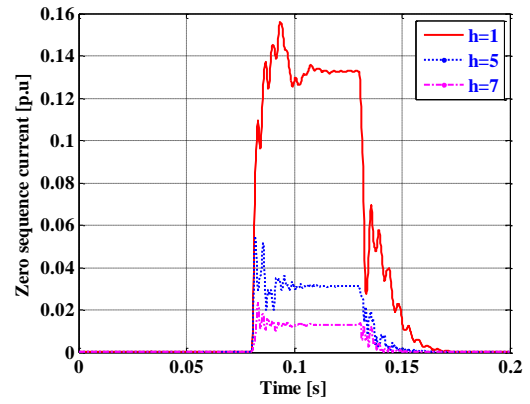
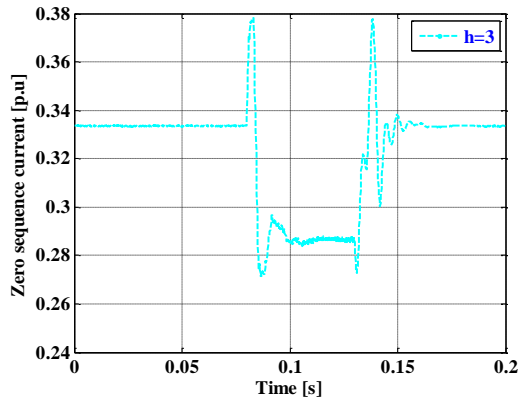
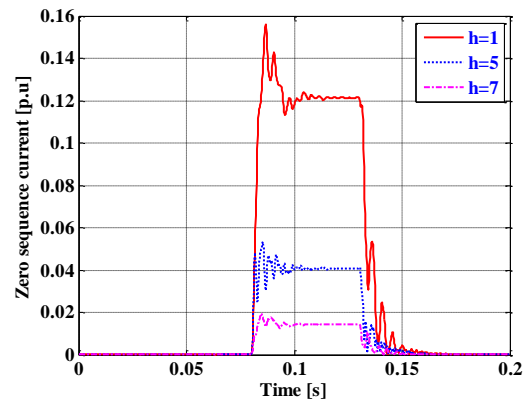
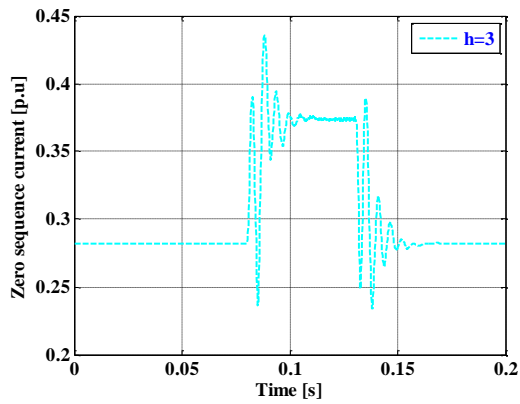


Figure 53: Time domain waveforms of output currents of phase a of (a) VSC 2 (b) VSC 3

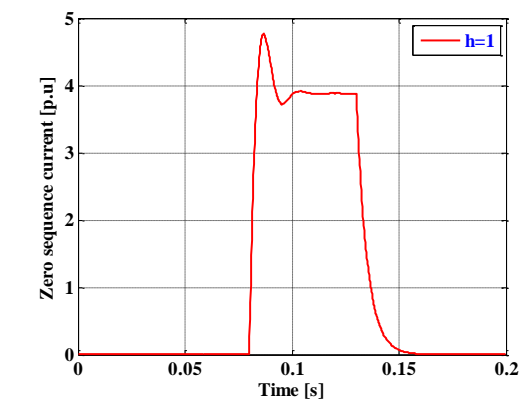
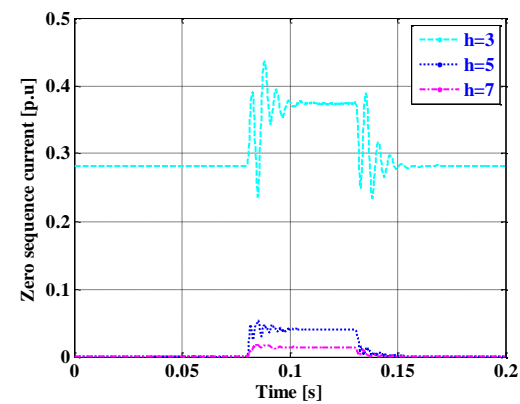
The harmonic components of the zero sequence currents of VSC 1, VSC 2, and VSC 3 are shown in Figure 54. From these plots it is evident that the 3rd harmonic component exists only when the system is under steady state while all the odd harmonic components, including the 3rd, are present during the disturbance (for visual clarity the 3rd plot is shown separately from the others in (a) and (b)). This phenomenon, and the remaining ones addressed below, is expected as predicted by the mathematical analysis presented in Section 3.5. The fundamental component of the zero sequence current of phase a in VSC 3 is higher relative to that in VSC 1 and VSC 2. This is due to the fact that a larger voltage appears at the terminals of VSC 3 during the disturbance interval than at VSC 1 and VSC 2.



(a)



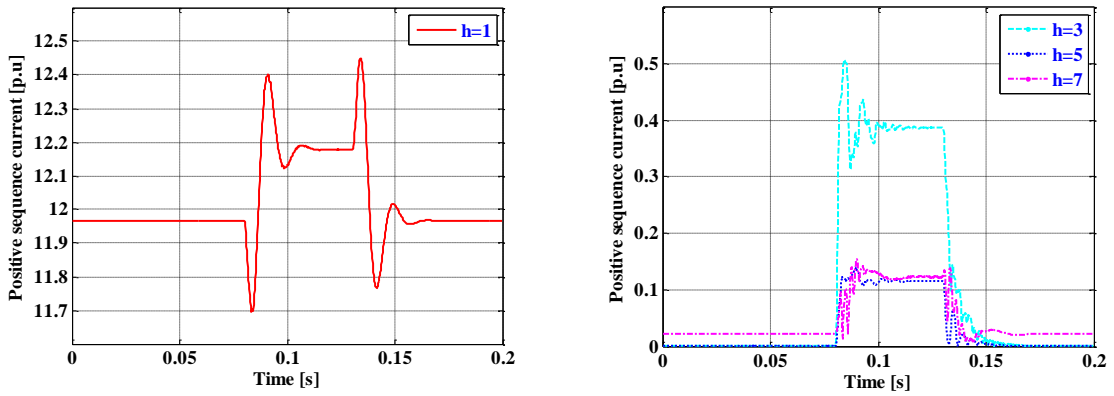
(b)



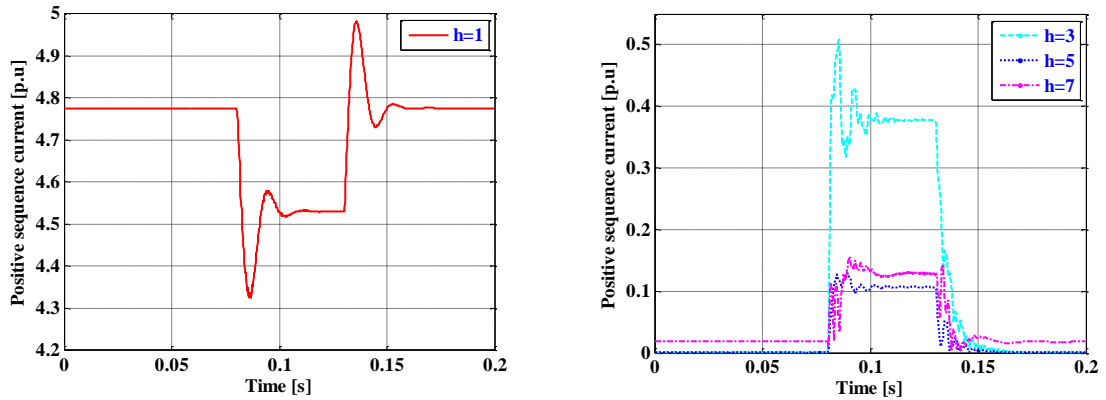
(c)

Figure 54: The zero sequence currents of (a) VSC 1 (b) VSC 2 (c) VSC 3

The harmonic content of the positive sequence currents of VSC 1, VSC 2, and VSC 3 are shown in Figure 55.1 and Figure 55.2. According to the mathematical discussion in Section 3.5, only the fundamental and the 7th harmonic currents are present in the steady state as predicted, while all odd harmonic currents are present during the disturbance interval.

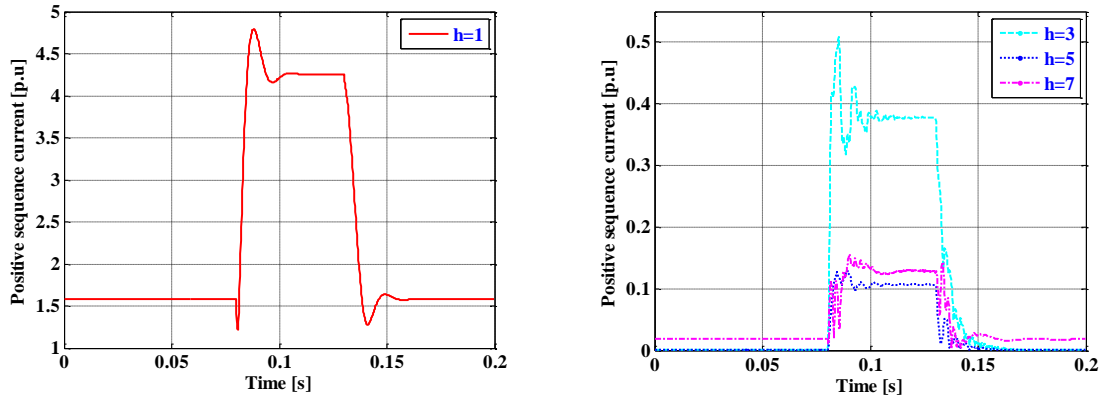


(a)



(b)

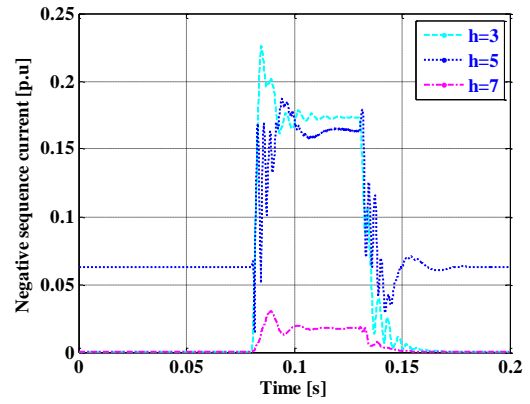
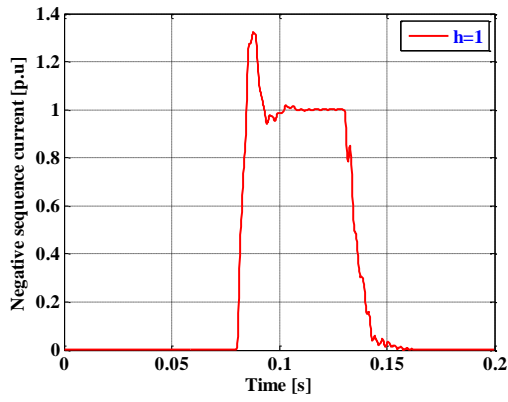
Figure 55.1: Positive sequence currents of (a) VSC 1 (b) VSC 2



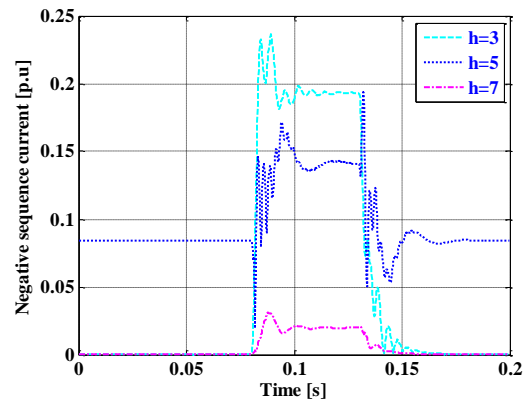
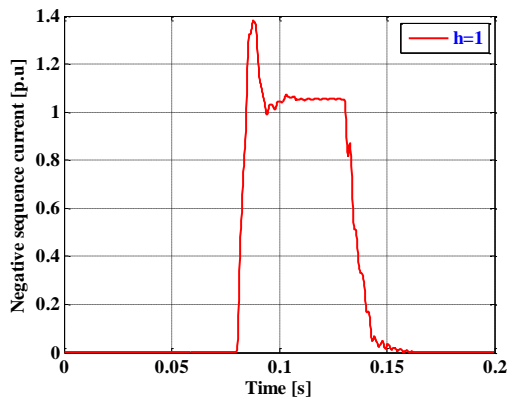
(a)

Figure 55.2: Positive sequence currents of (a) VSC 3

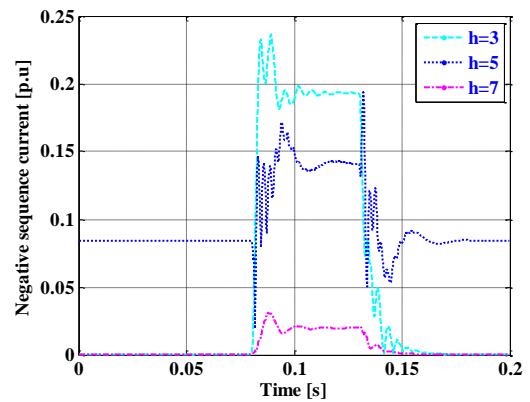
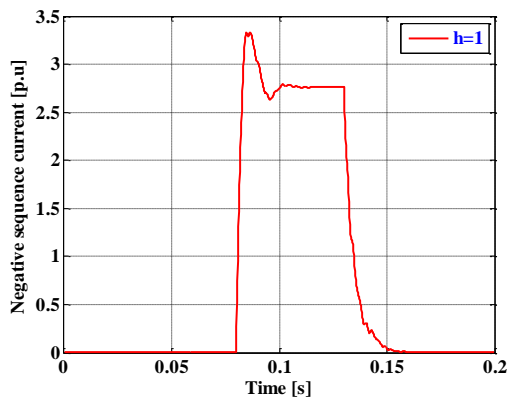
The harmonic content of the negative sequence currents for VSC 1, VSC 2, and VSC 3 are shown in Figure 56, below. Again, according to the mathematical discussion in Section 3.5, only the 5th harmonic of the negative sequence currents appears during the steady state as predicted, while all the odd harmonics are present within the disturbance interval.



(a)



(b)



(c)

Figure 56: The negative sequence currents of (a) VSC 1 (b) VSC 2 (c) VSC 3

The time domain waveforms of the positive sequence currents of VSC 1 and VSC 2 are shown in Figure 57. These plots, as expected, show sinusoidal behavior during steady state and slightly (almost invisible) non-sinusoidal behavior through the disturbance interval. Please note that it is nearly impossible to determine from these plots when and where the disturbance in the system occurs, especially if it is very small and/or it is present for a short duration, such as the one under study. This detection of small disturbances is another advantage that is highlighted by the availability and utilization of the proposed model.

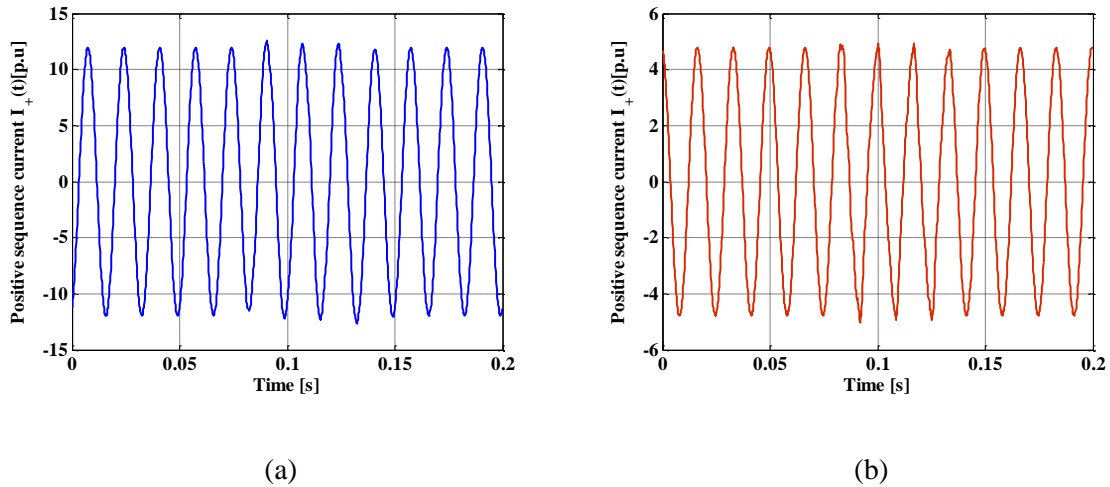


Figure 57: Time domain waveform of the positive sequence currents of (a) VSC 1 (b) VSC 2

4.3.4 Validation of the proposed DHD method of the GUPFC

The validation method discussed in Section 3.6.3 is applied to the output currents of VSC 1, and the resulting time domain waveforms of the three-phases are shown in Figure 58.1(a). The plots of these currents, generated by both methods, show non-

discernible difference. This procedure is repeated for VSC 2 and VSC 3 and the results are shown in Figure 58.2(a) and (b), with the same evidence. This allows the conclusion that the proposed GUPFC DHD model has been validated.

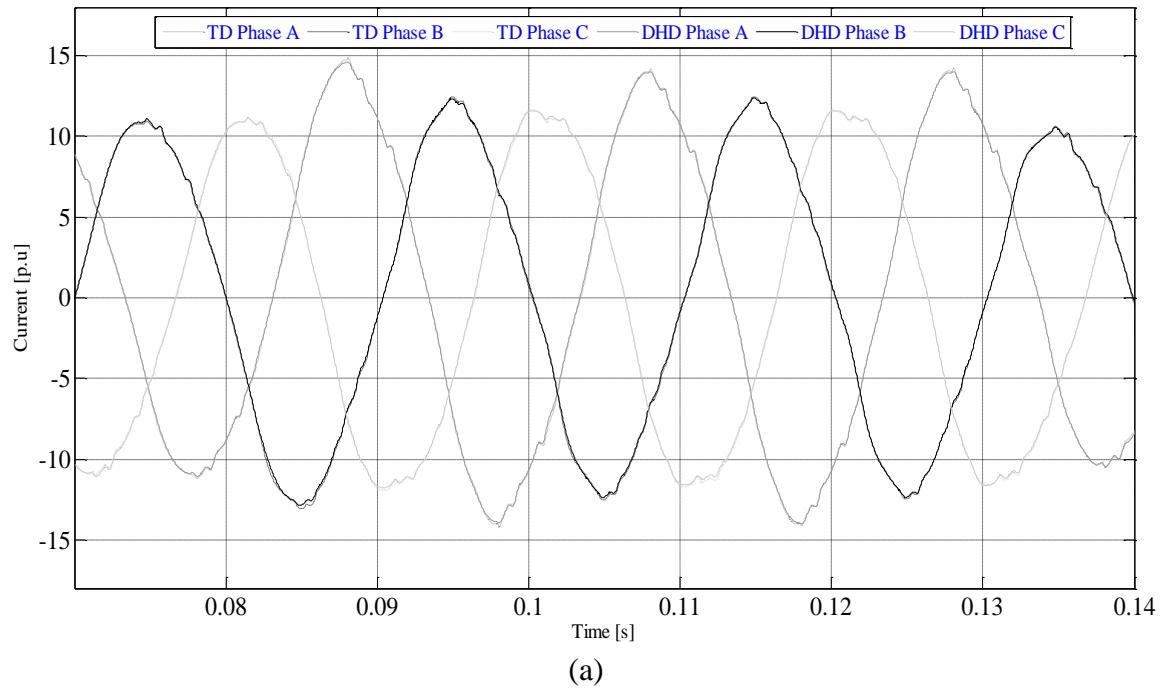
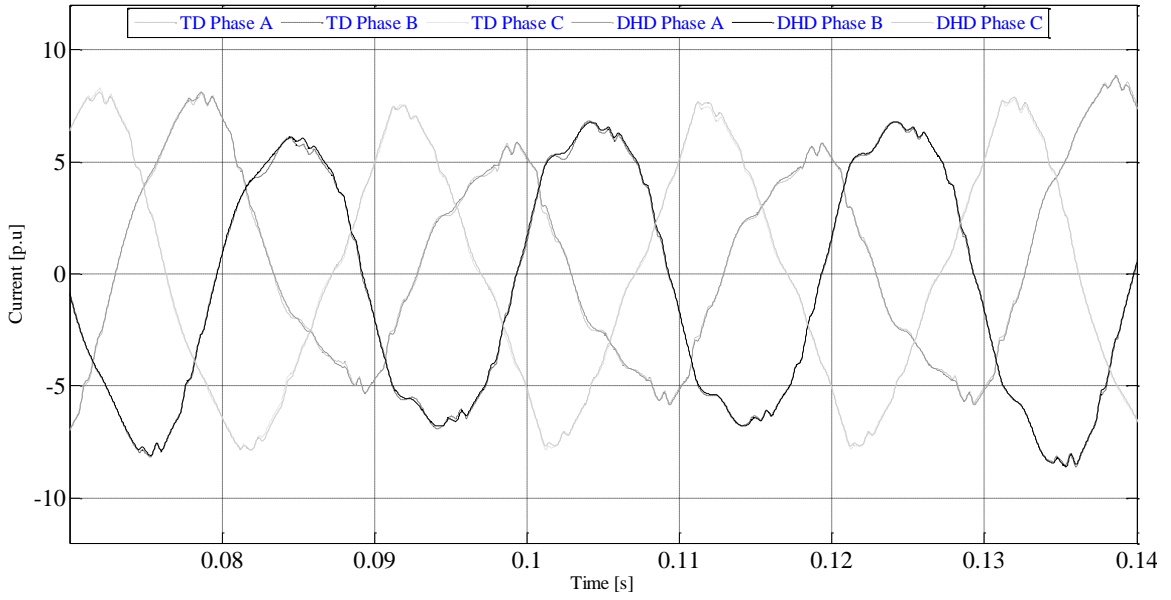
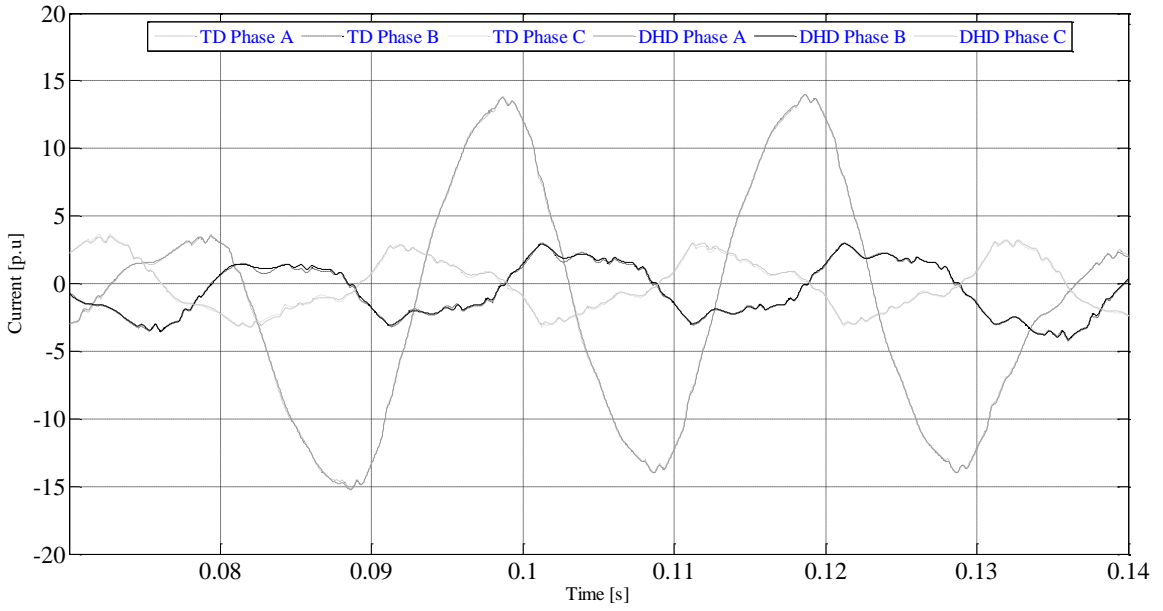


Figure 58.1: Time domain waveforms of currents of each phase of (a) VSC 1



(a)



(b)

Figure 58.2: Time domain waveforms of currents of each phase of (a) VSC 2

(b) VSC 3

4.4 Interline power flow controller

The IPFC can provide series compensation for multiple lines [45]. In order to attain optimal utilization of the whole transmission system, the strong or under-loaded lines are forced to assist the weaker or over-loaded ones. This is the fundamental concept behind the IPFC configuration which has two VSCs connected in series to two transmission lines as shown in. These VSCs are connected back-to-back across a common DC link, which enables any VSC within the IPFC to transfer real power to any other, thus smoothing the real power transfer among the transmission system lines. If the VSC injects voltage in quadrature with the transmission line current, it can provide only reactive power compensation, and any other phase relationship between them engage in managing of real power as well.

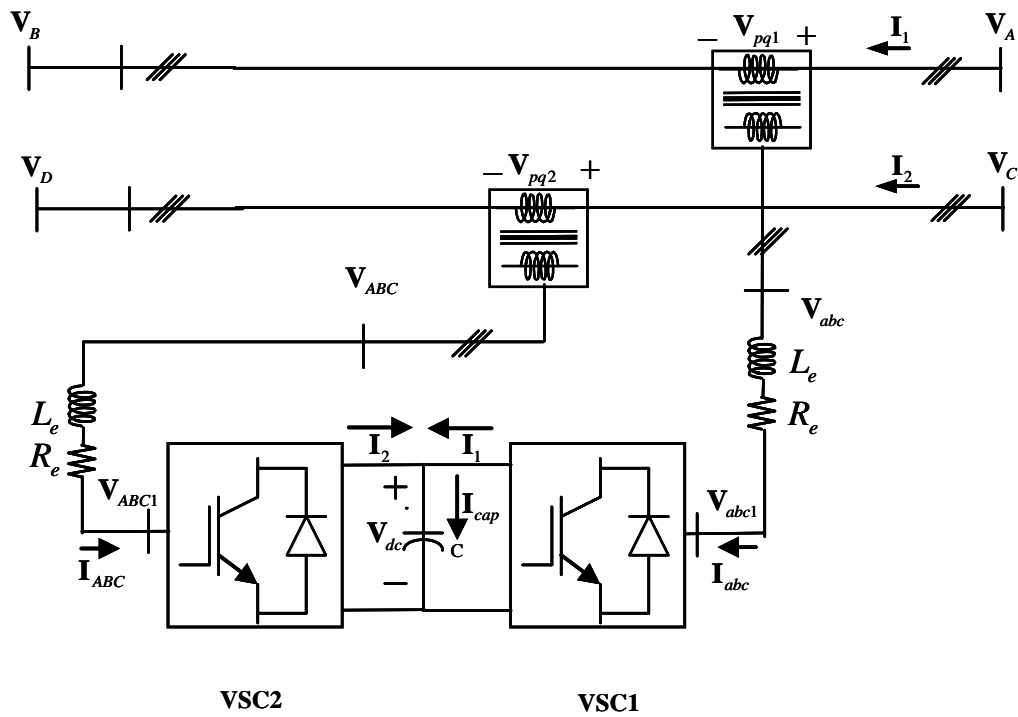


Figure 59: Interline power flow controller

IPFC is therefore capable of providing comprehensive real and reactive power compensation of the selected range of transmission system thus reducing the effect of the dynamic disturbances in the system.

In general, series compensation is used to increase the real power flow over the transmission line. The SSSC is an example of a series compensation device which is effective in maintaining the load balancing in the transmission system. However, it fails to control the reactive power flow, thus leading to inefficiency in load balancing of the lines. This problem becomes more conspicuous when the reactive to resistive line impedance ratio, (X/R) , is low. By nature, the series compensation curtails only the reactance of the line and therefore X/R ratio decreases resulting in an increase in the reactive power flow and thereby increasing the losses in the line. The IPFC design, along with independently controllable reactive series compensation of each individual line, addresses the above mentioned problem with its ability to perform direct real power transfer between the compensated lines. This innovative design facilitates the following:

- Power demand transfer from overloaded to under-loaded lines
- Augments the implementation of the overall compensating system for dynamic disturbances.
- Real and reactive power balancing between the lines

In sum, an IPFC is capable of providing a highly effective design for the management of power transmission at a multi-line substation. The derivation presented in the following Section is one of the contributions of this research to the state of power systems analysis by extending the application of the DHD modeling to the IPFC.

4.4.1 Development of the dynamic harmonic domain model of the IPFC

The three-phase voltages and currents on the AC sides of the IPFC are $\mathbf{v}_{ABC1}(t)$, $\mathbf{v}_{abc1}(t)$, $\mathbf{i}_{ABC}(t)$ and $\mathbf{i}_{abc}(t)$, respectively, and can be expressed in terms of the DC-side voltage $v_{dc}(t)$; the DC -side currents $i_1(t)$ and $i_2(t)$, and the switching functions as given in (4.18). Each VSC consists of six switches as shown in Figure A-1, Appendix A. The following state-space equations describe the dynamics of the IPFC:

$$\frac{d\mathbf{v}_{dc}(t)}{dt} = \frac{1}{C}(\mathbf{q}_{s1}(t)\mathbf{i}_{abc}(t) + \mathbf{q}_{s2}(t)\mathbf{i}_{ABC}(t)) \quad (4.38)$$

$$\frac{d\mathbf{i}_{abc}(t)}{dt} = -\frac{R_e}{L_e}\mathbf{i}_{abc}(t) + \frac{1}{L_e}(\mathbf{v}_{abc}(t) - \mathbf{p}_{s1}(t)v_{dc}(t)) \quad (4.39)$$

$$\frac{d\mathbf{i}_{ABC}(t)}{dt} = -\frac{R_e}{L_e}\mathbf{i}_{ABC}(t) + \frac{1}{L_e}(\mathbf{v}_{ABC}(t) - \mathbf{p}_{s2}(t)v_{dc}(t)) \quad (4.40)$$

VSC 1 and VSC 2 are connected in series with the transmission system and the boundary conditions for this controller are

$$\begin{aligned} \mathbf{i}_{abc}(t) &= \mathbf{i}_1(t) & \mathbf{v}_{abc}(t) &= \mathbf{v}_A(t) - \mathbf{v}_B(t) \\ \mathbf{i}_{ABC}(t) &= \mathbf{i}_2(t) & \mathbf{v}_{ABC}(t) &= \mathbf{v}_C(t) - \mathbf{v}_D(t) \end{aligned} \quad (4.41)$$

Substitution of (4.41) into the state equations (4.38), (4.39) and (4.40) of IPFC yields

$$\begin{bmatrix} \frac{d\mathbf{i}_1(t)}{dt} \\ \frac{d\mathbf{i}_2(t)}{dt} \\ \frac{d\mathbf{v}_{dc}(t)}{dt} \end{bmatrix} = \begin{bmatrix} -\frac{R_e}{L_e} & 0 & -\frac{1}{L_e}\mathbf{p}_{S1}(t) \\ 0 & -\frac{R_e}{L_e} & -\frac{1}{L_e}\mathbf{p}_{S2}(t) \\ \frac{1}{C}\mathbf{q}_{S1}(t) & \frac{1}{C}\mathbf{q}_{S2}(t) & 0 \end{bmatrix} \begin{bmatrix} \mathbf{i}_{abc}(t) \\ \mathbf{i}_{ABC}(t) \\ v_{dc}(t) \end{bmatrix} \quad (4.42)$$

$$+ \frac{1}{L_e} \begin{bmatrix} \mathbf{v}_A(t) - \mathbf{v}_B(t) \\ \mathbf{v}_C(t) - \mathbf{v}_D(t) \\ 0 \end{bmatrix}$$

The state-space IPFC model in (4.42) can be transformed into a DHD representation by making use of the procedure presented in Section 3.2. The resulting DHD model is given by

$$\begin{bmatrix} \dot{\mathbf{I}}_1(t) \\ \dot{\mathbf{I}}_2(t) \\ \dot{\mathbf{V}}_{dc}(t) \end{bmatrix} = \begin{bmatrix} -\frac{R_e}{L_e}\mathbf{U}_1 - \mathbf{D}(jm\omega_0) & \mathbf{O}_4 & -\frac{1}{L_e}(\mathbf{P}_{S1}) \\ \mathbf{O}_4 & -\frac{R_e}{L_e}\mathbf{U}_1 - \mathbf{D}(jm\omega_0) & -\frac{1}{L_e}\mathbf{P}_{S2}(t) \\ \frac{1}{C}\mathbf{Q}_{S1}(t) & \frac{1}{C}\mathbf{Q}_{S2}(t) & -\mathbf{D}(jm\omega_0) \end{bmatrix} \quad (4.43)$$

$$\begin{bmatrix} \mathbf{I}_1(t) \\ \mathbf{I}_2(t) \\ \mathbf{V}_{dc}(t) \end{bmatrix} + \frac{1}{L_e} \begin{bmatrix} \mathbf{V}_A(t) - \mathbf{V}_B(t) \\ \mathbf{V}_C(t) - \mathbf{V}_D(t) \\ \mathbf{O} \end{bmatrix}$$

The solution of DHD state equations (4.43) gives complete information about the harmonics in the IPFC, under both steady and dynamic state conditions. This solution of (4.43) can be obtained by setting $\dot{\mathbf{I}}_1(t)$, $\dot{\mathbf{I}}_2(t)$, and $\dot{\mathbf{V}}_{dc}(t)$ to zero, resulting in

$$\begin{bmatrix} \mathbf{I}_1(t) \\ \mathbf{I}_2(t) \\ \mathbf{V}_{dc}(t) \end{bmatrix} = -\mathbf{G}_I(t)^{-1} \frac{1}{L_e} \begin{bmatrix} \mathbf{V}_A(t) - \mathbf{V}_B(t) \\ \mathbf{V}_C(t) - \mathbf{V}_D(t) \\ \mathbf{O} \end{bmatrix} \quad (4.44)$$

where

$$\mathbf{G}_I(t) = \begin{bmatrix} -\frac{R_e}{L_e} \mathbf{U}_1 - \mathbf{D}(jm\omega_0) & \mathbf{O}_4 & -\frac{1}{L_e} (\mathbf{P}_{S1}) \\ \mathbf{O}_4 & -\frac{R_e}{L_e} \mathbf{U}_1 - \mathbf{D}(jm\omega_0) & -\frac{1}{L_e} \mathbf{P}_{S2}(t) \\ \frac{1}{C} \mathbf{Q}_{S1}(t) & \frac{1}{C} \mathbf{Q}_{S2}(t) & -\mathbf{D}(jm\omega_0) \end{bmatrix}$$

and \mathbf{U}_1 is the unit matrix (303×303). \mathbf{O} and \mathbf{O}_4 are the zero matrices with dimensions (101×1) and (303×303) respectively.

The solution of equations (4.44) are used as the initial conditions for solving (4.43) only if inverse of $\mathbf{G}_I(t)$ exists.

4.4.2 Simulation of proposed DHD model of IPFC

A case study, similar to that described for the GUPFC, is considered, with the following changes: Under steady state conditions, the bus per phase voltages V_A , V_B , V_C , and V_D are in per unit at a frequency of 60 Hz,

$$\begin{aligned}
v_{Aa}(t) &= 1.5 \sin \omega_0 t & v_{Ba}(t) &= \sin \omega_0 t \\
v_{Ab}(t) &= 1.5 \sin(\omega_0 t - 120^\circ) & v_{Bb}(t) &= \sin(\omega_0 t - 120^\circ) \\
v_{Ac}(t) &= 1.5 \sin(\omega_0 t + 120^\circ) & v_{Bc}(t) &= \sin(\omega_0 t + 120^\circ) \\
v_{Ca}(t) &= 1.4 \sin \omega_0 t & v_{Da}(t) &= \sin \omega_0 t \\
v_{Cb}(t) &= 1.4 \sin(\omega_0 t - 120^\circ) & v_{Db}(t) &= \sin(\omega_0 t - 120^\circ) \\
v_{Cc}(t) &= 1.4 \sin(\omega_0 t + 120^\circ) & v_{Dc}(t) &= \sin(\omega_0 t + 120^\circ)
\end{aligned} \tag{4.45}$$

A disturbance of 50% at the phase a of the bus-B is assumed, starting at 0.08 seconds and lasting for 0.04 seconds. This simulation starts at $t_0=0$ seconds and ends at the final time $t_f=0.2$ seconds and an integration time step 0.2 ms. For accuracy, 50 harmonics were considered. The simulations are performed using MATLAB[®] software.

The control system shown in Figure 24 is again used to maintain constant DC-side voltage across the capacitor in the IPFC dynamic model. Figure 60 shows the harmonic content of the DC voltage, without and with control system during the disturbance. These results are obtained with a controller, using a time constant (T) of 0.001 seconds and a gain (K) of 5. Due to the unbalanced nature of the disturbance, non-characteristic harmonics are present in the system.

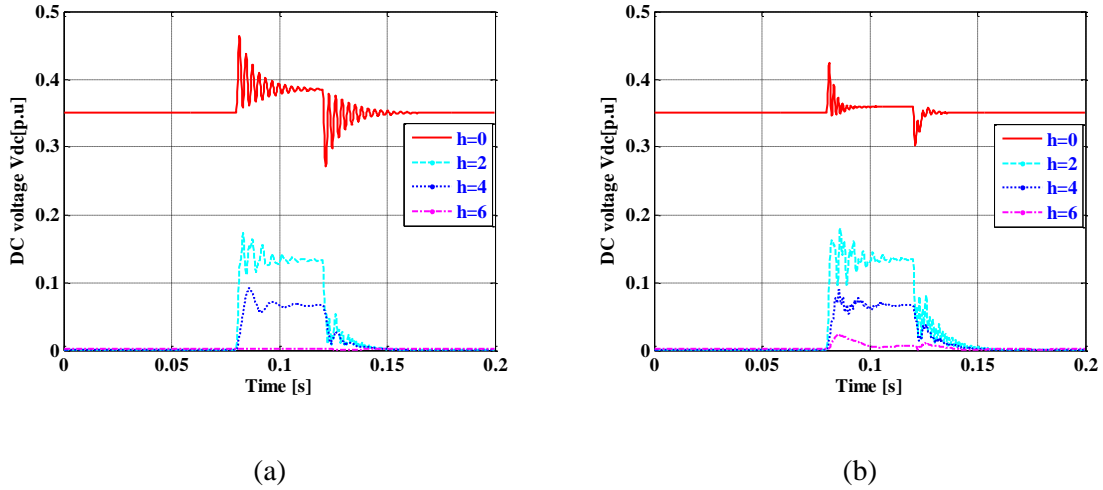


Figure 60: DC-side voltage of IPFC (a) Without control system (b) With control system

The DC component of the voltage on the DC side of the capacitor increases by 25% of its steady state value, as shown in Figure 60(a). These results clearly demonstrate that during the disturbance the control system does decrease the distortion of the DC component of the voltage on the DC side. They actually show that it is very close to its steady state value while the remaining harmonic voltages have not changed. However, there is a change in the 6th harmonic voltage with the control, but this can also be eliminated by proper gain and time constant values.

Keeping the DC voltage constant during the disturbance further helped to minimize some of the power quality indices, at the terminals of the IPFC, such as the THD in the output currents of VSC 1, presented in Figure 61. This is due to the fact that keeping the DC side voltage close to its steady state value during the disturbance interval causes increase in fundamental component of per-phase output currents of VSC 1, which further leads to the reduction in the THD of those currents.

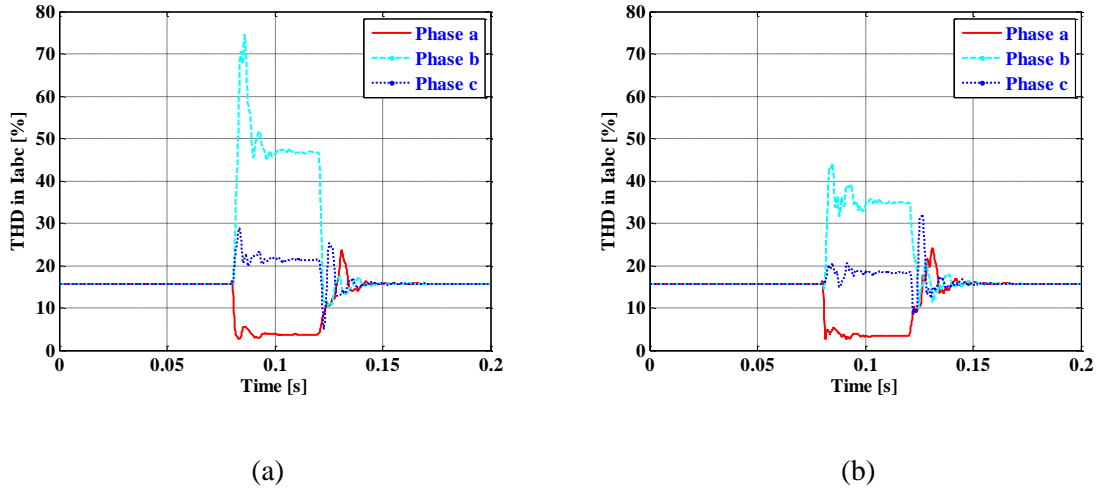


Figure 61: The THD in the output currents of VSC 1 (a) Without control system (b) With control system

The time plots of output currents of VSC 1 and VSC 2 of phase a , over the steady state and disturbance intervals, depicting the actual voltage waveforms, are shown in Figure 62(a) and Figure 63(a), respectively. These plots are derived from the harmonic domain information of the corresponding current and voltage. They exhibit more distortions during the disturbance than when in normal period. This is due to the fact that VSC 1 is connected between the buses A and B and the voltage that appears across its terminals is the difference between the voltages at those buses. This difference is increased by 50% of its steady state value at phase a of VSC 1, during the disturbance interval. This leads to an increase in the output current at phase a of VSC 1. The individual magnitudes of the most dominant harmonics of these are shown in Figure 62(b), and Figure 63(b), respectively. It is observed that the output voltage of VSC 1 of phase a is reduced by a considerable magnitude. This is because the increase in the output

current at phase a of VSC 1 causes a larger drop at its terminals thus leading to a decrease in the voltage of the same during the disturbance period.

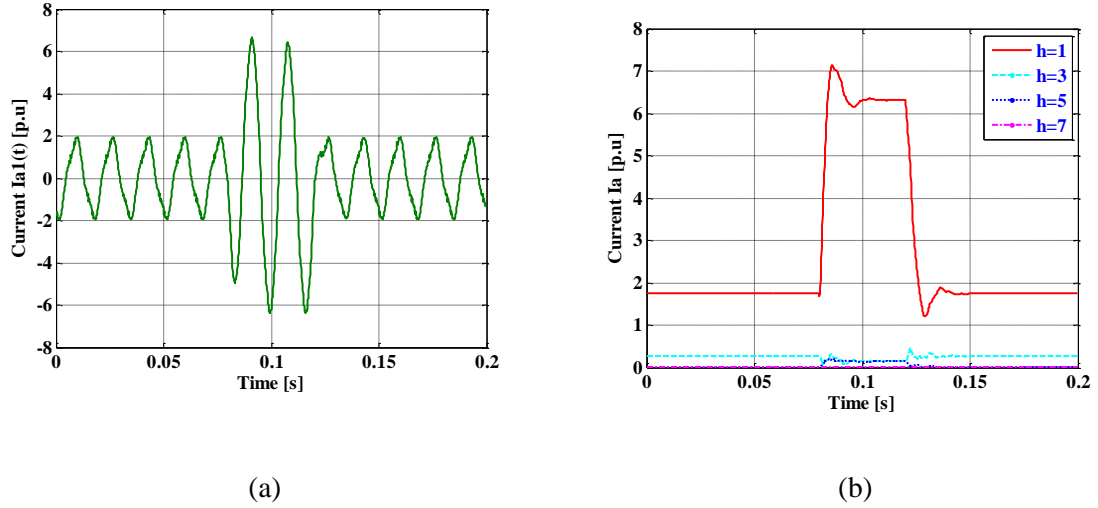


Figure 62: The output current of phase a of VSC 1 (a) Current waveform (b) Current harmonic content

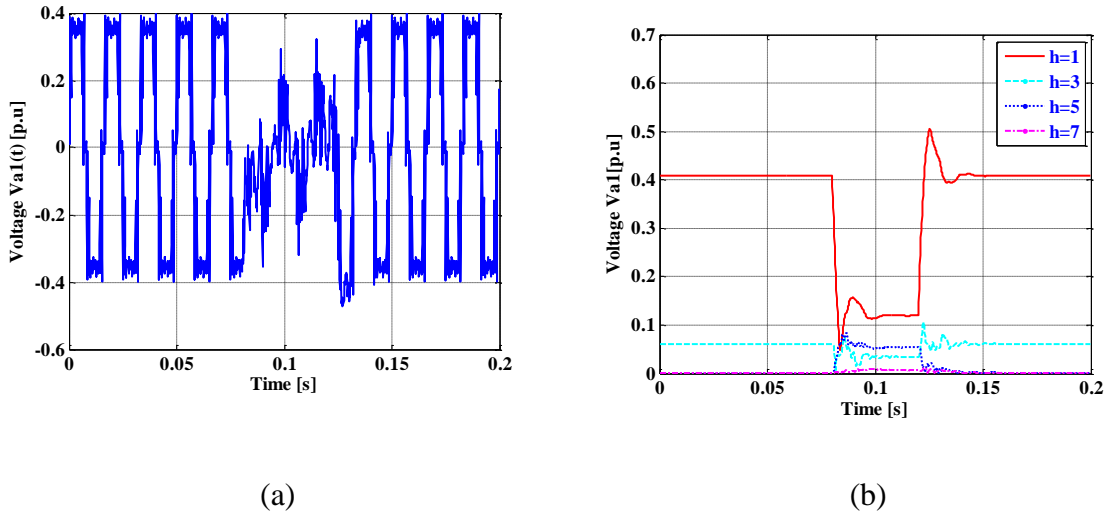


Figure 63: The output voltage of phase a of VSC 1 (a) Voltage waveform (b) Voltage harmonic content

The time domain waveforms of voltages and currents of phase a of VSC 2 are shown in Figure 64(a) and Figure 65(a), respectively. The harmonic components of output voltage and current of VSC 2 of phase a are presented in Figure 64(b) and Figure 65(b), respectively. Although the VSC 2 terminals are not connected to the bus, where the voltage has changed during the disturbance period, the increase in the DC side voltage during that interval causes an increase in the fundamental component of the phase a voltage of VSC 2. The drop in the fundamental component of output current of phase a of VSC 2 is due to the change in the DC side voltage.

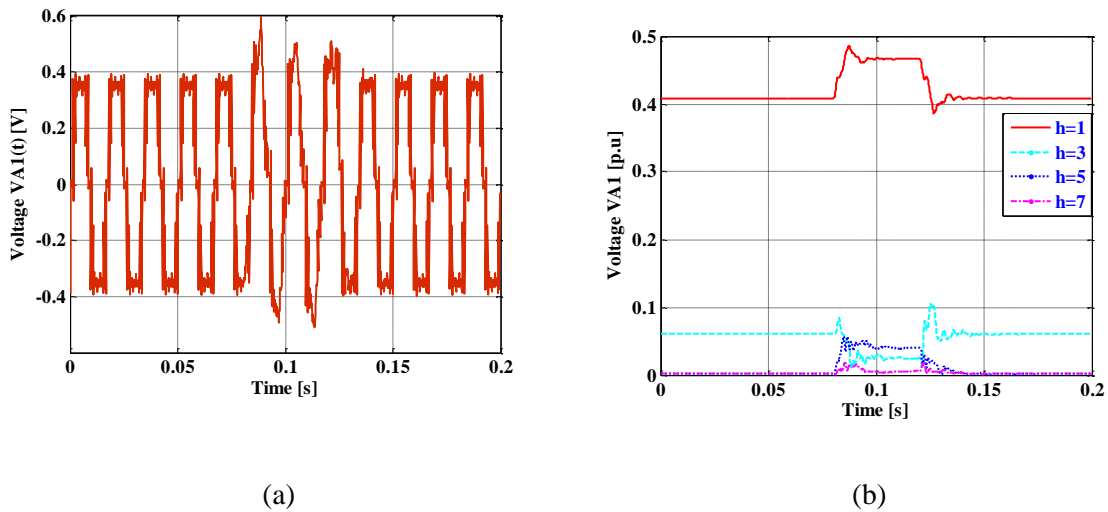


Figure 64: The output voltage of phase a of VSC 2 (a) Voltage waveform (b) Voltage harmonic content

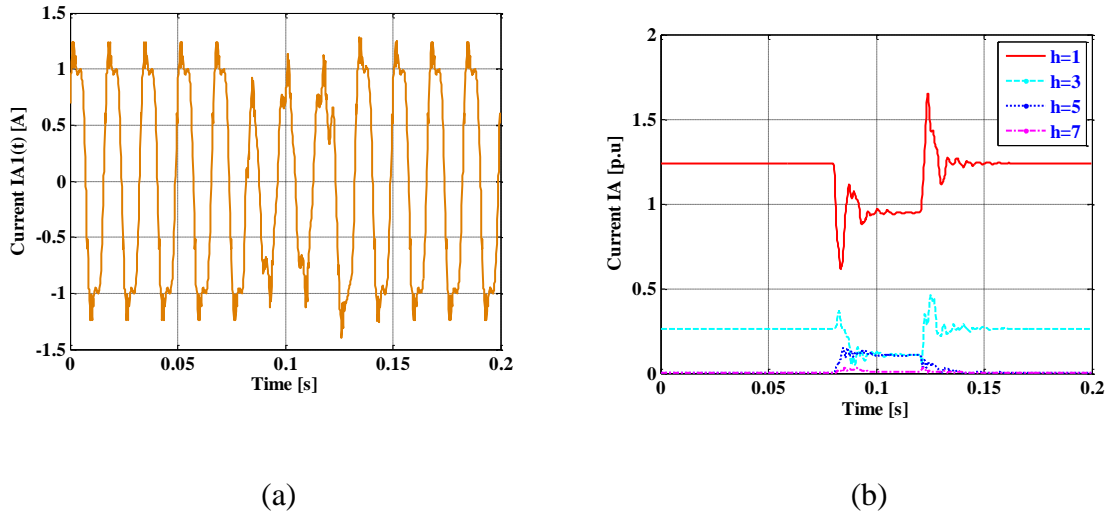


Figure 65: The output current of phase a of VSC 2 (a) Current waveform (b) Current harmonic content

During a disturbance, the output voltages of the two VSCs of the DHD model of the IPFC register significant change in their harmonic response. It may be important to reemphasize that it is nearly impossible to deduce this information from time domain simulations. The sensitive characteristic of the harmonics is useful to determine several power quality indices. Some of these indices such as the RMS values of per-phase output currents and voltages, and per-phase output apparent powers of VSC 1 are shown in Figure 66. The per-phase RMS output currents increased because of a raise in the output voltage of phase a of VSC 1. This increase causes a larger drop in the impedance of a line connected to VSC 1, which further reduces phase a output voltage. The variation of per-phase output apparent power is due to the mutual effects of per-phase output voltages and currents of VSC 1. The variation in per-phase output currents of VSC 2 is due to the change in the DC side voltage during the disturbance interval.

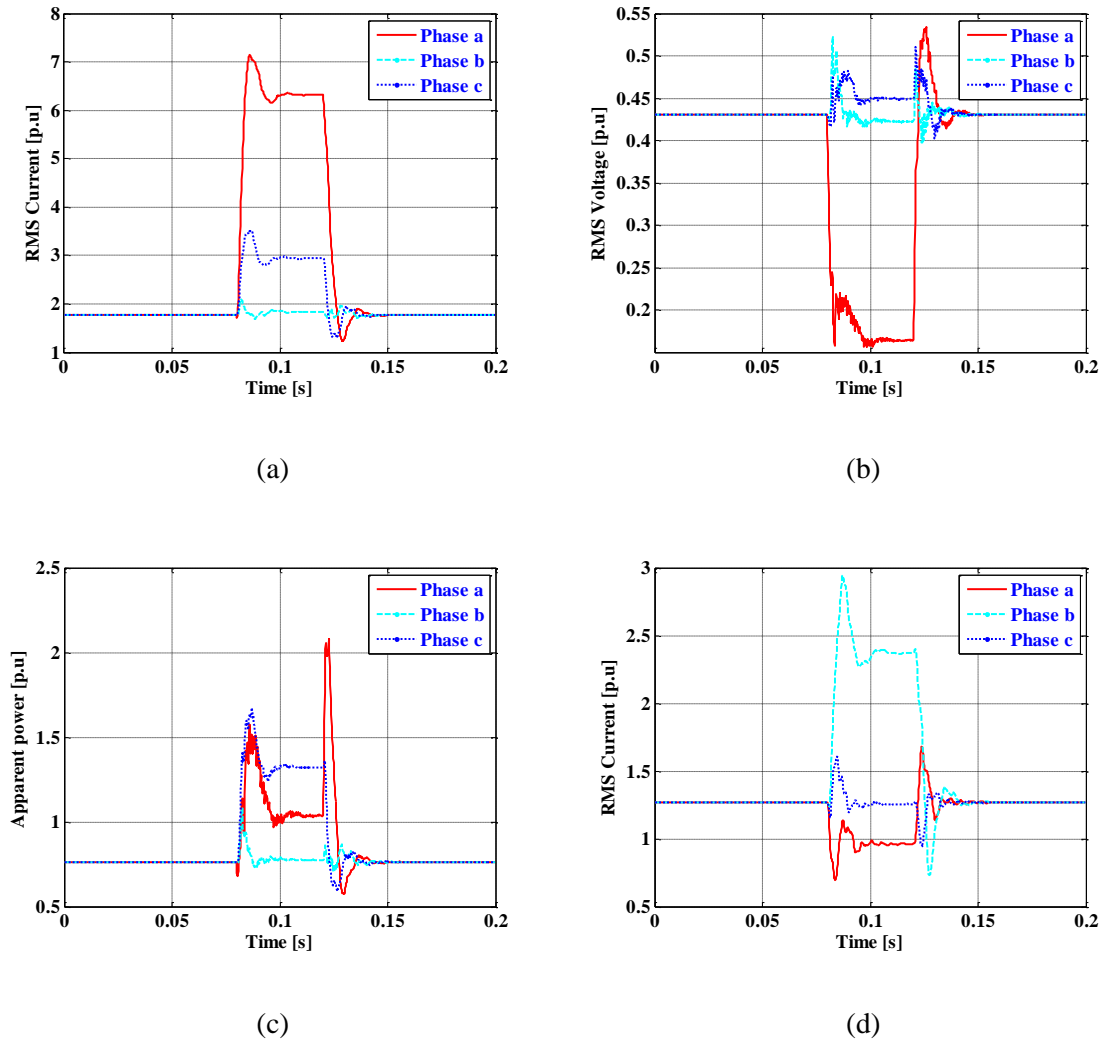
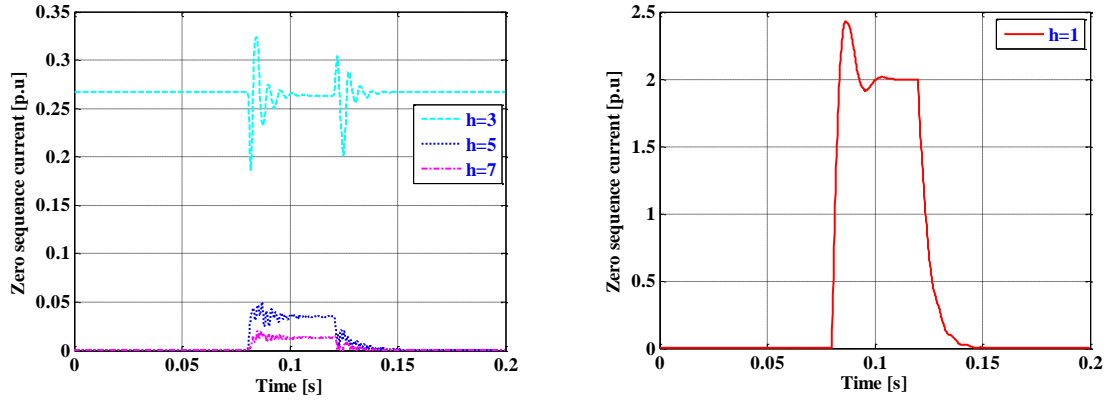


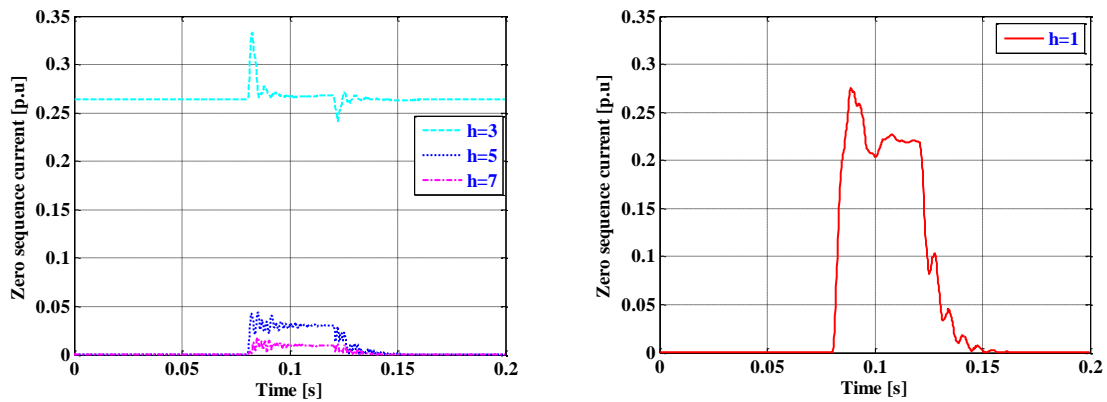
Figure 66: Power quality indices (a) RMS values of the output currents of VSC 1 (b) RMS values of the output voltages of VSC 1 (c) Per-phase output apparent powers of VSC 1 (d) RMS values of the output currents of VSC 2

The harmonic components of zero sequence currents of VSC 1 and VSC 2 are shown in Figure 67. Here, it can be observed that the 3rd harmonic component alone is present during steady state while all the odd harmonic currents, including the 3rd, are present during the disturbance (for clarity the fundamental harmonic component plot is shown separately from the others in (a) and (b)). This phenomenon, and all the remaining

ones addressed below, are expected as predicted by the mathematical analysis presented in Section 3.5.



(a)

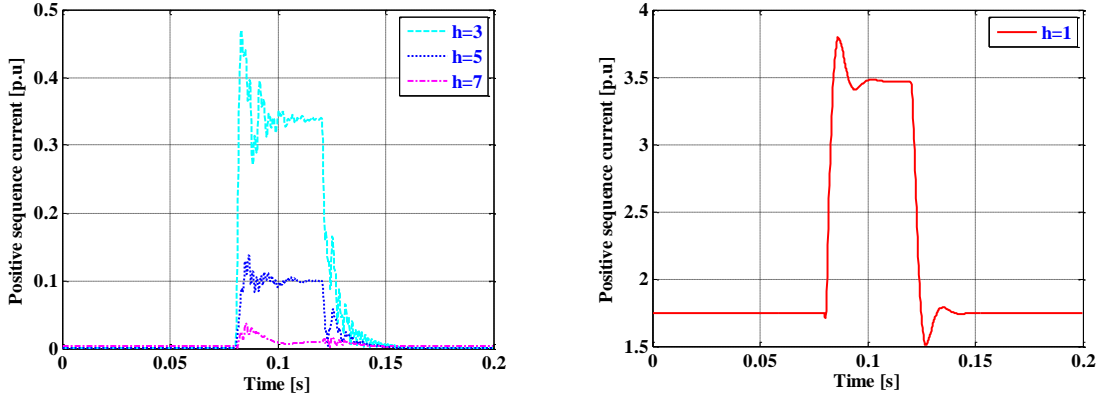


(b)

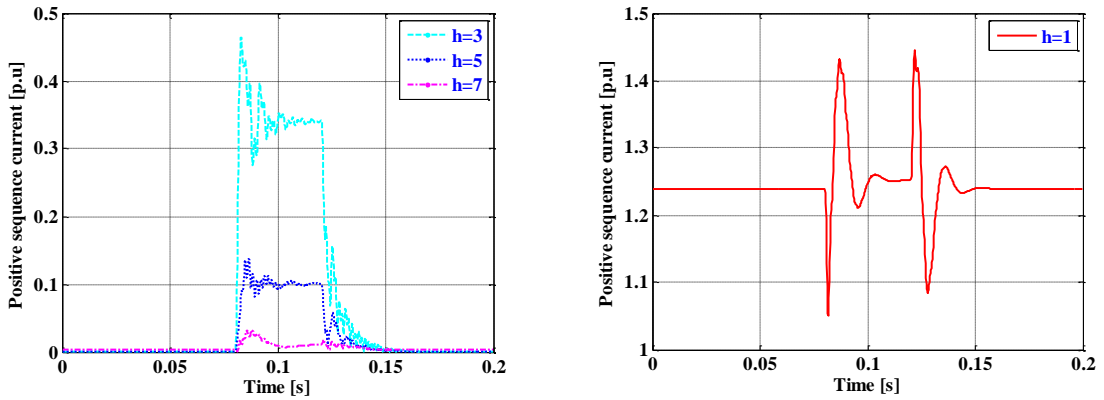
Figure 67: The zero sequence currents of (a) VSC 1 (b) VSC 2

The harmonic content of the positive sequence currents of VSC 1 and VSC 2 are shown in Figure 68. From these plots it is observed that the fundamental and the 7th harmonics are present during the steady state (the fundamental shown separately from

others in Figure 68(b)), and all the odd harmonic currents are present during the disturbance interval.



(a)

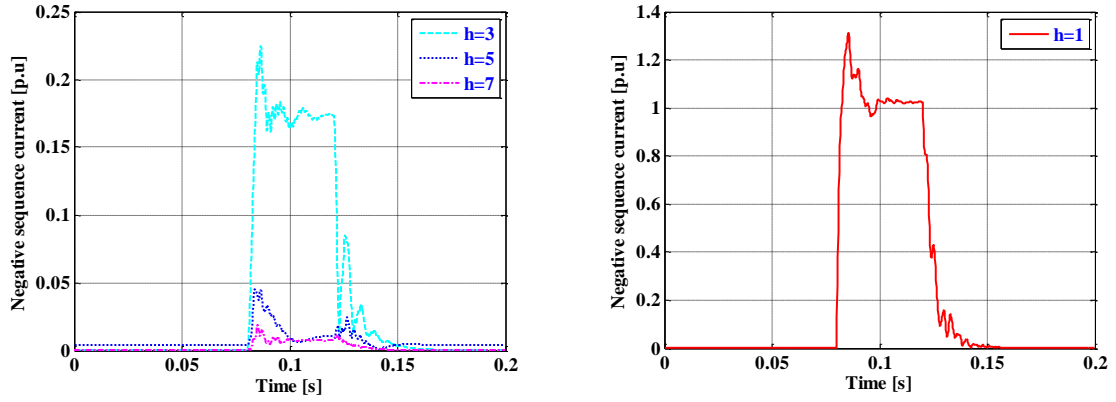


(b)

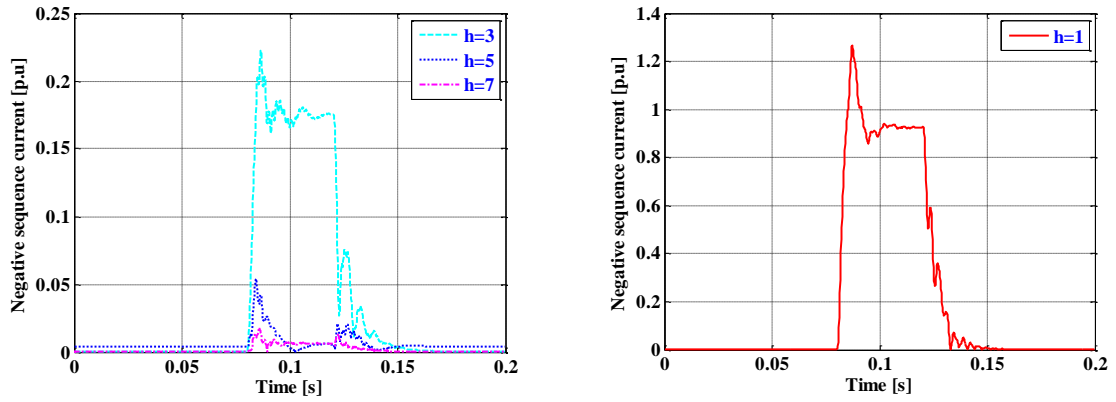
Figure 68: The positive sequence currents of (a) VSC 1 (b) VSC 2

The harmonic content of negative sequence currents of VSC 1 and VSC 2 are shown in Figure 69. These plots clearly show that only the 5th harmonic component, albeit small, is present during the steady state and that all the odd harmonics are present

during the disturbance. A detailed explanation regarding the sequence currents is given in Section 3.5.



(a)

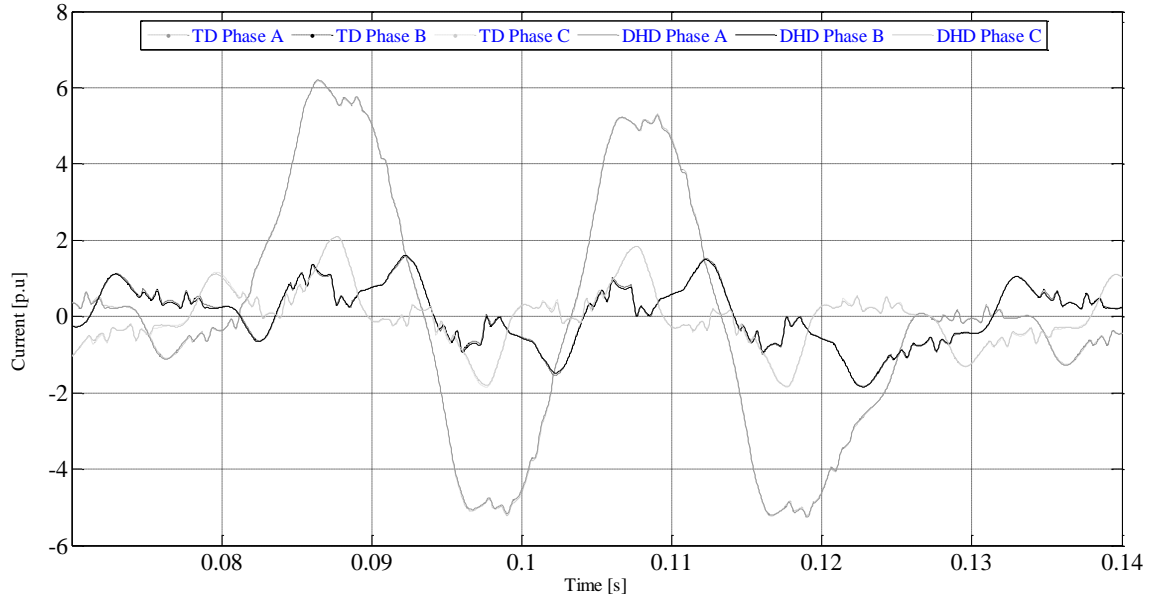


(b)

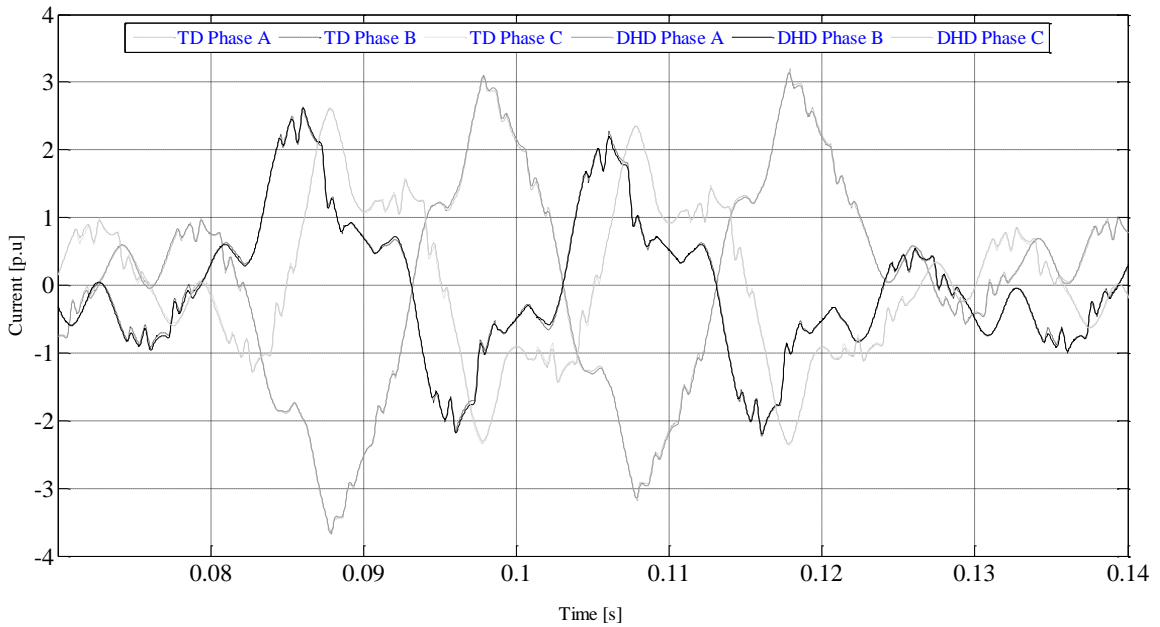
Figure 69: The negative sequence currents of (a) VSC 1 (b) VSC 2

4.4.3 Validation of the proposed DHD model of the IPFC

The validation method discussed in Section 3.6.3 is applied to the output currents of VSC 1, and the resulting time domain waveforms of the three-phases are shown in Figure 70(a). The plots of these currents show that they are indiscernible. The same procedure is repeated for VSC 2 and the results are shown in Figure 70(b), with the same conclusion. This allows the deduction that the proposed IPFC DHD model has been validated.



(a)



(b)

Figure 70: Time domain waveforms of currents of each phase of (a) VSC 1 and (b) VSC 2

4.5 Generalized interline power flow controller

The GIPFC consists of four VSCs [46]–[48], as shown in Figure 71. It is configured with one converter connected in shunt and the other three in series with three independent transmission lines. The shunt controller in the GIPFC injects three-phase currents and the series controllers inject three-phase voltages into the AC system.

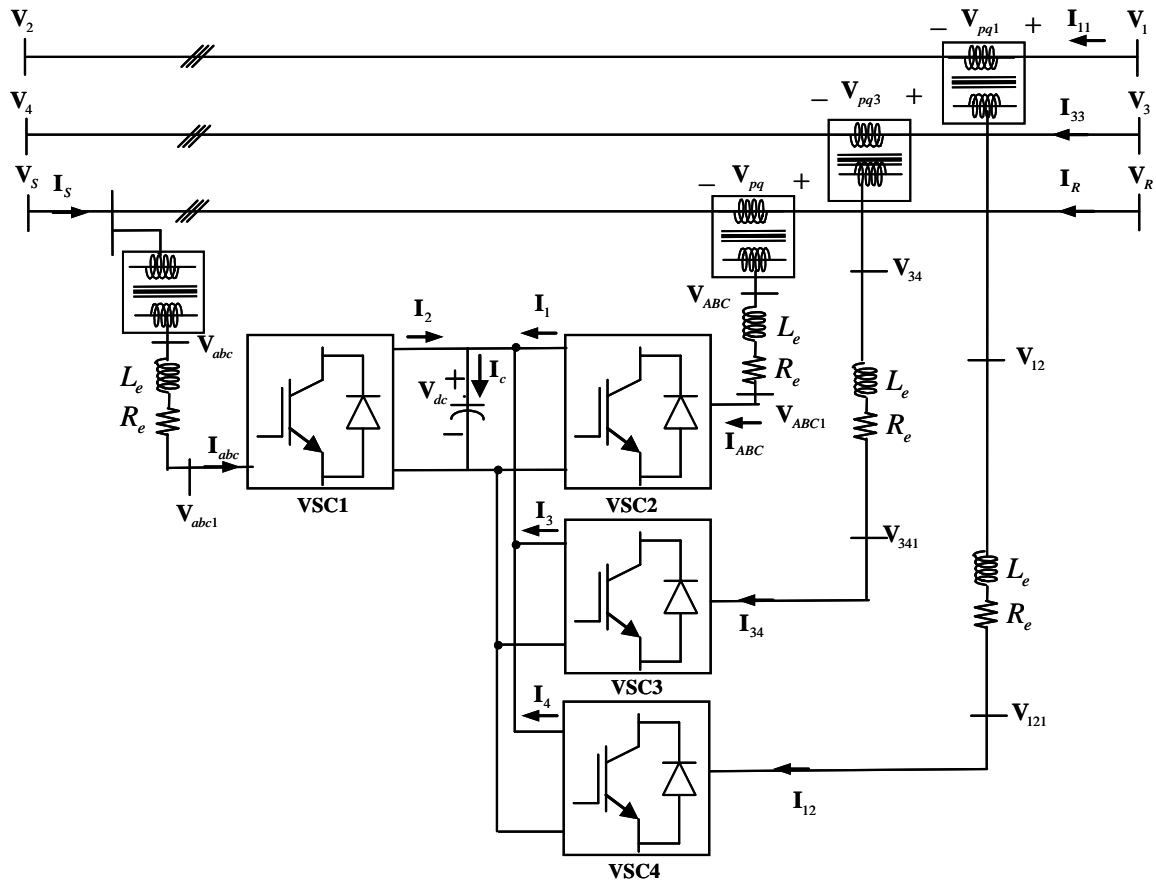


Figure 71: Generalized interline power flow controller

These converters are operated by a common DC link, a storage capacitor, and are connected back-to-back, which helps to provide real power transfer. The GIPFC allows the injection of a controllable series voltage simultaneously on each line, thus facilitating

the control of power transfer in each one of them. It also controls the magnitude and phase angle of the series voltage that it injects into each line. This is an advantage to its configuration as it becomes capable of independently controlling different power levels at each transmission line. In the following Section, the development of the proposed GIPFC HD model is presented.

4.5.1 Development of the harmonic domain model of the GIPFC

In the GIPFC- VSC 2, VSC 3 and VSC 4 are connected in series and VSC 1 in shunt, shown in Figure 71. The equations of the voltage source converters 1, 2 and 3 are the same as (4.1), (4.3) and (4.5) , respectively. The voltage equations for VSC 4 are

$$\begin{aligned} \mathbf{V}_{12} &= \left(\mathbf{Z}_e + \mathbf{P}_{s4} \mathbf{Z}_{\text{cap}} \mathbf{Q}_{s4} \right) \mathbf{I}_{12} - \mathbf{P}_{s4} \mathbf{Z}_{\text{cap}} \mathbf{I}_{dc} + \mathbf{P}_{s4} \mathbf{V}_0 \\ \mathbf{V}_{dc} &= \mathbf{Z}_{\text{cap}} \mathbf{Q}_{s4} \mathbf{I}_{12} - \mathbf{Z}_{\text{cap}} \mathbf{I}_{dc} + \mathbf{V}_0 \end{aligned} \quad (4.46)$$

Solving (4.1), (4.3), (4.5) and (4.46) yields

$$\mathbf{V}_{abc} = \left(\mathbf{Z}_e + \frac{\mathbf{P}_{s1} \mathbf{Z}_{\text{cap}} \mathbf{Q}_{s1}}{2} \right) \mathbf{I}_{abc} + \frac{\mathbf{P}_{s1} \mathbf{Z}_{\text{cap}} \mathbf{Q}_{s2}}{2} \mathbf{I}_{ABC} + \mathbf{P}_{s1} \mathbf{V}_0 \quad (4.47)$$

$$\mathbf{V}_{ABC} = \left(\mathbf{Z}_e + \frac{\mathbf{P}_{s2} \mathbf{Z}_{\text{cap}} \mathbf{Q}_{s2}}{2} \right) \mathbf{I}_{ABC} + \frac{\mathbf{P}_{s2} \mathbf{Z}_{\text{cap}} \mathbf{Q}_{s1}}{2} \mathbf{I}_{abc} + \mathbf{P}_{s2} \mathbf{V}_0 \quad (4.48)$$

$$\mathbf{V}_{34} = \left(\mathbf{Z}_e + \frac{\mathbf{P}_{s3} \mathbf{Z}_{\text{cap}} \mathbf{Q}_{s3}}{2} \right) \mathbf{I}_{34} + \frac{\mathbf{P}_{s3} \mathbf{Z}_{\text{cap}} \mathbf{Q}_{s1}}{2} \mathbf{I}_{abc} + \mathbf{P}_{s3} \mathbf{V}_0 \quad (4.49)$$

$$\mathbf{V}_{12} = \left(\mathbf{Z}_e + \frac{\mathbf{P}_{s4} \mathbf{Z}_{\text{cap}} \mathbf{Q}_{s4}}{2} \right) \mathbf{I}_{12} + \frac{\mathbf{P}_{s4} \mathbf{Z}_{\text{cap}} \mathbf{Q}_{s1}}{2} \mathbf{I}_{abc} + \mathbf{P}_{s4} \mathbf{V}_0 \quad (4.50)$$

The boundary conditions are

$$\begin{aligned} \mathbf{I}_{ABC} &= \mathbf{I}_R & \mathbf{I}_{34} &= \mathbf{I}_{33} \\ \mathbf{I}_{abc} &= \mathbf{I}_S + \mathbf{I}_R & \mathbf{I}_{12} &= \mathbf{I}_{11} \end{aligned} \quad (4.51)$$

$$\begin{aligned} \mathbf{V}_{ABC} &= \mathbf{V}_R - \mathbf{V}_S & \mathbf{V}_{12} &= \mathbf{V}_1 - \mathbf{V}_2 \\ \mathbf{V}_{34} &= \mathbf{V}_3 - \mathbf{V}_4 & \mathbf{V}_{abc} &= \mathbf{V}_S \end{aligned} \quad (4.52)$$

Substitution of (4.51) and (4.52) into equations from (4.47) to (4.50) yields

$$\begin{bmatrix} \mathbf{V}_R \\ \mathbf{V}_S \\ \mathbf{V}_3 - \mathbf{V}_4 \\ \mathbf{V}_1 - \mathbf{V}_2 \end{bmatrix} = \begin{bmatrix} \mathbf{A}_1 & \mathbf{A}_2 & \mathbf{A}_3 & \mathbf{A}_4 \\ \mathbf{B}_1 & \mathbf{B}_2 & \mathbf{B}_3 & \mathbf{B}_4 \\ \mathbf{C}_1 & \mathbf{C}_2 & \mathbf{C}_3 & \mathbf{C}_4 \\ \mathbf{D}_1 & \mathbf{D}_2 & \mathbf{D}_3 & \mathbf{D}_4 \end{bmatrix} \begin{bmatrix} \mathbf{I}_R \\ \mathbf{I}_S \\ \mathbf{I}_{33} \\ \mathbf{I}_{11} \end{bmatrix} + \begin{bmatrix} \mathbf{P}_{S1} + \mathbf{P}_{S2} \\ \mathbf{P}_{S1} \\ \mathbf{P}_{S3} \\ \mathbf{P}_{S4} \end{bmatrix} \mathbf{V}_0 \quad (4.53)$$

The set of equations (4.53) constitutes the HD model of the GIPFC where

$$\begin{aligned} \mathbf{A}_1 &= 2\mathbf{Z}_e + \frac{(\mathbf{P}_{s1} + \mathbf{P}_{s2})}{2} \mathbf{Z}_{\text{cap}} \frac{(\mathbf{Q}_{s1} + \mathbf{Q}_{s2})}{2} & \mathbf{A}_3 &= \mathbf{B}_3 = 0 \\ \mathbf{A}_2 &= \mathbf{Z}_e + \mathbf{Z}_{\text{cap}} \mathbf{Q}_{s1} \frac{(\mathbf{P}_{s1} + \mathbf{P}_{s2})}{2} & \mathbf{B}_2 &= \mathbf{Z}_e + \frac{\mathbf{P}_{s1} \mathbf{Z}_{\text{cap}} \mathbf{Q}_{s1}}{2} \\ \mathbf{B}_1 &= \mathbf{Z}_e + \mathbf{P}_{s1} \mathbf{Z}_{\text{cap}} \frac{(\mathbf{Q}_{s1} + \mathbf{Q}_{s2})}{2} & \mathbf{A}_4 &= \mathbf{B}_4 = 0 \end{aligned} \quad (4.54)$$

$$\begin{aligned}
\mathbf{D}_1 &= \frac{\mathbf{P}_{s4} \mathbf{Z}_{\text{cap}} \mathbf{Q}_{s1}}{2} & \mathbf{C}_1 &= \frac{\mathbf{P}_{s3} \mathbf{Z}_{\text{cap}} \mathbf{Q}_{s1}}{2} \\
\mathbf{D}_2 &= \frac{\mathbf{P}_{s4} \mathbf{Z}_{\text{cap}} \mathbf{Q}_{s1}}{2} & \mathbf{C}_2 &= \frac{\mathbf{P}_{s3} \mathbf{Z}_{\text{cap}} \mathbf{Q}_{s1}}{2} \\
\mathbf{D}_3 &= 0 & \mathbf{C}_3 &= \mathbf{Z}_e + \frac{\mathbf{P}_{s3} \mathbf{Z}_{\text{cap}} \mathbf{Q}_{s3}}{2} \\
\mathbf{D}_4 &= \mathbf{Z}_e + \frac{\mathbf{P}_{s4} \mathbf{Z}_{\text{cap}} \mathbf{Q}_{s4}}{2} & \mathbf{C}_4 &= 0
\end{aligned} \tag{4.55}$$

Under different operating conditions, the HD model that is presented in (4.53) helps to obtain the harmonic response of this controller and also in furthering resonance studies. In the following Section, the proposed DHD model for the GIPFC is developed.

4.5.2 Development of the dynamic harmonic domain model of the GIPFC

Notation wise, the three-phase voltages and currents on the AC side of the GIPFC are $\mathbf{v}_{abc1}(t)$, $\mathbf{v}_{ABC1}(t)$, $\mathbf{v}_{341}(t)$, $\mathbf{v}_{121}(t)$, $\mathbf{i}_{abc}(t)$, $\mathbf{i}_{ABC}(t)$, $\mathbf{i}_{34}(t)$ and $\mathbf{i}_{12}(t)$, respectively, and can be expressed in terms of DC-side voltage $\mathbf{v}_{dc}(t)$, DC-side current $i_1(t)$, $i_2(t)$, $i_3(t)$, $i_4(t)$ and the switching functions as

$$\begin{aligned}
\mathbf{v}_{abc1}(t) &= \mathbf{p}_{s1}(t) \mathbf{v}_{dc}(t) & i_1(t) &= \mathbf{q}_{s1}(t) \mathbf{i}_{abc}(t) \\
\mathbf{v}_{ABC1}(t) &= \mathbf{p}_{s2}(t) \mathbf{v}_{dc}(t) & i_2(t) &= \mathbf{q}_{s2}(t) \mathbf{i}_{ABC}(t) \\
\mathbf{v}_{341}(t) &= \mathbf{p}_{s3}(t) \mathbf{v}_{dc}(t) & i_3(t) &= \mathbf{q}_{s3}(t) \mathbf{i}_{34}(t) \\
\mathbf{v}_{121}(t) &= \mathbf{p}_{s4}(t) \mathbf{v}_{dc}(t) & i_4(t) &= \mathbf{q}_{s4}(t) \mathbf{i}_{12}(t)
\end{aligned} \tag{4.56}$$

where $\mathbf{p}_{s1}(t)$, $\mathbf{p}_{s2}(t)$, $\mathbf{p}_{s3}(t)$, $\mathbf{q}_{s1}(t)$, $\mathbf{q}_{s2}(t)$ and $\mathbf{q}_{s3}(t)$ are transformation vectors [10],

which are given in (4.18):

The following state equations describe the dynamics of the GIPFC:

$$\frac{d v_{dc}(t)}{dt} = \frac{1}{C} (\mathbf{q}_{s1}(t) \mathbf{i}_{abc}(t) + \mathbf{q}_{s2}(t) \mathbf{i}_{ABC}(t) + \mathbf{q}_{s3}(t) \mathbf{i}_{34}(t)) \quad (4.57)$$

$$\frac{d \mathbf{i}_{abc}(t)}{dt} = -\frac{R_e}{L_e} \mathbf{i}_{abc}(t) + \frac{1}{L_e} (\mathbf{v}_{abc}(t) - \mathbf{p}_{s1}(t) v_{dc}(t)) \quad (4.58)$$

$$\frac{d \mathbf{i}_{ABC}(t)}{dt} = -\frac{R_e}{L_e} \mathbf{i}_{ABC}(t) + \frac{1}{L_e} (\mathbf{v}_{ABC}(t) - \mathbf{p}_{s2}(t) v_{dc}(t)) \quad (4.59)$$

$$\frac{d \mathbf{i}_{34}(t)}{dt} = -\frac{R_e}{L_e} \mathbf{i}_{34}(t) + \frac{1}{L_e} (\mathbf{v}_{34}(t) - \mathbf{p}_{s3}(t) v_{dc}(t)) \quad (4.60)$$

$$\frac{d \mathbf{i}_{12}(t)}{dt} = -\frac{R_e}{L_e} \mathbf{i}_{12}(t) + \frac{1}{L_e} (\mathbf{v}_{12}(t) - \mathbf{p}_{s4}(t) v_{dc}(t)) \quad (4.61)$$

The boundary conditions are

$$\begin{aligned} \mathbf{i}_{abc}(t) &= \mathbf{i}_R(t) + \mathbf{i}_S(t) & \mathbf{v}_{abc}(t) &= \mathbf{v}_S(t) \\ \mathbf{i}_{ABC}(t) &= \mathbf{i}_R(t) & \mathbf{v}_{ABC}(t) &= \mathbf{v}_R(t) - \mathbf{v}_S(t) \\ \mathbf{i}_{34}(t) &= \mathbf{i}_{33}(t) & \mathbf{v}_{34}(t) &= \mathbf{v}_3(t) - \mathbf{v}_4(t) \\ \mathbf{i}_{12}(t) &= \mathbf{i}_{11}(t) & \mathbf{v}_{12}(t) &= \mathbf{v}_1(t) - \mathbf{v}_2(t) \end{aligned} \quad (4.62)$$

Substitution of above (4.62) in (4.57)- (4.61), yields

$$\frac{d v_{dc}(t)}{dt} = \frac{1}{C} \left(\mathbf{q}_{s1}(t) \mathbf{i}_S(t) + (\mathbf{q}_{s1}(t) + \mathbf{q}_{s2}(t)) \mathbf{i}_R(t) + \mathbf{q}_{s3}(t) \mathbf{i}_{33}(t) + \mathbf{q}_{s4}(t) \mathbf{i}_{11}(t) \right) \quad (4.63)$$

$$\frac{d (\mathbf{i}_R(t) + \mathbf{i}_S(t))}{dt} = -\frac{R_e}{L_e} (\mathbf{i}_R(t) + \mathbf{i}_S(t)) + \frac{1}{L_e} (\mathbf{v}_S(t) - \mathbf{p}_{s1}(t) v_{dc}(t)) \quad (4.64)$$

$$\frac{d \mathbf{i}_R(t)}{dt} = -\frac{R_e}{L_e} \mathbf{i}_R(t) + \frac{1}{L_e} (\mathbf{v}_R(t) - \mathbf{v}_S(t) - \mathbf{p}_{s2}(t) v_{dc}(t)) \quad (4.65)$$

$$\frac{d\mathbf{i}_{33}(t)}{dt} = -\frac{R_e}{L_e}\mathbf{i}_{33}(t) + \frac{1}{L_e}(\mathbf{v}_{34}(t) - \mathbf{p}_{s3}(t)v_{dc}(t)) \quad (4.66)$$

$$\frac{d\mathbf{i}_{12}(t)}{dt} = -\frac{R_e}{L_e}\mathbf{i}_{11}(t) + \frac{1}{L_e}(\mathbf{v}_{12}(t) - \mathbf{p}_{s4}(t)v_{dc}(t)) \quad (4.67)$$

Substituting (4.30) into (4.29) gives

$$\frac{d\mathbf{i}_s(t)}{dt} = -\frac{R_e}{L_e}\mathbf{i}_s(t) + \frac{2\mathbf{v}_s(t)}{L_e} - \frac{\mathbf{v}_R(t)}{L_e} + \frac{v_{dc}(t)}{L_e}(\mathbf{p}_{s2}(t) - \mathbf{p}_{s1}(t)) \quad (4.68)$$

The state-space equations(4.28), (4.30), (4.31) and (4.32) of the GIPFC are

$$\begin{bmatrix} \frac{d\mathbf{i}_R(t)}{dt} \\ \frac{d\mathbf{i}_s(t)}{dt} \\ \frac{d\mathbf{i}_{33}(t)}{dt} \\ \frac{d\mathbf{i}_{11}(t)}{dt} \\ \frac{dv_{dc}(t)}{dt} \end{bmatrix} = \begin{bmatrix} -\frac{R_e}{L_e} & 0 & 0 & 0 & -\frac{\mathbf{p}_{s2}(t)}{L_e} \\ 0 & -\frac{R_e}{L_e} & 0 & 0 & -\left(\frac{\mathbf{p}_{s1}(t) - \mathbf{p}_{s2}(t)}{L_e}\right) \\ 0 & 0 & -\frac{R_e}{L_e} & 0 & -\frac{\mathbf{p}_{s3}(t)}{L_e} \\ 0 & 0 & 0 & -\frac{R_e}{L_e} & -\frac{\mathbf{p}_{s4}(t)}{L_e} \\ \frac{\mathbf{q}_{s1}(t) + \mathbf{q}_{s2}(t)}{C} & \frac{\mathbf{q}_{s1}(t)}{C} & \frac{\mathbf{q}_{s3}(t)}{C} & \frac{\mathbf{q}_{s4}(t)}{C} & 0 \end{bmatrix} \begin{bmatrix} \mathbf{i}_R(t) \\ \mathbf{i}_s(t) \\ \mathbf{i}_{33}(t) \\ \mathbf{i}_{11}(t) \\ v_{dc}(t) \end{bmatrix} + \begin{bmatrix} 1 & -1 & 0 & 0 & 0 \\ -1 & 2 & 0 & 0 & 0 \\ 0 & 0 & 1 & 0 & 0 \\ 0 & 0 & 0 & 1 & 0 \\ 0 & 0 & 0 & 0 & 0 \end{bmatrix} \begin{bmatrix} \mathbf{v}_R(t) \\ \mathbf{v}_s(t) \\ \mathbf{v}_{34}(t) \\ \mathbf{v}_{12}(t) \\ v_{dc}(t) \end{bmatrix} \quad (4.69)$$

The state-space model in (4.69) can be transformed into a DHD representation by making use of the procedure described in Section 3.2. The resulting DHD model of the GIPFC is

$$\begin{bmatrix} \dot{\mathbf{I}}_R(t) \\ \dot{\mathbf{I}}_S(t) \\ \dot{\mathbf{I}}_{33}(t) \\ \dot{\mathbf{I}}_{11}(t) \\ \dot{\mathbf{V}}_{dc}(t) \end{bmatrix} = [\mathbf{G}_1(t) \ \mathbf{G}_2(t)] \begin{bmatrix} \mathbf{I}_R(t) \\ \mathbf{I}_S(t) \\ \mathbf{I}_{33}(t) \\ \mathbf{I}_{11}(t) \\ \mathbf{V}_{dc}(t) \end{bmatrix} + \frac{1}{L_e} \begin{bmatrix} \mathbf{U}_1 & -\mathbf{U}_1 & \mathbf{O}_4 & \mathbf{O}_4 & \mathbf{O}_2 \\ -\mathbf{U}_1 & 2\mathbf{U}_1 & \mathbf{O}_4 & \mathbf{O}_4 & \mathbf{O}_2 \\ \mathbf{O}_4 & \mathbf{O}_4 & \mathbf{U}_1 & \mathbf{O}_4 & \mathbf{O}_2 \\ \mathbf{O}_4 & \mathbf{O}_4 & 0 & \mathbf{U}_1 & \mathbf{O}_2 \\ \mathbf{O}_1 & \mathbf{O}_1 & \mathbf{O}_1 & \mathbf{O}_1 & \mathbf{O}_3 \end{bmatrix} \begin{bmatrix} \mathbf{V}_R(t) \\ \mathbf{V}_S(t) \\ \mathbf{V}_{34}(t) \\ \mathbf{V}_{12}(t) \\ \mathbf{O} \end{bmatrix} \quad (4.70)$$

where

$$\mathbf{G}_1(t) = \begin{bmatrix} -\frac{R_e}{L_e} \mathbf{U}_1 - \mathbf{D}(jm\omega_0) & \mathbf{O}_4 & \mathbf{O}_4 \\ \mathbf{O}_4 & -\frac{R_e}{L_e} \mathbf{U}_1 - \mathbf{D}(jm\omega_0) & \mathbf{O}_4 \\ \mathbf{O}_4 & \mathbf{O}_4 & -\frac{R_e}{L_e} \mathbf{U}_1 - \mathbf{D}(jm\omega_0) \\ \mathbf{O}_4 & \mathbf{O}_4 & \mathbf{O}_4 \\ \frac{\mathbf{Q}_{S1}(t) + \mathbf{Q}_{S2}(t)}{C} & \frac{1}{C} \mathbf{Q}_{S1}(t) & \frac{1}{C} \mathbf{Q}_{S3}(t) \end{bmatrix}$$

$$\mathbf{G}_2(t) = \begin{bmatrix} \mathbf{O}_4 & -\frac{1}{L_e} \mathbf{P}_{S2}(t) \\ \mathbf{O}_4 & -\left(\frac{\mathbf{P}_{S1}(t) - \mathbf{P}_{S2}(t)}{L_e} \right) \\ \mathbf{O}_4 & -\frac{1}{L_e} \mathbf{P}_{S3}(t) \\ -\frac{R_e}{L_e} \mathbf{U}_1 - \mathbf{D}(jm\omega_0) & -\frac{1}{L_e} \mathbf{P}_{S4}(t) \\ \frac{1}{C} \mathbf{Q}_{S4}(t) & -\mathbf{D}(jm\omega_0) \end{bmatrix}$$

and \mathbf{U}_1 is the unit matrix (303×303). \mathbf{O} , \mathbf{O}_1 , \mathbf{O}_2 , \mathbf{O}_3 and \mathbf{O}_4 are the zero matrices with dimensions (101×1) , (101×303) , (303×101) , (101×101) and (303×303) respectively.

The solution of the DHD equation (4.70) gives complete information of harmonics in the GIPFC equipment under steady and dynamic state conditions.

Again, the steady state solution of (4.70) can be obtained by setting $\dot{\mathbf{I}}_R(t)$, $\dot{\mathbf{I}}_S(t)$, $\dot{\mathbf{I}}_{33}(t)$, $\dot{\mathbf{I}}_{11}(t)$ and $\dot{\mathbf{V}}_{dc}(t)$ to zero. Thus the following algebraic equation represents the GIPFC in steady state

$$\begin{bmatrix} \mathbf{I}_R(t) \\ \mathbf{I}_S(t) \\ \mathbf{I}_{33}(t) \\ \mathbf{I}_{11}(t) \\ \mathbf{V}_{dc}(t) \end{bmatrix} = \frac{1}{L_e} [\mathbf{G}_1(t) \ \mathbf{G}_2(t)]^{-1} \begin{bmatrix} \mathbf{U}_1 & -\mathbf{U}_1 & \mathbf{O}_4 & \mathbf{O}_4 & \mathbf{O}_2 \\ -\mathbf{U}_1 & 2\mathbf{U}_1 & \mathbf{O}_4 & \mathbf{O}_4 & \mathbf{O}_2 \\ \mathbf{O}_4 & \mathbf{O}_4 & \mathbf{U}_1 & \mathbf{O}_4 & \mathbf{O}_2 \\ \mathbf{O}_4 & \mathbf{O}_4 & 0 & \mathbf{U}_1 & \mathbf{O}_2 \\ \mathbf{O}_1 & \mathbf{O}_1 & \mathbf{O}_1 & \mathbf{O}_1 & \mathbf{O}_3 \end{bmatrix} \begin{bmatrix} \mathbf{V}_R(t) \\ \mathbf{V}_S(t) \\ \mathbf{V}_{34}(t) \\ \mathbf{V}_{12}(t) \\ \mathbf{O} \end{bmatrix} \quad (4.71)$$

The solutions of these steady state equations (4.71) are used as the initial condition for solving (4.70).

4.5.3 Simulation of the proposed DHD model of GIPFC

The GIPFC DHD model in (4.70) is used to investigate the dynamic response of harmonics to a given disturbance. PWM switching was used, and the switching function was calculated using the harmonic elimination method, to eliminate harmonics $i = 5, 7, 11, 13,$ and 17 . The magnitude of the fundamental of the inverter AC voltage can be adjusted by controlling the voltage across the capacitor. This can be achieved by changing the phase angle of the operation of the inverter switches with respect to the AC

system. In this case a phase angle of 15° is considered. The per-phase equivalent leakage inductance and winding resistance of the transformer and the capacitance of the DC capacitor are $L_e=0.2\text{mH}$, $R_e=0.04\ \Omega$, and $C=5000\ \mu\text{F}$, respectively. Under the steady state conditions the bus per phase voltages V_A , V_B , V_C , and V_D in per unit at a frequency of 60 Hz are

$$\begin{aligned}
v_{Sa}(t) &= 1.1 \sin \omega_0 t & v_{Ra}(t) &= 1.3 \sin \omega_0 t \\
v_{Sb}(t) &= 1.1 \sin(\omega_0 t - 120^\circ) & v_{Rb}(t) &= 1.3 \sin(\omega_0 t - 120^\circ) \\
v_{Sc}(t) &= 1.1 \sin(\omega_0 t + 120^\circ) & v_{Rc}(t) &= 1.3 \sin(\omega_0 t + 120^\circ) \\
\\
v_{1a}(t) &= 1.8 \sin \omega_0 t & v_{2a}(t) &= \sin \omega_0 t \\
v_{1b}(t) &= 1.8 \sin(\omega_0 t - 120^\circ) & v_{2b}(t) &= \sin(\omega_0 t - 120^\circ) \\
v_{1c}(t) &= 1.8 \sin(\omega_0 t + 120^\circ) & v_{2c}(t) &= \sin(\omega_0 t + 120^\circ) \\
\\
v_{3a}(t) &= 1.5 \sin \omega_0 t & v_{4a}(t) &= 1.2 \sin \omega_0 t \\
v_{3b}(t) &= 1.5 \sin(\omega_0 t - 120^\circ) & v_{4b}(t) &= 1.2 \sin(\omega_0 t - 120^\circ) \\
v_{3c}(t) &= 1.5 \sin(\omega_0 t + 120^\circ) & v_{4c}(t) &= 1.2 \sin(\omega_0 t + 120^\circ)
\end{aligned} \tag{4.72}$$

A disturbance is assumed in the voltage starting at 0.07 seconds and lasting for 0.05 seconds, and during the disturbance, the phase a voltage of $v_{1a}(t)$ is 150% of its value. The simulation starts at $t_0=0$ seconds with final time $t_f=0.2$ seconds and uses an integration time step of $\Delta t=0.16667$ ms. For accuracy, the simulation requires to include the calculation of 50 harmonics.

For proper operation of the GIPFC, it is necessary to keep the DC voltage across the capacitor as constant as possible throughout the simulation period. For this purpose, the control system shown in Figure 24 is again used in the simulation of the GIPFC DHD model. The simulation results presented in Figure 72 show that, through the disturbance interval, the DC component of the voltage on the DC side increased by 23% of its steady state value without control system. This variation depends on the severity of the fault.

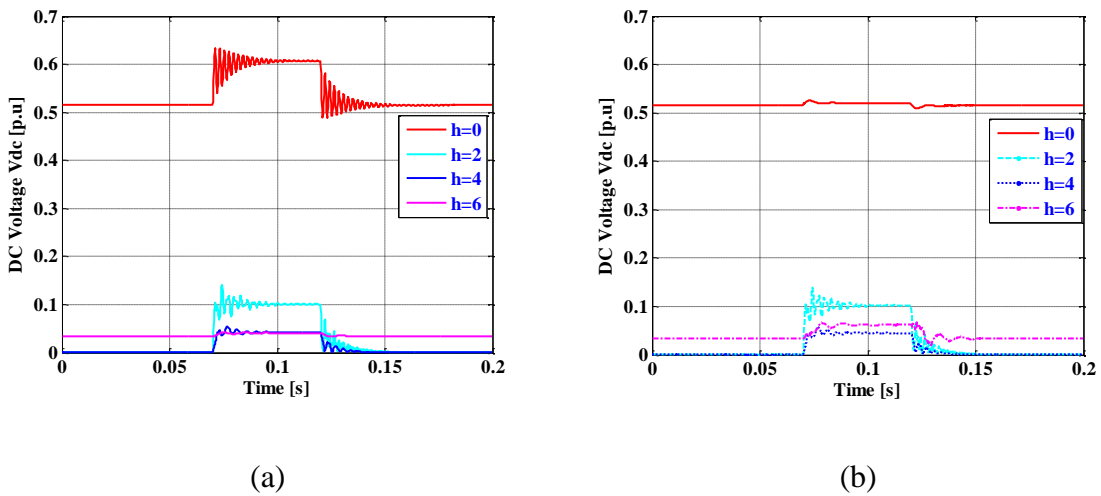


Figure 72: DC-side voltage of GIPFC, (a) Without control system (b) With control system

The results obtained clearly demonstrate that the control system, shown in Figure 24, does minimize the distortion of the DC component of the voltage on the DC side during the disturbance, to a value very close to its steady state value. The remaining harmonic voltages are unchanged. However, there is a slight change in the 6th harmonic voltage with the control, but this can also be reduced by proper gain and time constant values. Keeping the DC voltage constant at the terminals of the GIPFC during the period of disturbance further helps to minimize some of the power quality indices such as the THD in the output current of phase *a* of VSC 4 and its harmonic components are

presented in Figure 74, and the output apparent power at the terminals of VSC 2, as shown in Figure 75.

The decrease in THD in per-phase output currents of VSC 1 is due to the fact that keeping the DC side voltage close to its steady state value during the disturbance interval causes an increase in the fundamental component of the per-phase output voltages of VSC 1, which further leads to the reduction in the THD of those currents. This variation is due to the change in the DC side voltage.

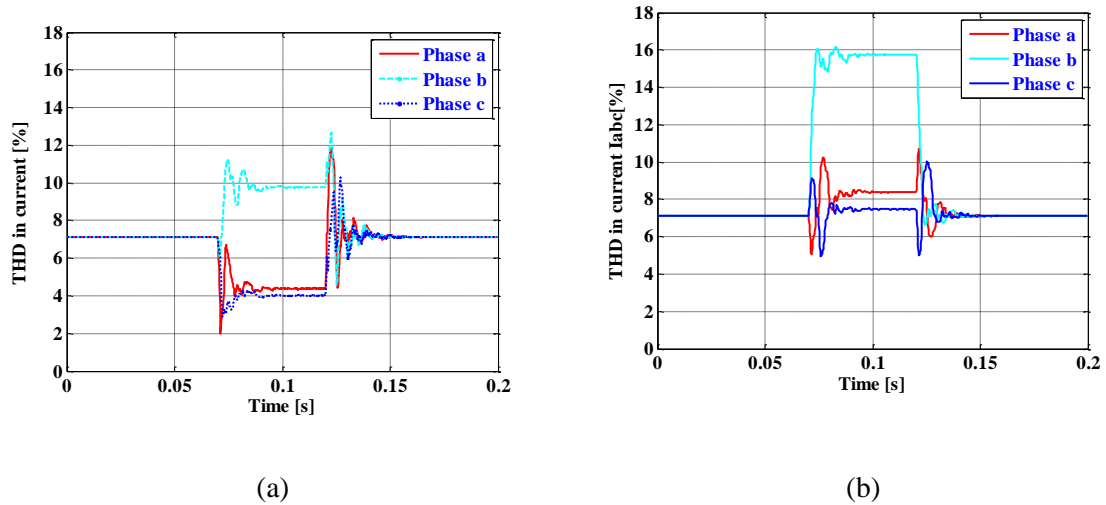


Figure 73: THD in output currents of VSC 1 (a) With control system (b) Without control system

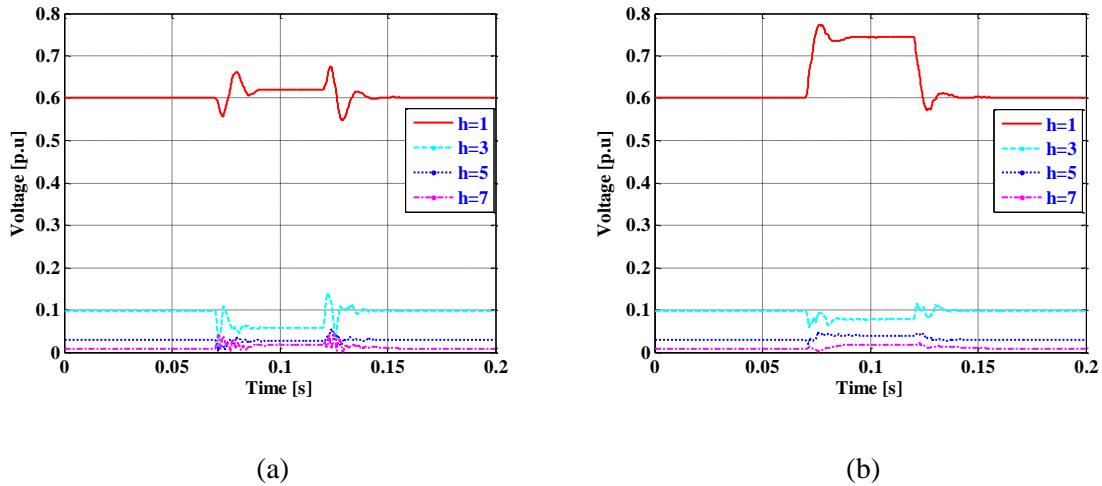


Figure 74: The harmonic content of output voltage of phase *a* of VSC 1 (a) With control system (b) Without control system

The increase in the DC side voltage during the disturbance interval causes an increase in per-phase output voltages and currents of VSC 2. The mutual effects of the variations in voltages and currents cause a further increase in the per-phase apparent power outputs of VSC 2, as shown in Figure 75.

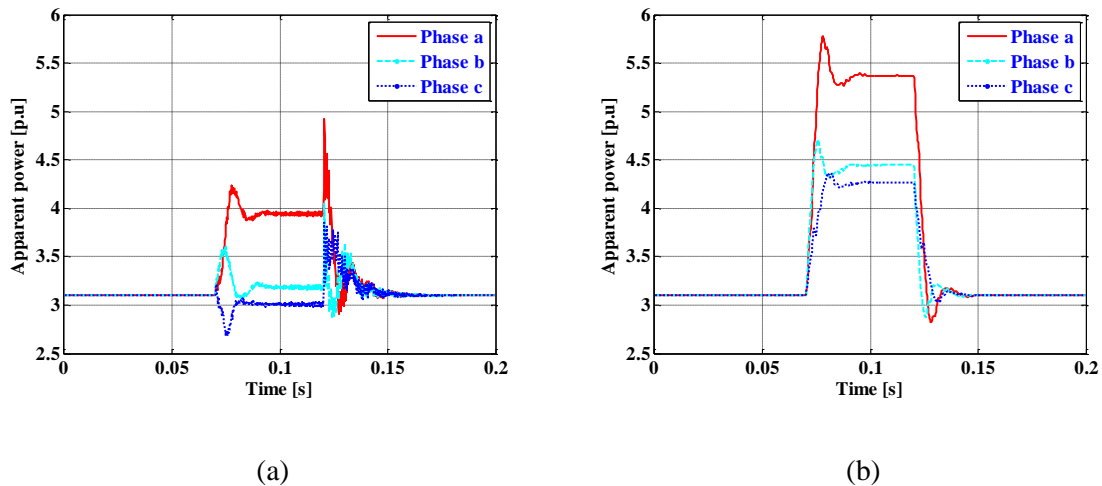
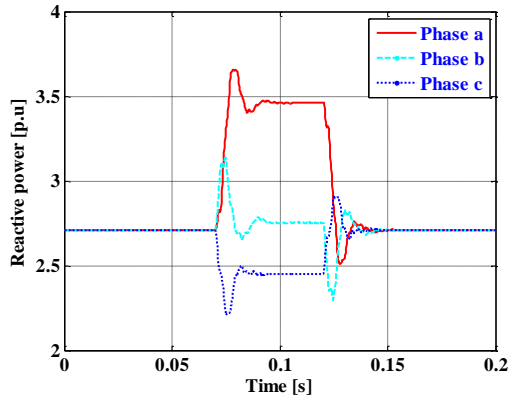
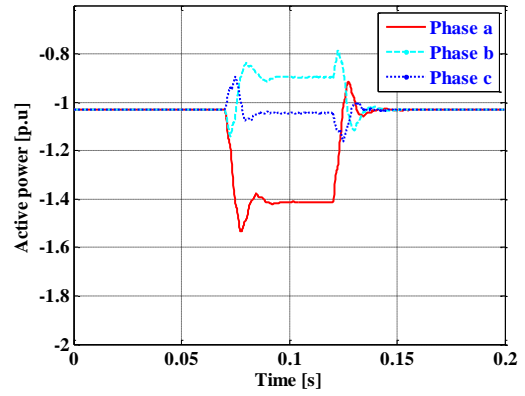


Figure 75: The harmonic content of output current of phase *a* of VSC 2 (a) With control system (b) Without control system

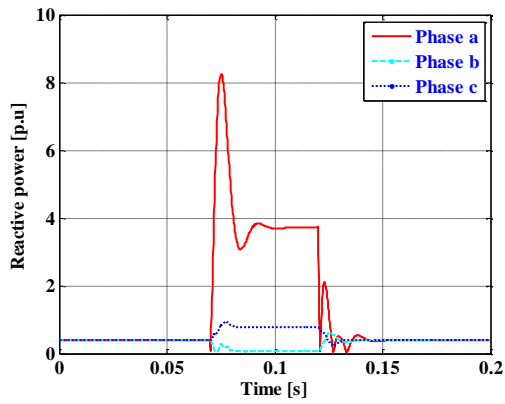
Harmonics possess sensitive characteristics during a disturbance thus facilitating the demonstration of several power quality indices. Some of these indices of the GIPFC are shown in Figure 76.1 and Figure 76.2. Though voltage and current at VSC 2 were positive, the phase angle between them is greater than 90° , causing negative active power at all three phases and evidently larger distortion at phase *a*. The remaining phase distortions depend on the variation of voltages and currents due to the disturbance and this reasoning holds good for the remaining active power outputs of VSC 3 and VSC 4. The rise in the per-phase reactive power outputs of VSC 2 and VSC 3 is due to an increase in the per-phase output currents and voltages of the same during the disturbance period. The VSC 4 is connected between the buses 1 and 2; their relationship is shown in (4.62). The voltage at bus 1 increased by 50% of its steady state value, resulting in more voltage and currents to appear at the terminals of VSC 4 during that period, whose mutual effects increase the per-phase reactive power output of VSC 4.



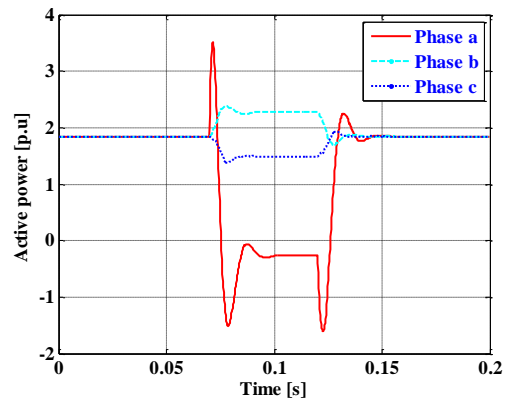
(a)



(b)

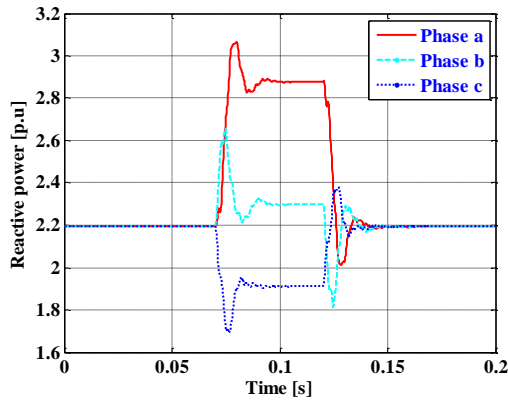


(c)

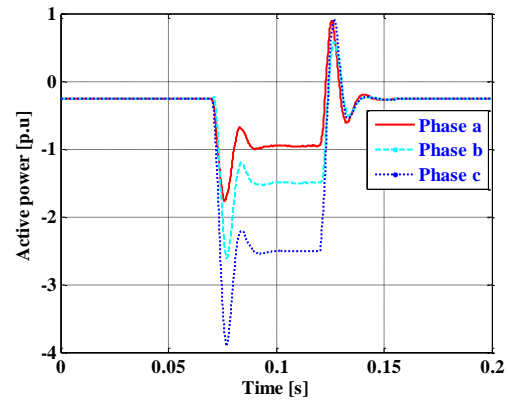


(d)

Figure 76.1: Power quality indices (a) The per-phase output reactive powers of VSC 2 (b) The per-phase output active powers of VSC 2 (c) The per-phase output reactive powers of VSC 4 (d) The per-phase output active powers of VSC 4



(a)

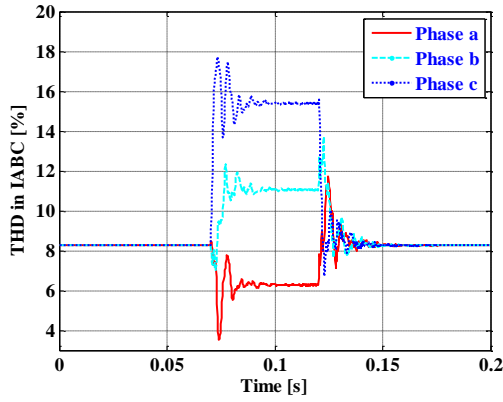


(b)

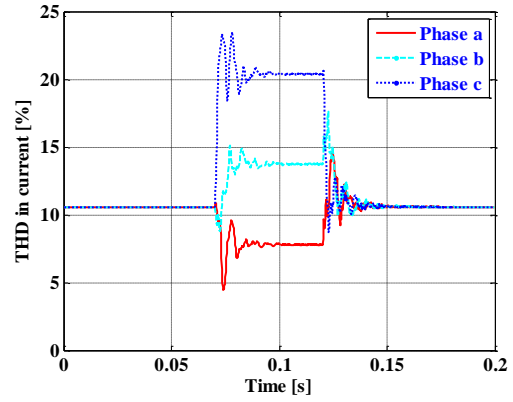
Figure 76.2: Power quality indices (a) The per-phase output reactive powers of VSC 3 (b)

The per-phase output active powers of VSC 1

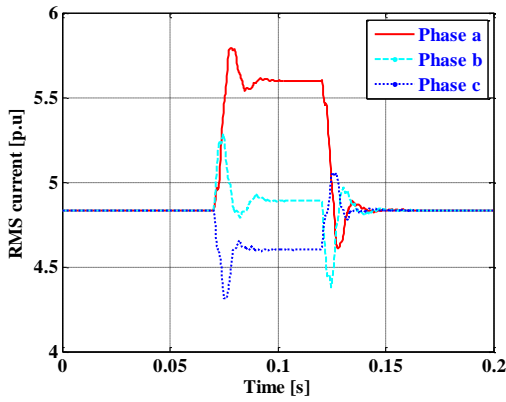
The RMS values of voltages and currents and the THD in output currents of VSC 4 are shown in Figure 77. Here, the dynamics of harmonics are more clearly evident during the disturbance. The increase in the per-phase output currents of VSC 2 is due to the change in the DC side voltage. The increase in the RMS value of current of VSC 4 is due to larger voltage that appears at its terminals.



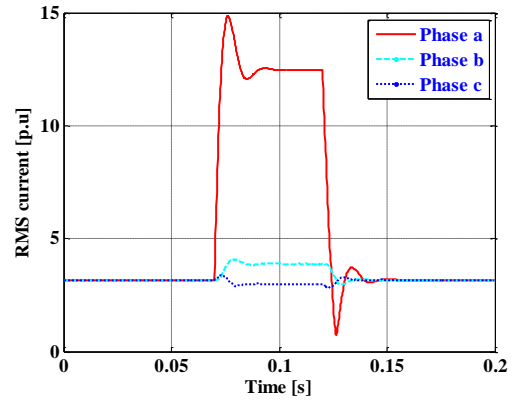
(a)



(b)



(c)



(d)

Figure 77: Power quality indices (a) THD in output currents of VSC 2 (b) THD in output currents of VSC 3 (c) RMS values of output currents of VSC 2 (d) RMS values of output currents of VSC 4

Apart from the fundamental, other harmonic contents of output voltages of phase *a* of VSC 1 and phase *b* of VSC 4 are presented in Figure 78(b) and Figure 79(b), respectively. The increase in RMS output current of phase *a* of VSC 4 causes larger voltage drop at the terminals of this phase. The time domain waveforms of the same are presented in Figure 78(a) and Figure 79(a), respectively.

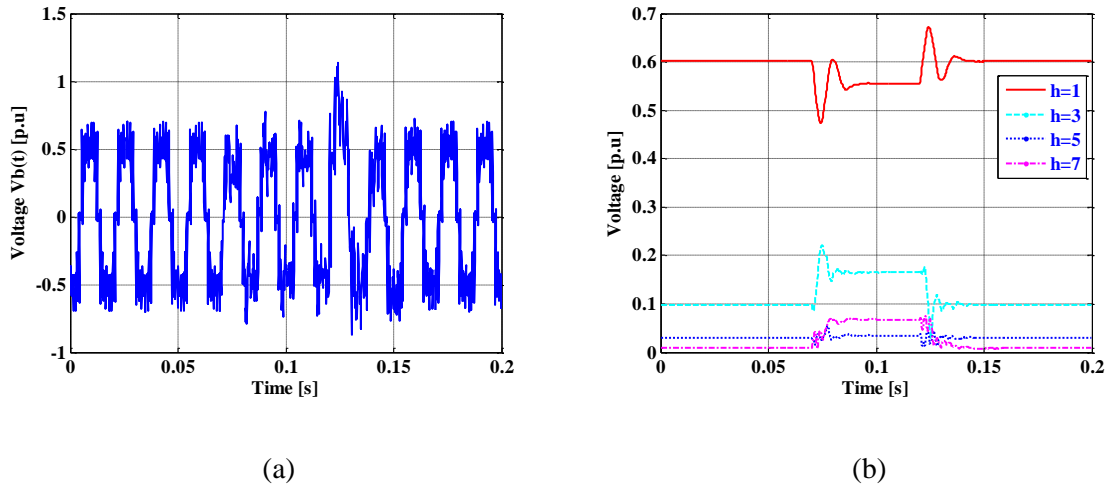


Figure 78: The output voltages of Phase *b* of VSC 1 (a) Voltage waveform(b) Voltage harmonic content

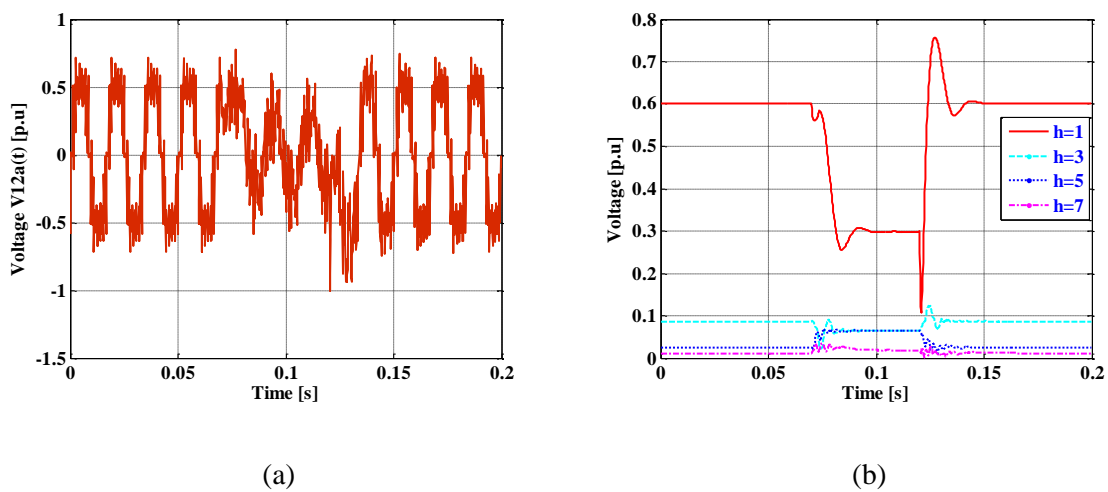
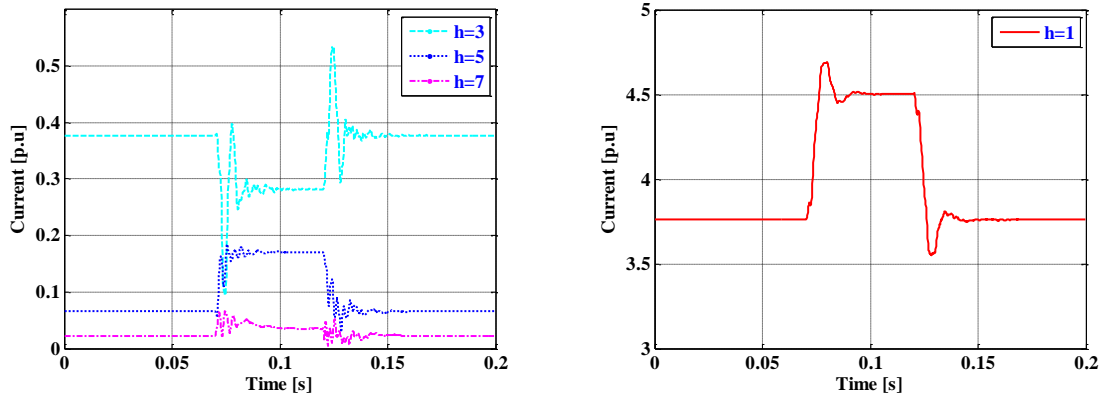


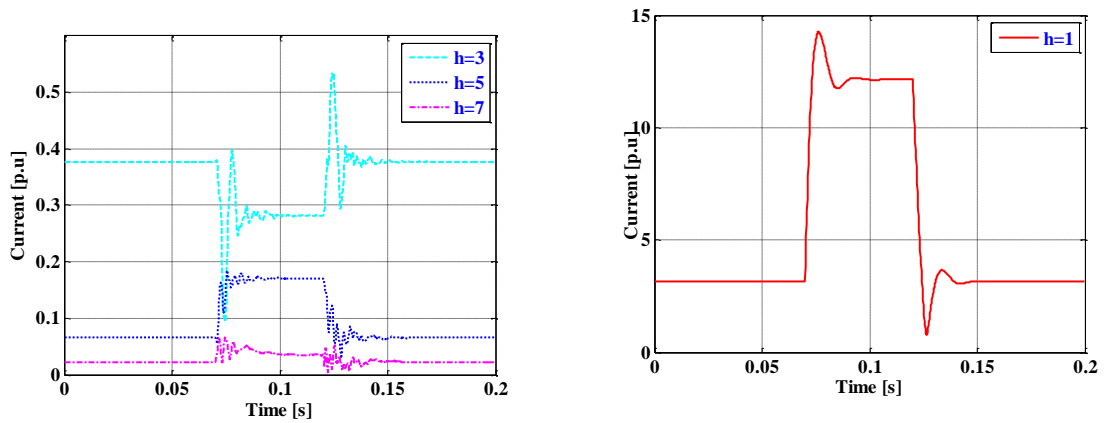
Figure 79: The output voltages of phase *a* of VSC 4 (a) Voltage waveform (b) Voltage harmonic content

Harmonic content of the output currents of phase *a* of VSC 3 and VSC 4 are shown in Figure 80. The increase in the fundamental component of the output current of phase *a* of VSC 3 can be attributed to the change in the DC side voltage. In VSC 4, this

increase is due to the rise in the voltage at its terminals. The time domain waveform of the same is shown in Figure 81.



(a)



(b)

Figure 80: The harmonic content of output current of phase *a* of (a) At VSC 3 (b) At

VSC 4

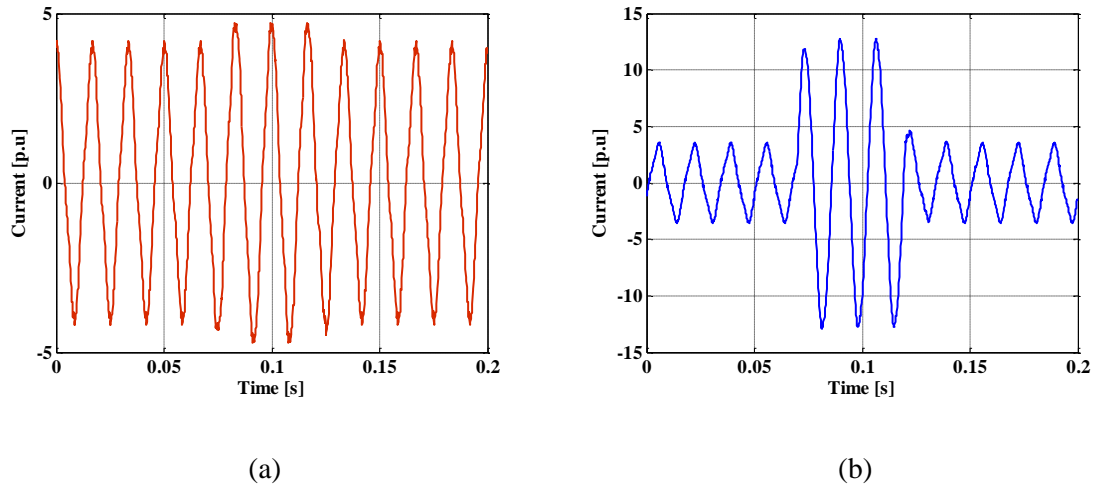


Figure 81: Time domain waveforms of output currents of phase a of (a) VSC 1 (b) VSC 4

The harmonic components of the negative sequence currents at VSC 1 and VSC 2 are shown in Figure 82. From these plots it can be observed that the 5th harmonic component alone is present during the steady state and all the odd harmonics are present during the disturbance (for clarity, the fundamental plot is shown separately from others in Figure 82(a) and (b)). This phenomenon is expected as predicted by the mathematical analysis in Section 3.5.

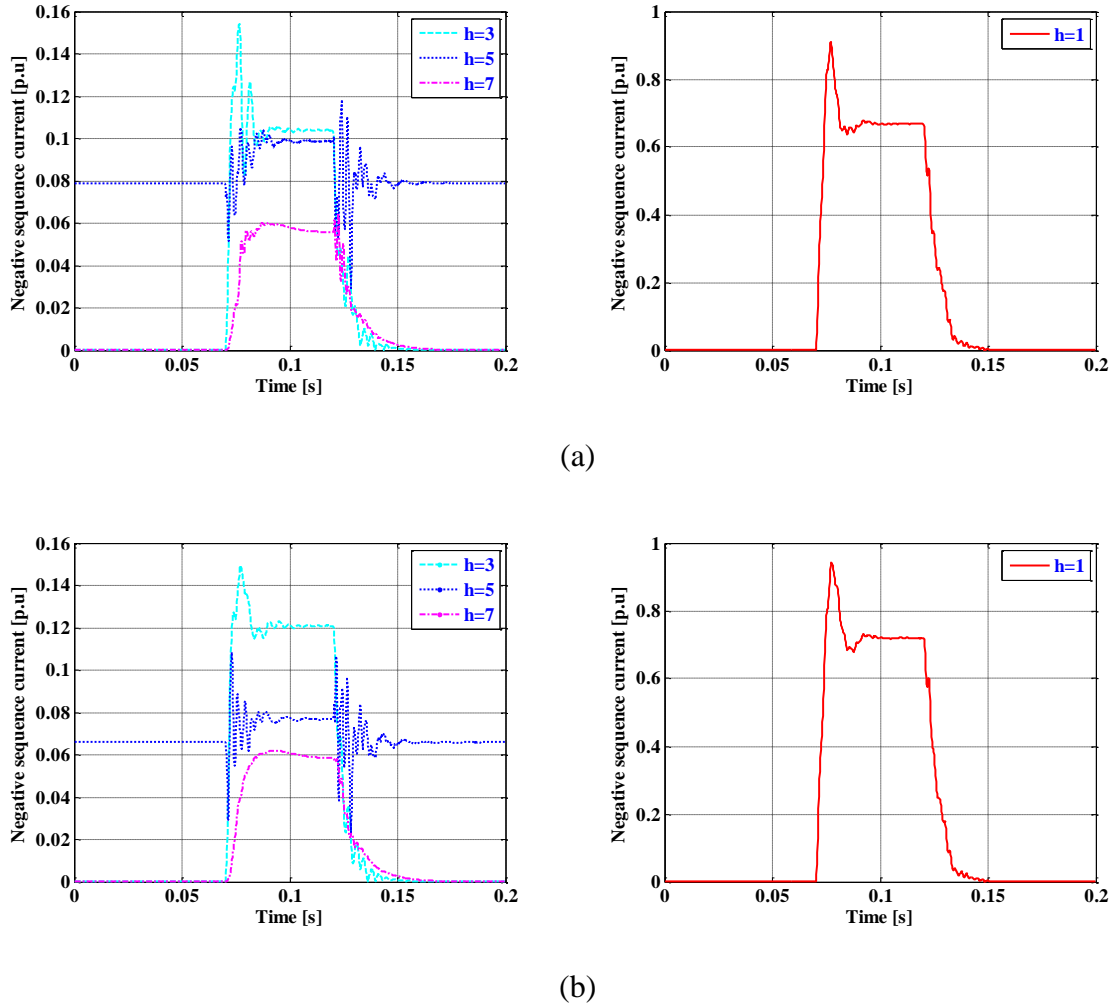
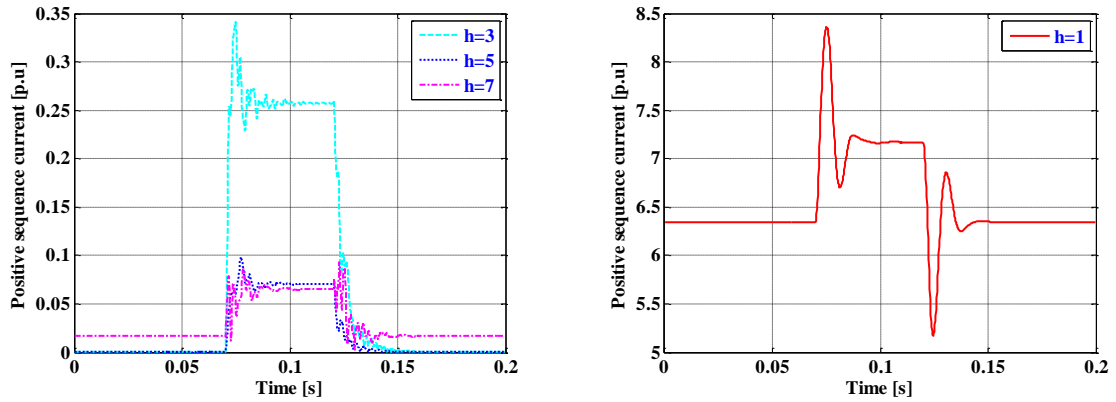
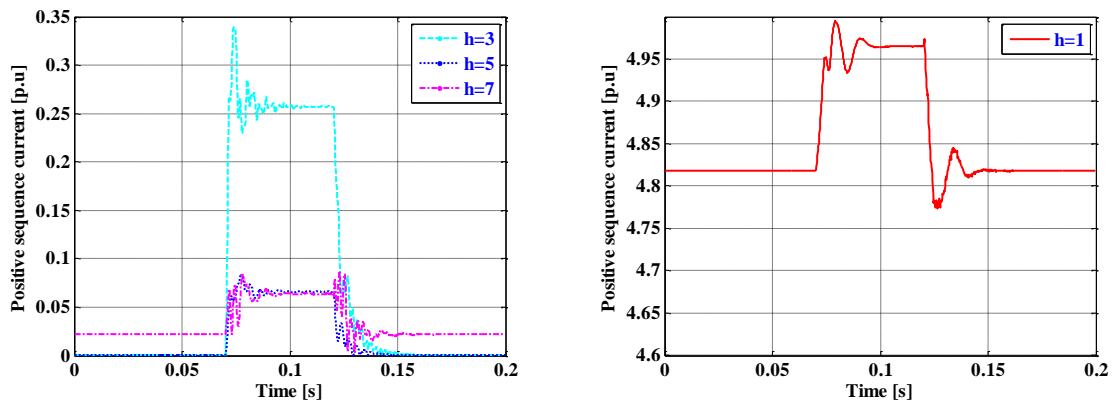


Figure 82: The negative sequence currents of (a) VSC 1 (b) VSC 2

The harmonic components of the positive sequence currents at VSC 1 and VSC 2 are shown in Figure 83. These plots show that the fundamental and the 7th harmonics are present during the steady state (the fundamental clearly shown separately from others in Figure 83(a) and (b)) and all the odd harmonics are present during the disturbance.



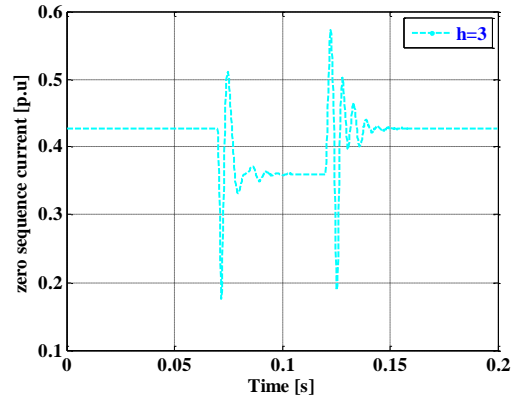
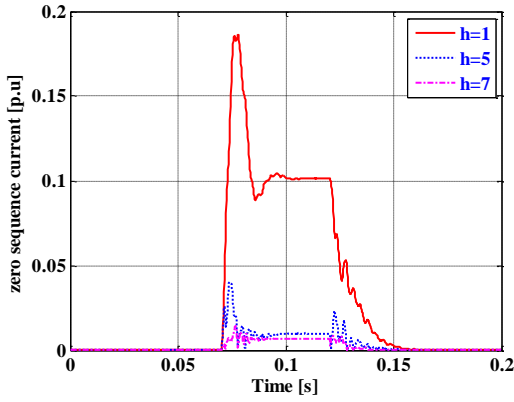
(a)



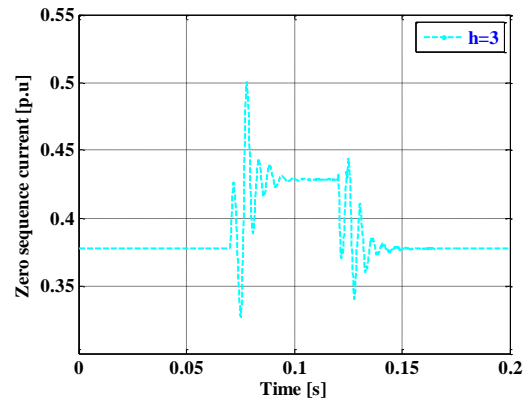
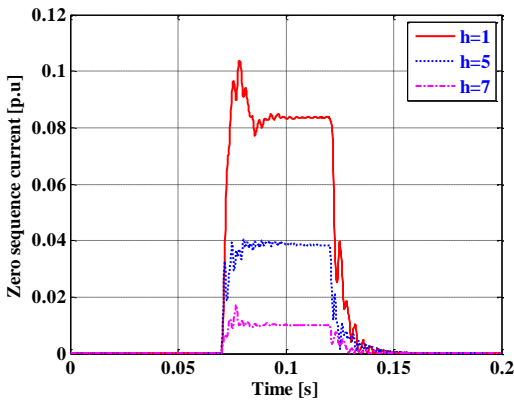
(b)

Figure 83: The positive sequence currents of (a) VSC 1 (b) VSC 2

Figure 84 shows the harmonic components of the zero sequence currents of VSC 1 and VSC 2. It is observed that the 3rd harmonic component alone is present during steady state and all the odd harmonic currents are present during the disturbance. A detailed explanation regarding the sequence currents is given in Section 3.5.



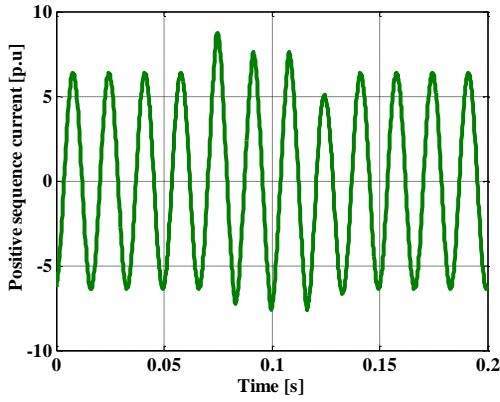
(a)



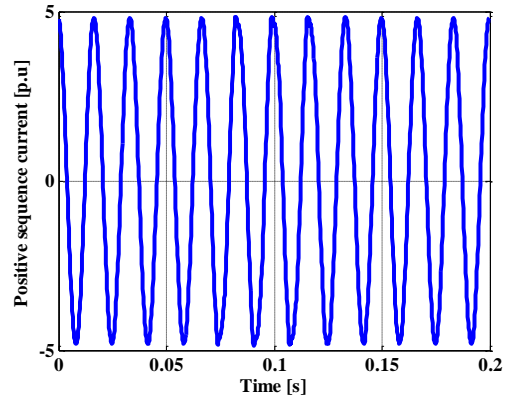
(b)

Figure 84: The zero sequence currents of (a) VSC 1 (b) VSC 2

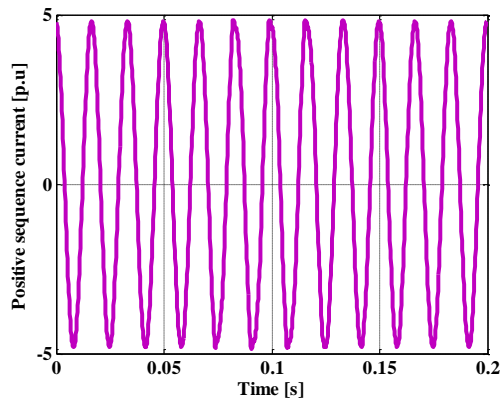
Time domain representation of the positive sequence currents of all VSCs are shown in Figure 85. Here, these currents have a waveform close to a sinusoidal and contain constant magnitudes in steady state but some change during the disturbance.



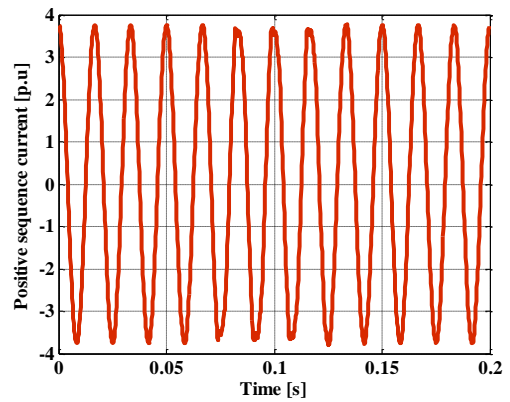
(a)



(b)



(c)

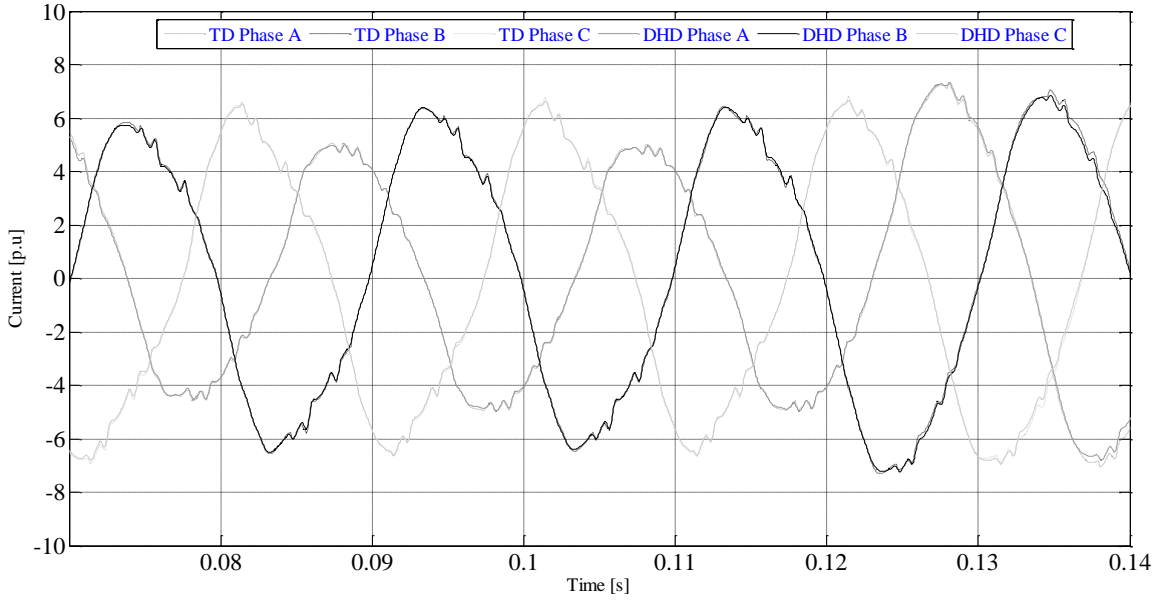


(d)

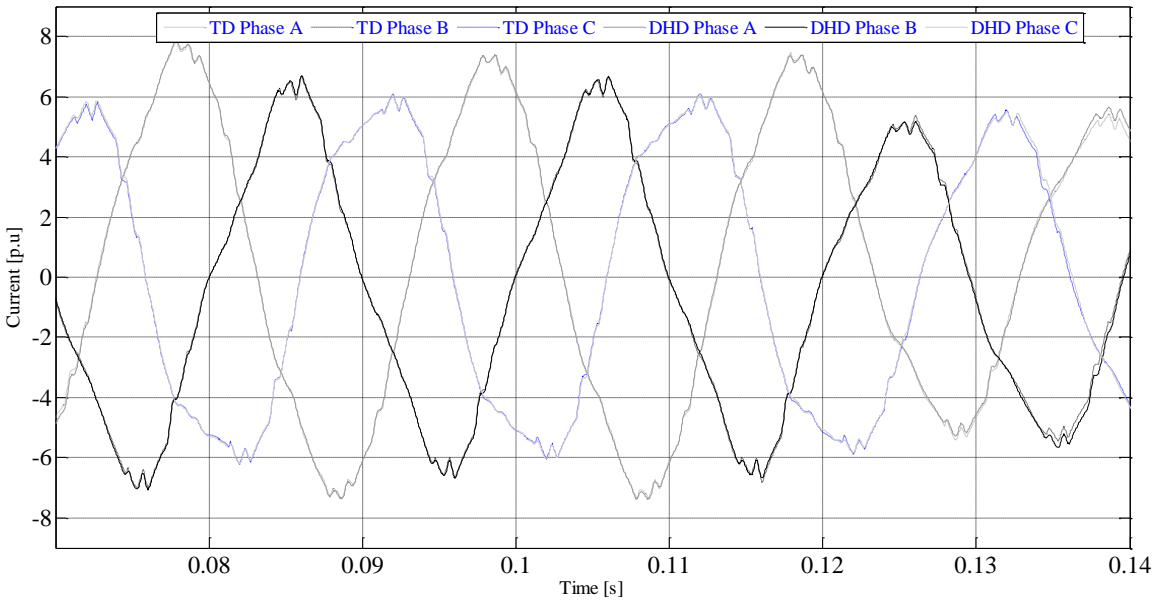
Figure 85: Time domain waveforms of the positive sequence currents of (a) VSC 1 (b) VSC 2 (c) VSC 3 (d) VSC 4

4.5.4 Validation of the proposed DHD model of the GIPFC

The validation methods discussed in Section 3.6.9 are applied to the outputs of VSC 1, and the resulting time domain waveforms of the three-phase waveforms are shown in Figure 86.1(a). The plots of these currents are indistinguishable.

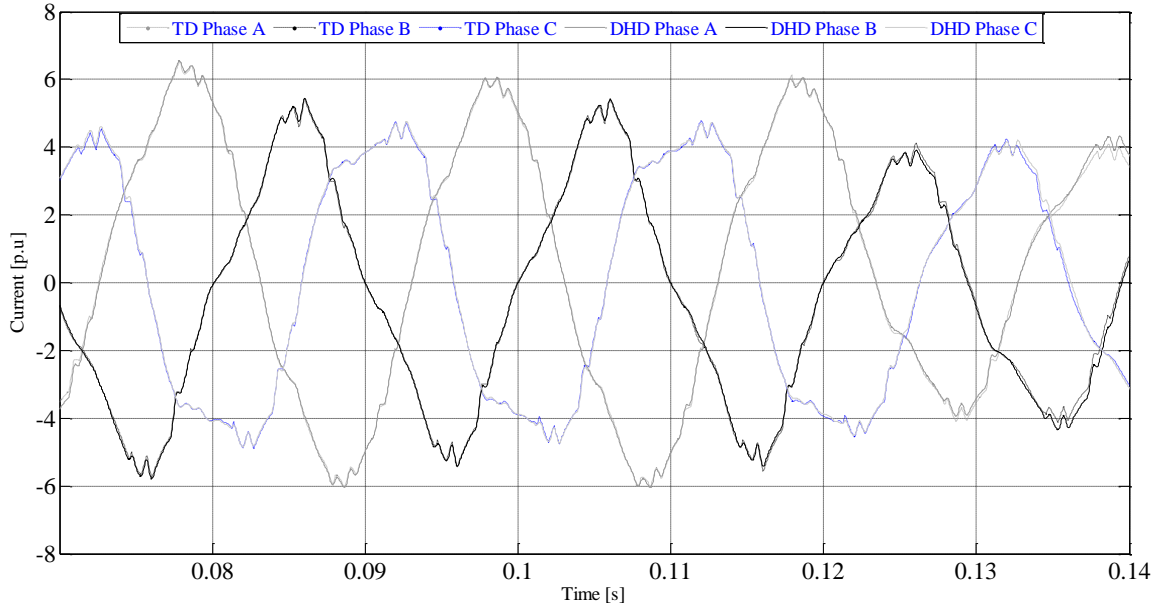


(a)

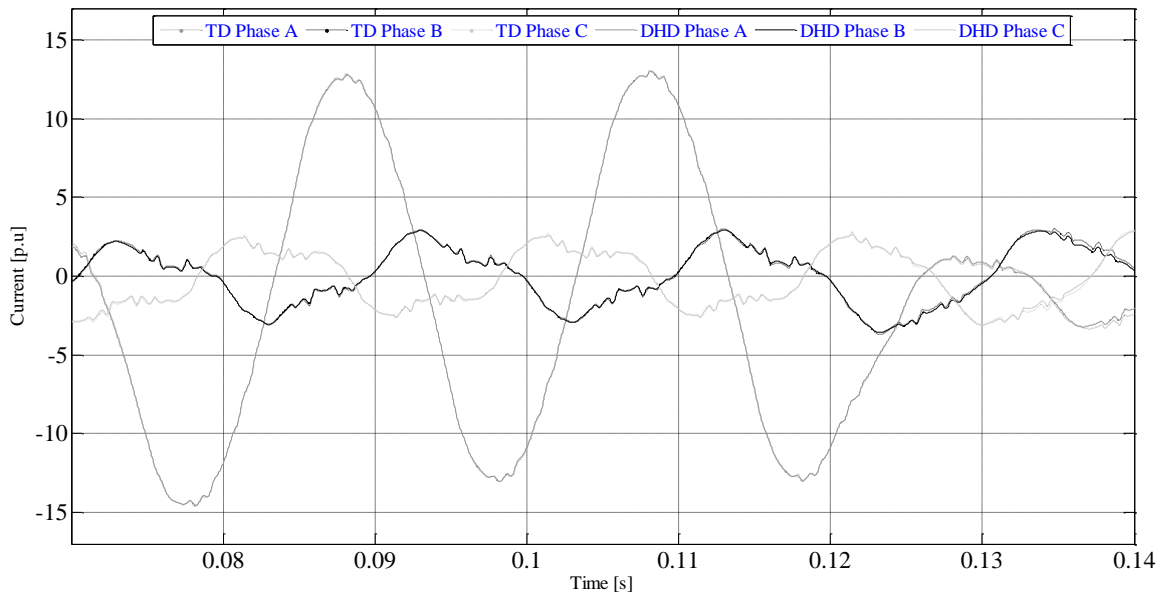


(b)

Figure 86.1: Time domain waveforms of currents of each phase of (a) VSC 1 (b) VSC 2



(a)



(b)

Figure 86.2: Time domain waveforms of currents of each phase of (a) VSC 3 (b) VSC 4

The same procedure is repeated for VSC 2, VSC 3, and VSC 4 and the results are shown in Figure 86.1(b), Figure 86.2(a), and (b), with the same evidence. This allows the inference that the proposed GIPFC DHD model has been validated.

4.6 Conclusion

Multi-line FACTS controllers provide more degrees of freedom in controlling the power system than when compared to STATCOM, SSSC or UPFC controllers. Thus, this investigation was aimed at developing Dynamic Harmonic Domain models of the GUPFC, IPFC, and GIPFC for the study of the evolution of harmonics with time during the transient onset by a disturbance. This chapter included the presentation of a simulation of the proposed models and the calculation of the power quality indices.

Two methods that provided time waveforms of the three phase currents of VSCs were used to validate the results obtained from the simulation of the proposed DHD models. The plots obtained were indiscernible. The investigation also developed Harmonic domain models of GUPFC and GIPFC devices. These models can be applied to resonance prediction analysis and harmonic propagation studies. The accessibility to the DHD models of these controllers can facilitate the design of power systems controls, and Harmonic information provided by their HD models can be used to determine harmonic distortion regions, which is the future research work to be contemplated.

CHAPTER V

ANALYSIS OF POWER QUALITY INDICES OF THE MULTI-LINE FACTS CONTROLLERS WITH VARIOUS SWITCHING FUNCTIONS

5.1 Introduction

The intended use of power electronic converters in transmission and distribution systems is to improve their reliability and power transfer capability. Since these converters are nonlinear devices, they produce undesirable distortions in the system voltage and current waveforms manifested in unwanted harmonics. These harmonics can be eliminated by proper switching of the semiconductor devices. This requires the production of pulses that determine the turn-on and turn-off intervals for these devices.

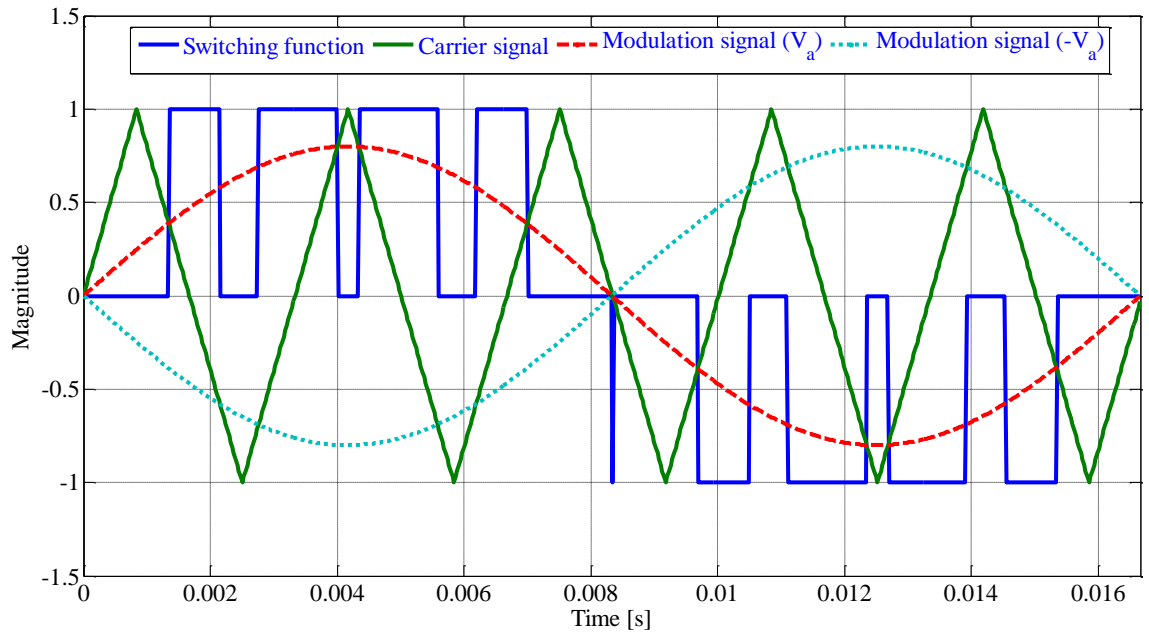
One of the well-known ways of producing the required series of pulses to achieve harmonic cancellation is the unipolar PWM switching technique [3]. The interest in introducing several switching functions is to study their effect on multiline FACTS controllers' performance and how these controllers are affected by using various switching functions.

In this chapter, the unipolar PWM switching technique is used and the procedure to produce it is discussed. Also introduced are multi-module PWM (MMPWM) switching functions [10] for analysis purposes, since they are later used in the simulations of the GUPFC and GIPFC DHD models that were developed in Chapter 4. Furthermore, this chapter also includes the comparison of several PQ indices of these controllers with respect to the corresponding switching functions, under steady state and disturbance conditions, and highlights the important observations. The outcome of this research effort is not available in the published literature. For the first time, the DHD models of GUPFC and GIPFC are analyzed using different MMPWM switching functions.

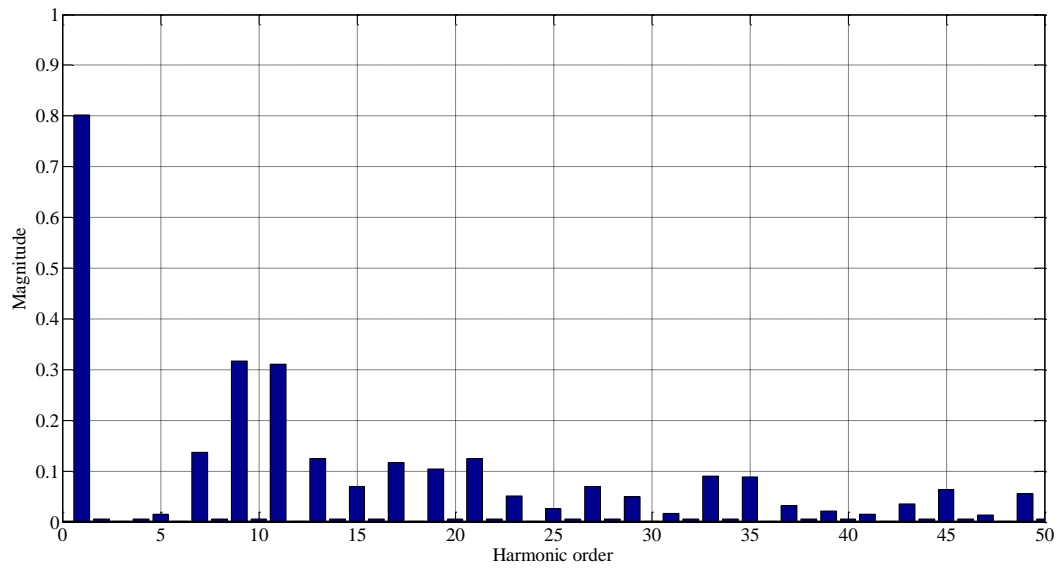
5.2 Pulse width modulation

A PWM signal is generated by comparing the modulation and carrier signals. The unipolar modulation requires two sinusoidal modulation signals, V_a and $-V_a$, which are of the same frequency and magnitude but 180 degrees out of phase, as shown in Figure 87. These two signals are compared with a carrier signal V_r , which is a triangular wave form with much higher frequency than the modulation signals. The ratio of peak value of carrier signal to the peak value of modulation signal is called the modulation index (MI). By varying the MI, various PWM signals can be generated. During the first half cycle, the switching waveform reaches '1' when V_a is greater than $|V_r|$, else it is zero. In the second half cycle, it reaches '-1' when $-V_a$ is greater than $|V_r|$, else it is zero. The final switching function and harmonic content of this waveform are as shown in Figure 87(a)

and (b), respectively. It is evident from Figure 87(b) that the first 6 harmonics and all the even harmonics are negligible in quantities. The THD of this switching waveform is 69.85 %.



(a)



(b)

Figure 87: Unipolar voltage switching function (a) with one PWM converter (b)

Harmonic content of the switching waveform

5.3 Multi-module switching function

The unipolar PWM technique has been extended to the MMPWM switching in which n number of PWM converters are connected in parallel. The switching function was generated by comparing the modulation signals with n number of carrier signals, each of which is phase-shifted by an angle that is given by

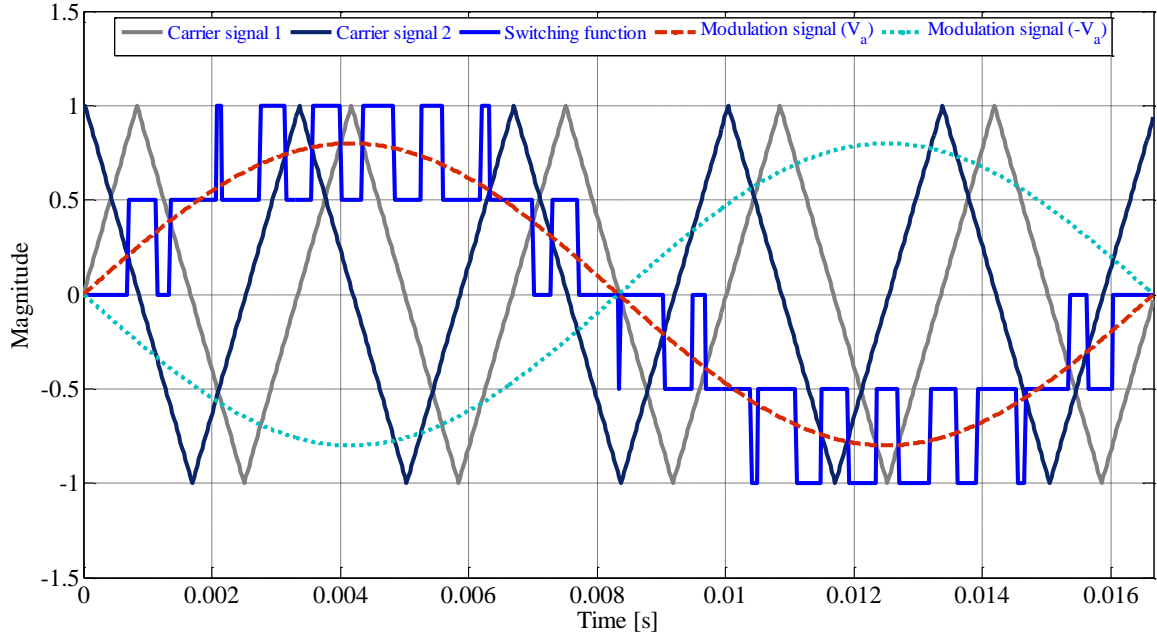
$$D_i = 2 * \pi * (m-1) / \text{number of PWM converters in parallel} \quad (5.1)$$

where m is 2,3..... n .

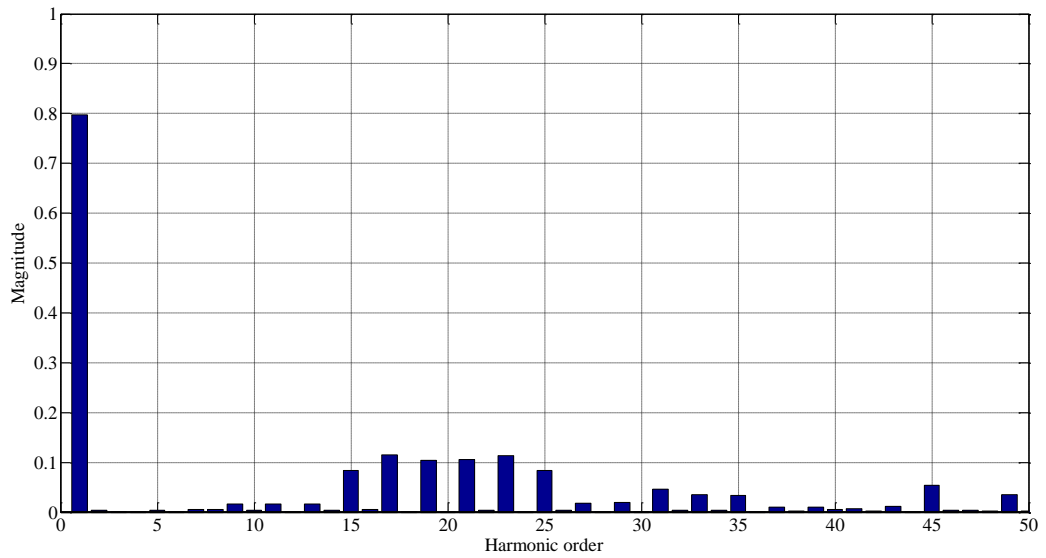
For n number of PWM converters that are connected in parallel, the magnitudes of the switching function are given by

$$SW = (SW_1 + SW_2 + \dots + SW_n) / n. \quad (5.2)$$

When two PWM converters are connected in parallel and the second carrier signal is phase-shifted by π radians whose frequency is five times that of the modulation signals, the resultant switching function and harmonic content of this waveform are as shown in Figure 88(a) and (b), respectively. It is evident from Figure 88(b) that the first 14 harmonics and all the even harmonics are nearly zero. The THD of this switching waveform is 33.96 %.



(a)



(b)

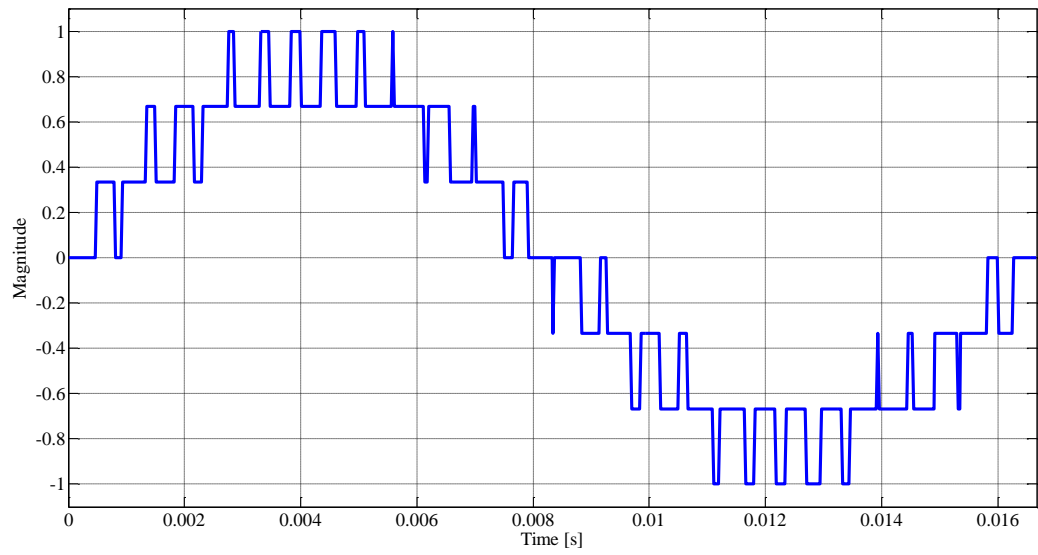
Figure 88: Unipolar voltage switching function (a) with two PWM converters (b)

Harmonic content of the switching waveform

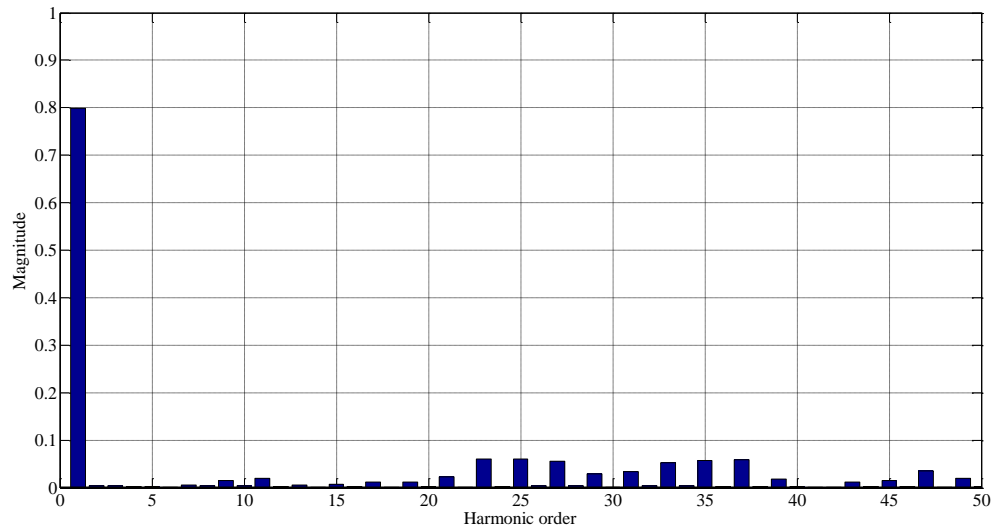
Now, when three PWM converters connected in parallel are considered, and the second and third carrier signals are phase-shifted by π and $4\pi/3$ radians, respectively, the magnitude of the resultant switching function is given by

$$SW = (SW1+SW2+ SW3)/3$$

Figure 89(a) and (b) show the resultant switching function and harmonic content of this waveform, respectively. It is obvious from Figure 89(b) that the first 20 harmonics and all the even harmonics are insignificant. The THD of this switching waveform is 20.0046 %.



(a)



(b)

Figure 89: Unipolar voltage switching function (a) with three PWM converters (b)

Harmonic content of the switching waveform

Table VI shows the configuration of the switching functions discussed so far, which include modulation frequency (MF), carrier signal frequency (CSF) and modulation index (MI) along with the total harmonic distortion of the resultant waveforms.

Table VI: Configuration of different switching functions

| Type | Number of PWM VSC's in parallel | MF | CSF | MI | Frequency modulation ratio | Number of harmonics | THD (%) |
|--------|---------------------------------|----|-----|-----|----------------------------|---------------------|---------|
| Type 1 | 3 | 60 | 300 | 0.8 | 5 | 50 | 20.005 |
| Type 2 | 2 | 60 | 300 | 0.8 | 5 | 50 | 33.962 |
| Type 3 | 1 | 60 | 300 | 0.8 | 5 | 50 | 69.845 |

From the above table it can be inferred that, in a unipolar switching function, the number of PWM converters connected in parallel is inversely proportional to the total harmonic distortion. The following section presents the simulations performed on the GUPFC DHD model, with the application of switching functions discussed in Table VI, in order to study their effect on its PQ indices.

5.4 Simulation of the DHD model of the GUPFC with multi-module switching

The DHD model of the GUPFC in Section 4.3.2 is used in this section. Three different switching functions are used to simulate the DHD model. By taking advantage of the sensitivity of the GUPFC model to harmonics, a comparison study is conducted to

observe how these switching functions affect the various power quality indices. The case study for this analysis is as follows.

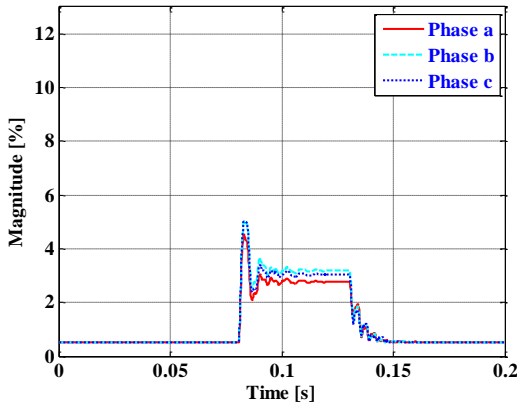
The DHD model of the GUPFC was used to investigate the dynamic response of harmonics to a given disturbance. In this study, three different types of PWM switching functions are used. The per-phase equivalent leakage inductance and winding resistance of the transformer and the capacitance of the DC capacitor are $L_e=0.2$ mH, $R_e=0.04$ Ω , and $C=5000$ μF , respectively. Under steady state conditions, the bus per-phase voltages V_S , V_R , and V_T in per unit at a frequency of 60 Hz, are

$$\begin{aligned} v_{S_a}(t) &= 1.5 \sin \omega_0 t & v_{S_b}(t) &= 1.5 \sin(\omega_0 t - 120^\circ) & v_{S_c}(t) &= 1.5 \sin(\omega_0 t + 120^\circ) \\ v_{R_a}(t) &= 1.6 \sin \omega_0 t & v_{R_b}(t) &= 1.6 \sin(\omega_0 t - 120^\circ) & v_{R_c}(t) &= 1.6 \sin(\omega_0 t + 120^\circ) \\ v_{T_a}(t) &= 1.95 \sin \omega_0 t & v_{T_b}(t) &= 1.95 \sin(\omega_0 t - 120^\circ) & v_{T_c}(t) &= 1.95 \sin(\omega_0 t + 120^\circ) \end{aligned} \quad (5.3)$$

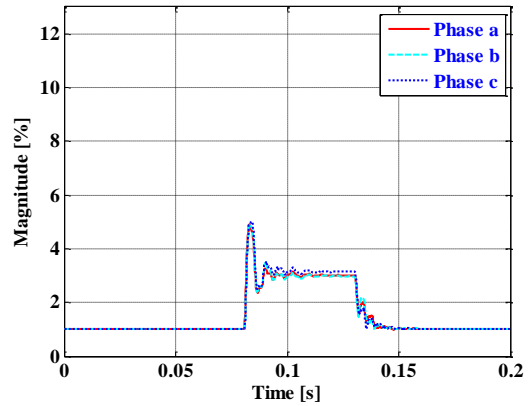
A disturbance in the system is assumed, starting at 0.08 seconds and lasting for 0.05 seconds, resulting in the reduction of the voltage on phase a of $v_T(t)$ by 50% of its given operating value. The simulation starts at $t_0=0$ and ends at the final time of $t_f=0.2$ seconds and uses an integration time step $\Delta t=0.2$ ms. For accuracy, a total of 50 harmonics were considered. The simulations were performed using MATLAB[®] software.

The resultant THD in VSC 1 output current of the GUPFC with the application of three switching functions, Type 1, Type 2, and Type 3, are shown in Figure 87, Figure 88 and Figure 89, respectively. The configurations of these switching functions are shown in Table VI. From these plots it is observed that the THD in current during steady state is lowest with Type 1 and highest with Type 3. The variation in this state is shown in Figure

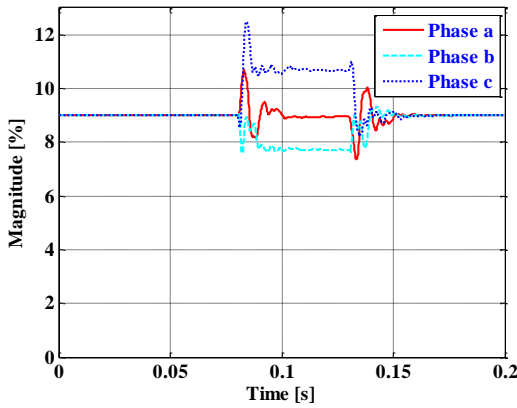
90(d). The variation of THD in current of each phase through the disturbance interval is lowest with Type 3 and highest with Type 1. The ITHD of all three VSCs of the GUPFC are shown in Table VII. THD in current of VSC 3 is greater compared to the other two VSCs. This is due to the fact that during the disturbance period phase *a* voltage at the terminals of VSC 3 is increased by 20 % of its steady state value.



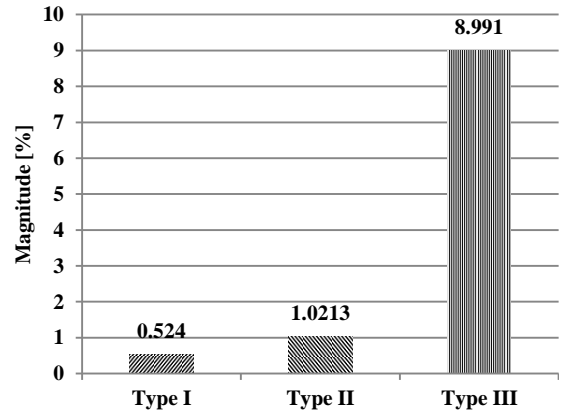
(a)



(b)



(c)



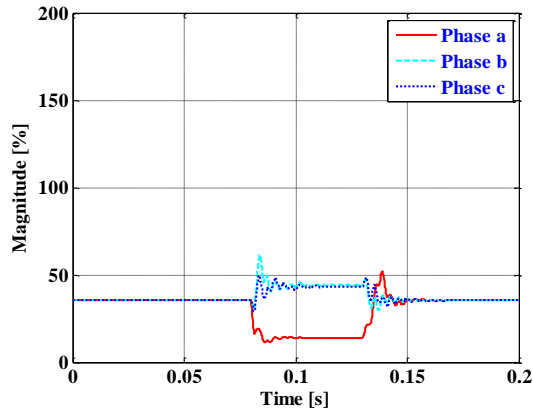
(d)

Figure 90: ITHD in VSC 1 output current (a) Type 1 (b) Type 2 (c) Type 3 (d) ITHD in steady state of VSC 1

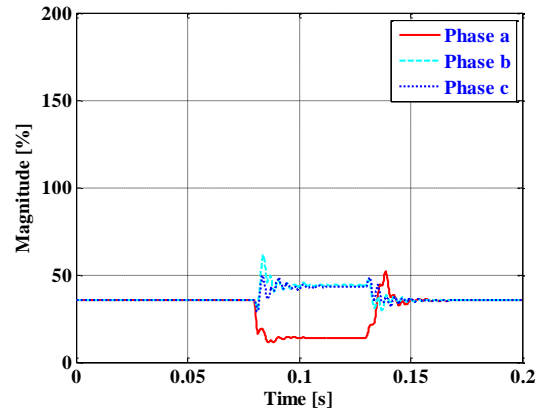
Table VII: THD in current of VSCs of the GUPFC through steady state

| Type | VSC 1 | VSC 2 | VSC 3 |
|-------------|--------------|--------------|--------------|
| Type 1 | 0.524 | 1.2548 | 3.8675 |
| Type 2 | 1.0213 | 2.7547 | 8.4829 |
| Type 3 | 8.991 | 17.9079 | 56.1952 |

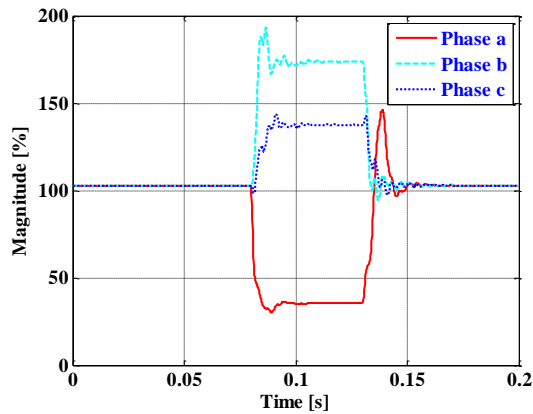
The resultant THD in VSC 1 output voltage of the GUPFC with the application of three switching functions, Type 1, Type 2, and Type 3, are shown in Figure 91(a), (b) and (c), respectively. This distortion is more with Type 3 and less with Type 1 through the steady state period as shown in Figure 91(d). The per phase variations during the disturbance interval are due to the change in DC side voltage and corresponding switching functions.



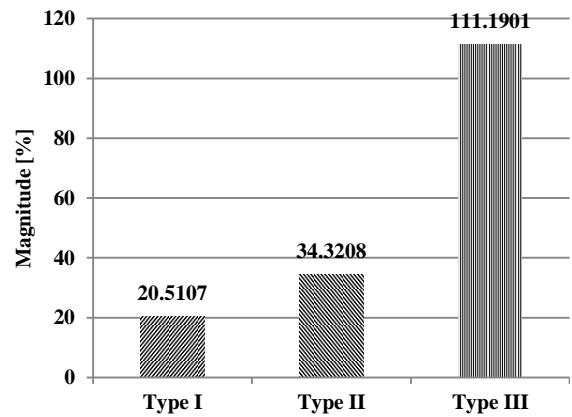
(a)



(b)



(c)



(d)

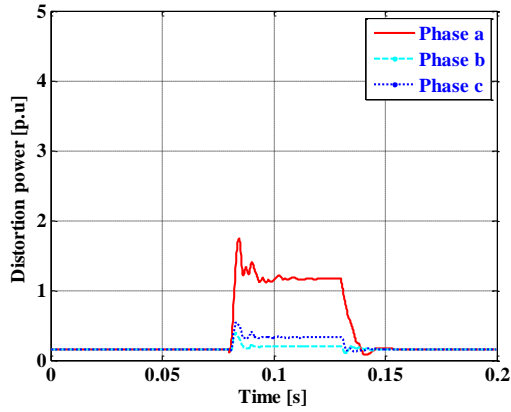
Figure 91: THD in VSC 1 output voltage (a) Type 1 (b) Type 2 (c) Type 3 (d) THD in steady state voltage of VSC 1

THD in current of VSCs of the GUPFC through steady state in all three VSCs of the GUPFC are shown in Table VIII.

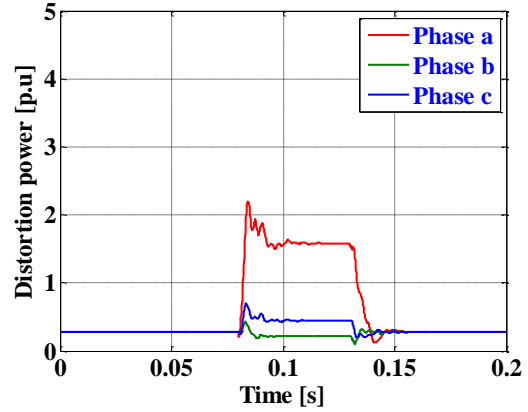
Table VIII: THD in voltage of VSCs of the GUPFC through steady state

| Type | VSC 1 | VSC 2 | VSC 3 |
|-------------|--------------|--------------|--------------|
| Type 1 | 20.5107 | 20.1938 | 20.1938 |
| Type 2 | 34.3208 | 35.4228 | 35.4228 |
| Type 3 | 111.1901 | 102.8312 | 102.8312 |

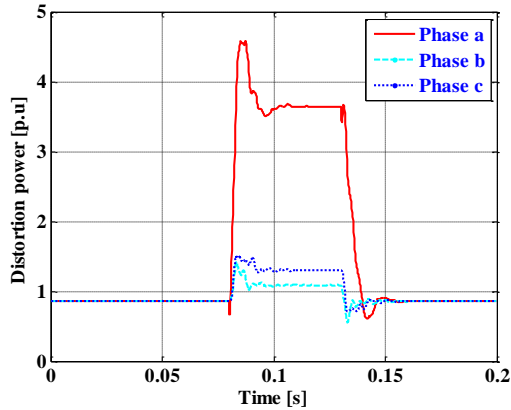
The distortion power output of VSC 3 of the GUPFC, with the application of three switching functions, Type 1, Type 2, and Type 3, are shown in Figure 92(a), (b), and (c), respectively. This distortion is more with Type 3 and less with Type 1 through the steady state period as shown in Figure 92(d).



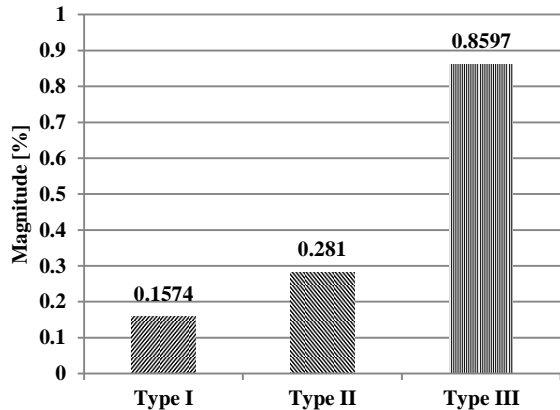
(a)



(b)



(c)



(d)

Figure 92: Distortion power output of VSC 3 (a) Type 1 (b) Type 2 (c) Type 3 (d)

Distortion power in steady state of VSC 3

In all three cases distortion is greater in phase *a* than the other phases. This is because voltage at the terminals at phase *a* of VSC 3 is increased by 20% of its steady state value through the distortion intervals. The distortion powers of all VSCs of the GUPFC are shown in Table IX. Among the three switching functions used in this section,

Type 1 causes lesser THD in voltages and currents, and also lesser distortion power outputs of VSCs.

Table IX: Distortion power outputs of VSCs of the GUPFC through steady state

| Type | VSC 1 | VSC 2 | VSC 3 |
|-------------|--------------|--------------|--------------|
| Type 1 | 1.2321 | 0.4757 | 0.1574 |
| Type 2 | 2.058 | 0.8381 | 0.281 |
| Type 3 | 7.0612 | 2.17 | 0.8597 |

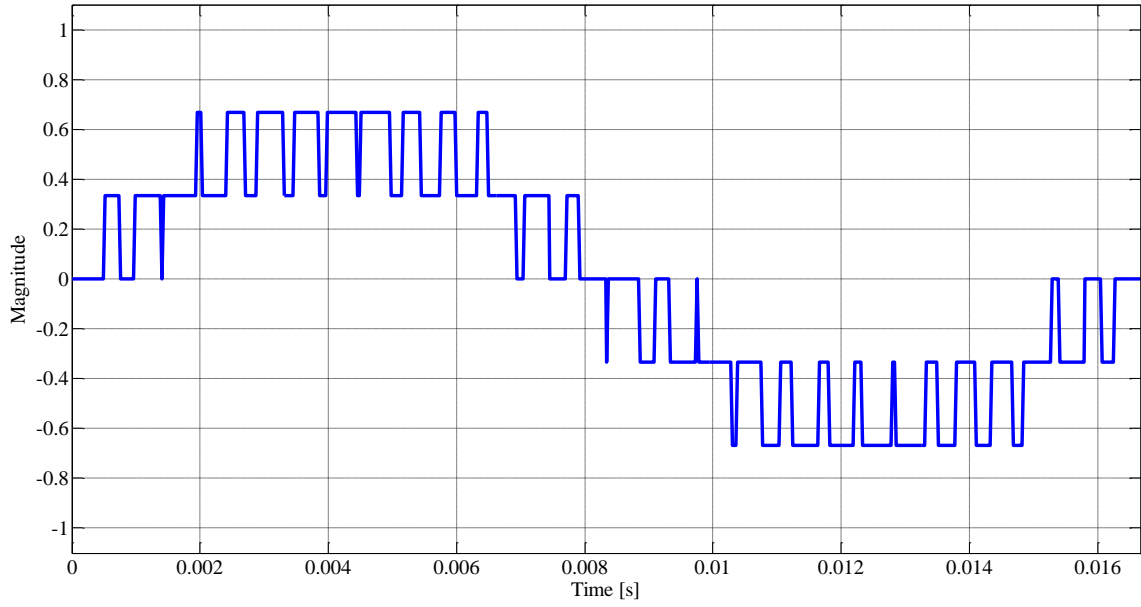
The following section presents the effect of the switching functions on the power quality indices of the GIPFC model in Chapter 4.

5.5 Simulation of the DHD model of the GIPFC with multi-module switching

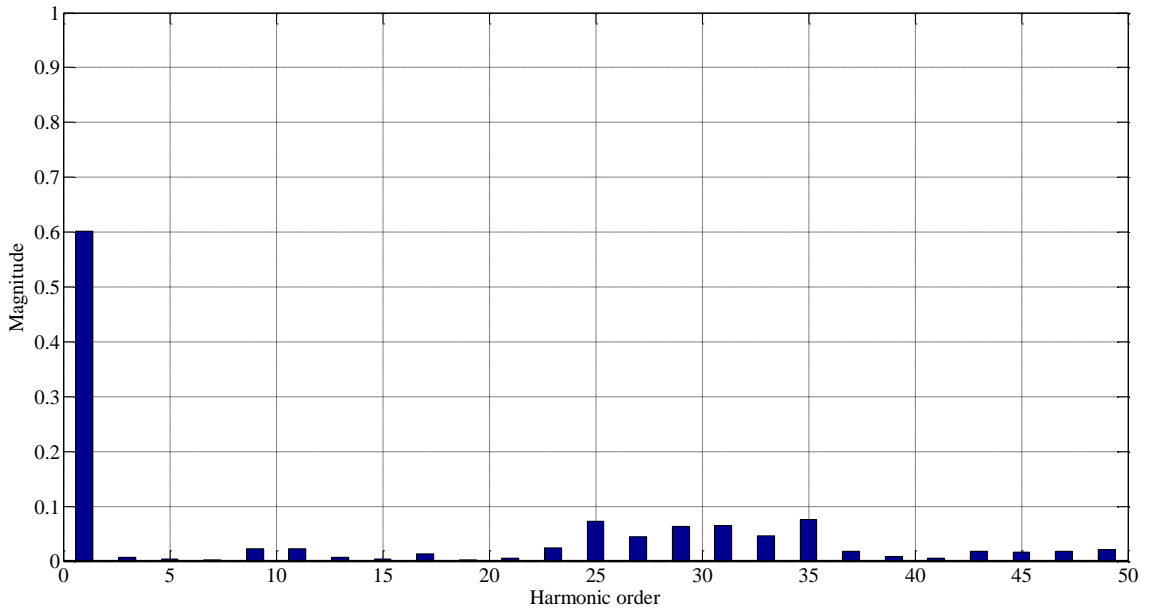
The dynamic GIPFC model was simulated using four kinds of switching functions, two of which were already discussed in the previous sections. The remaining two switching functions are generated by keeping the number of PWMs to three, connected in parallel and constant modulation frequency, and by varying either the MI or the frequency modulation ratio. Among the three switching functions used in the previous section for the analysis of the GUPFC, the application of multi-pulse switching function with three VSCs is the most advantageous one in reducing the THD in voltages and currents. Therefore, three VSCs are used for multi-pulse switching in this section. Apart from the switching function obtained from harmonic elimination method, and Type 1 switching function (which is named as Case A from now onwards) used for the GUPFC

analysis, the other two are developed by making minor changes, and details of those are shown in Table X.

One of the two switching functions is generated by keeping the number of PWMs to three, connected in parallel, with modulation frequency 60, MI equal to 0.6, and frequency modulation ratio equal to 6. The THD in the resultant switching wave is 27.31%. This switching function and harmonic content are shown in Figure 93(a) and (b) respectively and this function is named as Case C.



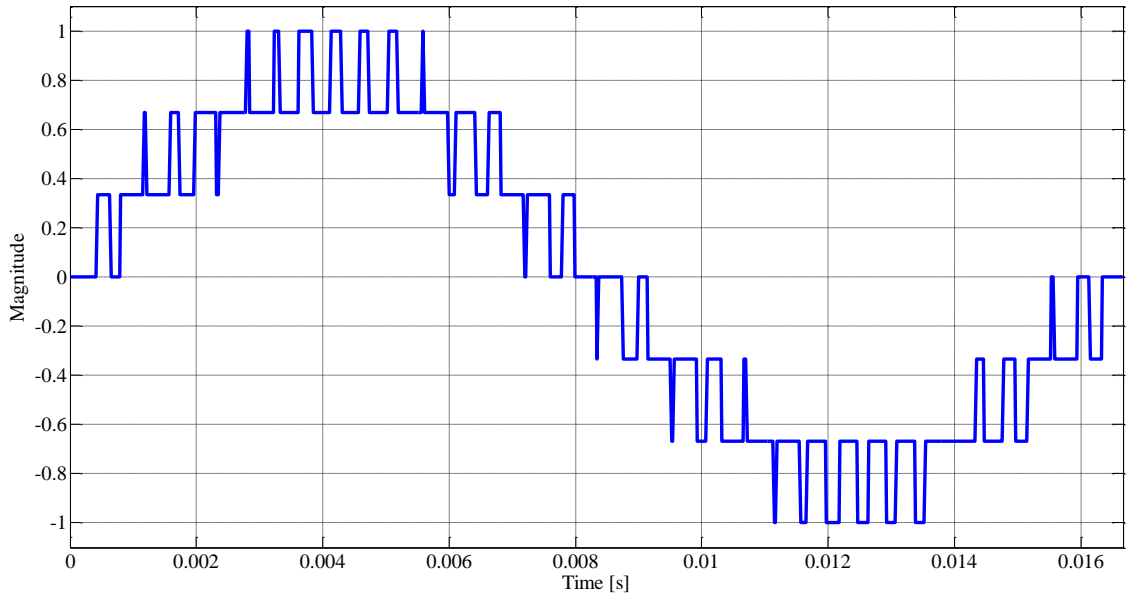
(a)



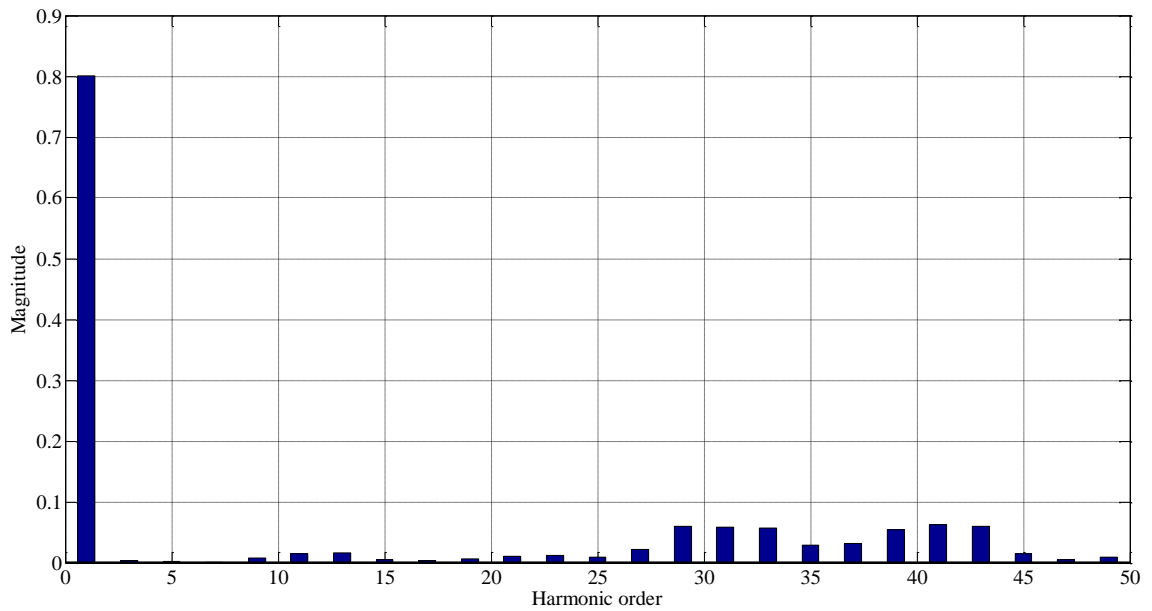
(b)

Figure 93: Switching function - Case C (a) with three PWM converters (b) Harmonic content of the switching waveform

The other switching function is generated by considering three PWMs, connected in parallel, with modulation frequency 60, MI equal to 0.8, and frequency modulation ratio equal to 6. The THD in the resultant switching wave is 19.5621%. The resultant switching function and harmonic content are shown in Figure 94(a) and (b) respectively. This switching function is named as Case D.



(a)



(b)

Figure 94: Switching function - Case D (a) with three PWM converters (b) Harmonic content of the switching waveform

Some of the switching functions discussed so far are organized in Table X and are used to analyze their effects on the GIPFC performance.

Table X: Selected switching functions

| Case | Number of PWM VSC's connected in parallel | MF | CSF | MI | Frequency modulation ratio | Number of harmonics | THD (%) |
|--------|--|----|-----|-----|----------------------------|---------------------|---------|
| Case A | 3 | 60 | 300 | 0.8 | 5 | 50 | 20.005 |
| Case B | Harmonic elimination method discussed in Section 3.3 | | | | | | 32.732 |
| Case C | 3 | 60 | 300 | 0.6 | 5 | 50 | 27.312 |
| Case D | 3 | 60 | 360 | 0.8 | 6 | 50 | 19.562 |

The DHD model of the GIPFC in Section 4.5.2 is used to investigate the dynamic response of harmonics to a given disturbance. PWM switching functions presented in the above table were used. The per-phase equivalent leakage inductance and winding resistance of the transformer and the capacitance of the DC capacitor are $L_e=0.2$ mH, $R_e=0.04$ Ω , and $C=5000$ μF , respectively. Under the steady state conditions the bus per phase voltages V_A , V_B , V_C , and V_D in per unit at a frequency of 60 Hz are

$$\begin{aligned}
 v_{Sa}(t) &= 1.1 \sin \omega_0 t & v_{Ra}(t) &= 1.3 \sin \omega_0 t \\
 v_{Sb}(t) &= 1.1 \sin (\omega_0 t - 120^\circ) & v_{Rb}(t) &= 1.3 \sin (\omega_0 t - 120^\circ) \\
 v_{Sc}(t) &= 1.1 \sin (\omega_0 t + 120^\circ) & v_{Rc}(t) &= 1.3 \sin (\omega_0 t + 120^\circ)
 \end{aligned}$$

$$\begin{aligned}
v_{1a}(t) &= 1.8 \sin \omega_0 t & v_{2a}(t) &= \sin \omega_0 t \\
v_{1b}(t) &= 1.8 \sin(\omega_0 t - 120^\circ) & v_{2b}(t) &= \sin(\omega_0 t - 120^\circ) \\
v_{1c}(t) &= 1.8 \sin(\omega_0 t + 120^\circ) & v_{2c}(t) &= \sin(\omega_0 t + 120^\circ) \\
v_{3a}(t) &= 1.5 \sin \omega_0 t & v_{4a}(t) &= 1.2 \sin \omega_0 t \\
v_{3b}(t) &= 1.5 \sin(\omega_0 t - 120^\circ) & v_{4b}(t) &= 1.2 \sin(\omega_0 t - 120^\circ) \\
v_{3c}(t) &= 1.5 \sin(\omega_0 t + 120^\circ) & v_{4c}(t) &= 1.2 \sin(\omega_0 t + 120^\circ)
\end{aligned} \tag{5.4}$$

A disturbance is assumed in the voltage starting at 0.07 seconds and lasting for 0.05 seconds, and during the disturbance, the phase *a* voltage of $v_{1a}(t)$ is 150% of its value. The simulation was started at $t_0 = 0$ seconds with final time $t_f = 0.2$ seconds and used an integration time step $\Delta t = 0.16667$ ms. For accuracy, the simulation was required to include the calculation of 50 harmonics. For these simulations, a control system was not used to keep the DC voltage constant across the capacitor. As mentioned before, the accurate harmonic information obtained from the simulation of the DHD model of the GIPFC is for power quality (PQ) assessment. Some of the PQ indices, such as active power, reactive power, apparent power, distortion power, RMS voltage and current, and THD in voltage and current in all three phases, are of interest for PQ assessment and control. The simulation was started at $t_0 = 0$ seconds with final time $t_f = 0.2$ seconds and used an integration time step $\Delta t = 0.1667$ ms. For accuracy, 50 harmonics were included for the simulation.

The simulation results presented in Figure 95 show the DC component of the DC side voltage with four different switching functions mentioned in Table X.

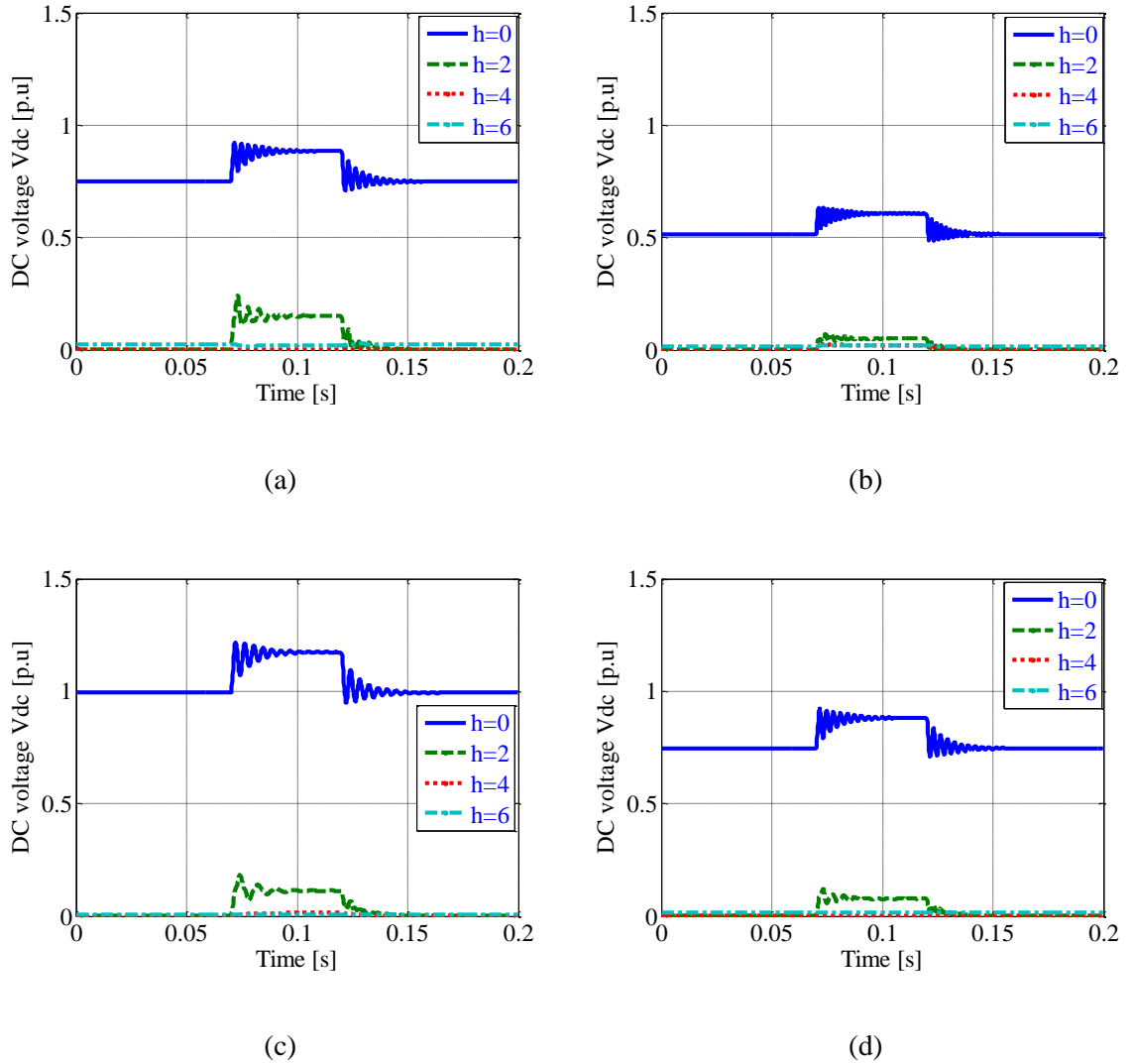


Figure 95: DC voltage (a) Case A (b) Case B (c) Case C (d) Case D

The following observations were made based on Figure 95:

- The DC component of the DC side voltage of the capacitor during steady state is at a maximum with Case C and at a minimum with Case B.
- Apart from the DC component, 2nd harmonic component is only present in all the Cases

- The larger the THD in switching functions, the lower the DC voltage.

The DC component of the DC voltages in Figure 95, during steady state period, was plotted in Figure 96. It is observed from the plot that the magnitude of the DC component is almost the same in Cases A and D as their THD in switching functions are almost equal and lowest with Case B as the THD is greatest among the switching wave forms that were considered.

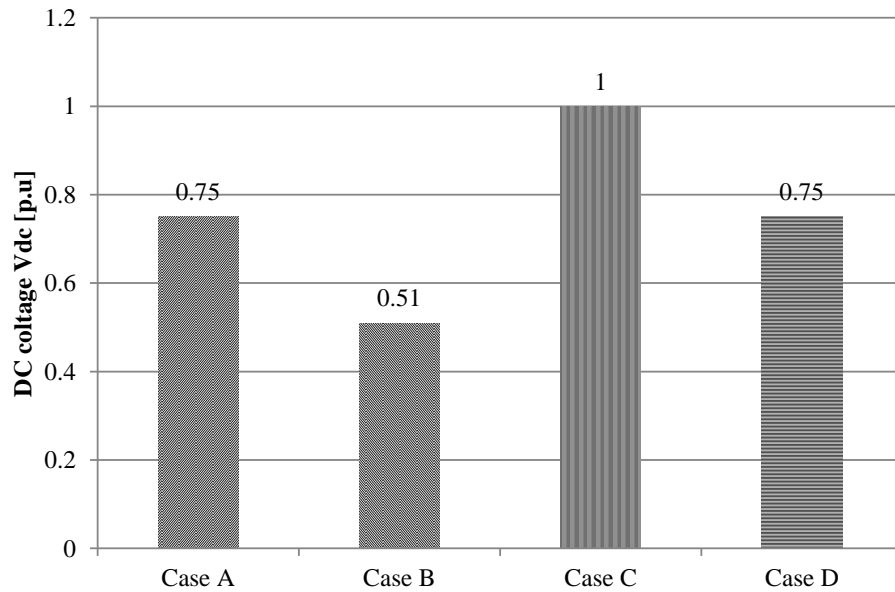


Figure 96: Magnitude of DC component of DC voltage during steady state

Distortion power during the steady state and average distortion power during the disturbance period with four switching functions in all three phases of all VSCs are listed in Table B-1, Appendix B.

Figure 97 shows the distortion power of all four VSCs during steady and transient periods for all the three phases. Out of these, Case B exhibits more distortion in three

phases of the VSC 1. Cases A and D display almost same distortion power in all three phases. The per-phase distortion and apparent powers (Figure 98) during the steady state period are greatest in Case B and lowest with Cases A and D. Largest distortion during the disturbance period for phase *b* occurred in Case B while for phase *a* the distortion and apparent powers dropped from their corresponding steady state values.

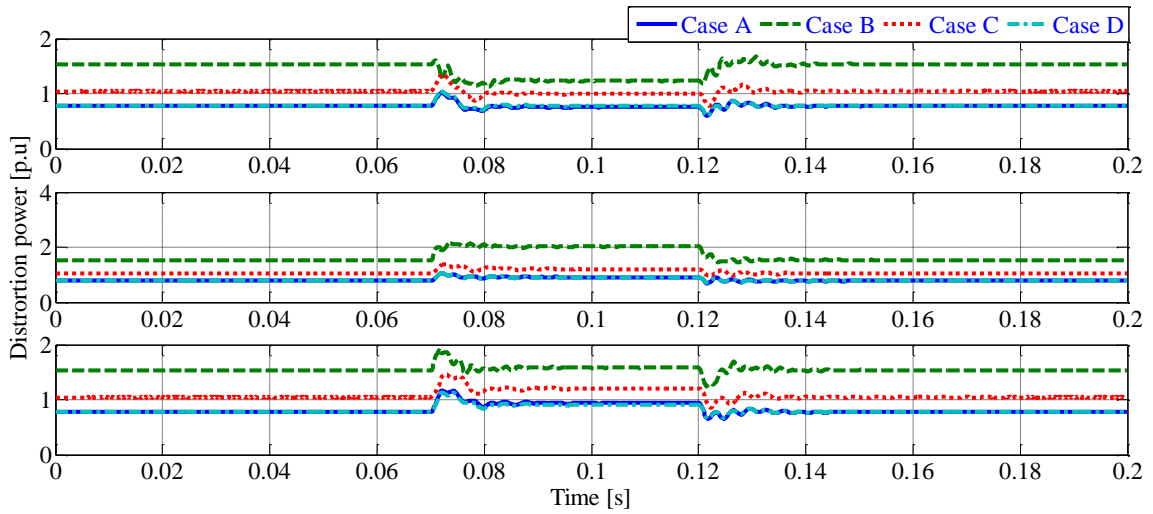


Figure 97: Distortion power output of all four VSCs

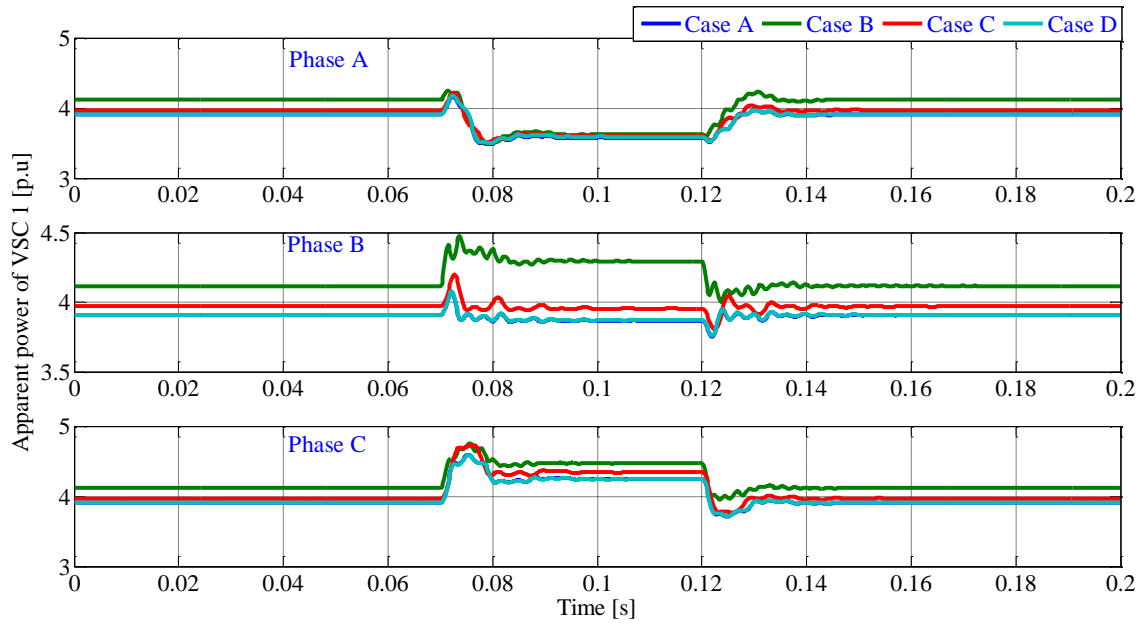


Figure 98: Apparent power output of all four VSCs

The THD in voltages and currents of VSC 1 for four switching cases are shown in Figure 99 and Figure 100, respectively. It is evident from these plots that, switching Cases A and D caused minimum distortion in voltages and currents of the three phases. The steady state values of THD in per-phase voltages and currents are almost the same, but some variations can be observed in them through the disturbance intervals, which are due to the changes in DC side voltage, terminal voltages in corresponding phases, and the switching functions. From these plots it can be inferred that the THD in switching waveform is high, and it also aggravates the distortions in voltages and currents of the VSCs.

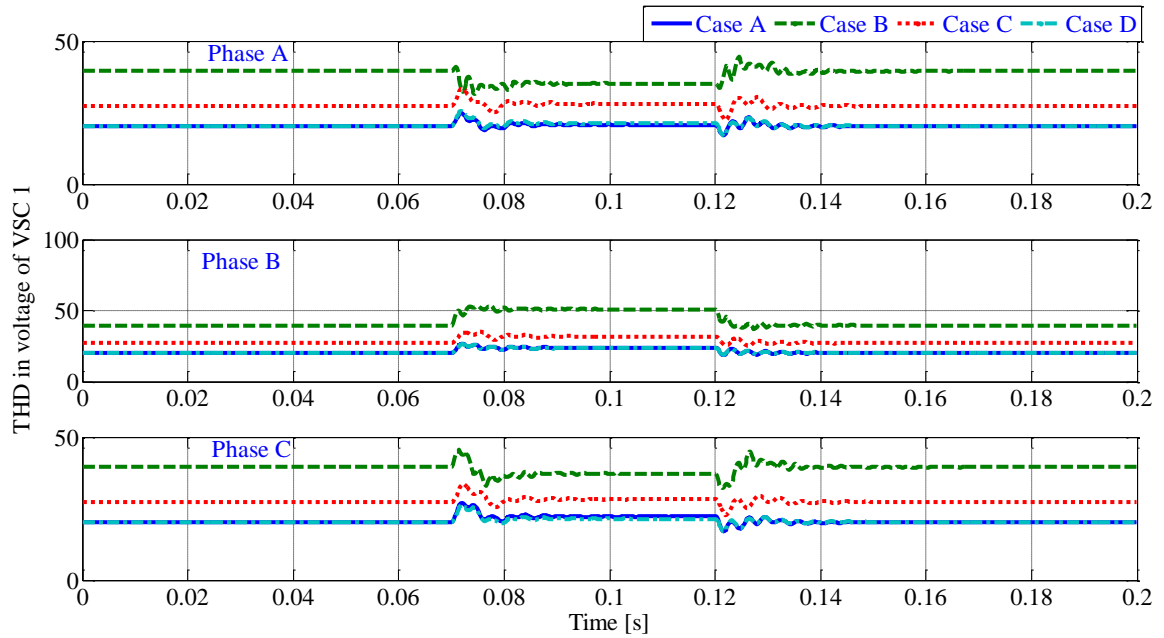


Figure 99: THD in output voltage of VSC 1

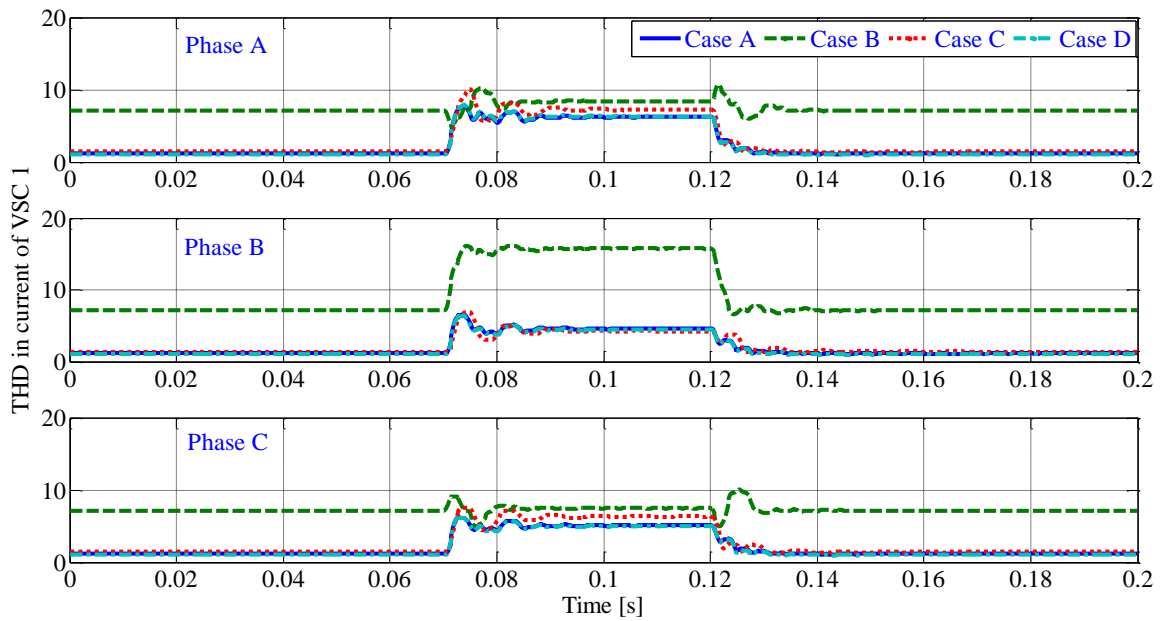


Figure 100: THD in output current of VSC 1

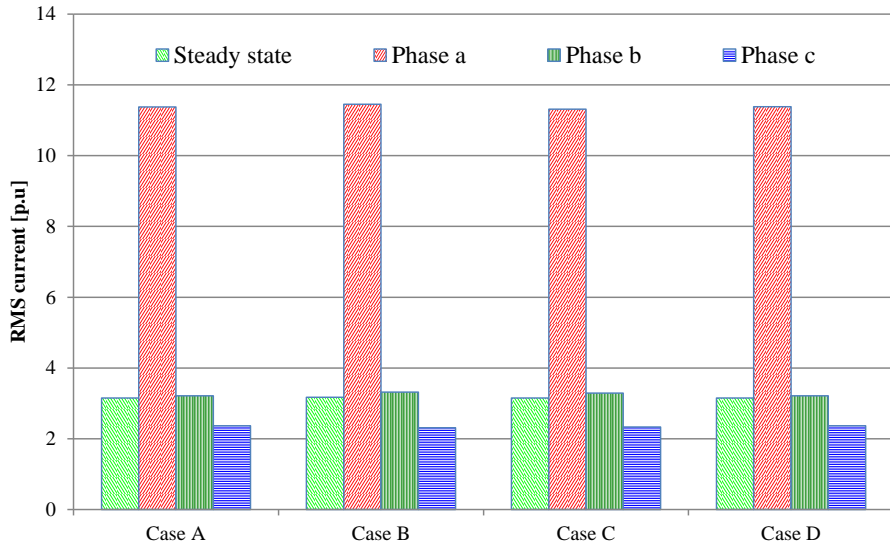
The following section is an attempt to compare the average per-phase changes in selected PQ indices of the GIPFC in order to observe the effect of these switching functions on them.

5.6 Comparison of average distortions with various switching functions

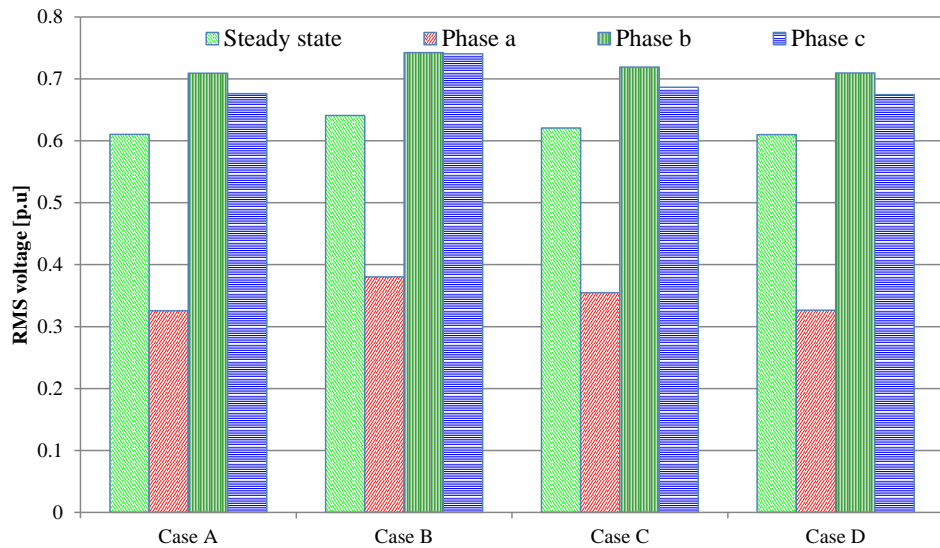
The information presented as bar graphs, in Figure 101, shows the per-phase average change in RMS output current and voltage of VSC 4 in response to the disturbance with the individual application of switching functions - Cases A, B, C and D. During the disturbance, phase *a* voltage, $v_1(t)$ of the GIPFC, is 150% of its original value. This change at VSC 4 is the most significant one out of all VSCs as it is directly connected to the line where $v_1(t)$ was changed. There is a 350% increase in phase *a* current from its steady state value while the average phase *b* current is very close, but average change in phase *c* is lower than that of the steady state current. The variations in phases *b* and *c* are due to the change in DC side voltage and their corresponding switching functions. The detailed information presented as bar graph in Figure B-1, Appendix B, shows the RMS values of output currents of the four VSC's of the GIPFC, in response to a disturbance with the individual application of switching functions - Cases A, B, C and D. The average change in magnitudes of RMS currents of all VSC's of the GIPFC during the disturbance period are presented in Table B-I, Appendix B.

The average change in the RMS value of output voltage of phase *a* of VSC 4 is lower than its steady state value. This can be attributed to the fact that the increase in

current during the disturbance produces more output current, which further leads to an increased voltage drop across the impedance that is connected to VSC 4. A prominent change is observed in Case B. The average change in voltages of phases *b* and *c* of VSC 4 are close to the steady state voltage.



(a)

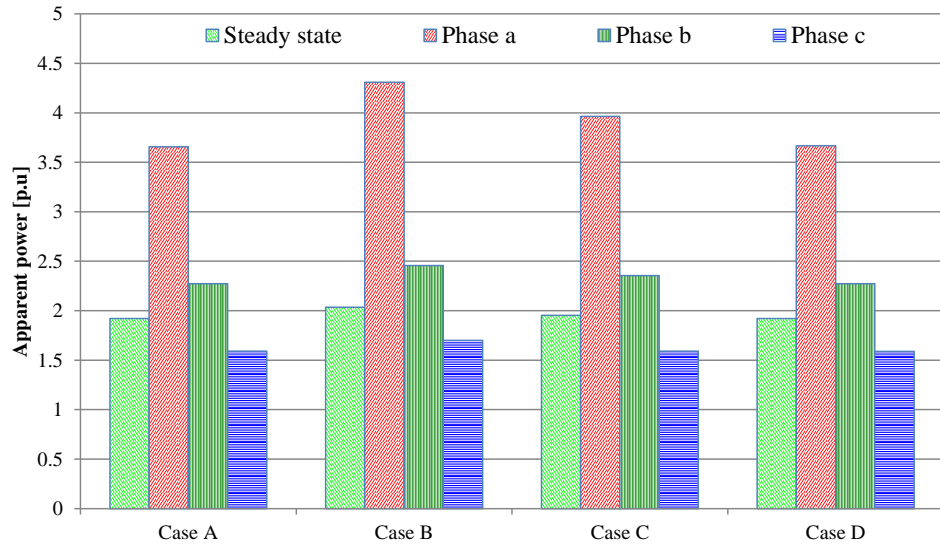


(b)

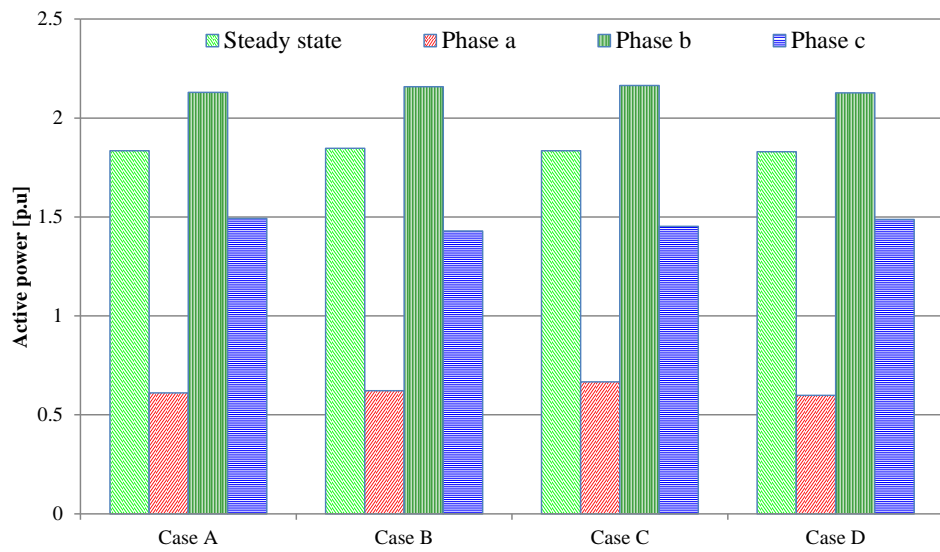
Figure 101: The average change in per-phase RMS values of VSC 4 of (a) The output current (b) The output voltage

The average change in per phase output, apparent, active, reactive and distortion powers of VSC 4 through the disturbance interval and steady state, in all four different

cases, are shown in Figure 102.1 and Figure 102.2. These variations are due to the change in voltages and currents at the terminals of VSC 4. The switching functions used in Cases A and D account for the same amount of average changes in the per-phase apparent power whereas Case B recorded increased variation in the same. The detailed information presented as bar graphs in Figure B-2, Figure B-3, Figure B-4 and Figure B-5, Appendix B, show the average change in distortion, apparent, active and reactive power outputs of the four VSC's of the GIPFC in response to a disturbance with the individual application of switching functions - Cases A, B, C and D. The average change in distortion, apparent, active and reactive power outputs of all VSC's of the GIPFC during the disturbance period are presented in Table B-II, Table B-III, Table B-IV and Table B-V, Appendix B, respectively.

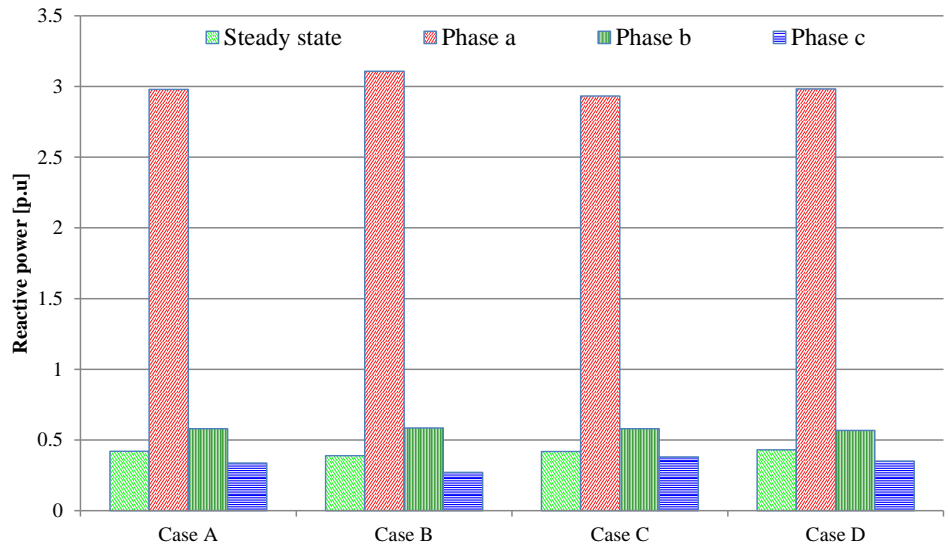


(a)

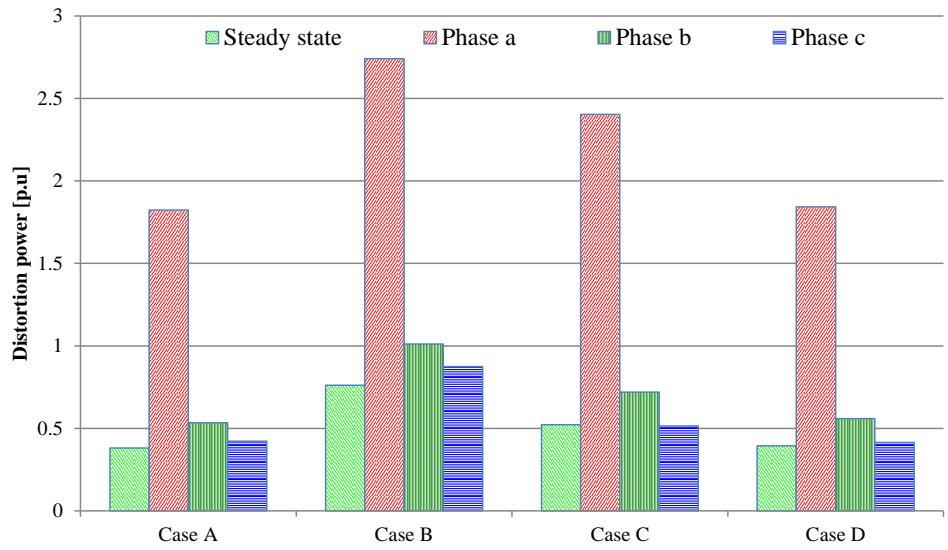


(b)

Figure 102.1: The average change in per-phase output (a) Apparent power (b) Active power



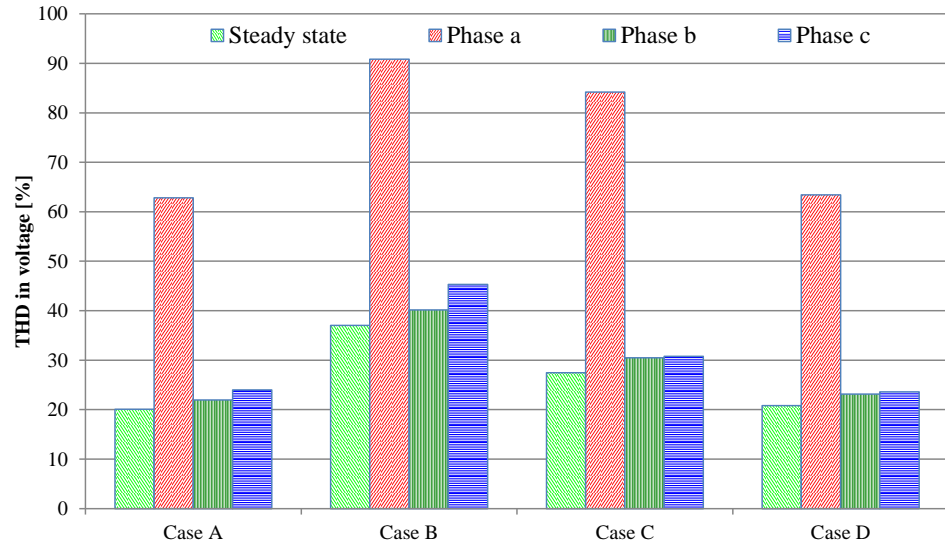
(a)



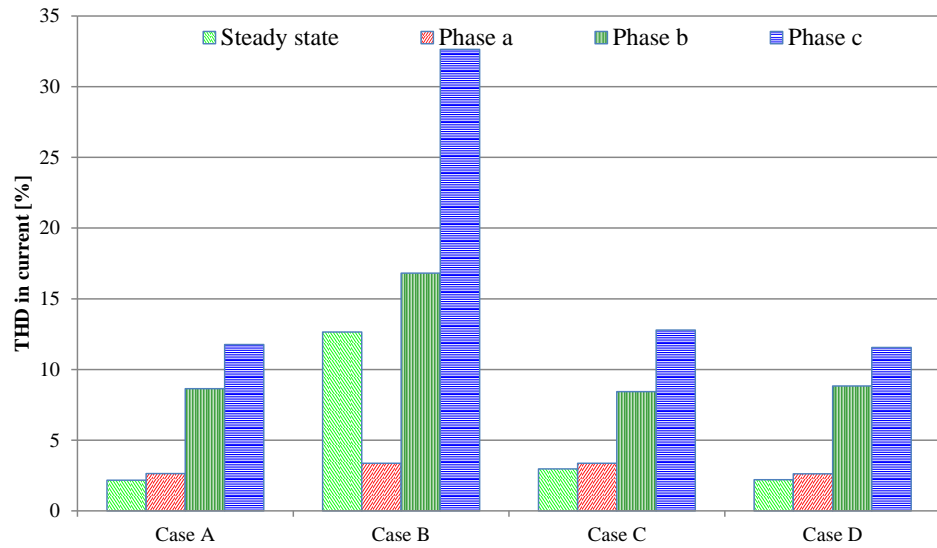
(b)

Figure 102.2: The average change in per-phase output (a) Reactive power (b) Distortion power of VSC 4

There is prominent distortion that can be observed in phase a during the disturbance interval in all four cases. The average change in distortion power of phase c is lowest with Case D and phase b is lowest with Case A. This change is more conspicuous in Case B due to the immense harmonic distortion of the switching function. There is noticeable average change in phase a in all four cases. This can be associated to the variation in voltage of phase a at the terminals of VSC 4 during the disturbance period. The average change in THD in voltages and currents of VSC 4 in the steady state as well as during the disturbance interval are shown in Figure 103. The maximum THD in voltage, as expected, can be observed in phase a due to variation of voltage at that phase during the disturbance interval. The higher distortion in Case B aggravates distortion in all the three phases in steady state as well as disturbance intervals.



(a)



(b)

Figure 103: The average change in per-phase THD in output (a) Voltage of VSC 4 (b)

Current of VSC 4

The detailed information presented as bar graph in Figure B-5, Appendix B, shows the average change in THD in currents of the four VSC's of the GIPFC in response to a disturbance with the individual application of switching functions - Cases A, B, C and D. The average change in THD in currents of all VSC's of the GIPFC during the disturbance period is presented in Table B-VI, Appendix B.

5.7 Conclusion

The DHD models of multiline FACTS controllers, the GUPFC and GIPFC, were simulated using multi-pulse switching functions. This study provided an understanding of the reaction of these controllers to various switching functions and their effect on the PQ indices under steady and disturbance periods. The average deviations in each phase of VSC of the GIPFC with various switching functions were calculated throughout the simulation period, and presented in bar graphs. It is also observed that the greater the distortion in the switching functions, the higher is the THD in output currents and voltages of the controllers. Out of all the switching functions that were considered for the simulations, Type 1 for the GUPFC and Case A/ Case D for the GIPFC yielded the most prominent results in power quality point of view. The usefulness of the dynamic models of multiline controllers that were developed in this research work helped to analyze their performance.

CHAPTER VI

CONCLUSIONS AND RECOMMENDATIONS FOR FUTURE WORK

6.1 Conclusions

Use of power electronics converters in large-scale power systems is gaining popularity due to the availability of semiconductor devices with enhanced performance and ratings. These devices have been in use across the globe in numerous applications such as HVDC transmission systems, FACTS, and custom power system (CUPS). Use of these devices in a wider range is warranted in order to enhance electrical and economic performances of the power transmission and distribution systems. However, power electronics converters produce undesirable voltage and current distortions, and harmonics because of their nonlinear behavior. Therefore, it is necessary to analyze the behavior of these controllers before they can be used in transmission systems.

WFFT and DHD methods are the most widely used methods to study the nonlinear behavior of power electronics converters. However, the main disadvantage of

the WFFT method is that the accuracy of the harmonic calculations is proportional to window size, specifically when disturbance intervals are very short. Therefore the DHD method was adopted in this work to develop the dynamic models of FACTS controllers (SSSC, UPFC, FC-TCR, TCSC, GUPFC, IPFC, and GIPFC) and study the dynamic behavior of the harmonics of these controllers. All of these models were simulated using PWM switching function. The GUPFC and GIPFC models were also simulated using multi-pulse switching functions.

Power quality of the DHD models was estimated by simulating them (using PWM switching) in the presence of voltage disturbance and the results are presented in Chapters 3 and 4. The results obtained from simulations demonstrated that the dynamic harmonic response of FACTS controllers is superior to that of time-domain simulations (WFFT). It was also observed that the DHD models developed in this research were able to estimate the dynamic response of FACTS controllers for a disturbance of lower magnitude and of shorter duration.

The dynamic harmonic information obtained from the DHD models for FACTS controllers is useful for power quality assessment and can be used as a tool for analyzing the system under the steady state and transient conditions. Proposed DHD models have the ability to determine the dynamic behavior of harmonics during transient conditions (unlike TD or HD models).

Harmonic domain (HD) models were also developed for the GUPFC, and the GIPFC. These models are useful for resonance prediction analysis and harmonic propagation studies.

UPFC, GUPFC, IPFC, and GIPFC controllers require a constant DC voltage and therefore feedback controllers that help maintain constant DC voltage constant were developed in this research. An attempt has been made to compare the power quality indices obtained by controlling the DC voltage at constant value and by allowing fluctuations in DC voltage. This process demonstrated the influence of a control system on power quality indices and explained how the controllers react to the control system during a disturbance.

Simulations were performed on the proposed DHD models (UPFC, GUPFC, IPFC, and GIPFC) in time and harmonic domains and the results were validated. Coincidence of magnitudes and frequencies of three phase currents of the VSCs was observed during validation.

Results from the simulations of GUPFC and GIPFC using multi-pulse switching functions demonstrated the reaction of these controllers to various switching functions and their effect on PQ indices (under steady and disturbance periods). Average deviations in each of the VSC phases of the GIPFC were computed through the simulation.

6.2 Future research work

DHD models for custom power devices such as DSTATCOM, DVR, and UPQC should be developed. Custom power devices are the best possible solutions to mitigate a set of power quality disturbances. They were first introduced by N. G. Hingorani in 1995 as an extension of the Flexible AC Transmission Systems (FACTS) concept to the distribution side [33] of the power system. However, the modeling of custom power

compensating devices using harmonic domain analysis has not been investigated. Harmonic assessment tools capable of modeling a wide range of nonlinear devices will be valuable resources in both the design and operation of future power networks that use custom power devices.

Commercially available custom power devices tend to protect against a group of common power quality disturbances. DSTATCOM, DVR, and UPQC devices can be used to mitigate disturbances such as voltage transients and fluctuations in the steady-state voltage levels that occur in the distribution system. A comprehensive comparative analysis of these devices for different applications and under different fault conditions has not been published. Such an analysis would be beneficial for selecting the proper device for a particular situation. In addition, if reliability data can be obtained from the manufacturers, a reliability analysis of these devices would be very valuable to design engineers.

It is necessary to identify operating points that could cause distortion due to the presence of resonant condition when FACTS controllers are embedded in large power systems. The frequency response characteristics of the multi-line FACTS controllers should be investigated.

The real Fourier and Hartley transforms require real algebra for conducting all operations. This includes relinearization process, polynomial evolution using self and mutual convolutions. More efficient iterative harmonic solutions can be achieved by the combined use of Hartley and real Fourier than those achieved using the complex Fourier harmonic domain [75]. Switching function representation using Fourier requires more number of coefficients than Walsh series. For a small degree of accuracy, Walsh series

requires lesser number of terms than Fourier. This should lead to efficient solutions [74]. Steady state and dynamic modeling of the FACTS controllers using alternative domains such as, real Fourier, Hartley, and Walsh in place of complex Fourier transforms should be investigated in order to find the suitable transform for a particular application.

Harmonic power flow when FACTS controllers are embedded in a larger power system and their interaction with the other circuit elements should be analyzed

The proposed DHD models harmonic outputs are used to design a control system to keep the DC side voltage constant in this research work. Since the harmonic information obtained from the proposed DHD models is more accurate than that from time domain simulations, this information should also be used to design control systems to control AC side real and reactive power in a transmission network.

REFERENCES

- [1] N.G. Hingorani, "High Power Electronics and Flexible AC Transmission Systems," *IEEE Power Engineering Review*, Vol. 8, No. 7, July 1988, pp. 3-4
- [2] N. Mohan, T.M. Undeland, W.P. Robbins, *Power Electronics: Converters, Applications, and Design*, John Wiley & Sons, New York, 1989.
- [3] N. G. Hingorani., L. Gyugyi., *Understanding FACTS: Concepts and Technology of Flexible AC Transmission Systems*, IEEE Press, New York, 2000.
- [4] S. Banerjee, G.C. Verghese, *Nonlinear Phenomena in Power Electronics*, IEEE Press, New York, 2001.
- [5] E. Acha, A. Semlyen, N. Rajakovic, "A Harmonic Domain Computational Package for Nonlinear Problems and its Application to Electric Arcs," *IEEE Transactions on Power Delivery*, Vol. 5, No. 3, July 1990, pp. 1390-1397.
- [6] J.A. Medina, *Power Systems Modelling in Harmonic Domain, PhD Thesis*, University of Canterbury, Christchurch, New Zealand, 1992.
- [7] E. Acha, A. Semlyen, and N. Rajakovic, "A harmonic domain computational package for nonlinear problems and its application to electric arcs," *IEEE Transactions on Power Delivery*, Vol. 5, July 1990, pp. 1390-1397.
- [8] E. Acha, "Modeling of Power System Transformers in the Complex Conjugate Harmonic Domain Space," Ph.D. dissertation, University of Canterbury, Christchurch, New Zealand, 1988.
- [9] A. Semlyem, N. Rajakovic, "Harmonic Domain Modeling of Laminated Iron Core," *IEEE Transactions on Power Delivery*, Vol. 4, No. 1, January 1989, pp 382-390.

- [10] E.Acha, and M. Madrigal, *Power Systems Harmonics: Computer modeling and analysis*, New York: Wiley, 2001.
- [11] G. T. Heydt, P. S. Fjeld, C. C Liu, D. Pierce, L. Tu, G. Hensley, “ Application of the windowed FFT to electrical power quality assessment,” Vol. 14, No. 4, pp. 1411–1416 October 1999.
- [12] G. N. Bathurst, B.C. Smith, N. R. Watson, J. Arillaga, “Modeling of HVDC transmission systems in the harmonic domain,” *IEEE Transactions on Power Delivery*, Vol. 14, No. 3, July 1999, pp. 1075–1080.
- [13] G. N. Bathurst, N. R. Watson, “Modeling of bipolar HVDC links in the harmonic domain,” *IEEE Transactions on Power Delivery*, Vol. 15, No. 3, July 2000, pp. 1034–1038.
- [14] Bruce C. Smith, “A harmonic domain model for the interaction of the HVdc converter with ac and dc systems,” Ph.D. dissertation, University of Canterbury, Christchurch, New Zealand, 1996.
- [15] M. Madrigal, “Modelling of Power Electronics Controllers for Harmonic Analysis in Power Systems,” Ph.D. dissertation, Univ. Glasgow, 2001.
- [16] L. Lima, A. Semlyen, M. R. Iravani, “Harmonic domain periodic steady-state modeling of power electronics apparatus: FC-TCR and TCSC,” *IEEE Transactions on Power Delivery*, Vol. 18, No. 3, July 2003, pp. 960–967.
- [17] H. García, M. Madrigal, B. Vyakaranam, R. Rarick, and F. E. Villaseca, “Dynamic Companion Harmonic Circuit Models for Analysis of Power Systems with Embedded Power Electronics Devices,” *Electric Power Systems Research Journal*, Vol. 81, No. 2, Feb 2011, pp. 340–346.

- [18] J. Rico, E. Acha, and T. J. E. Miller, "Harmonic domain modeling of three phase Thyristor-controlled reactors by means of switching vectors and discrete convolutions," *IEEE Transactions on Power Delivery*, Vol. 9, July 1994, pp. 1609–1615.
- [19] M. Madrigal, and E. Acha, "Modelling of Custom Power Equipment using Harmonic Domain Techniques," *Proceedings of the 9th International Conference on Harmonics and Quality of Power*, Vol. 1, October 2000, pp. 264–269.
- [20] C. D. Collins, G. N. Bathurst, N. R. Waston, and A. R. Wood, "Harmonic domain approach to STATCOM modeling," *IEE Proceedings on Generation, Transmission, Distribution*, Vol. 152, No. 2, March 2005, pp. 194–200.
- [21] C.D. Collins, N.R. Waston, and A. R. Wood, "Unbalanced SSSC modeling in the harmonic domain," *Proceedings of the 7th International Power Engineering Conference*, Vol. 2 , Nov. 2005, pp. 705–710.
- [22] C. D. Collins, "FACTS device modeling in the harmonic domain," Ph.D. Dissertation, Univ. Canterbury, New Zealand, 2006.
- [23] C. D. Collins, N. R. Waston, and A. R. Wood, "UPFC modeling in the harmonic domain," *IEEE Transactions on Power Delivery*, Vol. 21, No. 2, April 2006, pp. 933–938.
- [24] J. Jesus Rico, M. Madrigal, and E. Acha, "Dynamic Harmonic Evolution Using the Extended Harmonic Domain," *IEEE Transactions on Power Delivery*, Vol. 18, No. 2, April 2003, pp. 587–594.

- [25] J. Jugo, A. Anakabe, J.M Collantes, “Control design in the harmonic domain for microwave and RF circuits,” *IEE proceedings Control Theory & Applications*, Vol. 150, No. 2, March 2003, pp. 127–131.
- [26] Madrigal and J. J. Rico, “Operational Matrices for the Analysis of Periodic Dynamic Systems,” *IEEE Transactions on Power System*, Vol. 19, No. 3, August 2004, pp. 1693–1695.
- [27] B. Vyakaranam, M. Madrigal, F. E. Villaseca, and R. Rarick, “Dynamic Harmonic Evolution in FACTS via the Extended Harmonic Domain Method,” Power and Energy Conference at the University of Illinois, Urbana-Champaign, IL, February 2010.
- [28] H. García, M. Madrigal, B. Vyakaranam, R. Rarick, and F. E. Villaseca, “Dynamic Companion Harmonic Circuit Models for Analysis of Power Systems with Embedded Power Electronics Devices,” *Electric Power Systems Research Journal* (Elsevier), October 2010, pp. 340–346.
- [29] Pável Zúñiga-Haro, “Harmonic Modeling of Multi-pulse SSSC,” *IEEE Bucharest Power Tech Conference*, Bucharest, Romania, October 2009, pp. 1–8.
- [30] H. García and M. Madrigal, “Modeling and analysis of a TCR-FC Reactive Power Compensator Using the Harmonic Domain,” *2009 Electronics, Robotics and Automotive Mechanics Conference*, December 2009, pp. 452–456.
- [31] ABB. (2007), *SVC to Increase Reliability and Reduce Congestion over Multiple 500 kV Lines* [online]. Available : <http://www.abb.com/>
- [32] G. Arindam, L. Gerard, *Power Quality Enhancement Using Custom Power Devices*, Kluwer Academic Publishers, Boston, 2002.

- [33] N.G. Hingorani, "Introducing custom power," *IEEE Spectrum*, June 1995, Vol. 32, No. 6, pp. 41–48.
- [34] Amit Kumar Jain and Raja Ayyanar, *Power Electronics*, McGraw-Hill, 2006.
- [35] North American Electric Reliability Corporation, "2007 Long-Term Reliability Assessment 2007–2016," Version 1.1, October 2007.
- [36] IEEE Standards Coordinating Committee 22-Power Quality, Annual report to the Standard board, February 25, 2002.
- [37] G.T. Heydt, "Power Quality Engineering," *IEEE Power Engineering Review*, Vol. 21, No. 9, September 2001, pp. 5-7.
- [38] M.H.J. Bollen, *Understanding Power Quality Problems: Voltage Sags and Interruptions*, IEEE Press, New York, 2000.
- [39] L. Gyugyi, C.D Schauder, K.K Sen, "Static synchronous series compensator: a solid-state approach to the series compensation of transmission lines," *IEEE Transactions on Power Delivery*, Vol. 12, No.1, July 1997, pp. 406– 417.
- [40] K.K Sen, "SSSC-static synchronous series compensator: theory, modeling, and application," *IEEE Transactions on Power Delivery*, Vol. 13, No.1, July 1998, pp. 241–246.
- [41] L. Gyugyi, "A Unified Power Flow Control Concept for Flexible AC Transmission Systems," *IEE proceedings-C*, Vol. 139, No.4, July 1992, pp. 323-331.
- [42] L. Gyugyi, C.D. Schauder, S.L. Williams, T.R. Rietman, D.R. Torgerson, A. Edris, "The Unified Power Flow Controller: A New Approach to Power Transmission Control," *IEEE Transactions on Power Delivery*, Vol. 10, No. 2, April 1995, pp. 1085-1093.

- [43] K.K. Sen, E.J. Stacey, "UPFC- Unified Power Flow Controller: Theory, Modeling, and Applications," *IEEE Transactions on Power Delivery*, Vol. 13, No. 4, October 1998, pp. 1453–1460.
- [44] B. Fardanesh, "Optimal Utilization, Sizing, and Steady-State Performance Comparison of Multiconverter VSC-Based FACTS Controllers," *IEEE Transactions on Power Delivery*, Vol. 19, No. 3, July 2004, pp. 1321–1327.
- [45] L. Gyugyi, K. K. Sen, C. D. Schauder, "The interline power flow controller concept: A new approach to power flow management in transmission systems," *IEEE Transactions on Power Delivery*, Vol. 14, No. 3, July 1999, pp. 1115–1123.
- [46] R.L Vasquez Arnez, and L. Cera Zanetta Jr., "Multi-Line Power Flow Control: An Evaluation of the GIPFC (Generalized Interline Power Flow Controller)," Proceedings of the International Conference on Power Systems Transients, June 2005.
- [47] R.L Vasquez Arnez, and L. Cera Zanetta Jr., "Operational Analysis and Limitations of the GIPFC (Generalized Interline Power Flow Controller)," *Power Tech*, June 2005, pp. 1–6.
- [48] R.L Vasquez Arnez, and L. Cera Zanetta Jr., "A Novel Approach for Modeling the Steady-State VSC-Based Multiline FACTS Controllers and Their Operational Constraints," *IEEE Transactions on Power Delivery*, Vol 23, No.1, January 2008, pp. 457–464.
- [49] P. C. Buddingh, "Even harmonic resonance – an unusual problem," Vol. 39, No. 4, pp. 1181–1186, Aug. 2003.

- [50] J. Arrillaga, B.C. Smith, N.R. Watson, A.R. Wood, *Power System Harmonic Analysis*, John Wiley & Sons, Chichester, 1997.
- [51] Semlyen, E. Acha, J. Arrillaga, “Newton-type algorithms for the harmonic phasor analysis of nonlinear power circuits in periodical steady-state with special reference to magnetic nonlinearities,” *IEEE Transactions on Power Delivery*, Vol. 3, No. 3, July 1988, pp. 1090–1098.
- [52] J. Arrilaga, A. Medina, M.L.V. Lisboa, M.A. Cavia, P. Sanchez, “The harmonic domain. A frame of reference for power system harmonic analysis,” *IEEE Transactions on Power System*, Vol. 10, No.1, February 1995, pp. 433–440.
- [53] S.R. Sanders, J.M. Noworolski, X.Z. Lui, and G.C. Verghese, “Generalized Averaging Method for Power Conversion Circuits,” *IEEE Transactions on Power Electronics*, Vol.6, No. 2, April 1991, pp. 251–259.
- [54] A. M. Stankovic, T. Aydin, “Analysis of asymmetrical faults in power systems using dynamic phasors,” *IEEE Transactions on Power Systems*, Vol. 15, No. 3, pp. 1062–1068, Aug 2000.
- [55] N. M. Wereley, “Linear time periodic systems: Transfer function, poles, transmission zeros and directional properties,” American Control Conference, pp. 1179–1184, June 1991.
- [56] H. S. Patel, R. G. Hoft, “Generalized Techniques of Harmonic Elimination and Voltage Control in Thyristor Inverters: Part I--Harmonic Elimination,” *IEEE Transactions on Industry Applications*, Vol. IA-9, No.1, June 1973, pp. 310–317.

- [57] J.E Hill, W.T.Norris, "Exact analysis of a multipulse shunt converter compensator or Statcon. I. Performance," *IEE Proceedings-Generation, Transmission and Distribution*, Vol. 144, No. 2, pp. 213–218, March 1997.
- [58] S. Qian, D. Chen, "Joint time-frequency analysis," *IEEE Signal Processing Magazine*, Vol. 16, No. 2, pp. 52–67, March 1999.
- [59] C. L. Fortescue, "Method of symmetrical co-ordinates applied to the solution of polyphase networks," Vol. 37, No. 2, pp. 1027–1115, 1918.
- [60] IEEE Standard 519-1992, Recommended Practices and Requirements for Harmonic Control in Electrical Power Systems.
- [61] L. L. Grigsby, *The Electric Power Engineering Handbook*, IEEE press, USA, (2001).
- [62] J. Arrillaga, N.R. Watson, S. Chen, *Power Quality Assessment*, John Wiley & Sons, Chichester, 2000.
- [63] G.T. Heydt, *Electric Power Quality*, Stars in a Circle Publications, Scottsdale, 1991.
- [64] Task Force on Harmonics Modeling and Simulation, "Modeling and Simulation of Power Propagation of Harmonics in Electric Power Networks, Part I: Concepts, Models, and Simulation Techniques," *IEEE Transactions on Power Delivery*, Vol. 11, No. 1, January 1996, pp. 452-465.
- [65] B. C. Smith, N. R. Watson, A. R. Wood, J. Arrillaga, "A Newton solution for the harmonic phasor analysis of AC/DC converters," *IEEE Transactions on Power Delivery*, Vol. 11, No.2, April 1996, pp. 965–971.

- [66] J. Endrenyi, *Reliability Modeling in Electrical Power Systems*, Wiley, New York, 1978.
- [67] M. Wereley, and S.R. Hall, "Linear Time Periodic Systems: Transfer Functions, Poles, Transmission Zeroes and Directional Properties," *Proceedings of the 1991 American Control Conference*, June 26–28, 1991, pp. 1179–1184.
- [68] M. Karimi-Ghartmani, R. Iravani, "Measurement of harmonics/inter-harmonics of time varying frequencies," *IEEE Transactions on Power Delivery*, Vol. 20, No. 1, pp. 23–31, Jan. 2005.
- [69] T.J.E. Miller, *Reactive Power Control in Electric Systems*, John Wiley & Sons, New York, 1982.
- [70] C. Fuerte-Esquivel, *Steady State Modelling and Analysis of Flexible AC Transmission Systems*, *PhD Thesis*, University of Glasgow, Scotland, 1997.
- [71] D.E. Rice, "A Detailed Analysis of Six-Pulse Converter Harmonic Currents," *IEEE Transactions on Industry Applications*, Vol. 30, No. 2, March/April 1994, pp. 294-304.
- [72] M. Madrigal, E. Acha, J.G. Mayordomo, R. Asensi, A. Hernandez, "Single-Phase PWM Converters Array for Three-Phase Reactive Power Compensation. Part II: Frequency Domain Studies," *Proceedings of IEEE-ICHQP 2000*, Orlando, USA, pp. 645-651.
- [73] K.S. Smith, L. Ran, J. Penman, "Dynamic Modelling of Unified Power Flow Controller," *IEE Proceedings Generation, Transmission and Distribution*, Vol. 144, No. 1, January 1997, pp. 7-12.

- [74] J. J. Rico, and E. Acha, " The use of switching functions and Walsh series to calculate waveform distortion in thyristor controlled compensated power circuits," *IEEE Transactions on Power Delivery*, Vol. 13, No. 4, pp. 1370 - 1377, Oct. 1998.
- [75] E. Acha, J. J. Rico, S. Acha, M. Madrigal, " Harmonic domain Modeling in Hartley's domain with particular Reference to three phase thyristor controlled reactors," *IEEE Transactions on Power Delivery*, Vol. 12, No. 4, pp. 1622 - 1628, Oct. 1997.

APPENDICES

APPENDIX A

The conventional three-phase voltage source converter [10] used in this research work is as follows:

A.1 Three-phase voltage source converter

Figure A-1 shows a conventional three-phase voltage source converter that consists of six anti-parallel diodes DER-D6, and six switches S1-S6. The number for each diode and switch indicates its order on being turned on. Total equivalent impedance, Z_e , indicates the equivalent resistance and reactance of the transmission line as well as the star-delta transformer. The line currents of the primary side of the transformer are proportional to line currents of the secondary side of the transformer. There is a phase shift of 120° between the three converter legs that are controlled.

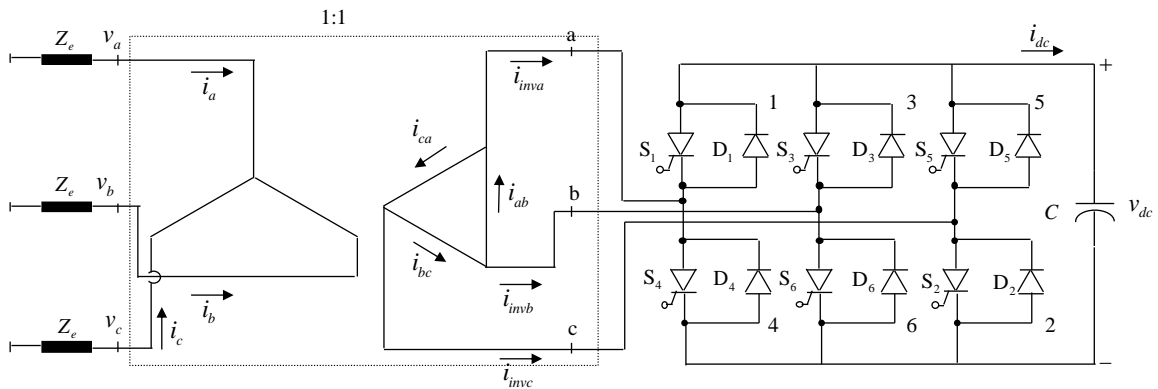


Figure A-1: Three-phase voltage source converter

A.2 Harmonic domain model of three-phase voltage source converter

The harmonic domain model of the three-phase voltage source converter is presented in [10] and it is used in this research work. This harmonic model is presented in this section.

The HD equations of the VSC model are given by

$$\begin{aligned}\mathbf{V}_{abc} &= [\mathbf{Z}_e + \mathbf{P}_s \mathbf{Z}_{cap} \mathbf{Q}_s] \mathbf{I}_{abc} + \mathbf{P}_s \mathbf{Z}_{cap} \mathbf{I}_{dc} + \mathbf{P}_s \mathbf{V}_0 \\ \mathbf{V}_{dc} &= \mathbf{Z}_{cap} \mathbf{Q}_s \mathbf{I}_{abc} + \mathbf{Z}_{cap} \mathbf{I}_{dc} + \mathbf{V}_0\end{aligned}$$

where L_e and R_e are the per-phase inductance and resistance of the transformer, \mathbf{U}_1 is the identity matrix, h is the number of harmonics chosen for the Fourier expansion, \mathbf{Z}_{cap} represents the equivalent impedance of the capacitor on the DC-side of the converter and C is the capacitance of the capacitor.

$$\mathbf{Z}_{cap} = \frac{1}{C} \mathbf{D}^{-1}(jh\omega_0) \quad \text{and} \quad \mathbf{Z}_e = R_e \mathbf{U}_1 + L_e \mathbf{D}(jh\omega_0)$$

$$\mathbf{V}_0 = \begin{bmatrix} 0 \\ \vdots \\ 0 \\ v_{cap}(0^+) \\ 0 \\ \vdots \\ 0 \end{bmatrix}$$

It is assumed that the capacitor is charged to $v_{cap}(0^+)$ from the previous period.

Also,

$$\mathbf{V}_{abc} = \begin{bmatrix} \mathbf{V}_a \\ \mathbf{V}_b \\ \mathbf{V}_c \end{bmatrix} \text{ and } \mathbf{I}_{abc} = \begin{bmatrix} \mathbf{I}_a \\ \mathbf{I}_b \\ \mathbf{I}_c \end{bmatrix}$$

where \mathbf{V}_{abc} and \mathbf{I}_{abc} are harmonic vectors of phase voltages and line currents, respectively. \mathbf{P}_s and \mathbf{Q}_s are transformation vectors [10] which are given by

$$\mathbf{P}_s = \begin{bmatrix} \mathbf{S}_{ab} \\ \mathbf{S}_{bc} \\ \mathbf{S}_{ca} \end{bmatrix} \text{ and } \mathbf{Q}_s = [\mathbf{S}_{ab} \quad \mathbf{S}_{bc} \quad \mathbf{S}_{ca}]$$

where \mathbf{S}_{ab} , \mathbf{S}_{bc} and \mathbf{S}_{ca} are the switching functions of the VSC .

APPENDIX B

B.1 Analysis of power quality indices of the GIPFC with various switching functions

The average per-phase change in several PQ indices of all VSC's of the GIPFC with various switching functions, under steady state and disturbance conditions are presented in this section.

Figure B-1 shows the average change in the per-phase RMS values of output currents of all the VSC's of the GIPFC in response to the disturbance with the individual application of switching functions - Cases A, B, C and D. During the disturbance, phase a voltage, $v_1(t)$ of the GIPFC, is 150% of its original value. This change at VSC 4 is the most significant one out of the four VSCs as it is directly connected to the line where $v_1(t)$ was changed.

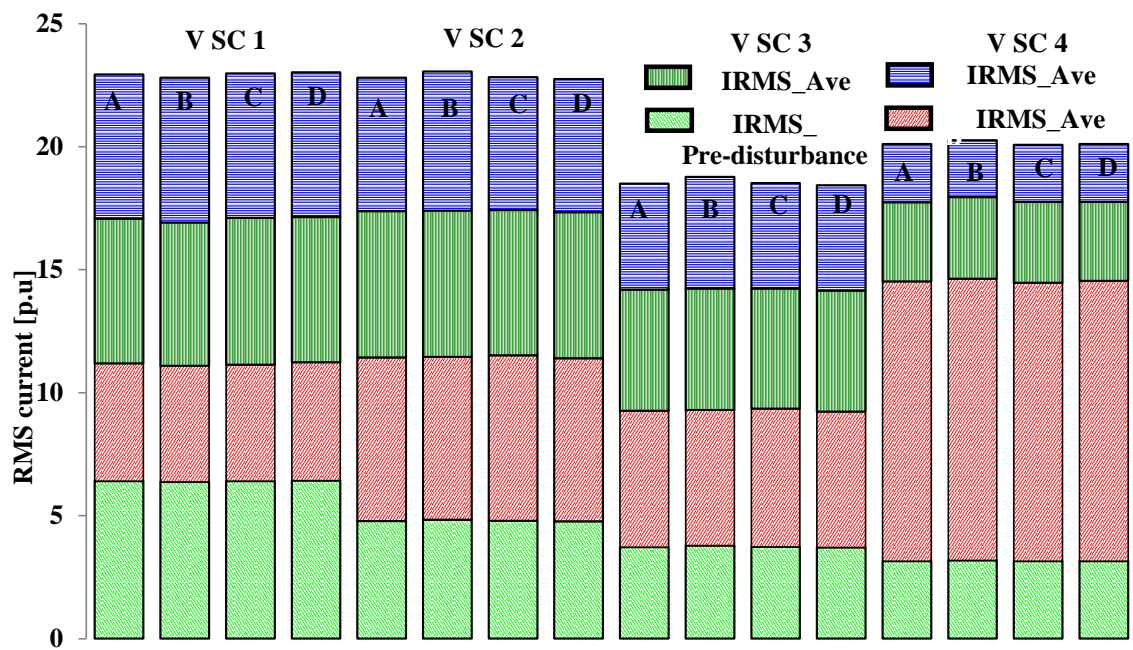


Figure B-1: RMS value of output current of all VSCs

The average change in magnitudes of RMS currents of all VSC's of the GIPFC during the disturbance period are presented in Table B-I.

Table B-I: RMS value of output current

| RMS value of output current during pre-disturbance period of VSC 1 | | Average RMS value of output current during disturbance period of VSC 1 | | |
|--|---------------------|--|-----------------------|-----------------------|
| Case | Steady State in p.u | Phase <i>a</i> in p.u | Phase <i>b</i> in p.u | Phase <i>c</i> in p.u |
| A | 6.3976 | 4.7834 | 5.892 | 5.8593 |
| B | 6.3609 | 4.7252 | 5.8277 | 5.8809 |
| C | 6.4005 | 4.7339 | 5.9714 | 5.8676 |
| D | 6.4171 | 4.8078 | 5.9113 | 5.8767 |
| RMS value of output current during pre-disturbance period of VSC 2 | | Average RMS value of output current during disturbance period of VSC 2 | | |
| A | 4.7807 | 6.643 | 5.9532 | 5.4248 |
| B | 4.8345 | 6.6152 | 5.942 | 5.6555 |
| C | 4.7837 | 6.7273 | 5.9041 | 5.4024 |
| D | 4.7667 | 6.6276 | 5.9388 | 5.4091 |
| RMS value of output current during pre-disturbance period of VSC 3 | | Average RMS value of output current during disturbance period of VSC 3 | | |
| A | 3.7191 | 5.5349 | 4.9329 | 4.3065 |
| B | 3.7803 | 5.5143 | 4.9334 | 4.5425 |
| C | 3.7222 | 5.6206 | 4.8912 | 4.2798 |
| D | 3.7044 | 5.5189 | 4.9182 | 4.29 |
| RMS value of output current during pre-disturbance period of VSC 4 | | Average RMS value of output current during disturbance period of VSC 4 | | |
| A | 3.1455 | 11.3755 | 3.2137 | 2.3637 |
| B | 3.1726 | 11.4535 | 3.316 | 2.3095 |
| C | 3.1452 | 11.3144 | 3.2848 | 2.3295 |
| D | 3.1482 | 11.3842 | 3.2106 | 2.3647 |

The information presented as bar graph in Figure B-2, shows the per-phase average change in distortion power output of the four VSC's of the GIPFC in response to a disturbance with the individual application of switching functions - Cases A, B, C and D. There is a 475% increase in average change in distortion power outputs of phase *a* of VSC 4 from its distortion power output during steady state value while the average change in distortion power outputs of phase *b* and phase *c* are very close to distortion power output during steady state. The variations in phases *b* and *c* are due to the change in DC side voltage and their corresponding switching functions.

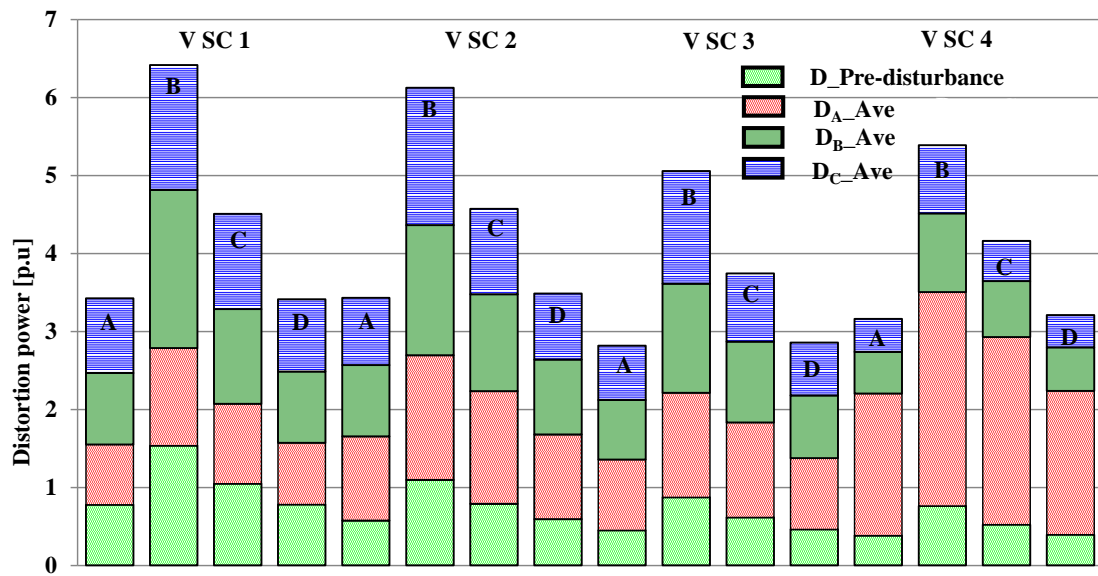


Figure B-2: Distortion power output of all VSCs

The average change in distortion power outputs of all VSC's of the GIPFC are presented in Table B-II. The average change in distortion power is more conspicuous in Case B due to the immense harmonic distortion of the switching function.

Table B-II: Distortion power output

| Distortion power output during pre-disturbance period of VSC 1 | | Average distortion power output during disturbance period of VSC 1 | | |
|--|---------------------|--|-----------------------|-----------------------|
| Case | Steady State in p.u | Phase <i>a</i> in p.u | Phase <i>b</i> in p.u | Phase <i>c</i> in p.u |
| A | 0.7757 | 0.7723 | 0.9185 | 0.9559 |
| B | 1.5337 | 1.2521 | 2.0268 | 1.6009 |
| C | 1.0458 | 1.0239 | 1.2169 | 1.2198 |
| D | 0.7784 | 0.7935 | 0.9142 | 0.9242 |
| Distortion power output during pre-disturbance period of VSC 2 | | Average distortion power output during disturbance period of VSC 2 | | |
| A | 0.575 | 1.078 | 0.9143 | 0.8634 |
| B | 1.0962 | 1.5986 | 1.6658 | 1.7634 |
| C | 0.7881 | 1.4458 | 1.242 | 1.0959 |
| D | 0.5931 | 1.0854 | 0.9603 | 0.8449 |
| Distortion power output during pre-disturbance period of VSC 3 | | Average distortion power output during disturbance period of VSC 3 | | |
| A | 0.4481 | 0.9069 | 0.7657 | 0.6939 |
| B | 0.8703 | 1.3415 | 1.4002 | 1.4428 |
| C | 0.6142 | 1.2186 | 1.0351 | 0.8759 |
| D | 0.4617 | 0.9124 | 0.8033 | 0.6785 |
| Distortion power output during pre-disturbance period of VSC 4 | | Average distortion power during disturbance period of VSC 4 | | |
| A | 0.3807 | 1.8233 | 0.5334 | 0.422 |
| B | 0.7605 | 2.7412 | 1.0111 | 0.8746 |
| C | 0.5213 | 2.404 | 0.7194 | 0.5145 |
| D | 0.394 | 1.842 | 0.5585 | 0.4144 |

The average change in the apparent power outputs of all VSC's of the GIPFC are shown in Figure B-3. This can be attributed to the fact that the increase in current during the disturbance at the terminals of VSC 4 produces more output current, which further leads to an increased voltage drop across the impedance that is connected to VSC 4. The variations in per phase apparent powers of all VSCs are due to the cumulative effect of variations due to change in voltages and currents.

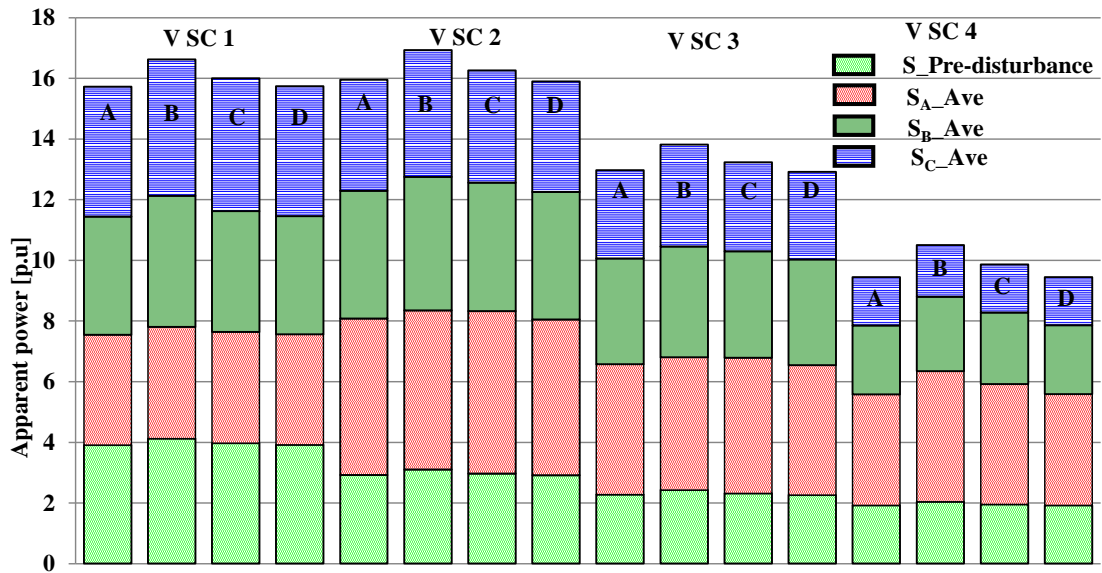


Figure B-3: Apparent power output of all VSCs

The average change in apparent power outputs of all VSC's of the GIPFC are presented in Table B-III.

Table B-III: Apparent power output

| Apparent power output during pre-disturbance period of VSC 1 | | Average apparent power output during disturbance period of VSC 1 | | |
|--|---------------------|--|-----------------------|-----------------------|
| Case | Steady State in p.u | Phase <i>a</i> in p.u | Phase <i>b</i> in p.u | Phase <i>c</i> in p.u |
| A | 3.9065 | 3.637 | 3.893 | 4.2841 |
| B | 4.1167 | 3.6865 | 4.3198 | 4.4998 |
| C | 3.9687 | 3.6655 | 3.9817 | 4.381 |
| D | 3.9089 | 3.6512 | 3.8958 | 4.2799 |
| Apparent power output during pre-disturbance period of VSC 2 | | Average apparent power output during disturbance period of VSC 2 | | |
| A | 2.9172 | 5.1579 | 4.2113 | 3.6607 |
| B | 3.0993 | 5.2483 | 4.4005 | 4.1771 |
| C | 2.969 | 5.3517 | 4.2348 | 3.6998 |
| D | 2.9074 | 5.1399 | 4.205 | 3.6398 |
| Apparent power output during pre-disturbance period of VSC 3 | | Average apparent power output during disturbance period of VSC 3 | | |
| A | 2.2694 | 4.2998 | 3.4906 | 2.9066 |
| B | 2.4235 | 4.3772 | 3.6544 | 3.3558 |
| C | 2.3102 | 4.4739 | 3.5093 | 2.9316 |
| D | 2.2594 | 4.2824 | 3.4832 | 2.8874 |
| Apparent power output during pre-disturbance period of VSC 4 | | Average apparent power during disturbance period of VSC 4 | | |
| A | 1.9194 | 3.6566 | 2.2718 | 1.5907 |
| B | 2.0339 | 4.3084 | 2.455 | 1.7006 |
| C | 1.9521 | 3.9639 | 2.3547 | 1.591 |
| D | 1.9202 | 3.6665 | 2.2716 | 1.587 |

The average change in the active power outputs of all VSC's of the GIPFC are shown in Figure B-4. The average change in active powers of VSC 4 through the disturbance is positive due to the fact that voltage appearing at the terminals of VSC 4 is more during the disturbance when compare to voltages appearing at the terminals of the remaining VSC's. These variations in per phase active powers of all VSCs are due to the cumulative effect of variations due to change in voltages and currents during the disturbance period.

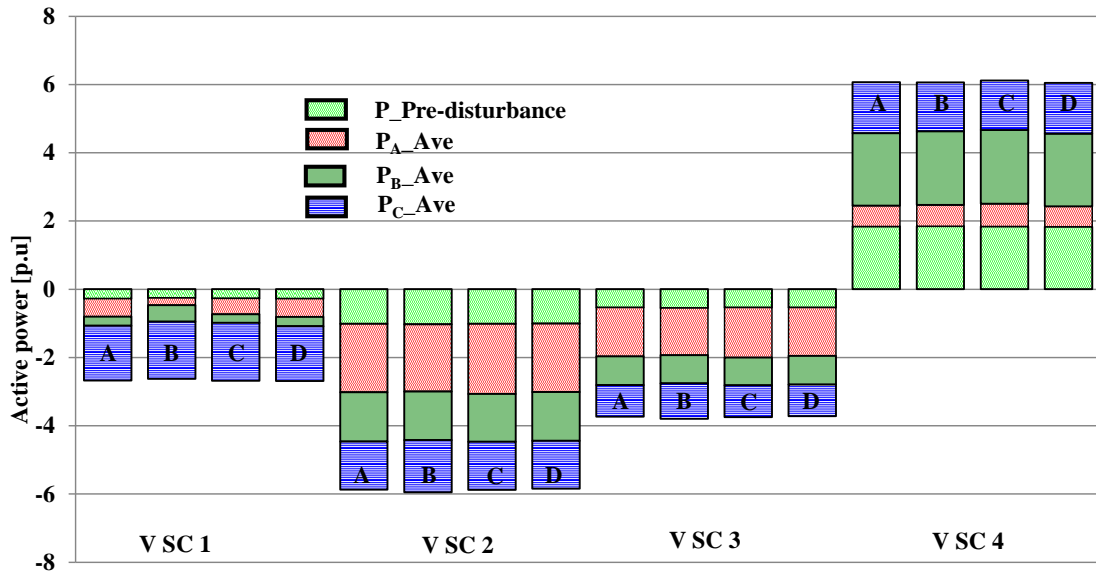


Figure B-4: Active power output of all VSCs

The average change in magnitudes of active power outputs of all VSC's of the GIPFC during the disturbance period are presented in Table B-IV.

Table B-IV: Active power output

| Active power output during pre-disturbance period of VSC 1 | | Average active power output during disturbance period of VSC 1 | | |
|--|---------------------|--|-----------------------|-----------------------|
| Case | Steady State in p.u | Phase <i>a</i> in p.u | Phase <i>b</i> in p.u | Phase <i>c</i> in p.u |
| A | -0.2774 | -0.5261 | -0.2699 | -1.6068 |
| B | -0.2625 | -0.2095 | -0.4782 | -1.6782 |
| C | -0.2758 | -0.4617 | -0.254 | -1.6907 |
| D | -0.2803 | -0.5319 | -0.2739 | -1.604 |
| Active power output during pre-disturbance period of VSC 2 | | Average active power output during disturbance period of VSC 2 | | |
| A | -1.0157 | -2.0086 | -1.4406 | -1.407 |
| B | -1.0316 | -1.9724 | -1.4211 | -1.5274 |
| C | -1.0168 | -2.055 | -1.4044 | -1.4089 |
| D | -1.0113 | -2.0015 | -1.4348 | -1.4013 |
| Active power output during pre-disturbance period of VSC 3 | | Average active power output during disturbance period of VSC 3 | | |
| A | -0.5408 | -1.4265 | -0.8455 | -0.9238 |
| B | -0.552 | -1.3853 | -0.8247 | -1.0347 |
| C | -0.5416 | -1.4664 | -0.8097 | -0.9321 |
| D | -0.5378 | -1.4212 | -0.8412 | -0.9199 |
| Active power output during pre-disturbance period of VSC 4 | | Average active power during disturbance period of VSC 4 | | |
| A | 1.8339 | 0.6111 | 2.1297 | 1.492 |
| B | 1.8461 | 0.6223 | 2.1573 | 1.4288 |
| C | 1.8342 | 0.6662 | 2.164 | 1.4518 |
| D | 1.8294 | 0.5984 | 2.1265 | 1.4872 |

The average change in the reactive power outputs of all VSC's of the GIPFC are shown in Figure B-5. These average variations in per-phase reative powers of all VSCs are due to the cumulative effect of variations due to change in voltages and currents during the disturbance period.

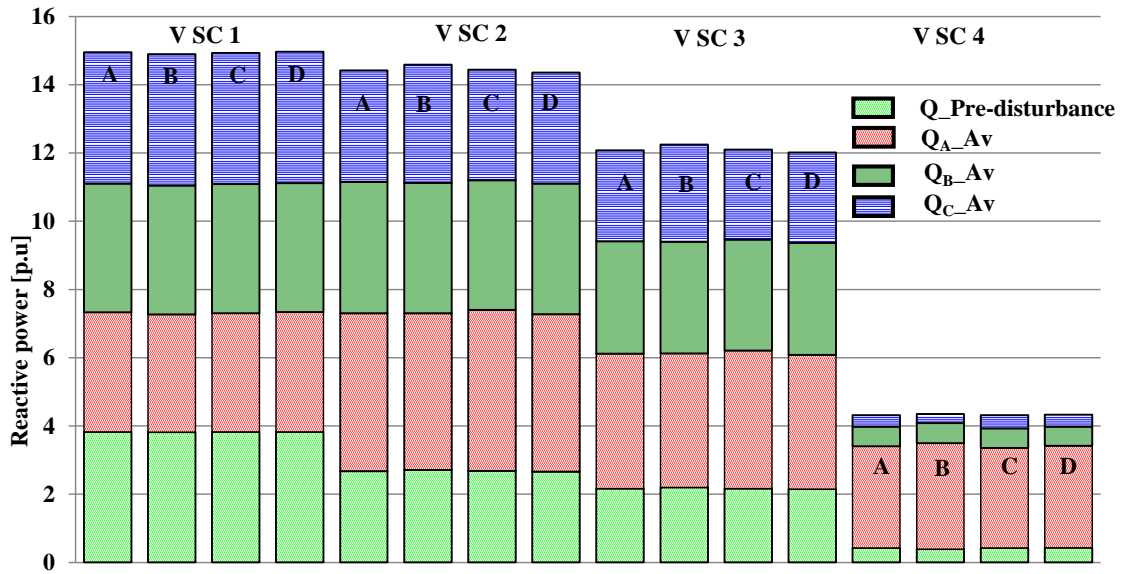


Figure B-5: Reactive power output of all VSCs

The average change in magnitudes of the reactive power outputs of all VSC's of the GIPFC during the disturbance period are presented in Table B-V.

Table B-V: Reactive power output

| Reactive power output during pre-disturbance period of VSC 1 | | Average reactive power output during disturbance period of VSC 1 | | |
|--|---------------------|--|-----------------------|-----------------------|
| Case | Steady State in p.u | Phase <i>a</i> in p.u | Phase <i>b</i> in p.u | Phase <i>c</i> in p.u |
| A | 3.8187 | 3.5081 | 3.7727 | 3.8459 |
| B | 3.8113 | 3.4513 | 3.7837 | 3.8466 |
| C | 3.8185 | 3.4828 | 3.781 | 3.8423 |
| D | 3.8203 | 3.5172 | 3.7763 | 3.8503 |
| Reactive power output during pre-disturbance period of VSC 2 | | Average reactive power output during disturbance period of VSC 2 | | |
| A | 2.6735 | 4.6263 | 3.85 | 3.267 |
| B | 2.7093 | 4.5927 | 3.8167 | 3.4644 |
| C | 2.6759 | 4.7245 | 3.7969 | 3.2403 |
| D | 2.6605 | 4.6076 | 3.834 | 3.2509 |
| Reactive power output during pre-disturbance period of VSC 3 | | Average reactive power output during disturbance period of VSC 3 | | |
| A | 2.158 | 3.9526 | 3.2985 | 2.6666 |
| B | 2.1935 | 3.9286 | 3.2727 | 2.8468 |
| C | 2.1602 | 4.0461 | 3.2536 | 2.6372 |
| D | 2.1454 | 3.9344 | 3.2829 | 2.651 |
| Reactive power output during pre-disturbance period of VSC 4 | | Average reactive power during disturbance period of VSC 4 | | |
| A | 0.4197 | 2.9801 | 0.5781 | 0.3361 |
| B | 0.3875 | 3.1074 | 0.5843 | 0.2705 |
| C | 0.4181 | 2.9319 | 0.5796 | 0.3791 |
| D | 0.4302 | 2.9824 | 0.5659 | 0.3493 |

The average change in THD in currents of all VSC's in the GIPFC in the steady state as well as during the disturbance period are shown in Figure B-6. The maximum deviation, as expected, can be observed in Case B due to the immense harmonic distortion of the switching function. The average change in THD in currents of all three phases of VSC 4 is more compared with the remaining phases are due to fact that the variation in voltage of phase *a* at the terminals of VSC 4 during the disturbance period.

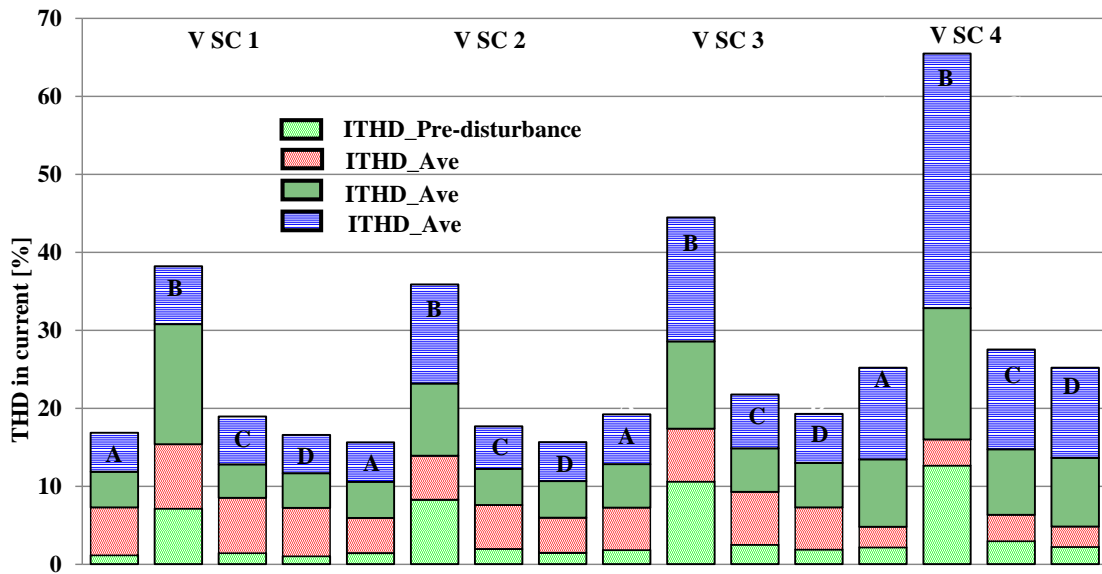


Figure B-6: THD in current of all VSCs

The average change in magnitudes of THD in currents of all VSC's of the GIPFC during the disturbance period are presented in Table B-VI.

Table B-VI: THD in output current

| THD in output current during pre-disturbance period of VSC 1 | | Average THD in output current during disturbance period of VSC 1 | | |
|--|---------------------|--|-----------------------|-----------------------|
| Case | Steady State in p.u | Phase <i>a</i> in p.u | Phase <i>b</i> in p.u | Phase <i>c</i> in p.u |
| A | 1.135 | 6.1391 | 4.5721 | 5.0024 |
| B | 7.1103 | 8.2572 | 15.4036 | 7.4244 |
| C | 1.414 | 7.0922 | 4.2969 | 6.1241 |
| D | 1.0013 | 6.2192 | 4.4414 | 4.9017 |
| THD in output current during pre-disturbance period of VSC 2 | | Average THD in output current during disturbance period of VSC 2 | | |
| A | 1.4205 | 4.5106 | 4.6086 | 5.0669 |
| B | 8.2556 | 5.6396 | 9.2779 | 12.6864 |
| C | 1.9437 | 5.6407 | 4.6387 | 5.4341 |
| D | 1.4513 | 4.49 | 4.7146 | 4.9944 |
| THD in output current during pre-disturbance period of VSC 3 | | Average THD in output current during disturbance period of VSC 3 | | |
| A | 1.8261 | 5.4227 | 5.5646 | 6.3948 |
| B | 10.5806 | 6.7874 | 11.1969 | 15.8773 |
| C | 2.4983 | 6.7599 | 5.6032 | 6.8747 |
| D | 1.8676 | 5.4011 | 5.6957 | 6.3092 |
| THD in output current during pre-disturbance period of VSC 4 | | Average THD in output current during disturbance period of VSC 4 | | |
| A | 2.1592 | 2.6308 | 8.6347 | 11.7622 |
| B | 12.6373 | 3.3558 | 16.8174 | 32.6449 |
| C | 2.9569 | 3.3518 | 8.4231 | 12.7791 |
| D | 2.1978 | 2.6105 | 8.8193 | 11.548 |

APPENDIX C

C.1 Matlab[®] code

The following MATLAB[®] code is used for the DHD model of FC-TCR

```
clc;

close all;

clear all;

kv=1;

Frequency_supply = 60;

w=2*pi*Frequency_supply;

Alpha_PhaseA=120*pi/180;

Alpha_PhaseB=120*pi/180;

Alpha_PhaseC=120*pi/180;

xtrans=0.001;

rtrans=0.01;

xcap=0.015;

xrea=0.003;%this is for FC-TCR

harmonics=15;

[I1,v20,Itr]=iniEHDSVC(kv, Alpha_PhaseA, Alpha_PhaseB,

Alpha_PhaseC,xtrans,rtrans,xcap,xrea,harmonics,w);

X0=[I1;v20;Itr];

t1=0:0.2e-4:0.2;
```

```

[t, X_FC-TCR]=ode45('EHDFC-TCRfunction',t1,X0);

save('initial_FC-TCR','t','X_FC-TCR')

load('initial_FC-TCR')

I11=X_FC-TCR(:,1:93);

V2abc=X_FC-TCR(:,94:186);

Itrabc=X_FC-TCR(:,187:279);

I1a=X_FC-TCR(:,1:31);

I1b=X_FC-TCR(:,32:62);

I1c=X_FC-TCR(:,63:93);

V2a=X_FC-TCR(:,94:124);

V2b=X_FC-TCR(:,125:155);

V2c=X_FC-TCR(:,156:186);

Itrca=X_FC-TCR(:,187:217);

Itrcb=X_FC-TCR(:,218:248);

Itrcc=X_FC-TCR(:,249:279);

%-----for plots-----

%%%%%%%%%%%%%%

%%%

set( 0, 'DefaultAxesFontSize', 18 )

set( 0, 'DefaultAxesFontName', 'Times New Roman' )

set( 0, 'DefaultAxesFontAngle', 'normal' )

gridState = 'on' ;

set( 0, 'DefaultAxesXGrid', gridState )

```

```

set( 0, 'DefaultAxesYGrid', gridState )
set( 0, 'DefaultAxesZGrid', gridState )
set( 0, 'DefaultTextFontSize', 18 )
set( 0, 'DefaultTextFontName', 'Times New Roman' )
set(0, 'DefaultAxesColor', 'w', ...
    'DefaultAxesXColor', 'k', ...
    'DefaultAxesYColor', 'k', ...
    'DefaultAxesZColor', 'k', ...
    'DefaultTextColor', 'blue', ...
    'DefaultLineColor', 'blue' );
set( 0, 'DefaultLineLineWidth', 3 );
figure1=figure;
plot(t,2*abs(I1a(:,17)), 'r', t, 2*abs(I1a(:,19)), 'g', t, 2*abs(I1a(:,21)), 'b', t, 2*abs(I1a(:,23)), 'y');
axis([2 10 0 350])
title('Current at FC-TCR- Phase a');xlabel('time [S]);ylabel('current [A]');
axes1 = axes('Parent',figure1,'FontWeight','bold','FontSize',14);
box('on');hold('all');
plot1 =
plot(t,2*abs(I1a(:,17)),t,2*abs(I1a(:,19)),t,2*abs(I1a(:,21)), 'Parent',axes1, 'Color',[0 0 0]);
set(plot1(1),'LineWidth',2,'DisplayName','h=1');
set(plot1(2),'LineWidth',1,'LineStyle','--','DisplayName','h=3');
set(plot1(3),'LineStyle',':','DisplayName','h=5');
xlabel('Time [s]','FontWeight','bold','FontSize',14);

```

```

ylabel('Current [A]','FontWeight','bold','FontSize',14);

title('Current at FC-TCR- Phase a');

legend1 = legend(axes1,'show');

set(legend1,'Position',[0.7586 0.7796 0.1453 0.141],'FontSize',14);

axis([0 5 0 16.5])

-----I1 RMS calculation and plot-----

Iar=sqrt(sum(abs(I1a).^*abs(I1a)));

Ibr=sqrt(sum(abs(I1b).^*abs(I1b)));

Icr=sqrt(sum(abs(I1c).^*abs(I1c)));

figure2=figure;

Iar1=sqrt(2)*Iar;Ibr1=sqrt(2)*Ibr;Icr1=sqrt(2)*Icr;

plot(t,Iar1,'r',t,Ibr1,'g',t,Icr1,'b')

axis([2 10 305 350])

xlabel('Time [s]');ylabel('Magnitude');title('FC-TCR RMS current [A]');

axes1 = axes('Parent',figure2,'FontWeight','bold','FontSize',14);

box('on');hold('all');

plot1 = plot(t,Iar1,t,Ibr1,t,Icr1,'Parent',axes1,'Color',[0 0 0]);

set(plot1(1),'LineWidth',2,'DisplayName','Phase a');

set(plot1(2),'LineWidth',1,'LineStyle','--','DisplayName','Phase b');

set(plot1(3),'LineStyle',':','DisplayName','Phase c');

xlabel('Time [s]','FontWeight','bold','FontSize',14);

ylabel('Magnitude','FontWeight','bold','FontSize',14);

title('FC-TCR RMS current [A]');

```

```

legend1 = legend(axes1,'show');

set(legend1,'Position',[0.7586 0.7796 0.1453 0.141],'FontSize',14);

-----End of I1 RMS calculation-----

V2a=X(:,94:124);V2b=X(:,125:155);V2c=X(:,156:186);

figure3=figure;

plot(t,2*abs(V2a(:,17)),'r',t,2*abs(V2a(:,19)),'g',t,2*abs(V2a(:,21)),'b',t,2*abs(V2a(:,23)),'
y');

axis([2 10 0 8]);

title('Voltage at FC-TCR -phase a');xlabel('time [S]');ylabel('Volatge [V]');

axes1 = axes('Parent',figure3,'FontWeight','bold','FontSize',14);

box('on');hold('all');

plot1
=
plot(t,2*abs(V2a(:,17)),t,2*abs(V2a(:,19)),t,2*abs(V2a(:,21)),'Parent',axes1,'Color',[0 0
0]);

set(plot1(1),'LineWidth',2,'DisplayName','h=1');

set(plot1(2),'LineWidth',1,'LineStyle','--','DisplayName','h=3');

set(plot1(3),'LineStyle',':','DisplayName','h=5');

xlabel('Time [s]','FontWeight','bold','FontSize',14);

ylabel('Volatge [V]','FontWeight','bold','FontSize',14);

title('Voltage at FC-TCR -phase a');

legend1 = legend(axes1,'show');

set(legend1,'Position',[0.7586 0.7796 0.1453 0.141],'FontSize',14);

axis([0 5 0 0.6])

```

```

-----V2 RMS calculation and plots-----
Var=sqrt(sum(abs(V2a).*abs(V2a)));
Vbr=sqrt(sum(abs(V2b).*abs(V2b)));
Vcr=sqrt(sum(abs(V2c).*abs(V2c)));
Var1=sqrt(2)*Var; Vbr1=sqrt(2)*Vbr; Vcr1=sqrt(2)*Vcr;
figure4=figure;
plot(t,Var1,'r',t,Vbr1,'g',t,Vcr1,'b')
axis([2 10 6.2 8.2])
xlabel('Time [s]');ylabel('Magnitude');title('RMS Volatge at FC-TCR [V]');
axes1 = axes('Parent',figure4,'FontWeight','bold','FontSize',14);
box('on');hold('all');
plot1 = plot(t,Var1,t,Vbr1,t,Vcr1,'Parent',axes1,'Color',[0 0 0]);
set(plot1(1),'LineWidth',2,'DisplayName','Phase a');
set(plot1(2),'LineWidth',1,'LineStyle','--','DisplayName','Phase b');
set(plot1(3),'LineStyle',':','DisplayName','Phase c');
xlabel('Time [s]','FontWeight','bold','FontSize',14);
ylabel('Magnitude','FontWeight','bold','FontSize',14);
title('RMS Volatge at FC-TCR [V]');
legend1 = legend(axes1,'show');
set(legend1,'Position',[0.7095 0.7816 0.1959 0.141],'FontSize',14);
-----End of V2 RMS calculation-----
Itcra=X(:,187:217);Itcrb=X(:,218:248);Itcrc=X(:,249:279);
figure5=figure;

```

```

plot(t,2*abs(Itcra(:,17)), 'r', t, 2*abs(Itcra(:,19)), 'g', t, 2*abs(Itcra(:,21)), 'b', t, 2*abs(Itcra(:,23))
), 'y');

axis([2 10 0 350])

title('TCR Current- Phase a'); xlabel('time [S]'); ylabel('current [A]');

axes1 = axes('Parent', figure5, 'FontWeight', 'bold', 'FontSize', 14);

box('on'); hold('all');

plot1 =
plot(t, 2*abs(Itcra(:,17)), t, 2*abs(Itcra(:,19)), t, 2*abs(Itcra(:,21)), 'Parent', axes1, 'Color', [0 0
0]);

set(plot1(1), 'LineWidth', 2, 'DisplayName', 'h=1');

set(plot1(2), 'LineWidth', 1, 'LineStyle', '--', 'DisplayName', 'h=3');

set(plot1(3), 'LineStyle', ':', 'DisplayName', 'h=5');

xlabel('Time [s]', 'FontWeight', 'bold', 'FontSize', 14);

ylabel('Current [A]', 'FontWeight', 'bold', 'FontSize', 14);

title('TCR Current- Phase a');

legend1 = legend(axes1, 'show');

set(legend1, 'Position', [0.7482 0.5772 0.1275 0.141], 'FontSize', 14);

-----ITCR RMS calculation and plot-----

Itcrar=sqrt(sum(abs(Itcra)'.*abs(Itcra)));

Itcrbr=sqrt(sum(abs(Itrcb)'.*abs(Itrcb)));

Itcrer=sqrt(sum(abs(Itrce)'.*abs(Itrce)));

figure6=figure;

Itcrar1=sqrt(2)*Itcrar;Itcrbr1=sqrt(2)*Itcrbr;Itcrer1=sqrt(2)*Itcrer;

```



```

plot(t,Itrcr1,'r',t,Itrcr1,'g',t,Itrcr1,'b')
axis([2 10 310 345])
xlabel('Time [s]);ylabel('Magnitude');title('TCR RMS current [A]');
axes1 = axes('Parent',figure6,'FontWeight','bold','FontSize',14);
box('on');hold('all');
plot1 = plot(t,Itrcr1,t,Itrcr1,t,Itrcr1,'Parent',axes1,'Color',[0 0 0]);
set(plot1(1),'LineWidth',2,'DisplayName','Phase a');
set(plot1(2),'LineWidth',1,'LineStyle','--','DisplayName','Phase b');
set(plot1(3),'LineStyle',':','DisplayName','Phase c');
xlabel('Time [s]','FontWeight','bold','FontSize',14);
ylabel('Magnitude','FontWeight','bold','FontSize',14);
title('TCR RMS current [A]');
legend1 = legend(axes1,'show');
set(legend1,'Position',[0.7482 0.5772 0.1275 0.141],'FontSize',14);
-----End of ITCR RMS calculation-----
-----current through capacitor-----
Icapa=I1a-Itrca;Icapb=I1b-Itrcb;Icapc=I1c-Itrc;
figure;
plot(t,2*abs(Icapa(:,17)),'r',t,2*abs(Icapa(:,19)),'g',t,2*abs(Icapa(:,23)),'b');
axis([2 10 0 350])
title('Capacitor Current- Phase a');xlabel('time [S]');ylabel('current [A]');
-----Cap Current RMS calculation and plot-----
Icapar=sqrt(sum(abs(Icapa)'.*abs(Icapa)));

```

```

Icapbr=sqrt(sum(abs(Icapb).^*abs(Icapb)));
Icapcr=sqrt(sum(abs(Icapc).^*abs(Icapc)));

figure;

Icapar1=sqrt(2)*Icapar;Icapbr1=sqrt(2)*Icapbr;Icapcr1=sqrt(2)*Icapcr;

plot(t,Icapar1,'r',t,Icapbr1,'g',t,Icapcr1,'b')

axis([2 10 0 7])

xlabel("Time [s]");ylabel("Magnitude");title('Capacitor RMS current [A]');

-----End of Cap Current RMS calculation-----

-----Apparent power calculation-----

Sa=Var1.*Iar1;Sb=Vbr1.*Ibr1;Sc=Vcr1.*Icr1;

Sa1=abs(Sa);Sb1=abs(Sb);Sc1=abs(Sc);

figure9=figure;

plot(t,abs(Sa1),'r',t,abs(Sb1),'g',t,abs(Sc1),'b')

axis([2 10 2000 2700])

xlabel("Time [s]");ylabel("Magnitude");title('Apparent power [VA]');

axes1 = axes('Parent',figure9,'FontWeight','bold','FontSize',14);

box('on');hold('all');

plot1 = plot(t,abs(Sa1),t,abs(Sb1),t,abs(Sc1),'Parent',axes1,'Color',[0 0 0]);

set(plot1(1),'LineWidth',2,'DisplayName','Phase a');

set(plot1(2),'LineWidth',1,'LineStyle','--','DisplayName','Phase b');

set(plot1(3),'LineStyle',':','DisplayName','Phase c');

xlabel("Time [s]','FontWeight','bold','FontSize',14);

ylabel("Magnitude','FontWeight','bold','FontSize',14);

```

```

title('Apparent power [VA]');
legend1 = legend(axes1,'show');
set(legend1,'Position',[0.7095 0.7816 0.1959 0.141],'FontSize',14);
-----End of Apparent power calculation-----
-----Active power calculation-----
Pa =sum(V2a'.*conj(I1a));
Pb =sum(V2b'.*conj(I1b));
Pc =sum(V2c'.*conj(I1c));
Pa1=2*Pa;Pb1=2*Pb;Pc1=2*Pc;
figure10=figure;
plot(t,Pa1,'r',t,Pb1,'g',t,Pc1,'b')
axis([2 10 -1500 1000])
xlabel('Time [s]');ylabel('Magnitude');title('Active power [W]');
axes1 = axes('Parent',figure10,'FontWeight','bold','FontSize',14);
box('on');hold('all');
plot1 = plot(t,Pa1,t,Pb1,t,Pc1,'Parent',axes1,'Color',[0 0 0]);
set(plot1(1),'LineWidth',2,'DisplayName','Phase a');
set(plot1(2),'LineWidth',1,'LineStyle','--','DisplayName','Phase b');
set(plot1(3),'LineStyle',':','DisplayName','Phase c');
xlabel('Time [s]','FontWeight','bold','FontSize',14);
ylabel('Magnitude','FontWeight','bold','FontSize',14);
title('Active power [W]');
legend1 = legend(axes1,'show');

```

```

set(legend1,'Position',[0.7095 0.7816 0.1959 0.141],'FontSize',14);

-----End of Active power calculation-----

-----Reactive power calculation-----

Qa = sqrt(sum(abs(V2a).^2.*abs(I1a).^2-V2a.*conj(I1a).*V2a.*conj(I1a)));
Qb = sqrt(sum(abs(V2b).^2.*abs(I1b).^2-V2b.*conj(I1b).*V2b.*conj(I1b)));
Qc = sqrt(sum(abs(V2c).^2.*abs(I1c).^2-V2c.*conj(I1c).*V2c.*conj(I1c)));
Qa1=2*abs(Qa);Qb1=2*abs(Qb);Qc1=2*abs(Qc);

figure11=figure;

plot(t,Qa1,'r',t,Qb1,'g',t,Qc1,'b')

axis([2 10 1700 2600])

xlabel('Time [s]');ylabel('Magnitude');title('Reactive power [VAR]');

axes1 = axes('Parent',figure11,'FontWeight','bold','FontSize',14);

box('on');hold('all');

plot1 = plot(t,Qa1,t,Qb1,t,Qc1,'Parent',axes1,'Color',[0 0 0]);

set(plot1(1),'LineWidth',2,'DisplayName','Phase a');

set(plot1(2),'LineWidth',1,'LineStyle','--','DisplayName','Phase b');

set(plot1(3),'LineStyle',':','DisplayName','Phase c');

xlabel('Time [s]','FontWeight','bold','FontSize',14);

ylabel('Magnitude','FontWeight','bold','FontSize',14);

title('Reactive power [VAR]');

legend1 = legend(axes1,'show');

set(legend1,'Position',[0.7095 0.732 0.1959 0.141],'FontSize',14);

```

```

-----End of Reactive power calculation-----
-----Distortion power calculation-----

Da = sqrt(Sa1.*Sa1-Pa1.*Pa1-Qa1.*Qa1);
Db = sqrt(Sb1.*Sb1-Pb1.*Pb1-Qb1.*Qb1);
Dc = sqrt(Sc1.*Sc1-Pc1.*Pc1-Qc1.*Qc1);

figure12=figure;

plot(t,Da,'r',t,Db,'g',t,Dc,'b')

axis([2 10 100 450])

xlabel('Time [s]');ylabel('Magnitude');title('Distortion power [VAD]');

axes1 = axes('Parent',figure12,'FontWeight','bold','FontSize',14);

box('on');hold('all');

plot1 = plot(t,Da,t,Db,t,Dc,'Parent',axes1,'Color',[0 0 0]);

set(plot1(1),'LineWidth',2,'DisplayName','Phase a');

set(plot1(2),'LineWidth',1,'LineStyle','--','DisplayName','Phase b');

set(plot1(3),'LineStyle',':','DisplayName','Phase c');

xlabel('Time [s]','FontWeight','bold','FontSize',14);

ylabel('Magnitude','FontWeight','bold','FontSize',14);

title('Distortion power [VAD]');

legend1 = legend(axes1,'show');

set(legend1,'Position',[0.7095 0.7816 0.1959 0.141],'FontSize',14);

-----End of distortion power calculation-----
-----THD II calculation-----

k=1;kk=1;shia=0;shib=0;shic=0;

```

```

for kk=1:10001

for k=18:31

I1ats(kk)=abs(I1a(kk,k)).^2/abs(I1a(kk,17)).^2+shia;

I1bts(kk)=abs(I1b(kk,k)).^2/abs(I1b(kk,17)).^2+shib;

I1cts(kk)=abs(I1c(kk,k)).^2/abs(I1c(kk,17)).^2+shic;

shia=I1ats(kk); shib=I1bts(kk);shic=I1cts(kk);

end

shia=0;shib=0;shic=0;

end

I1ath=sqrt(abs(I1ats))*100;I1bth=sqrt(abs(I1bts))*100;I1cth=sqrt(abs(I1cts))*100;

figure13=figure;

plot(t,I1ath,'r',t,I1bth,'g',t,I1cth,'b');%axis([2 10 1.5 6.5]);

xlabel('Time [s]');ylabel('Magnitude [%]');title('THD in I1 (SVR current)');

axes1 = axes('Parent',figure13,'FontWeight','bold','FontSize',14);

box('on');hold('all');

plot1 = plot(t,I1ath,t,I1bth,t,I1cth,'Parent',axes1,'Color',[0 0 0]);

set(plot1(1),'LineWidth',2,'DisplayName','Phase a');

set(plot1(2),'LineWidth',1,'LineStyle','--','DisplayName','Phase b');

set(plot1(3),'LineStyle',':','DisplayName','Phase c');

xlabel('Time [s]','FontWeight','bold','FontSize',14);

ylabel('Magnitude [%]','FontWeight','bold','FontSize',14);

title('THD in I (FC-TCR current)');

legend1 = legend(axes1,'show');

```

```

set(legend1,'Position',[0.7095 0.7816 0.1959 0.141],'FontSize',14);

-----End of THD II calculation-----

-----THD V2 claculation-----

k=1;kk=1;shia=0;shib=0;shic=0;

for kk=1:10001

for k=18:31

    V2ats(kk)=abs(V2a(kk,k)).^2/abs(V2a(kk,17)).^2+shia;
    V2bts(kk)=abs(V2b(kk,k)).^2/abs(V2b(kk,17)).^2+shib;
    V2cts(kk)=abs(V2c(kk,k)).^2/abs(V2c(kk,17)).^2+shic;
    shia=V2ats(kk); shib=V2bts(kk);shic=V2cts(kk);

end

shia=0;shib=0;shic=0;

end

V2ath=sqrt(abs(V2ats))*100;V2bth=sqrt(abs(V2bts))*100;V2cth=sqrt(abs(V2cts))*100;

figure14=figure;

plot(t,V2ath,'r',t,V2bth,'g',t,V2cth,'b');%axis([2 10 4 18])

xlabel('Time [s]');ylabel('Magnitude [%]');title('THD in V2 (Volatge at FC-TCR)');

axes1 = axes('Parent',figure14,'FontWeight','bold','FontSize',14);

box('on');hold('all');

plot1 = plot(t,V2ath,t,V2bth,t,V2cth,'Parent',axes1,'Color',[0 0 0]);

set(plot1(1),'LineWidth',2,'DisplayName','Phase a');

set(plot1(2),'LineWidth',1,'LineStyle','--','DisplayName','Phase b');

set(plot1(3),'LineStyle',':','DisplayName','Phase c');

```

```

xlabel('Time [s]', 'FontWeight', 'bold', 'FontSize', 14);
ylabel('Magnitude [%]', 'FontWeight', 'bold', 'FontSize', 14);
title('THD in V2 (Volatge at FC-TCR)');
legend1 = legend(axes1, 'show');
set(legend1, 'Position', [0.7095 0.7816 0.1959 0.141], 'FontSize', 14);
-----End of THD V2 calculation-----
-----THD Itr calculation-----
k=1;kk=1;shia=0;shib=0;shic=0;
for kk=1:10001
for k=18:31
    Itrats(kk)=abs(Itcra(kk,k)).^2/abs(Itcra(kk,17)).^2+shia;
    Itrbts(kk)=abs(Itrcb(kk,k)).^2/abs(Itrcb(kk,17)).^2+shib;
    Itrcts(kk)=abs(Itrcc(kk,k)).^2/abs(Itrcc(kk,17)).^2+shic;
    shia=Itrats(kk); shib=Itrbts(kk);shic=Itrcts(kk);
end
shia=0;shib=0;shic=0;
end
Itrath=sqrt(abs(Itrats))*100;Itrbth=sqrt(abs(Itrbts))*100;Itrcth=sqrt(abs(Itrcts))*10
0;
figure15=figure;
plot(t,Itrath, 'r',t,Itrbth, 'g',t,Itrcth, 'b');% axis([2 10 1.5 6.5]);
xlabel('Time [s]');ylabel('Magnitude [%]');title('THD in Itr (Current through TCR)');
axes1 = axes('Parent',figure15, 'FontWeight', 'bold', 'FontSize', 14);

```



```

box('on');hold('all');

plot1 = plot(t,Itrcrath,t,Itrcrbth,t,Itrcrcth,'Parent',axes1,'Color',[0 0 0]);

set(plot1(1),'LineWidth',2,'DisplayName','Phase a');

set(plot1(2),'LineWidth',1,'LineStyle','--','DisplayName','Phase b');

set(plot1(3),'LineStyle',':','DisplayName','Phase c');

xlabel('Time [s]','FontWeight','bold','FontSize',14);

ylabel('Magnitude [%]','FontWeight','bold','FontSize',14);

title('THD in Itr (Current through TCR)');

legend1 = legend(axes1,'show');

set(legend1,'Position',[0.7095 0.7816 0.1959 0.141],'FontSize',14);

-----End of THD Itr calculation-----

```

% This is the sub function for EHDFC-TCR problem

```

function dXdt=EHDFC-TCRfunction(t,X)

```

```

kv=1;

```

```

w=2*pi*60;

```

```

Alpha_PhaseA=120*pi/180;

```

```

Alpha_PhaseB=120*pi/180;

```

```

Alpha_PhaseC=120*pi/180;

```

```

xtrans=0.001;

```

```

rtrans=0.01;

```

```

xcap=0.015;

```

```

xrea=0.003;

```

```

harmonics=15;

```

```

Le=xtrans/w;

Re=rtrans;

C=1/(w*xcap);

Lre=xrea/w;

ye2=zeros(2*harmonics+1,2*harmonics+1);

N=1;

for k=-harmonics:harmonics

    ye(N,N)=rtrans+i*k^(sign(xtrans))*xtrans;

    N=N+1;

end

ye2(harmonics+1,harmonics+1)=rtrans+1e-9;

ye1 = inv(ye2)

ye=[ye1 ye1*0 ye1*0; ye1*0 ye1 ye1*0 ;ye1*0 ye1*0 ye1];

ycap=inv(form_Zm(0,-xcap,h));

N=1;

for k=-harmonics:harmonics

    ycap (N,N)=0+i*k^(sign(-xcap))* -xcap;

    N=N+1;

end

ycap (harmonics+1,harmonics+1)=rtrans+1e-9;

ycap_wye=[ycap ycap*0 ycap*0; ycap*0 ycap ycap*0 ;ycap*0 ycap*0 ycap];

U1=form_Zm(1,0,h);

o=zeros(2*harmonics+1,2*harmonics+1);

```

```

o1=[o o o;o o o;o o o];
N=1;
for k=-harmonics:harmonics
    D (N,N)=0+i*k^(sign(w))* w;
    N=N+1;
end
D (harmonics+1,harmonics+1)=0+1e-9;
o2=zeros(93,1);
Dd=[D o o;o D o;o o D];
A4=-(Re/Le)*U1;
A5=(-1/Le)*U1;
A1=[A4 o o;o A4 o;o o A4]-Dd;
A2=[A5 o o;o A5 o;o o A5];
A3=[U1/C o o;o U1/C o;o o U1/C];
error1=1;
iter1=0;
vap1=kv;
vbp1=kv;
vcp1=kv;
va11=zeros(2*harmonics+1,1);
va11(harmonics)=-i*vap1/2*exp(-i*0*pi/180);
va11(harmonics+2)=-i*vap1/2*exp(i*0*pi/180);
vb11=zeros(2*harmonics+1,1);

```

```

vb11(harmonics)=i*vbp1/2*exp(-i*-120*pi/180);
vb11(harmonics+2)=-i*vbp1/2*exp(i*-120*pi/180);
vc11=zeros(2*harmonics+1,1);
vc11(harmonics)=i*vcp1/2*exp(-i*120*pi/180);
vc11(harmonics+2)=-i*vcp1/2*exp(i*120*pi/180);
v11=[va11;vb11;vc11];
va21 = va11;
vb21 = vb11;
vc21 = vc11;
v201=[va21;vb21;vc21];
ytcr_ab_delta= calc_tcr(va21-vb21,Alpha_PhaseA, harmonics,1,xtcr); [10]
ytcr_bc_delta= calc_tcr(vb21-vc21,Alpha_PhaseB, harmonics,1,xtcr); [10]
ytcr_ca_delta= calc_tcr(vc21-va21,Alpha_PhaseC, harmonics,1,xtcr); [10]
ytcr_delta=[ytcr_ab_delta+ytcr_ca_delta   -ytcr_ab_delta           -ytcr_ca_delta
            -ytcr_ab_delta           ytcrc_bc_delta+ytcr_ab_delta   -ytcr_bc_delta
            -ytcr_ca_delta           -ytcr_bc_delta           ytcrc_ca_delta+ytcr_bc_delta]/3;
ysvc=ycap_wye+ytcr_delta;
v21=inv(ye+ysvc)*ye*v11;
va21=v21(1:2*harmonics+1);
vb21=v21(2*harmonics+2:4*harmonics+2);
vc21=v21(4*harmonics+3:6*harmonics+3);
[sigma1a1,sigma2a1,thetaxa1] = thy_turn_on_off(va21,Alpha_PhaseA,harmonics);
[10]

```

```

sva1=calc_s(sigma1a1,sigma2a1,thetaxa1,harmonics); [10]
sa1=calc_Fm(sva1,harmonics); [10]
[sigma1b1,sigma2b1,thetaxb1] = thy_turn_on_off(vb21,Alpha_PhaseB,harmonics);
[10]
svb1=calc_s(sigma1b1,sigma2b1,thetaxb1,harmonics); [10]
sb1=calc_Fm(svb1,harmonics); [10]
[sigma1c1,sigma2c1,thetaxc1] = thy_turn_on_off(vc21,Alpha_PhaseC,harmonics);
[10]
svc1=calc_s(sigma1c1,sigma2c1,thetaxc1,harmonics); [10]
sc1=calc_Fm(svc1,harmonics); [10]
%-----
error2=1;iter2=0;
if t>=0.05 && t<=0.1
    vap2=1.2*kv;vbp2=1.05*kv;vcp2=1.1*kv;
    va12=zeros(2*harmonics+1,1);
    va12(harmonics)=-i*vap2/2*exp(-i*0*pi/180);
    va12(harmonics+2)=-i*vap2/2*exp(i*0*pi/180);
    vb12=zeros(2*harmonics+1,1);
    vb12(harmonics)=-i*vbp2/2*exp(-i*-122*pi/180);
    vb12(harmonics+2)=-i*vbp2/2*exp(i*-122*pi/180);
    vc12=zeros(2*harmonics+1,1);
    vc12(harmonics)=-i*vcp2/2*exp(-i*118*pi/180);
    vc12(harmonics+2)=-i*vcp2/2*exp(i*118*pi/180);

```

```

v12=[va12;vb12;vc12];

v11=v12;

[va22,vb22,vc22]=source_harmonics(vap2,vbp2,vcp2,0,-122,118,harmonics);

va22=zeros(2*harmonics+1,1);

va22(harmonics)=i*vap2/2*exp(-i*0*pi/180);

va22(harmonics+2)=-i*vap2/2*exp(i*0*pi/180);

vb22=zeros(2*harmonics+1,1);

vb22(harmonics)=i*vbp2/2*exp(-i*-122*pi/180);

vb22(harmonics+2)=-i*vbp2/2*exp(i*-122*pi/180);

vc22=zeros(2*harmonics+1,1);

vc22(harmonics)=i*vcp2/2*exp(-i*118*pi/180);

vc22(harmonics+2)=-i*vcp2/2*exp(i*118*pi/180);

v202=[va22;vb22;vc22];

ytr_ab_delta= calc_tcr(va22-vb22,Alpha_PhaseA, harmonics,1,xtr); [10]

ytr_bc_delta= calc_tcr(vb22-vc22,Alpha_PhaseB, harmonics,1,xtr); [10]

ytr_ca_delta= calc_tcr(vc22-va22,Alpha_PhaseC, harmonics,1,xtr); [10]

ytr_delta=[ytr_ab_delta+ytr_ca_delta   -ytr_ab_delta           -ytr_ca_delta
            -ytr_ab_delta           ytr_bc_delta+ytr_ab_delta   -ytr_bc_delta
            -ytr_ca_delta           -ytr_bc_delta           ytr_ca_delta+ytr_bc_delta]/3;

ysvc=ycap_wye+ytr_delta;

v22=inv(ye+ysvc)*ye*v12;

va22=v22(1:2*harmonics+1);

vb22=v22(2*harmonics+2:4*harmonics+2);

```

```

vc22=v22(4*harmonics+3:6*harmonics+3);

[sigma1a2,sigma2a2,thetaxa2] = thy_turn_on_off(va22,Alpha_PhaseA,harmonics);

[10]

sva2=calc_s(sigma1a2,sigma2a2,thetaxa2,harmonics); [10]

sa2=calc_Fm(sva2,harmonics); [10]

sa1=sa2;

[sigma1b2,sigma2b2,thetaxb2] = thy_turn_on_off(vb22,Alpha_PhaseB,harmonics);

[10]

svb2=calc_s(sigma1b2,sigma2b2,thetaxb2,harmonics); [10]

sb2=calc_Fm(svb2,harmonics); [10]

sb1=sb2;

[sigma1c2,sigma2c2,thetaxc2] = thy_turn_on_off(vc22,Alpha_PhaseC,harmonics);

[10]

svc2=calc_s(sigma1c2,sigma2c2,thetaxc2,harmonics); [10]

sc2=calc_Fm(svc2,harmonics); [10]

sc1=sc2;

end

%-----

A6=[(1/Lre)*sa1 o o;o (1/Lre)*sb1 o;o o (1/Lre)*sc1];

U21=[v11;o2;o2];

A11=[A1 A2 o1;A3 o1-Dd -A3;o1 A6 o1-Dd];

dXdt=A11*X+(1/Le)*U21;

```